The Dissertation Committee for Xiaoguang Zheng Certifies that this is the approved version of the following dissertation:

Long-Wavelength, High-Speed Avalanche Photodiodes and APD Arrays

Committee:

____
Joe C. Campbell, Supervisor

____
Archie L. Holmes, Jr.

____
Dean P. Neikirk

____
John G. Ekerdt

____
Ananth Dodabalapur

Long-Wavelength, High-Speed Avalanche Photodiodes and APD Arrays

by

Xiaoguang Zheng, B.S., M.S.E.E.

Dissertation

Presented to the Faculty of the Graduate School of
the University of Texas at Austin
in Partial Fulfillment
of the Requirements
for the Degree of
Doctor of Philosophy

The University of Texas at Austin

December 2004

Dedicated

To

my parents, my wife, and my daughter

Acknowledgements

I feel very indebted to my advisor, Professor Joe C. Campbell. I joined his research team in the year 1999. With his great patience, I gradually excavated a path along which I explored a limited part of unknown territories in the avalanche photodetector world. His guidance, encouragement, and constant support were indeed vital to my graduate studies at UT Austin. His dedication and enthusiasm for photodetector research have been and will continue to be tremendously beneficial to me in my future career pursuits.

I want to express my deep gratitude to Dr. Archie L. Holmes, Jr., who has provided strong support for my research. I benefited greatly from discussions with him and was inspired by his sharp insights. I would like to thank Dr. Dean P. Neikirk, Dr. John G. Ekerdt, and Dr. Ananth Dodabalapur for serving on my dissertation committee and kindly going through my dissertation. I am very grateful to Dr. Larry Coldren at the University of California, Santa Barbara, for the strong MBE material support from his team, which was essential for my research. I am grateful to Dr. David Tzeng of Multiplex Inc. for his support on my integrated APD receiver studies. I am very thankful to Dr. Joseph Boisvert of Spectrolab Inc. for the support his team provided for my InAlAs APD array study. I would like to thank Dr. Stephane Demiguel for his support and collaboration on my waveguide APD study. I am also grateful to Dr. Jean Decobert and Dr. Nadine Tscherptner of Alcatel Inc. in France for their excellent waveguide APD epi-structure.

I also acknowledge my gratitude to Dr. John P. R. David at the University of Sheffield (UK) for his many incisive discussions on my AlGaAs APD studies.

I would like to thank my fellow group members, Ping Yuan, Geffory Kinsey, Shuling Wang, Xiaowei Li, Ning Li, Feng Ma, Ariane L. Beck, Gauri Karve, Bo Yang, Jean Hsu, Zhengmao Ye, Jungwoo Oh, Jeremy Schaub, Charles C. Collins, Sebastian Csutak, and Ting Li. It is impossible to enumerate all the contributions they made to my research but to name a few: Ping Yuan, Geffory Kinsey, Jeremy Schaub, and Ting Li showed remarkable patience as my mentors when I first joined this wonderful team and continued to be supportive even after their gradation. Feng Ma, Shuling Wang, and Xiaowei Li provided helpful information for my AlGaAs APD study with their excellent impact ionization modeling. Ning Li has been very helpful with my speed measurements. He also helped with my wafer bonding experiments. Jean Hsu was a great contributor for the InAlAs APD array study and did a lot excellent work for APD device processing and characterization.

I want to thank Xiaoguang Sun and Jeffery B. Hurst from the MBE group both for growing many crystals used in my AlGaAs APD and wafer-bonded APD studies and for their fruitful collaborations. Many special thanks go to Andrew Huntington and Chad Wang of the University of California, Santa Barbara, for providing me with many wonderful wafers for my APD focal-plane array study and 10Gb/s telecommunication APD study. They all deserve special recognition for their contributions.

I want to express special thanks to Ariane Beck and Jeff B. Hurst. Jeff proofread 3 Chapters of my dissertation, and Ariane put in a lot of her time and efforts in proofreading the rest of it.

Last but wholehearted thanks go to my wife, Minghong Li, and my daughter Wenting, for their unreserved and constant love and support.

Long-Wavelength, High-Speed Avalanche Photodiodes and APD Arrays

Publication No._____________

Xiaoguang Zheng, Ph.D.
The University of Texas at Austin, 2004
Supervisor: Joe C. Campbell

In optical receivers avalanche photodiodes (APDs) are frequently the photodetectors of choice due to high sensitivity afforded by their internal gain. APD noise and bandwidth are strongly dependent on the carrier impact ionization statistics in the APD gain region. Low noise comparable to silicon APDs was observed in $Al_{0.9}Ga_{0.1}As$ APDs, due to larger carrier impact ionization coefficients ratio. A long-wavelength AlGaAs APD was therefore developed using a direct wafer-bonding technology to demonstrate long-wavelength absorption on GaAs substrates. For InP-based long-wavelength APDs, InAlAs lattice-matched to InP provides better noise and speed performances than InP due to larger ratio of carrier impact ionization coefficients. A thinner InAlAs layer provides even lower multiplication noise and a higher gain-bandwidth product than a bulk material due to pronounced carrier dead-space effect. Demonstrating high-speed, high-sensitivity APDs for fiber-optic communications is one of the primary tasks for this work. For 10Gb/s tele-communications, high carrier saturation velocities (>10^7cm/s) in $In_{0.53}Ga_{0.47}As$ allow a thick absorbing layer (>=1µm) in APDs. In order to improve APD sensitivity, a thin InAlAs material was further incorporated to achieve high avalanche gains with less bandwidth penalty. A ~-29.5dBm optical receiver sensitivity was achieved using a 200-nm InAlAs APD. For the 40Gb/s applications, carrier saturation velocity sets an upper limit of absorbing layer thickness to less than a quarter micron. It is necessary to separate photon absorption from carrier transport to fundamentally circumvent speed constraint on APD's responsivity. One solution is using a waveguide structure through which the incoming light is coupled into a thin absorbing layer in a direction normal to that carriers transport. Using this type of device structure, sensitivity becomes a function of device length rather than just the absorbing layer thickness. An InAlAs waveguide APD with both high responsivity (>0.62A/W) and broad bandwidth (>34GHz) was demonstrated, based on this scheme. In addition to telecommunications, long-wavelength InAlAs APDs, which provide broad wavelength coverage, high detection sensitivity, high gain uniformity, low dark currents at room temperature, and broad bandwidth, are also promising for the near-infrared three-dimensional imaging applications. A high-speed 40X40 InAlAs APD array was demonstrated for this application.

Table of Contents

Chapter 1

Introduction

As early as two centuries ago, people learned, intuitively, the idea of communicating with each other using light. During the Western Zhou Dynasty in China (781−770 BC), an “alerting system” was built in which “warning messages” could be transmitted, using lighting-torches, for hundreds of miles through relaying-towers, even though its performance was sensitive to the climate. The development of optical communication technologies has continued throughout human history. In 1880, four years after the invention of the first telephone, Alexander Graham Bell proposed his method of optical communication. Only with the invention of lasers, photodetectors, and most importantly, the low-loss silica optical fibers, was the dream of optical communication realized. Photodetector sensitivity and speed, which are crucial to a telecommunications system, strongly influence the number of optical repeaters required, thus determining the overall system cost, performance, and reliability [1-1]. Imaging and sensor related applications have also become areas for high-sensitivity, high-speed long-wavelength photodetectors. The avalanche photodiode (APD), which provides high-sensitivity as well as high-speed, is one of the most important types of photodetectors for these applications.

1.1 APDs for Telecommunications Applications

An optical fiber communication system consists of optical transmitters for the signal source, optical fibers for signal transmission, and optical receivers for signal detection. High-speed electronic signals are converted into optical signals through the transmitter and are subsequently coupled into the transmission medium – optical fibers. For digital systems these optical signals then travel along the optical fibers in the form of optical pulses. At the receiving end the optical receiver recovers the optical signals, which are often highly attenuated due to transmission loss, and converts them back into electrical signals. A photodetector in the front end of the optical receiver module plays a crucial role for the optical-to-electrical (O-to-E) signal conversion, in terms of both sensitivity and speed. These two characteristics, sensitivity and speed, are the key performance criteria for the telecommunications photodetector design. High sensitivity requires a large absorbing volume in order to obtain high responsivity in a photodetector. On the other hand, high operation bandwidth (speed) is achieved by shrinking the device active region to minimize the carrier transit time. Consequently, there is a performance tradeoff linked to the thickness of the absorbing layer. At a specific operational data rate, which is regulated by existing communication standards, such as 10Gb/s (actually 9,9853Gb/s) for the OC-192 and four times higher for OC-768, successful photodetector design becomes a task of achieving maximum sensitivity at a required device speed.

Avalanche photodiodes, which have been studied for more than 35 years, can fundamentally relieve this speed-sensitivity constraint. An APD provides higher detection sensitivity than a *p-i-n* photodiode, assuming similar device dimension, due to internal avalanche gain via carrier impact ionization. Even though APDs have many disadvantages, compared to *p-i-n* photodiodes, such as complicated device structure, stringent material quality requirements, inferior temperature stability, higher reverse bias, excessive shot noise, and degraded bandwidth at high gains, high performance APDs are still the preferred detector for many applications.

For 10Gb/s telecommunications APDs, high saturation velocities of carriers (>10^7 cm/s) allow the use of a relatively thick absorbing layer (i.e. ≥1μm). This greatly simplifies the APD's optical coupling design by simply using a normalized backside-illumination scheme in conjunction with a proper anti-reflection coating. As a result, a typical unity-gain external quantum efficiency of ≥50% can be easily achieved at wavelength of 1.55μm. In order to achieve higher responsivity recent research has focused on identifying better materials or improved device structures, to obtain the highest avalanche gain with minimum bandwidth penalty.

For a 40Gb/s APD, the carrier saturation velocity sets the upper limit on absorption layer thickness to less than a quarter micron. To acquire more efficient optical to electrical conversion within such a thin absorption layer, it is necessary to separate the incoming photon absorption from the carrier transport, which will fundamentally circumvent device speed constraints on photon absorption. Using a resonant cavity, the optical to electrical conversion efficiency can be greatly improved from the multiple passes of the incident light through the absorbing layer [1-2]-[1-5]. But this approach adds considerable complexity to the device design, material growth, device fabrication, and, most of all, generates an extremely narrow absorption spectrum, due to the cavity resonance, that leads to wavelength specific operation. An alternative for enhancing APD sensitivity is use of a waveguide structure, through which incoming light is coupled into the absorbing layer in a direction normal to carrier transport. In this type of device structure, sensitivity becomes a function of device length rather than the thickness, and better optical to electrical conversion is expected due to a relatively longer optical absorption length. This method is simpler but more effective in comparison to the resonant-cavity scheme. Difficulty still exists in coupling light from the optical fiber, from which the beam-waist is usually several microns in diameter, into a fairly thin absorbing layer that is far less than a micron in thickness [1-6]-[1-9].

One of the main directions of my research was to develop high-sensitivity, high-speed avalanche photodetectors for both 10Gb/s and 40Gb/s applications. Accordingly, avalanche photodiodes, using bulk InGaAs as the absorbing material and a thin InAlAs material as the gain region material, were developed to demonstrate high-sensitivity at 10Gb/s data rate. Integration of those APDs with amplification circuits resulted in high APD receiver sensitivity. Based on the InGaAs/InAlAs/InP material system, the first high-responsivity evanescently coupled avalanche photodetector was demonstrated for 40Gb/s telecommunications needs, by using a multimode input waveguide scheme. This waveguide avalanche photodiode has exhibited high unity-gain responsivity, as well as a high gain-bandwidth product, under small signal conditions.

1.2 APDs for Imaging Applications

Long-haul, high-bit-rate optical receivers utilize APDs because they provide better sensitivity than *p-i-n* photodiodes. In addition to this application, APDs can be fabricated in a two-dimensional focal-plane array to meet the requirements of imaging applications, such as high resolution position emission tomography (PET)

[1-10], detection of internally reflected Cherenkov light (DIRC) [1-11], or scintillating fiber readouts [1-12], where silicon APDs have already been widely used as a compact solid-state alternative to photo-multiplier tubes (PMTs). Furthermore, rapidly emerging three-dimensional (3-D) near-infrared imaging applications [1-13] require focal-plane APD arrays that have broad wavelength coverage ($0.8\mu m \leq \lambda \leq 2.0\mu m$). In addition to this wavelength requirement, infrared photodetector arrays should also provide high detection sensitivity, high gain uniformity, and low dark currents at room temperature, to meet stringent imaging quality requirements. Finally, operation bandwidth is another critical issue for fabricating imaging photodetector arrays because a sampling rate over 1Gsps is required in a 3-D imaging system to obtain the necessary spatial resolution. Every APD device in the entire focal-plane array must be fabricated to concurrently satisfy all of the above necessities. For this reason, my research diverged from telecommunications APDs into developing long-wavelength focal-plane APD arrays and large-area APD sensors, based on similar InP material systems.

1.3 Organization of Dissertation

All of my finished research has focused on studies of long-wavelength compound APDs and arrays, based either on GaAs or InP material systems. In Chapter 2, commonly used photodetectors and the requirements for APDs are introduced. Chapter 3 presents general APD design methods and several specific issues related to the design of high-speed APDs with separate absorption, charge, and multiplications (SACM) regions. In Chapter 4, multiplication noise characteristics of $Al_xGa_{1-x}As$ avalanche photodiodes with various *Al* concentrations are presented. In Chapter 5, temperature dependence of breakdown voltage, multiplication noise, and impact ionization coefficients of $Al_xGa_{1-x}As$ avalanche photodiodes are reported for a wide temperature range. In Chapter 6, the first GaAs-based long-wavelength avalanche photodiode is demonstrated using a direct wafer bonding (DWB) technique. In Chapter 7, InGaAs/InAlAs focal-plane APD arrays are presented. In Chapter 8, large-area InGaAs/InAlAs APD results are demonstrated for infrared sensor applications. Dark current characteristics of MBE-grown InGaAs/InAlAs APDs are also thoroughly analyzed. In Chapter 9, a high-sensitivity integrated receiver is demonstrated by integrating a high-speed InGaAs/InAlAs APD with a commercially available pre-amplifier and a limiting amplifier. APD results, as well as receiver-related design, fabrication, and testing issues, are also discussed in this chapter. In Chapter 10, a novel multimode evanescently-coupled waveguide APD, with a high gain-bandwidth product and a high unity-gain responsivity is demonstrated. In Chapter 11, the work in this dissertation is summarized, and future directions for further APD performance improvement are proposed.

Chapter 2

Requirements for Long-Wavelength Avalanche Photodiodes

Fiber-optic communication systems have already become the dominant backbone of modern information technology. The fast-booming telecommunication markets, especially those for networking-related applications, have imposed great challenges to the current technologies. Ever-increasing demands of fiber-optic communication systems require optoelectronic components that provide larger signal processing capacity, higher data transmission rate, superior reliability, and most importantly, lower cost. In fiber-optic communication systems, photodiodes are not only essential but also very critical components through which the fast information-carrying optical signals are transformed back into electrical signals for further de-multiplexing and decoding at relatively lower data rates. In 3D-imaging applications, APDs and read-out circuits actually construct an array of optical receivers. The role that an APD plays in an optical receiver demands that they must meet stringent system requirements, both on performance and on signal capacity. Since a photodiode is normally utilized at the front end of an optical receiver, the signal-to-noise ratio (SNR) of the photodiode directly affects the overall SNR of the optical receiver. High SNR photodiodes are therefore indispensable to obtain high-sensitivity optical receivers. The requirement of high data transmission rate poses another challenge for photodiodes. To satisfy this demand, considerable effort has been focused, over the past 20 years, on developing high-speed photodetectors. As a consequence, various types of photodetectors, such as MSM photodiodes, *p-i-n* photodiodes, avalanche photodiodes (APDs), etc., have been developed to meet those requirements [2-1]-[2-11].

2.1 Criteria of Photodiode's Performance

The attenuation characteristic of a silica optical fiber, as shown in Fig. 2.1, determines the operating wavelength ranges adopted for long-haul fiber-optic communication systems.

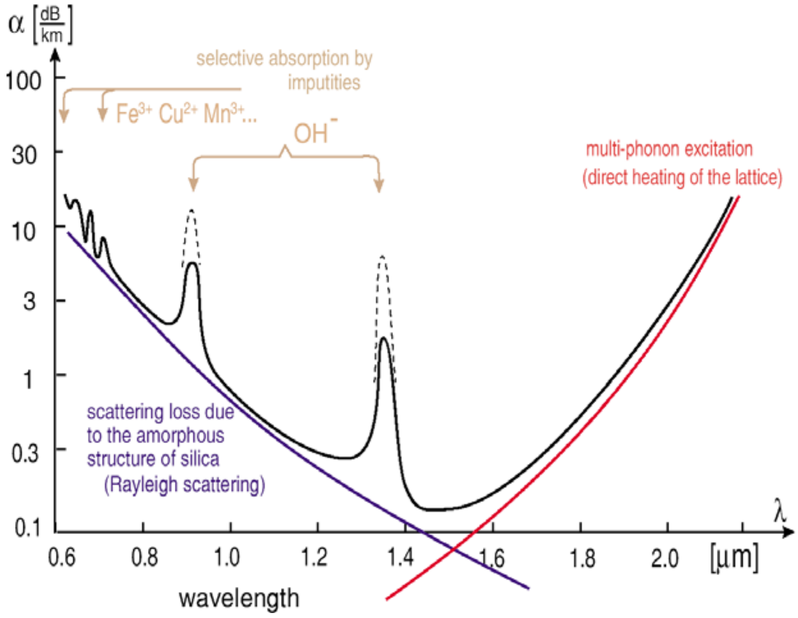

Fig2.1 Typical optical absorption loss characteristics of a silica fiber

Since silica optical fiber exhibits minimum dispersion at wavelength near 1.3μm and minimum optical loss at 1.55μm, respectively, these two wavelengths have become widely accepted standards for both light emitters and photodetectors in long-haul fiber-optic communication systems. This is the most important specification for photodetector designers. It determines the *detection wavelength* of a photodiode, and thus determines the semiconductor materials and device structures to be used for photodiode design and fabrication. From the material point of view, with the exception of germanium (bandgap energy Eg ~0.6eV), no natural semiconductors are available to satisfy the bandgap requirement for a long wavelength photodiode that has an upper detection wavelength edge up to 1.6μm. There exist, however, at least two inherent disadvantages of germanium, (1) small bandgap value, and (2) indirect nature of its energy band minima.

The small bandgap of *Ge* leads to high noise in detectors at room temperature and above, due to high dark current levels. Furthermore, germanium material has material and technical limitations that have kept it from direct optoelectronic integration.

Fortunately, several III-V compound alloys can be used as suitable alternative light absorbing materials in the long-wavelength detection ranges. Fig. 2.2 shows a diagram of bandgap energy as a function of lattice constant for many of the compound semiconductors. Some III-V ternaries and quaternaries such as InGaAs, GaAsSb, and InGaAsP that are lattice-matched to InP substrates exhibit appropriate long wavelength absorption properties. More specifically, $In_{0.53}Ga_{0.47}As$, which has a wavelength cut-off edge extending up to ≥1.7µm and covers both 1.3µm and 1.55µm transmission windows of optical fibers, is frequently used for long-haul fiber-optic communication photodetectors, as has been illustrated in Fig. 2.

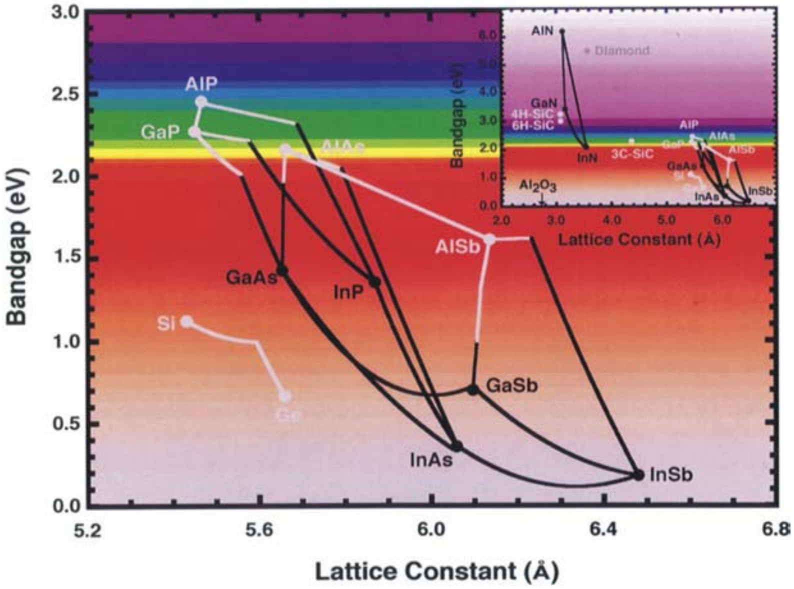

Fig. 2.2 Energy band gap of most semiconductors and alloys

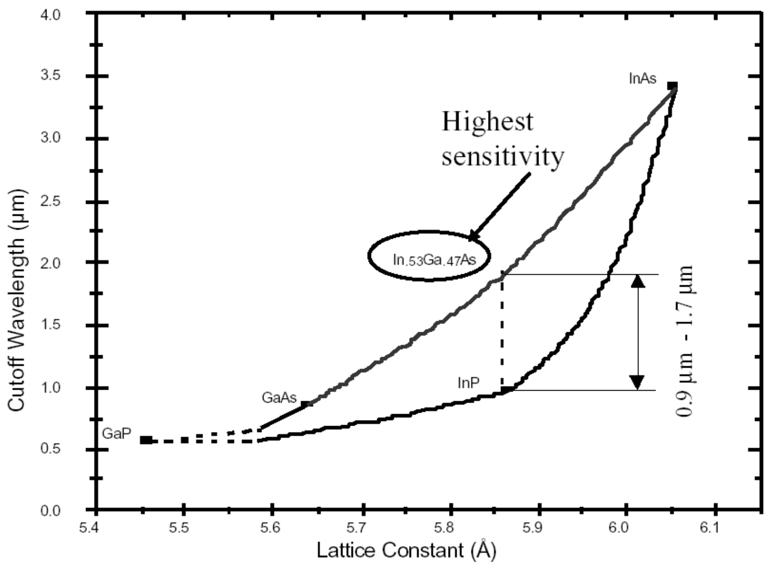

Fig. 2.3 Cut-off wavelength of InP-lattice-matched $In_{0.53}Ga_{0.47}As$

Responsivity R, defined as the photocurrent generated per unit incident light power, which is expressed in terms of *A/W*, is commonly used to characterize optical-to-electrical conversion efficiency of a photodetector. This is another important parameter for assessing a photodiode's performance. Responsivity can be equivalently characterized in term of the *external quantum efficiency*, η_{ext}, which is 100% when each incoming photon excites an electron-hole pair that is eventually collected by the electrodes. Based on the above definitions, the relation between responsivity R and external quantum efficiency η_{ext} can be expressed as

$$\eta_{ext} = \frac{I / e}{P / h\nu} = \frac{h\nu}{e} R \ , \tag{2.1}$$

where I is the photo-generated current, P is the incident optical power, $h\nu$ is the incoming photon energy, and e is the electron charge. In order to obtain high signal to noise ratio (*SNR)* optical receivers and thus maximize the separation between optical repeaters in a long-haul system, photodetectors with high responsivity or high external quantum efficiency are always desired.

However, responsivity, or external quantum efficiency, cannot be used alone to determine the total *SNR* of a photodiode. Practically, the *noise* of a photodiode will also degrade its *SNR*. The ability of an optical receiver to detect presence or absence of input optical signals rests upon its ability to discriminate between the minimum detectable input optical signal power and the noise power generated by the integrated receiver itself within an identical working bandwidth. The noise is one of the most critical parameters of photodetectors. Normally, the noise is described in terms of noise power spectrum density $<i^2>$, which is the quadratic mean of the noisy current within a unity frequency bandwidth. The total noise appearing in an infrared communication system may come from a variety of noise sources, which are generally categorized into three types: (1) photodetector noise, (2) amplifier noise, and (3) noise from the background optical radiation. For photodiodes operating at high frequencies, thermal noise and shot noise are two main types of noise sources, which can be characterized by a uniform noise spectral density within the entire detection wavelength range. Thermal noise originates from *Brownian* motion of carriers that exists in any type of resistive components. It is usually expressed as

$$< i_{thermal}^{2} >= \frac{4kT}{R}B , \tag{2.2}$$

where B is the operation bandwidth, T is the absolute temperature, k is the Boltzmann constant, and R is the load resistance. Shot noise is another critical type of noise in a photodiode, which is correlated with the discrete and random nature of the charge (carrier) movement. It can be expressed as

$$< i_{shot}^{2} >= 2eIB \ , \tag{2.3}$$

where e is the electron charge, I is the current flow through the photodiode, and B is the photodiode bandwidth. Since these two random noise sources are statistically independent, the summation of their quadratic mean value gives the total noise current density $<i_n^2>$ in the photodiode

$$< i_{n}^{2} >=< i_{thermal}^{2} > + < i_{shot}^{2} >= \frac{4kT}{R}B + 2eIB \ , \tag{2.4}$$

From this equation, it can be inferred that high resistance is desirable to reduce the thermal noise and to enhance the *SNR* of a photodetector. However, the resulting high *RC* constant reduces the bandwidth of the detector and thus degrades the overall *SNR* of an integrated optical receiver. As a result, for high-speed applications, tradeoffs must be made both at the device-level and at the circuit-level.

Bandwidth is another important factor for telecommunications photodiode design. The bandwidth of photodiodes needs to be high enough to support high data transmission rate in a long-haul telecom system. The bandwidth of a PIN photodiode is primarily determined by the following factors: (1) the election and hole transit times, (2) the *RC* time constant, (3) minority carrier diffusion, (4) carrier trapping at hetero-interfaces, and (5) signal delay due to photodiode packaging.

The transit times depend on the device active region thickness and the electron and hole saturation velocities. The most common approach to reducing the transit times is to utilize thin absorbing layers.

When a significant portion of the incident photon absorption occurs out of the depleted region where the electric field intensity is very low, the photo-generated carriers will transport via carrier diffusion, a process that is much slower compared to carrier drift. Since the diffusion time can be comparable to the carrier lifetime, the efficiency and the bandwidth will be adversely affected if diffusion is a dominant effect. To circumvent these limitations the photodiode structure is usually designed so that the entire absorbing layer is depleted.

If heterostructures are necessary in a photodiode design, carrier trapping due to conduction band and valence band discontinuities can also restrict the bandwidth. Carriers trapped at heterojunctions escape by recombination through interface traps or thermionic emission; both are slow processes. Hole trapping is more significant in a long-wavelength InGaAs/InP photodiode because the valence band offset is larger (~0.4*eV*) at the InP/InGaAs interface than that of the conduction band. Practically, in a long-wavelength photodiode design either a moderately high electric field is applied at the hetero-interface or the band discontinuity is graded with a compositional alloy so that carrier-trapping effect can be greatly reduced.

The *RC* time constant is usually reduced by decreasing the photodiode active area, which, in turn, lowers total junction capacitance. However a small device area can result in high contact resistance, which will increase *RC* constant. Packaging induced parasitic will cause bandwidth degradation, but can be addressed using advanced device bonding technology.

2.2 Commonly Used Semiconductor Photodetectors

2.2.1 Metal-Semiconductor-Metal Photodiodes

The simplest photodiode structure is the Metal-Semiconductor-Metal (MSM) photodiode, as shown in Fig. 2.4.

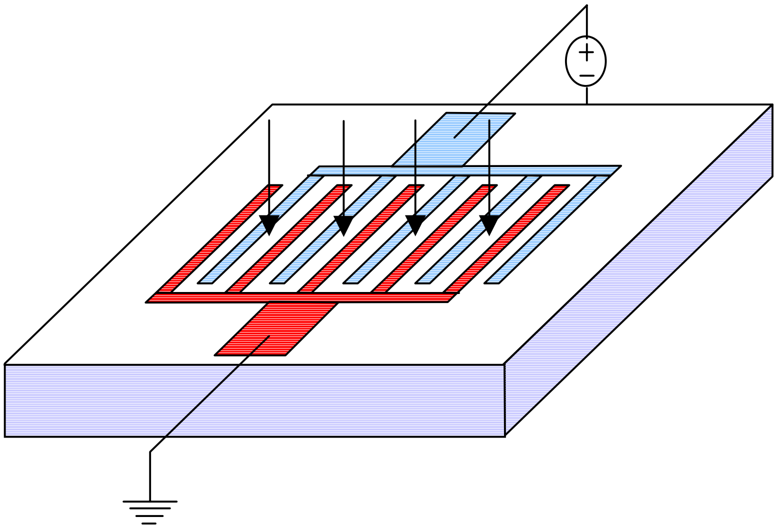

Fig. 2.4 Typical device structure of a Metal-Semiconductor-Metal photodiode

An MSM photodiode is formed by depositing two Schottky metal contacts on an unintentionally-doped semiconductor material, usually in the form of inter-digitated patterns. Due to their inherently planarized device structure and the fact that both contacts are on the top surface, MSM photodiodes are well suited for monolithic integration with subsequent microelectronic circuitry. This is the most prominent advantage of MSM detectors when compared with other types of photodiodes. The second advantage of an MSM photodiode is its potential for high-speed operation. Normally, the semiconductor region below and between the metal contacts is completely depleted. Under illumination, the photo-generated carriers in this region are immediately swept toward the metal electrodes. The response time of this type of photodiode is determined primarily by the transit time of the photo-generated carriers and the *RC* time constant. Since the Schottky junction capacitance of the MSM structure is usually very small, most photodetector bandwidth records have been achieved using MSM photodiodes. For example, with a spacing of approximately 1 μm between the metal fingers MSM photodiodes can achieve a bandwidth up to 50 GHz. By using a sub-micron photolithography the finger dimension and, thus, the junction capacitance can be greatly reduced. An MSM photodiode with an electrical bandwidth of 510 GHz has been demonstrated by using deep sub-micron fabrication technology [2-12].

One big disadvantage of the MSM type photodiode is its poor external quantum efficiency. Since the Schottky metal contacts are located on the device surface, almost half of the incident photons are blocked due to the contact shadowing effect. This problem can be solved, to an extent, by using transparent metal contacts or by using backside illumination. Another disadvantage of an MSM photodiodes is their relatively high dark current levels. Even at low electric field, the dark current level of an MSM photodiode is high due primarily to the high thermionic emission rate over the metal-semiconductor barriers. Using wider bandgap semiconductor materials, such as GaAs, AlGaAs, or InAlAs, the metal-semiconductor barrier height can be increased so that junction leakage (dark) current of a MSM diode is suppressed to a level comparable to a *p-n* junction. For long-wavelength applications, the narrow band-gap $In_{0.53}Ga_{0.47}As$ is commonly used as the absorbers. Low barrier height of Schottky contacts on $In_{0.53}Ga_{0.47}As$ often leads to intolerable high dark current level. A wide bandgap semiconductor, such as InAlAs, is normally grown on top of the narrow bandgap absorbing material to increase the barrier height and therefore decrease the total dark current density. This, however, can result in hole trapping, which degrades the bandwidth unless a graded layer is also utilized. The resulting penalty, therefore, is a somewhat more complex epitaxial growth process.

Due to the reasons discussed above, MSM photodiodes are not commonly used for long-haul fiber-optic communications, even though they can achieve wide bandwidths and compatibility with amplification circuitry.

2.2.2 *p-i-n* Photodiodes

The most extensively used semiconductor photodetector is the *p-i-n* photodiode. A schematic of a typical *p-i-n* structure and the electric field profile in the device are shown in Fig. 2.5. *P-i-n* photodiodes have been widely used in the fiber-optic communications, because they can achieve wide bandwidth, low dark current density, low noise, and high quantum efficiency. The *p-i-n* structure consists of an unintentionally doped layer (*n*- or *p*-, depending on the junction formation technique) sandwiched between p^+ and n^+ regions. Due to fairly low background doping level in the unintentionally-doped region, the free carriers are usually completely depleted at a low reverse bias, or sometimes even at a zero bias. Consequently, the electric field in the photodiode is almost totally confined within the intrinsic region and it is approximately constant throughout the depletion region.

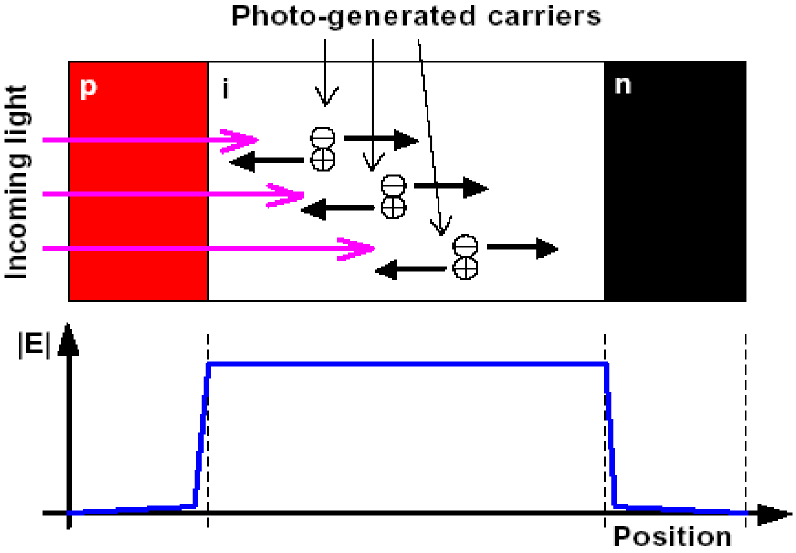

Fig. 2.5 Typical device structure of a *p-i-n* photodiode

In the depleted absorbing layer the photo-generated carriers travel at their saturation velocity v_{sat}. Similar to the MSM photodiode, the bandwidth of a *p-i-n* photodiode is determined by the carrier transit times or by the *RC* time constant. Since transit time, junction capacitance, and quantum efficiency are interdependent, in the design of a wide bandwidth *p-i-n* photodiode involves performance tradeoffs. Given a *p-i-n* diode with a totally depleted absorption layer, the external quantum efficiency, η_{ext}, can be written as

$$\eta_{ext} = (1 - R)(1 - e^{-\alpha d}), \tag{2.5}$$

where d is the width of the absorption region, α is the absorption coefficient, R is the reflectivity at the surface. The transit time component of the bandwidth for a *p-i-n* having total depletion region thickness D, is given by the expression [2-2]

$$f_{tr} \cong \frac{3.5\bar{v}}{2\pi D}, \quad \frac{1}{\bar{v}^4} = \frac{1}{2}\left(\frac{1}{v_e{}^4} + \frac{1}{v_h{}^4}\right) \tag{2.6}$$

where v_e and v_h are the electron and hole saturation velocities, respectively. The RC contribution to the bandwidth is

$$f_{RC} = \frac{1}{2\pi\tau_{RC}}, \qquad \tau_{RC} = RC, \tag{2.7}$$

It is primarily determined by the photodiode junction capacitance thus can be controlled through adjusting the device area to a value that is consistent with a desired bandwidth. For an optimal photodiode design, the total bandwidth of a *p-i-n* photodiode is expressed by the following equation [2-2]

$$B = \frac{1}{\sqrt{\left(\frac{1}{f_{RC}}\right)^2 + \left(\frac{1}{f_t}\right)^2}} \ \text{(Hz)}. \tag{2.8}$$

According to Equation (2.5), both a low reflectivity value (R) at the incidental light surface and a large absorbing region thickness are desirable to achieve a high quantum efficiency value and a low junction capacitance. However, a thicker absorber will decrease the photodiode bandwidth due to longer carrier transit time. Consequently, there exists a tradeoff between speed and quantum efficiency for *p-i-n* photodiode design. This tradeoff can be addressed by decoupling light absorption from the carrier transport. One solution is to use a resonant cavity [2-

13]~[2-15]. Another method is to use a waveguide device structure in which light travels perpendicular to the electrical path [2-16]. These two approaches will be discussed in detail in the next chapter.

2.2.3 Avalanche Photodiodes

In its simplest form, an avalanche photodiode (APD) has a similar device structure to a *p-i-n* photodiode, as shown in Fig. 2.5. However, unlike the *p-i-n*, the APD is always biased at a voltage that is close to its breakdown. Through the carrier impact ionization process, an APD provides more electron-hole pairs from the same amount of primary photo-generated carriers, compared to a *p-i-n* photodiode. To achieve gain in an APD, the electric field strength in the intrinsic region needs to be high enough to initiate for impact ionization, as illustrated in Fig. 2.6. The optical-to-electrical conversion efficiency of an APD, in terms of its external quantum efficiency, is greatly boosted by this carrier impact ionization process. If we assume the same optical absorption volume dimension for both a *p-i-n* and an APD, the external quantum efficiency of the APD can be written as

$$\eta_{ext} = M \cdot (1 - R)(1 - e^{-\alpha d}), \tag{2.9}$$

where d is the thickness of the absorption region, α is the absorption coefficient, R is the reflectivity of light incidental surface, and M is the avalanche gain obtained through carrier impact ionization. The gain M is given by the expression

$$M = \frac{i_{photo} - i_{dark}}{i_{primary,photo} - i_{primary,dark}}, \tag{2.10}$$

where i_{photo} and i_{dark} are the multiplied photocurrent and dark current, $I_{primary,photo}$ and $i_{primary,dark}$ are the primary photocurrent and dark current measured prior to the onset of carrier multiplication.

While M can be very large, the actual usable value of M for fiber optic receivers is normally between 10 and 20 depending on what kind of materials and device structures are used. The reason is that the impact ionization process is a stochastic process. Consequently, the total number of impact ionization events that result from a single carrier injected into the high field region varies from carrier to carrier. This is the source of "excess" noise of an avalanche photodiode.

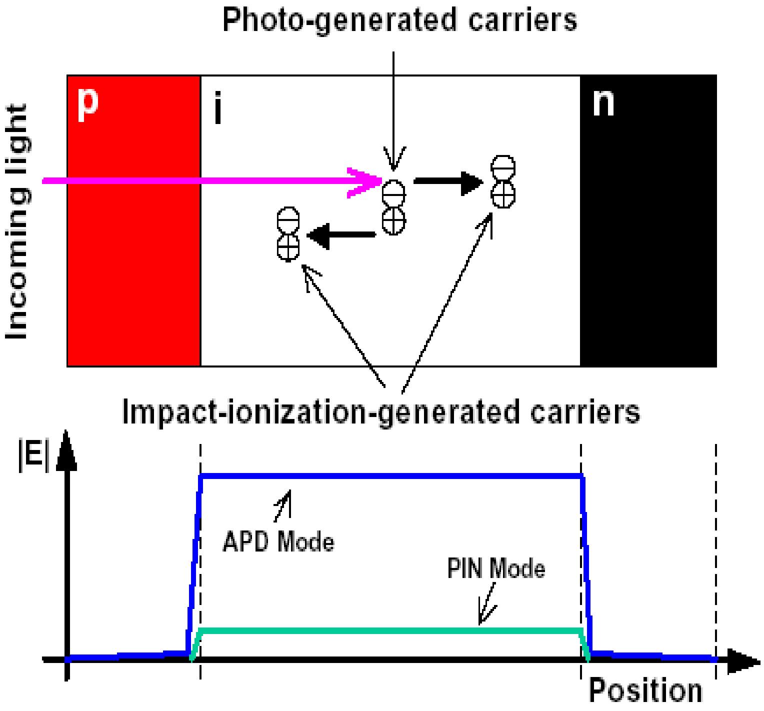

Fig. 2.6 Typical device structure of an avalanche photodiode

As has been discussed previously, in each APD there exists a high electric field region in which sufficient energy is provided to the photo-generated carriers to cause carrier impact ionization. As a result, offspring carriers are generated, all of which contribute to the APD gain. The statistical nature of this impact ionization process results in fluctuations in the number of secondary carriers (electron-hole pairs) generated from each parent carrier, which in turn leads to fluctuations the ensemble APD gain [2-17] [2-18]. This type of gain fluctuation will cause variations in the APD output current and increase the APD's total shot noise power above that of the multiplied shot noise power. Based on the statistics of the gain fluctuation, the APD excess noise can be characterized using an *excess noise factor*, *F(M)*, which is a measure of the standard deviation of the multiplication gain over its mean square value

$$F(M) = \frac{< M^2 >}{< M >^2} \quad . \tag{2.11}$$

According to the local impact ionization model developed by McIntyre [2-19] in which carrier impact ionization coefficients (i.e., the probabilities of impact ionization per unity distance) were assumed to be only a function of electric field strength, the value of the excess noise factor *F(M)* is directly determined by the ratio (the *k* value) of electron and hole impact ionization coefficients (here α for electrons and β for holes), as

$$F(M) = kM + (1-k)(2 - \frac{1}{M}) , \tag{2.12}$$

where $k=\beta/\alpha$ ($\beta<\alpha$) or $k=\alpha/\beta$ ($\alpha<\beta$), depending on which one is greater. Fig. 2.7 plots the calculated *F(M)* as a function of *M* for various values of *k*. Based on the local model, we can predicate that larger difference between carrier impact ionization coefficients leads to lower excess noise in an APD.

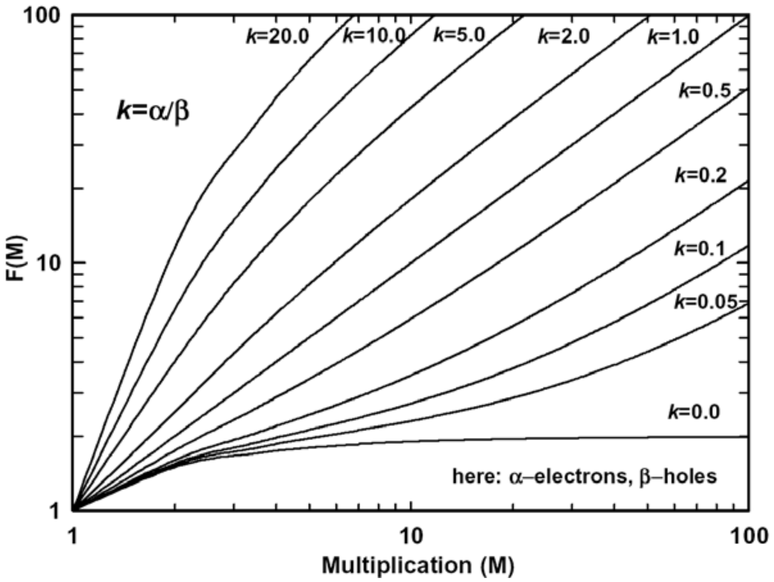

Fig. 2.7 Excess noise of an avalanche photodiode as a function of its multiplication gain, as predicated by the local-field model [2-20]

Another phenomenon associated with carrier multiplication is the effect of the gain process on bandwidth. At higher gains one primary carrier impact ionization event induces many consecutive impact ionization events. When $k \neq 0$ the sequential electron and hole impact ionizations creates "feedback loops" that cause an intrinsic device speed penalty and imposes an upper limit on the APD bandwidth, in terms of the gain-bandwidth product. This gain-bandwidth product is a well-accepted figure of merit for assessing APD speed performance. Even though the fundamental physics of APD speed degradation is straightforward, complicated calculations are necessary for detailed quantitative discussions [2-20]. However, a simplified illustration, as shown in Fig. 2.8, illustrates the origin of the gain-bandwidth product.

One extreme (worst) case is shown in the upper graph of Fig. 2.8, where $k=\beta/\alpha=1$. In this case, any single primary carrier, if accelerated in an adequately high electric field, is able to generate exactly two offspring carriers after each impact ionization event. As a consequence, one photo-generated primary carrier is enough to generate a chain of unlimited impact ionization events. The resulting bandwidth is therefore virtually zero. On the contrary, in another extreme (best) case where $\beta=0$, all the impact-ionization-generated holes traverse the multiplication region without initiating an impact ionization event. The resulting APD bandwidth is not limited by the gain dynamics, based on the local impact ionization model [2-20]. The calculated APD bandwidth at different k values as a function of multiplication gain is plotted in Fig. 2.9,

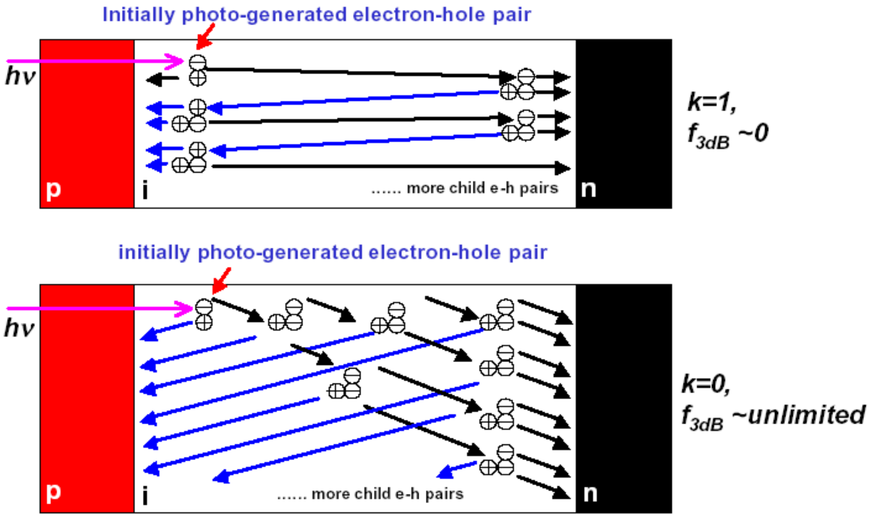

Fig. 2.8 Illustration of APD bandwidth degradation due to impact ionization

For the local field model, the performance of an APD is determined by its *k* value, an intrinsic property of each specific material. Lower values *k* of result in lower noise and higher gain bandwidth produces. As the APD multiplication layer is thinned, higher electric field is required to achieve a specific gain value than in a thicker device. It is well known that the impact ionization rate curves for electrons and holes merge at high electric fields [2-21], causing *k* to approach unity. Therefore it might be expected that the excess noise would increase as the multiplication thickness decreases. On the other hand, the opposite has been observed experimentally. The excess noise actually decreases in thin APDs [2-22]. This phenomenon has been attributed to the pronounced dead-space effect in thin multiplication layer APDs [2-22]~[2-25].

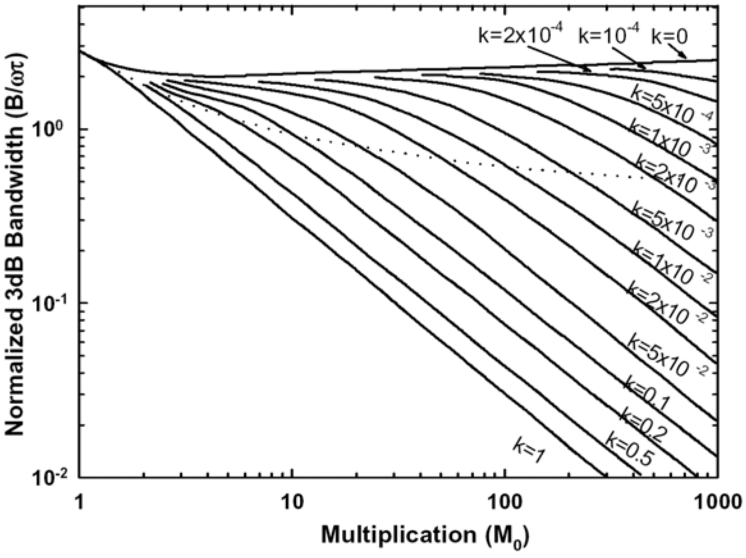

Fig. 2.9 APD bandwidth degradation, as predicated by local-field theory

The APD excess noise, fortunately, is actually determined by more factors than just a single *k*-value constraint. When a carrier, either a hole or an electron, initially enters the high-field region it must travel for a certain distance, the so-called dead-space, before it gains enough energy from the electric field to undergo a next impact ionization event. After impact ionization, the carriers typically occupy near the bottom of the energy band. Consequently, they are also subject to the dead-space effect. In thick devices this distance is negligible compared to the total device thickness, therefore the dead-space effect plays a minor role in the noise characteristics of thick APDs. As the device becomes thinner, however, the effect of dead space becomes more noticeable. As a result, the impact ionization events are more localized in a specific spatial range in the gain region and thus the gain process. The impact ionization event is more deterministic. This results in narrower gain spreading and lower excess noise. It is now very well known that thin APDs result in low excess noise in most III-V compound APDs [2-22]~[2-25]. A specific example is shown in Fig. 2.10, which shows noise measurements on a series of homojunction InAlAs APDs with various multiplication region thickness values. It is clear that excess noise decreases as the APD multiplication layer thickness is reduced, an indication of pronounced non-local effects in thin APDs. Further studies, enlightened by knowledge of the significance of the non-local effect in thin APDs, showed that APD excess noise can be further reduced by more pronounced localization of impact ionization events within a multiple-thin-layer structure, which has become known as impact-ionization-engineering (IIE) [2-26].

We have discussed several basic design rules to achieve low noise and high-speed APDs: 1) use materials that have lower ionization coefficient ratio (*k*) values,

2) design APDs with thin multiplication regions (dead-space effect), 3) use multiple thin layer structures to enhance the dead-space effect.

.

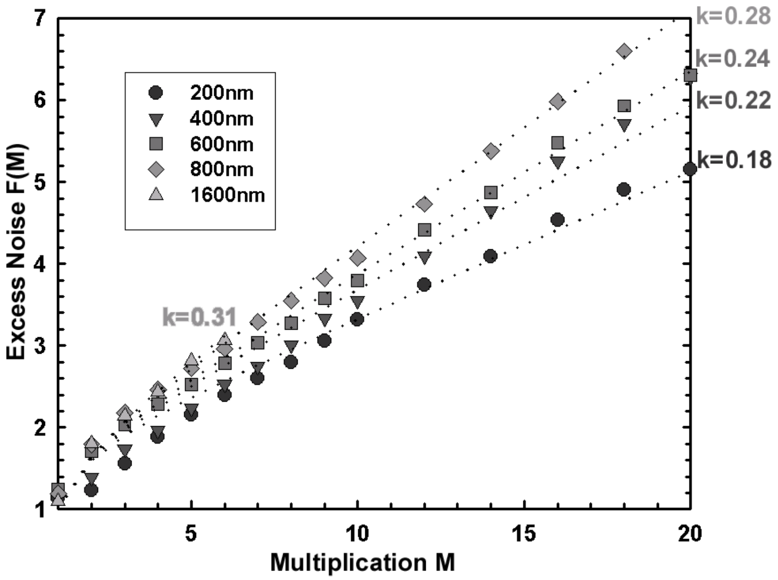

Fig. 2.10 Excess noise reduction in InAlAs APDs, as a function of layer thickness

2.2.4 Advantage of an APD over a *p-i-n* photodiode

As has been discussed in section 2.2, the primary noise sources of a *p-i-n* photodiodes are shot noise and thermal noise. Since these two noise sources are statistically independent, the resulting total noise power within a working bandwidth, B, may be expressed as

$$< i_{pin}^{2} >= 2e(I_{photo} + I_B + I_D)B + 4kTB / R \qquad (2.13)$$

where I_{photo}, I_B, and I_D are photocurrent, background-radiation-induced current, and dark current, respectively; R is the equivalent impedance determined by both photodiode output resistance and input impedance of the following electrical pre-amplifier stage, as shown in the top graph of Fig. 2.11.

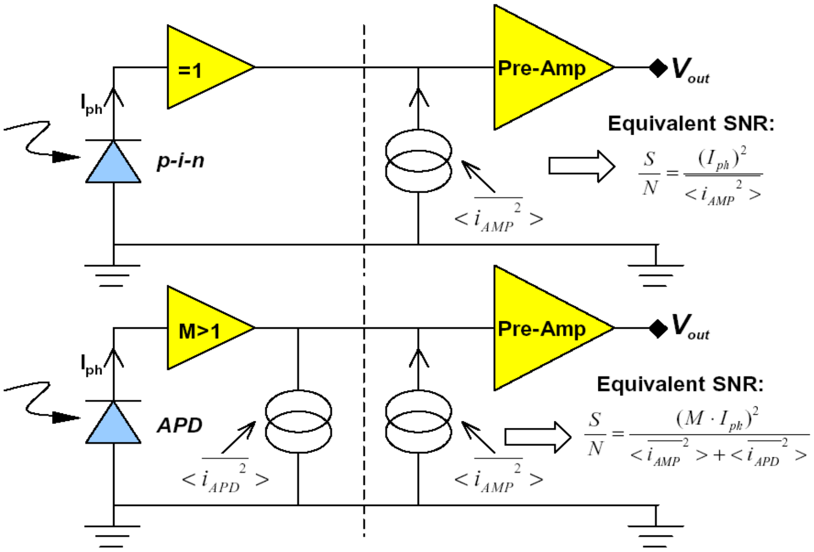

Fig. 2.11 Sensitivity comparison between *p-i-n* and APD optical receivers

Typically, as shown in Fig.2.11, the total noise power generated by a *p-i-n* photodiode is actually much less than that generated from the following pre-amplifier, which is primarily determined by transistor thermal noise. Therefore, the shot noise term of the *p-i-n* photodiode does not contribute significantly in the overall signal-to-noise ratio expression of a *p-i-n* receiver (2.13).

In an APD + pre-amplifier configuration, however, the signal power term in its *SNR* expression is boosted by a factor of M^2, which greatly enhances the receiver sensitivity if the total excess noise term from the APD is still negligible compared to a the noise contribution from the preamplifier. In this case, the APD itself is almost equivalent to an excess-noise-free photodetector, only with its photoresponse (the signal term) boosted by the current gain. This type of APD receiver configuration will provide much higher signal-to-noise ratio than a conventional *p-i-n* receiver because of the electrical amplification associated with extremely low APD noise and wide bandwidth. A low noise, high-speed APD will greatly relieve the burden for trade-offs between receiver noise and bandwidth, especially for those high data rate (i.e. ≥40Gb/s) applications.

The actual sensitivities of APD receivers at different APD excess noise levels (different *k* values) are illustrated in Fig. 2.12. The sensitivity of a reference *p-i-n* receiver is also plotted assuming identical integration conditions. At high gains the multiplied APD shot noise term associated with a non-zero *k*-value is generally not negligible in comparison with the thermal noise generated by a low noise electrical pre-amplifier. As a consequence, the total equivalent electrical noise of an APD receiver, which includes noise both from the APD and the following receiver circuit

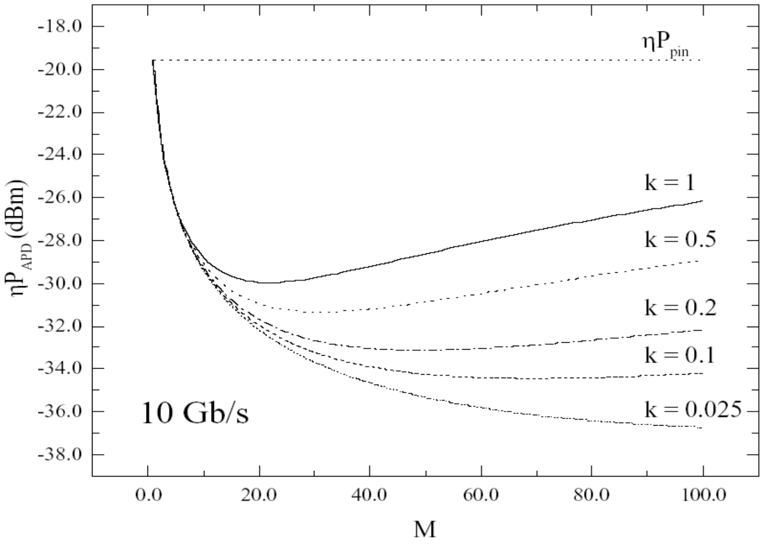

Fig. 2.12 Sensitivity comparison between a *p-i-n* receiver and APD receivers that have various *k* factors, based on the local impact ionization model

thermal noise is therefore written as

$$< i_{apd}^2 >=< i_{av}^2 > + < i_{thermal}^2 >= 2e(I_{ph} + I_B + I_D)BM^2F(M) + \frac{4kTB}{R} \quad (2.14)$$

According to (2.1), an APD receiver's total ensemble signal-to-noise power ratio thus becomes, in simplified form,

$$\left(\frac{S}{N}\right)_{power} = \frac{\left(\frac{e\eta_{ext}P_{inc}}{h\nu}\right)^2}{\left[2e(I_{ph} + I_B + I_D)F(M) + \frac{4kT}{RM^2}\right]\cdot B}, \quad (2.15)$$

From Equation (2.15), we can see that the optimum value of APD receiver sensitivity can be reached when the excess noise factor *F(M)* and the unwanted noise currents (I_B and I_D) both reach their minima.

Comparing to a *p-i-n* photodiode, the APD gain value (*M*) actually reduces the thermal noise contribution to a receiver's *SNR* by a factor of M^2 and increases the total signal-to-noise ratio of the APD receiver, as shown in (2.15). However, as can be easily seen from (2.15), the total shot noise term is multiplied by a factor *F(M)*. A noise penalty therefore will occur as *F(M)* increases with *M*. Furthermore, higher dark current level I_D, together with the background noise term I_B, also set a limit of achievable sensitivity of the APD receiver, even if the excess noise factor *F(M)* is very low and the thermal noise term is negligible after low noise electrical amplification at high gains. Consequently, both the APD excess factor (*F(M)*) and its dark current level (I_D) must be minimized in order to achieve a high APD receiver sensitivity.

From the discussions above, we may conclude that there exists an optimum

APD gain value that maximizes the APD receiver signal-to-noise ratio, assuming a finite *F(M)* factor associated with a specific *k* value and an acceptably low dark current level, as shown in Fig. 2.12. In addition, the internal gain of an avalanche photodiode relaxes the gain requirement of the subsequent preamplifiers, which results in higher performance from relatively simpler (and probably less costly) amplification circuitry. This is why an APD receiver usually achieves at least 5 to 10 dB better sensitivity than a *p-i-n* optical receiver. For high-bit-rate fiber-optic transmission systems and other applications associated with the requirements of high-sensitivity and high-speed photodetectors, such as applications for *IR* imaging and for eye-safe sensors, an avalanche photodiode is frequently the ideal photodetector of choice.

2.3 Summary

Based on above discussions, I can simply derive a brief conclusion that for many practical applications, either telecom-related or imaging-related, low noise and wide bandwidth APDs are beneficial. It is also known that by using a low *k*-value material, a thin material, or an impact-ionization-engineered device structure, low noise, high-speed APDs can be achieved. APD receivers have a great advantage, in terms of receiver sensitivity, over both MSM and *p-i-n* optical receivers when the APD has reasonably low dark current, low noise, and sufficient bandwidth. Minimizing APD excess noise and dark current levels is therefore critical to achieving high sensitivity optical receivers, both for telecommunications and 3-D imaging applications.

Chapter 3

Avalanche Photodiode Design, Processing, and Characterization

As has been discussed previously, the excess noise of an APD is critical to the ultimate sensitivity of telecommunications APD receivers. Moreover, in 3-D imaging applications, where weak *SWIR* (*S*hort *W*avelength *I*nfra-*R*ed) signals are detected by APDs in a focal-plane array prior to amplification in the following read-out circuitry, the sensitivity and bandwidth of APDs eventually determine the spatial detection range and the spatial resolution of the system. Device design, material growth, and fabrication technology are critical to the performance of APDs and arrays. In this chapter, fundamental APD design methods, as well as a few high-speed SACM APD related design issues, will be discussed. Device fabrication processes, plus device measurement methods for characterizing telecommunications APDs and focal-plane APD arrays, will also be presented.

3.1 APD Electrical Design

For a given speed requirement, two basic parameters, the equivalent unity-gain external quantum efficiency or responsivity and the avalanche (multiplication) gain at a specific operation bias value, are two key factors that contribute to the sensitivity of receivers that utilize APDs.

The first principle in a practical APD design is therefore to increase the unity-gain external quantum efficiency as much as possible. In order to achieve the highest detection sensitivity, the absorption volume of an avalanche photodiode is always maximized subject to the speed requirement. The total external quantum efficiency is

$$\eta_{ext} = M \cdot (1 - R)(1 - e^{-\alpha d}) \tag{3.1}$$

where the d is longitudinal dimension of the absorbing region, α is optical absorption coefficient of the absorbing media, R is the reflection coefficient at the incident light interface, and M is the avalanche gain. However, the maximum absorption thickness is, to some extent, determined by lattice matching. If lattice-mismatched heterostructures are involved in the absorbing layers, it is necessary to keep the dimension of each layer within its critical thickness so as to avoid forming dislocations in the epitaxial structures. These defects, if present, will cause high leakage current, induce premature breakdown, and even lead to device failure [3-1].

The design second goal is to achieve high gain. As has been discussed in Chapter 2, a low noise multiplication region is essential for an APD to operate at high gain values with minimal speed and noise penalties. As a consequence, low noise materials and structures, such as thin InAlAs or InGaAs/InAlAs heterostructures, are preferred as the multiplication region material for long-wavelength telecommunications APDs [3-2]-[3-5].

Even if lattice mismatch is not a consideration, the influence of carrier transit-time on the total depletion layer thickness of an APD must be taken into consideration. Since carriers generated in a photodiode must traverse the whole depleted active region to be collected by the contact layers, the transit time of those carriers sets an upper limit on the photodiode bandwidth. In a simplified situation where a simple *p-i-n* photodiode has a depletion width of w, assuming all carriers travel at the same saturation velocity v_{sat}, the 3-*dB* bandwidth can be estimated using the following saturation velocity approximation

$$f_{3dB} = \frac{1}{2\pi \bar{\tau}_{transit}}, \qquad \bar{\tau}_{transit} = \frac{w}{v_{sat}}, \tag{3.2}$$

For a high-speed APD structure in which carrier multiplication exists, however, the situation becomes more complicated; this will be discussed in 3.1.2.

The parasitic resistance and capacitance of an avalanche photodiode set another limit on its 3-*dB* bandwidth. As has been discussed above, the depletion layer of an APD needs to be thinned to minimize carrier transit time limit. As a consequence, the junction capacitance of the APD will increase and the resulting *RC* time constant will eventually dominate APD bandwidth. Using a first-order approximation, it is not difficult to determine the RC component of the bandwidth

$$f_{3dB} = \frac{1}{2\pi \tau_{RC}}, \qquad \tau_{RC} = RC \tag{3.4}$$

where *R* is the total equivalent load resistance and *C* is the total equivalent junction capacitance, based on a simplified photodiode circuit model [3-6]. To achieve both high sensitivity and high operation speed, it is frequently necessary to compromise external quantum efficiency and, the carrier transit time.

3.1.1 Design for Simple *p-i-n* Structure APDs

An APD may be as simple as a *p-i-n* structure, as shown in Fig.3.1. For example, the APDs utilized for noise studies frequently have a *p-i-n* structure that is satisfactory to simplify material growth, device processing, and the noise measurements. In this type of simple *p-i-n* device structure, a unintentionally-doped '*i*' region acts as a multiplication region to provide gain, while either the p^+-doped or the n^+-doped contact layer serves as the absorption region to presumably fulfill either a pure electron injection (*p-i-n*) or a pure hole injection (*n-i-p*), respectively, into the multiplication region.

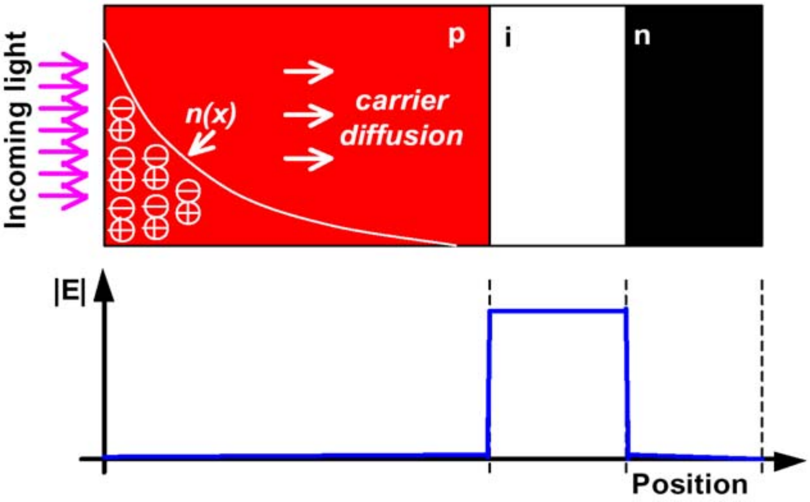

Fig. 3.1 Photon absorption and carrier transport in simple *p-i-n* structure

However, this type of device structure is not suitable for the high-speed operation. One reason for this is that the slow diffusion of minority carriers through the thick absorbing layer. Moreover, even for thick absorbing layers, a small fraction of the incoming photons can still reach the multiplication region, which results in mixed carrier injection. This type of mixed carrier generation in the multiplication region, if not negligible, will degrade both the noise and speed of the APD, as has been discussed in Chapter 2. Hence, in order to achieve high-speed operation, an

APD device structure needs to be designed to separate photon absorption from carrier multiplication and to utilize carrier drift rather than carrier diffusion.

3.1.2 Separate Absorption, Charge, Multiplication APDs

To address the issues discussed above, a SACM (Separate Absorption, Charge, and Multiplication) APD structure as shown in Fig. 3.2, which decouples light absorption from carrier multiplication, has been developed [3-7].

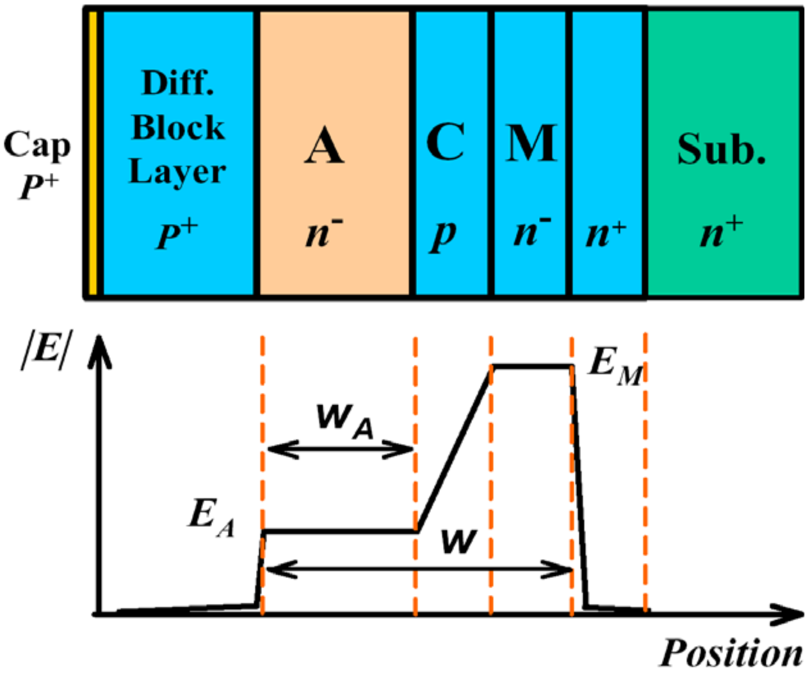

Fig. 3.2 Device structure and E-field distribution in a SACM APD

A SACM APD structure includes an absorbing region and a multiplication region separated by a charge (field buffer) region. The main advantage of a SACM APD structure over a simple *p-i-n* structure is that the photon absorption process and the carrier multiplication process are spatially separated and can be optimized individually. In long-wavelength SACM APDs, the absorption material is usually a narrow band-gap material and the electric field in this region needs to be low to eliminate carrier tunneling. The multiplication region, however, is normally a wide band-gap material where the electric field strength needs to be high enough to provide APD gain.

In order to satisfy the requirements for different electric field strength values in these two regions, a moderately doped charge layer is sandwiched between them. The electric field decreases linearly from a high value (normally > 750KV/cm in a thin $In_{0.52}Al_{0.48}As$ APD) to a much lower electric field to avoid noticeable tunneling in the absorbing region. The electric field in the absorbing region will force all the photo-generated electrons to drift towards the multiplication region. Since all the incoming photons are absorbed in the $In_{0.53}Ga_{0.47}As$ region, this structure effectively eliminates mixed carrier injection. For the reasons discussed above, the SACM device structure was selected as the primary device structure for my focal plane APD array studies and for my telecommunication APD studies.

3.1.3 A Few Issues in the SACM APD structure design

The first issue to be discussed for a SACM APD structure design is how to optimize its electric field profile in the various regions of the device. In a SACM structure, only a moderately high electric field in the absorbing region is expected so that no tunneling will occur. But, as has been recently observed in my high-speed APD studies, carrier multiplication in the absorbing region, even a small amount, is extremely detrimental to APD speed performance. The electric field strength that causes an observable tunneling effect in the InGaAs (≥200KV/cm at room temperature) is higher than the electric field strength required for noticeable low field carrier multiplication (≥180KV/cm) [3-8]. Any electric field strength within this range will cause carrier multiplication in the InGaAs absorbing region, whereas no obvious tunneling can be observed.

The impact of carrier multiplication in the absorbing region of an APD both on its DC and on its transient performance can be illustrated using figures 3.3 (a) to 3.3 (c).

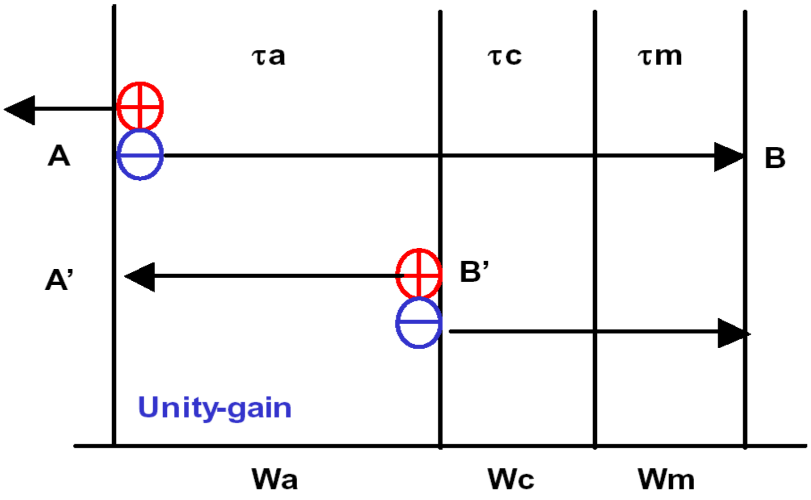

Fig. 3.3 (a) Carrier generation in an APD, at unity gain

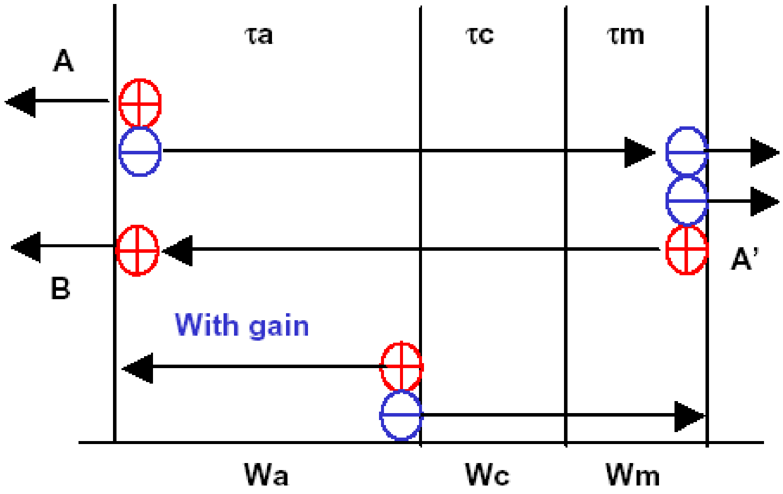

Fig. 3.3 (b) Carrier generation in an APD, with gain only in multiplication region

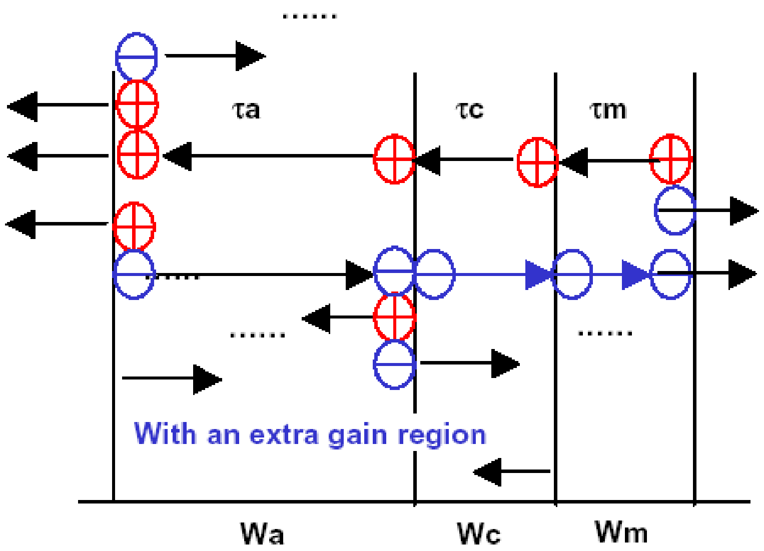

Fig. 3.3 (c) Carrier generation in an APD, with gain both in absorption region and multiplication region

Assume a simplest case, as shown in Fig. 3.3 (a), where a SACM APD is biased at its unity-gain. Since the electric field is relatively low and no carrier multiplication exists within this APD, both its dark current level, which primarily originates from the thermal generation in the depleted regions, and its transient time limit, which is determined by the longest carrier transit path ("*A*" to "*B*" for electrons and "*B′*" to "*A′*" for holes, depending which one is slower), reach their lowest value, just like in a dual-depletion region *p-i-n* photodiode.

As the reverse bias increases, carrier multiplication in the gain region will occur and cause an increase in the multiplied dark current, compared to the initial value corresponding to unity gain, as is illustrated in Fig. 3.3 (b). Assuming that a δ-shape-like photo-generated carrier distribution profile was initially built up close to the *p*-side depletion edge within the device and ignoring carrier diffusion, all photo-generated holes will be immediately collected by the *p*-side contact and all electrons will move toward the *n*-side in the accelerating electric field, while keeping the δ-like pulse shape. Those electrons will then generate secondary carriers and subsequent offspring in the multiplication region. All electrons will be collected at the *n*-side and all multiplied holes will move back to the *p*-side. A longer carrier transit path, from "*A*" to "*A′*" and then back to "*B*", as shown in Fig. 3.3 (b), will reduce the APD bandwidth at low gains. All the initial photo-generated electrons, as shown in the graph, will take an average transit time $\tau_e = w/v_{e,sat}$ to reach the multiplication region edge, where $v_{e,sat}$ is the saturated electron velocity in the absorbing region. Those carriers will then undergo multiplication in an average time period, τ_m, which is inversely proportional to APD's gain-bandwidth product. The secondary holes will then travel another time period, $\tau_h = w/v_{h,sat}$, before being collected by the *p*-contact layer. The total 3-dB bandwidth of an APD therefore can be estimated, based on the saturation velocity approximation, as

$$f_{3dB} \propto \frac{1}{2\pi(\bar{\tau}_e + \bar{\tau}_m + \bar{\tau}_h)}, \quad \bar{\tau}_e = \frac{w}{v_{e,sat}}, \quad \bar{\tau}_h = \frac{w}{v_{h,sat}}, \quad \bar{\tau}_m = \frac{2\pi}{G \cdot B}, \tag{3.3}$$

where $v_{e,sat}$ and $v_{h,sat}$ are saturated velocities of electrons and holes in the absorbing layer, and $G{\cdot}B$ is APD's gain-bandwidth product. From (3.3) we can see that, even given an ideal multiplication material that has virtually an infinite $G{\cdot}B$ product, carrier feedback will cause the bandwidth of an APD to be lower than that of a *p-i-n* with an equivalent depletion layer thickness.

As shown in Fig. 3.3 (c), carrier multiplication in the absorbing layer, even very slight, will generate longer carrier feedback loops. These carrier feedback loops between absorbing and multiplication regions not only increase the APD dark current level, degrade its bandwidth at low gains, but also corrupt its gain-bandwidth product. The net result, as can be easily imagined, is equivalent to a thick gain-region APD that has a higher excess noise factor value and an inferior gain-bandwidth product. This situation, therefore, is what an APD designer tries to avoid.

Accordingly, optimization of the electric field profile in a SACM APD is tremendously important. One criterion is set by the upper limit of the electric field strength in the absorbing region, as has been already discussed. Also, for SACM APDs with a depleted absorber, the electric field strength in the absorbing region cannot be too low, for example, below 45 KV/cm [3-9]. Otherwise, holes in the absorbing region cannot reach their saturation velocity, which will adversely affect the bandwidth. Typical carrier transfer characteristic of both electrons and holes in the $In_{0.53}Ga_{0.47}As$ material are shown in Fig. 3.4.

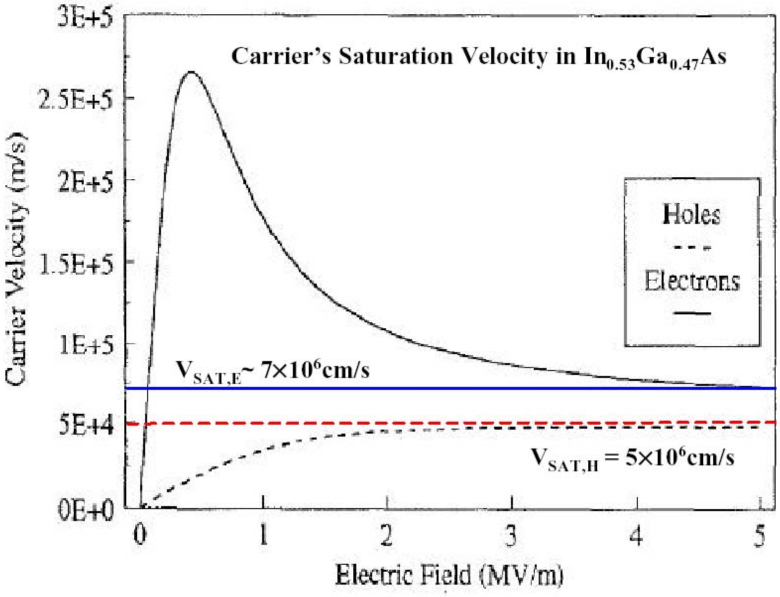

Fig. 3.4 Saturation velocities of electrons and holes in $In_{0.53}Ga_{0.47}As$

The criteria for optimizing the electric field profile in a SACM APD are better illustrated in Fig. 3.5, where the deep depletion approximation is assumed in all depleted active regions to simplify the illustration. Another issue in the SACM APD design is to properly adjust the charge layer doping level to get the desired electric field profile. From an epitaxial growth point of view, the charge doping level used for wafer growth is usually inconsistent with the calculated value. There are several reasons for this. For MBE grown wafers one cause is fluctuations of the *Be* flux. The *Be* doping level thus needs to be calibrated before each growth by using calibration samples. Practically, the charge layer doping level can be examined by measuring simple test devices from the dummy sample. Punch-through voltage measurements, which correspond to the voltage at which the depletion region edge reaches the absorption layer, can be used to determine the charge layer doping level. If, after testing dummy devices, no punch-through is observed, the charge doping can be inferred as too high and further SIMS analysis is recommended to quantify the doping level in the charge region. Once the punch-through can be observed and is lower than what was expected, the charge doping can be modified by simple calculations.

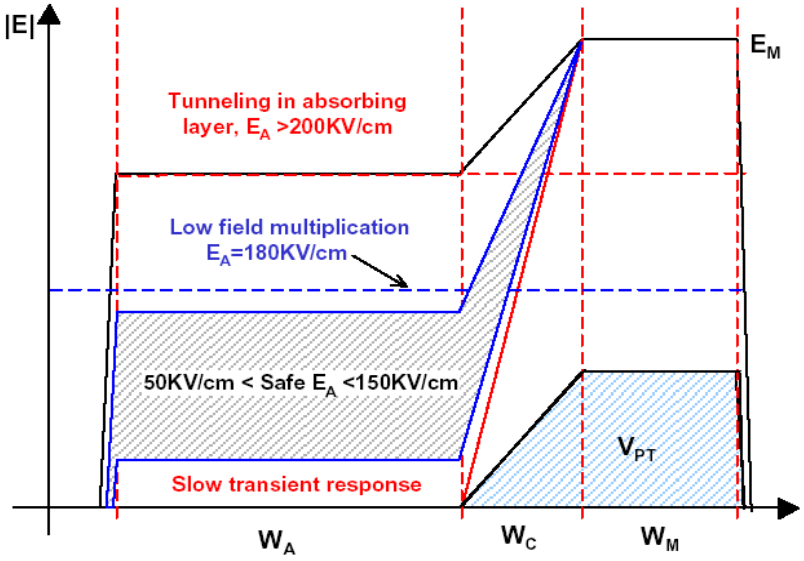

Fig. 3.5 Criteria for the electric profile in a SACM APD design

There are basically two ways to modify the total charge in APD charge layer to obtain an appropriate punch-through value and a satisfactory electric field profile in the device. The first way is to adjust the charge doping level while keep a fixed charge layer thickness, as shown in Fig. 3.6.

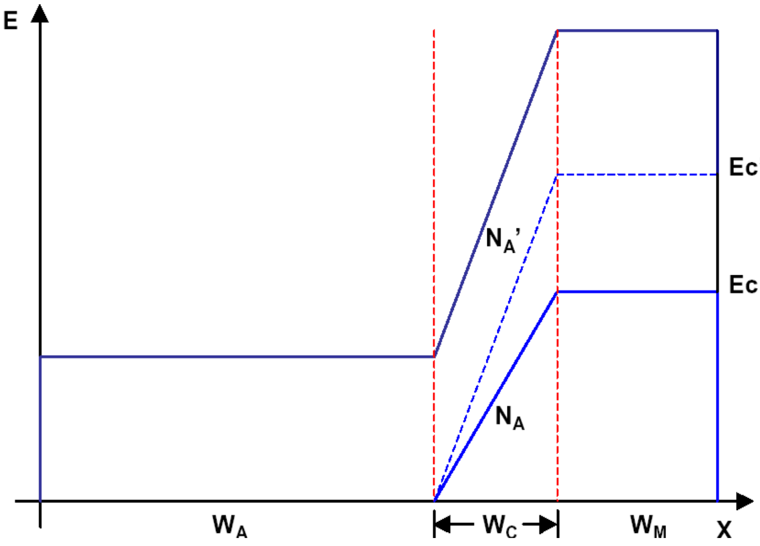

Fig. 3.6 Total charge amount adjustment by changing doping level

It is assumed that the doping levels in both the *p*- and *n*-contact layers are high enough, and the electric field is completely confined in the depleted absorption region after punch-through. We also assume that the background doping levels in the absorption region and the multiplication region are sufficiently low that the electric field profile is flat in all these regions. The punch-through voltages before and after charge doping modification, V_p and V_p', respectively, may be expressed as

$$V_{pt} = \left(\frac{1}{2} W_C + W_M \right) \cdot E_C \, , \quad V'_{pt} = \left(\frac{1}{2} W_C + W_M \right) \cdot E'_C \, . \tag{3.5}$$

The gradients of electric field strength in the charge layer before and after doping adjustment are

$$Slope_1 = \frac{E_C}{W_C} = \frac{q \cdot N_A}{\varepsilon_r \cdot \varepsilon_o} \, , \qquad Slope_2 = \frac{E'_C}{W_C} = \frac{q \cdot N'_A}{\varepsilon_r \cdot \varepsilon_o} \, , \tag{3.6}$$

The ratio of the punch-through before and after charge doping adjustment is

$$\left(\frac{V_{pt}}{V'_{pt}} \right) = \frac{W_C + 2 \cdot W_M}{W_C + 2 \cdot W_M} \cdot \frac{E_C}{E'_C} \, . \tag{3.7}$$

This gives the following relation between the punch-through voltage and doping concentration before and after charge layer doping modification

$$\frac{V_{pt}}{V'_{pt}} = \frac{N_A}{N'_A} \, . \tag{3.8}$$

The final doping level after charge layer modification is

$$N'_A = \left(\frac{V'_{pt}}{V_{pt}} \right) \cdot N_A \, . \tag{3.9}$$

The second way to correct the total charge amount is by modifying the charge layer thickness while keeping the original doping level. In this case, the field gradient remains constant, as shown in Fig. 3.7.

$$Slope_1 = \frac{E_C}{W_C} = \frac{q \cdot N_A}{\varepsilon_r \cdot \varepsilon_o} = Slope_2 = \frac{E'_C}{W'_C} = \frac{q \cdot N_A}{\varepsilon_r \cdot \varepsilon_o} \tag{3.10}$$

Punch-through before and after charge modification can be calculated as

$$V_{pt} = \left(\frac{1}{2}W_C + W_M\right)\cdot E_C, \quad V'_{pt} = \left(\frac{1}{2}W'_C + W_M\right)\cdot E'_C. \tag{3.11}$$

The ratio of punch-through voltages is

$$\left(\frac{V_{pt}}{V'_{pt}}\right) = \frac{W_C + 2\cdot W_M}{W'_C + 2\cdot W_M}\cdot\frac{E_C}{E'_C}. \tag{3.12}$$

This can also be expressed as

$$\left(\frac{V_{pt}}{V'_{pt}}\right) = \frac{W_C + 2\cdot W_M}{W'_C + 2\cdot W_M}\cdot\frac{W_C}{W'_C}. \tag{3.13}$$

So the expected charge layer thickness is

$$W'_C = \sqrt{{W_M}^2 + \left(\frac{V'_{pt}}{V_{pt}}\right)\cdot\left(W_C + 2\cdot W_M\right)\cdot W_C} - W_M. \tag{3.14}$$

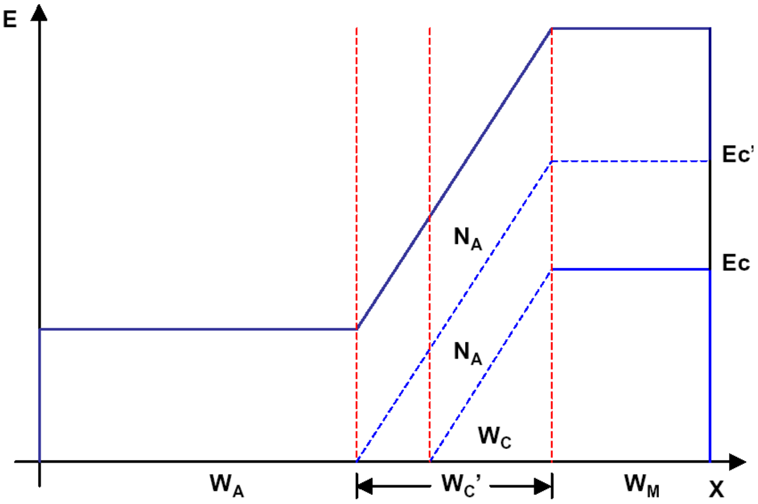

Fig. 3.7 Total charge amount adjustment by changing charge layer thickness

The electric field strengths both in the absorbing region and the multiplication region can be individually optimized, either by charge doping level adjustment or by changing the thickness. For an APD with a very thin multiplication region, as in an ultra-high-speed (i.e. ≥40Gb/s) long-wavelength InGaAs/InAlAs APD or in an IIE APD structure, lower charge doping level is always preferred to avoid possible tunneling in the thin multiplication layer. For structures that require very high charge levels, increasing the charge by layer thickness is preferred. Accordingly, to obtain an adequate punch-through voltage in a high-speed (thin) SACM APD, the second option is usually preferred.

3.2 APD Optical Coupling Design

3.2.1 Resonant-Cavity Avalanche Photodiode

Similar to a vertical cavity surface emitting laser (VECSL) diode, the quantum efficiency of a thin-absorbing-layer photodiode may be greatly improved by using a resonant cavity. Through careful design of its position in a resonant cavity, multiple reflections cross the thin absorbing layer will significantly enhance the photoresponse of an APD. As shown in Fig. 3.8, alternating layers of high and low refractive index semiconductor materials grown on the substrate, with a thickness corresponding to 1/4 of the resonance wavelength of the cavity, form the bottom distributed Bragg reflector (DBR) with an extremely high reflection coefficient. Another DBR stack, either grown or deposited by evaporation above the absorption layer, forms another reflecting mirror with a moderate reflection coefficient. If the distance between these two DBR stacks is a multiple of the half resonance wavelength of the cavity, constructive interference will occur within the cavity. Normal incident light at the resonant wavelength undergoes multiple reflections across the absorbing layer. This results in almost complete absorption. As a result, the unity-gain external quantum efficiency can be greatly enhanced by this type of device structure [3-10].

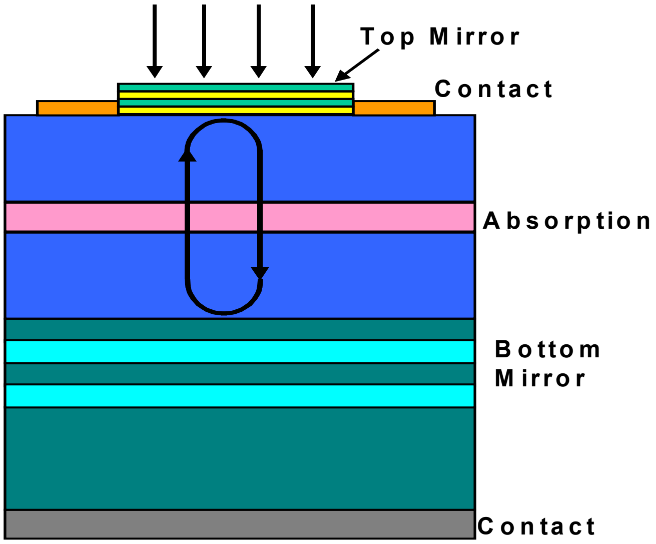

Fig. 3.8 Typical device structure of a resonant cavity APD

The maximum achievable quantum efficiency of a resonant cavity is given by

$$\eta_{\max} = \frac{(1+R_2 e^{-\alpha d})(1-R_1)(1-e^{-\alpha d})}{(1-\sqrt{R_1 R_2}\,e^{-\alpha d})^2}, \qquad (3.15)$$

where α is the absorption coefficient, *d* is the cavity length, and R_1 and R_2 are the top and bottom mirror reflectivity, respectively.

3.2.2 Wave-guided Avalanche Photodiode

Even though a F-P cavity can provide a high external quantum efficiency value for both lasers and photodetectors, the extremely narrow optical spectrum caused by cavity the resonance, which is quite desirable for most lasers, is not at all favorable for photodetectors. The application requirements and material growth issues require. Wide detection wavelength range is preferred for almost all types of photodetectors [3-11]. Another way to improve the external quantum efficiency for a thin absorbing layer APD is to absorb the light in a direction normal to the carrier transport direction. This type of structure, shown in Fig. 3.9, decouples the responsivity from the transit time component of the bandwidth. The absorbing layer can be thin, which gives a short transit time for the electronics and holes that travel normal to the epitaxial layers. The photons, on the other hand, travel in the plane of the absorbing region and can have a long optical path length, which enables high responsivity. Therefore, the APD bandwidth is only limited by the RC time constant and a difficulty for the electrical design is significantly relaxed. The photodiode structure itself is normally designed as a slab waveguide to confine the incoming light into a specific mode (single-mode type), or several modes (multimode type), as much as possible in order to maximize the light absorption in this specified absorbing region. To form this type of slab waveguide, a core (absorbing) layer with a high refractive index value is normally sandwiched between two low-index-value cladding layers, allowing light propagation only along the lateral direction of the device without dispersing into the other regions outside the absorber. In this type of device structure the external quantum efficiency is a function of device length rather than the device thickness. The external quantum efficiency of waveguide photodiodes, if properly designed, can be equal to that of conventional normal incidence devices or carefully designed resonant cavity structure [3-12]. In my 40Gb/s telecommunication APD design, a novel waveguide structure is to be adopted to achieve both a high bandwidth and a good gain-bandwidth product to satisfy the requirements for both speed and sensitivity.

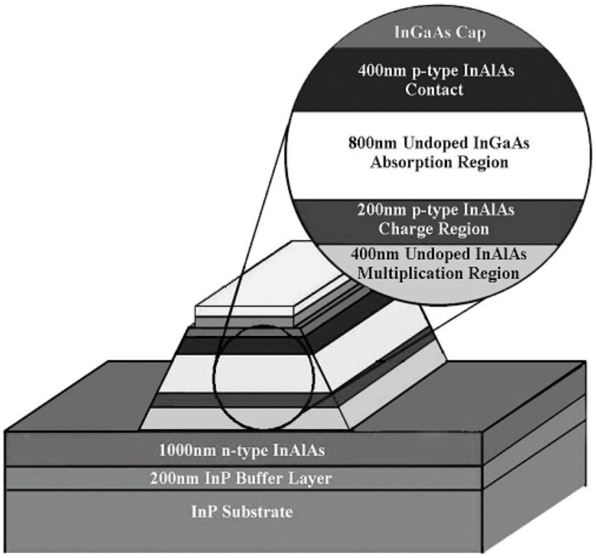

Fig. 3.9 Typical device structure of a high-speed waveguide APD

3.3 APD Device Processing

3.3.1 Processing Simple-mesa APDs

To test an APD wafer quality, a simple device structure can be fabricated by etching mesas in order to provide device isolation between *p*- and *n*-type contacts. For most of the home-grown wafers this process usually starts with the backside Indium removal on a hot plate at an elevated temperature (200°C), This is, of course, not a necessary step for the Indium-free wafers. The next several steps consist of wafer surface cleaning by Acetone in an ultrasonic bath, followed by IPA and DI water rinsing. After coating with photo-resist (normally AZ5124, 4000rpm, 40 seconds) and pre-baking (90°C, 10 minutes), mesa patterns are defined by photo-mask alignment and exposure (0.8-1.0 minute), development (developer AZ 725, 20-30 seconds), post-bake (120°C, 30 minutes), and wet-chemical etching in a phosphoric etchant ($H_3PO_4{:}H_2O_2{:}H_2O = 1{:}1{:}10$) at room temperature while stirring. The etching rate was calibrated as 0.4~0.5 μm/min for InGaAs and InAlAs materials.

Mesa passivation is followed in a Plasma-Therm PECVD chamber at an elevated temperature (285°C). A SiO_2 film is used for device passivation under a deposition condition of N_2O flow rate: 30sccm; $SiCH_4$ flow rate: 1000sccm; background pressure: 100mTorr; RF power: 30Watts. The growth rate is calibrated to approximately 60 Å/min and a 2000 Å thick SiO_2 film is normally used to obtain reliable device passivation. After mesa passivation, the top contact mask patterns are defined by a standard photolithography, as described above. After 10 minutes post-bake, the SiO_2 film is etched in a buffered oxide etchant (BOE) solution for 1 minute.

Then the samples are loaded into the CHA chamber for Cr (200 Å)/Au (1000 Å) metal film deposition. Once the metal deposition is finished, the samples are unloaded from the CHA and then a lift-off step is performed in Acetone. Then the whole processing steps are repeated for the *n*-type contact metallization with a composite Ni (100 Å)/AuGe (400 Å)/Au (1000 Å) metal film, followed by a rapid thermal annealing (400^{o}C, 40 seconds) step.

This simple-mesa device processing only needs one mesa etching step, one passivation step, and two metallization steps. After that, simple-mesa-APD samples are ready for the DC, quantum efficiency, or the noise characterization. The cross-section of a finished simple-mesa APD device is illustrated in Fig. 3.10.

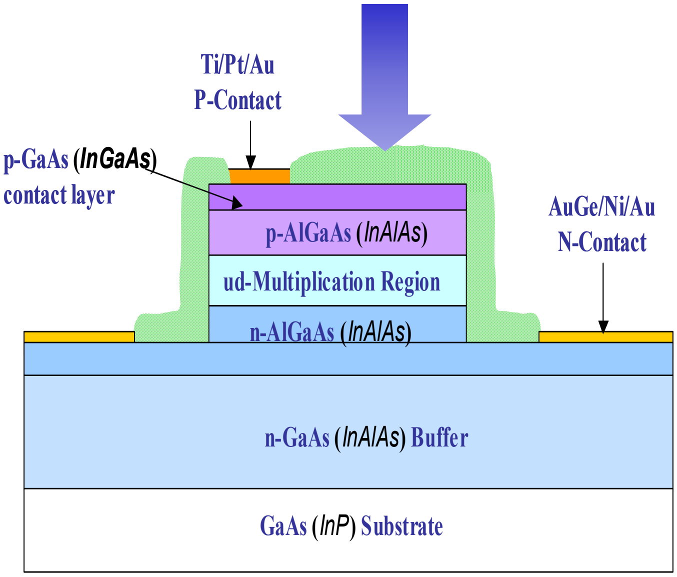

Fig. 3.10 Typical finished simple-mesa APD for noise study

3.3.2 Processing High-speed APDs

For a high-speed APD, since the active area of the APD is usually small compared to a simple-mesa APD for noise or for QE characterization, metal contact pads are usually necessary for high-speed testing or for further integration with an electrical amplifier. Consequently, the high-speed APD structure is usually grown on a semi-insulating substrate on which metal contact pads are fabricated to minimize the parasitic capacitance between them. These metal pads need to be in a planarized form for microwave probing. Most of the processing complexity comes from fabrication of the pads, for which either a polymer isolation technique or an air-bridge based technology is used. The entire processing flow chart is shown in Fig.3.11 (a) to (f).

3.3.2.1 P-type metallization and annealing

Top contact metal is made using a SiO_2-asisted lift-off process. A 2000 Å SiO_2 film is deposited for this purpose. After definition of the *p*-metal patterns (where AZ5209 is preferred), wafers are dipped in a buffered oxide etchant prior to metal deposition to remove the oxide. To achieve a decent *p*-type ohmic contact, 1) a narrow bandgap *p*-cap layer should be used, which is usually heavily doped up to $>10^{19}$ cm^{-3}, and 2) a metal that has a large work function is preferred (such as *Pt*, *Pd*, etc.). While the valence band edge of $In_{0.53}Ga_{0.47}As$ lies 0.25eV below the vacuum level (electron affinity energy) and 5.5eV for GaAs, and most metal work functions are below 5eV, finding a good *p*-contact metal is difficult.

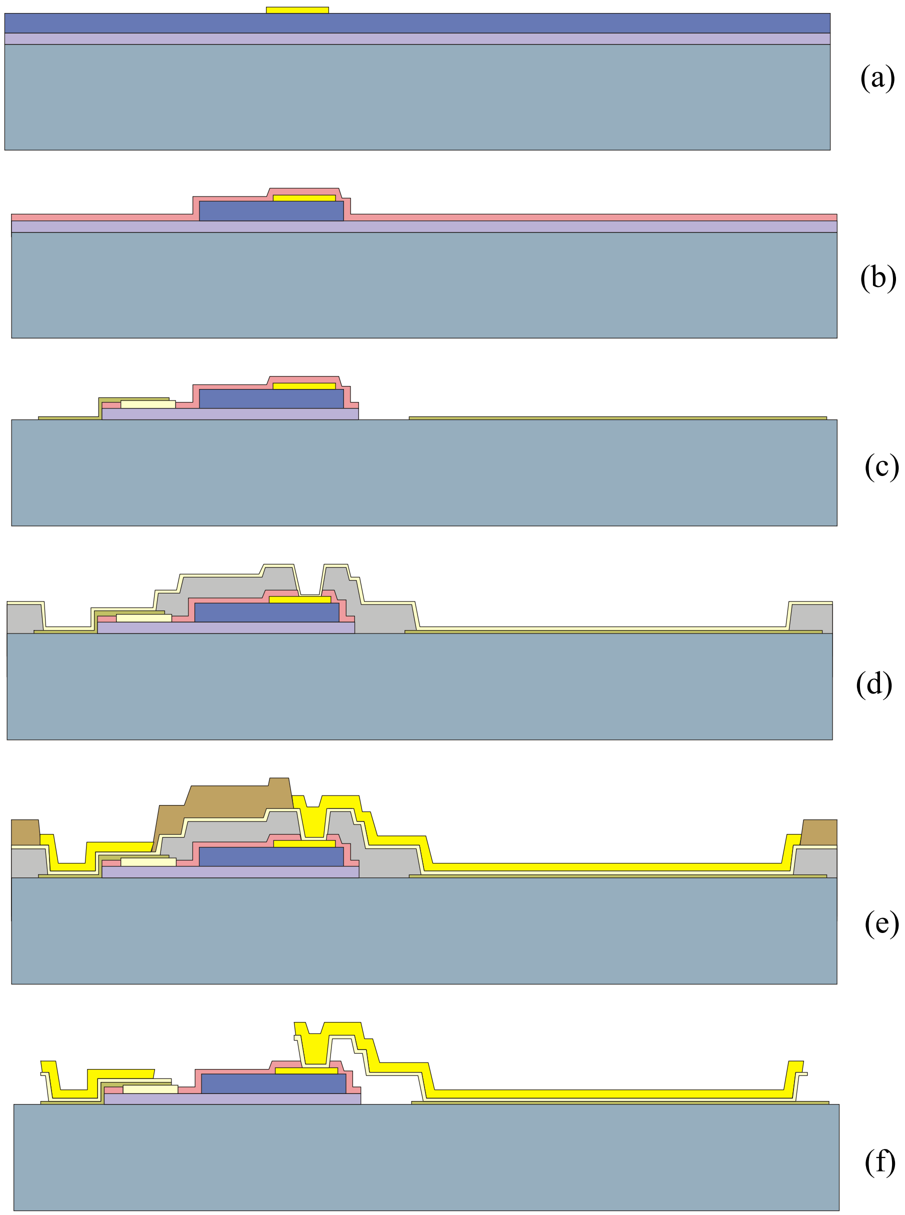

Fig. 3.11 (a) - (f) Typical full-scale high-speed APD processing flow chart

High surface state densities will further make the *p*-ohmic contact formation difficult to achieve due to the surface energy pinning effect. A titanium (100 Å), platinum (300 Å), and gold (1000 Å) contact normally provides reasonably low contact resistance. Here the thin, low work function Titanium layer (φ=4.33) is only used for good adhesion; the real ohmic contact is formed when platinum (φ=5.65) has migrated to the metal-semiconductor interface after proper annealing.

With adequate annealing, Palladium is another high work function metal for good *p*-type ohmic contact. An AuZn alloy could provide even lower contact resistance if properly deposited and annealed. This is attributed to the Zn diffusion from AuZn alloy into the $In_{0.53}Ga_{0.47}As$ cap layer to form an extremely heavily-doped region at the metal-semiconductor interface after annealing.

Metal contacts are annealed in a rapid thermal annealing (RTA) chamber at an elevated temperature. The purpose is to alloy these as-deposited metal layers with the semiconductor surface to achieve low specific contact resistance. The RTA chamber is purged with dry nitrogen to avoid oxidation during annealing. The standard anneal condition for the Ti-Pt-Au contact is 420º C for 30 sec. The specific contact resistance is usually measured by the standard transmission line model (TLM) method. The above annealing condition yields a specific contact resistance - $9.6\times10^{-6}\ \Omega\cdot cm^2$ for a Ti-Pt-Au contact on a heavily-doped *p*-type InGaAs cap layer, as shown in Fig. 3.12. The top contact metal sometimes is intentionally defined to extend to the mesa edge, as in the case of waveguide APD processing, to fulfill the so-called self-aligned metallization with respect to the mesa region. In this case, the *p*-metal is actually used as a mask for *p*-mesa etching and annealing should be performed prior to the mesa definition. Otherwise, the metal may flow over the edge of the mesa during annealing and thus cause a short to the device.

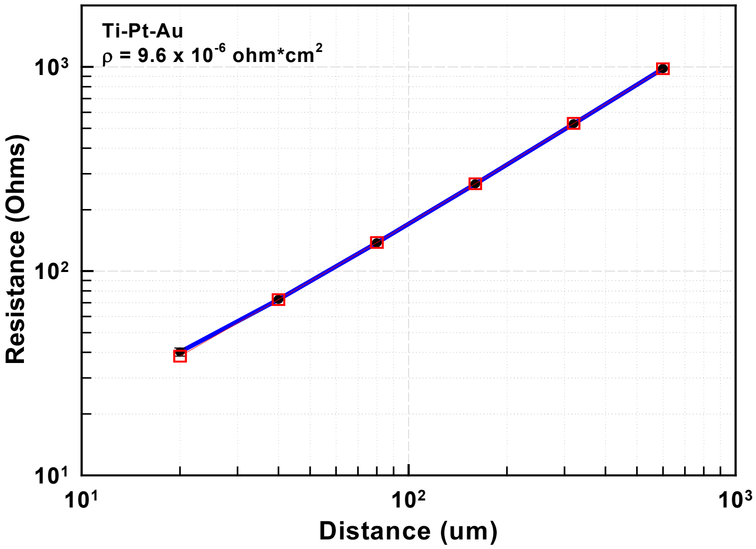

Fig. 3.12 Typical TLM pattern measurement results of Ti-Pt-Au on InGaAs

3.3.2.2 P-mesa Etching

In most cases, mesa patterns are defined using a standard photolithography. Either a wet chemical etch or an RIE can be utilized to define *p*-mesa patterns, on GaAs-based or on InP-based material systems. Since mesa etching will introduce defects and damage on mesa sidewalls, etching is an extremely important step in high-speed APD processing. To obtain APD devices that have the least dark current, etching conditions should be optimized. For this purpose, both wet chemical etching and RIE were studied and compared.

Starting with wet chemical etching experiments, four different types of wet chemicals; a buffered sulphuric acid, a buffered phosphoric acid, a bromine-methanol solution, and a saturated bromine-water (SBW) solution were studied for their etching properties. The ingredients of the sulphuric etchant were sulphuric acid: hydrogen peroxide: DI water (1: 1: 8). The phosphoric etchant was composed of phosphoric acid: hydrogen peroxide: DI water (1: 1: 10). The bromine-methanol etchant was obtained by adding bromine into methanol with a volume ratio of 1:200. To obtain the saturated bromine-water solution, pure bromine was added into DI water and then stirred until the bromine was mixed uniformly in the water. Fig 3.13 (a) through (h) shows the mesa morphology and DC characteristics obtained from the relevant devices, respectively. Even the device sidewall surface was very smooth after saturated bromine water solution, as shown in Fig. 3.13 (a), the sidewall was very steep and thus the electric field strength on the sidewall was the highest among all these four types of devices. The I-V measurement results were consistent with the SEM observations: devices etched with SBW solution exhibited severe early breakdown and excessive leakage dark current due to high electric field at the mesa edges. Mesa sidewalls with buffered H_2SO_4 solution also exhibited relatively higher dark currents at high biases due to rough sidewall surface generated by the etching. The best results came from the wet etch using the bromine-methanol solution and the buffered H_3PO_4 etchant. Mesa sidewalls were smooth and exhibited a bevel curvature; I-V curves exhibited both proper breakdown and low dark current levels, in comparison with that from the other two types of etching.

For etching mesas on AlGaAs, GaAs, InGaAs, and InAlAs materials, a 1:1:10 buffered H_3PO_4 solution is preferred, and etching rate was calibrated as -0.4

μm/min. To etch InP or InGaAsP mesas, however, a bromine-methanol etchant is preferred because buffered H_3PO_4 solution doesn't attack InP and InGaAsP quaternaries. For this reason, an SiO_2 film is normally utilized as an etching mask instead of the PR mask pattern, which is dissolved in methanol. The etch rate of InP in a 0.5% bromine-methanol solution is - 0.2 μm/min and will decrease over the course of minutes, due to evaporation of bromine into the air.

Since most wet chemical etchings are isotropic, the under-cut should be taken into consideration during mesa etching. For very small mesas with dimensions less than 10×10 μm^2, or for those critical dimensions that need to be accurately controlled, as in the fabrication of waveguide APDs where dimensions are very critical to the device's responsivity, a reactive ion etch is usually preferred. Unlike the wet etching, RIE is basically an anisotropic process. Less undercutting of the mesa sidewalls occurs using a well-controlled RIE condition. For example, using a 1:1 $BCl_3/SiCl_4$ gas mix at an RF power of 150 W, InGaAs/InAlAs layers are etched at the rate of 0.1 μm/min, which is comparatively slow in comparison with wet etching. It is even more detrimental that dry etching will cause more damages than the wet etch and thus create rough sidewall morphology on the mesa surface. Furthermore, the bevel shape is relatively steep, in comparison with wet etching, and the shape is hard to control during etching. As a result, a brief (≤30 sec.) wet etch of mesa patterns is normally necessary, following a RIE process, in order to form an acceptable bevel shape and polish the sidewall surface of device mesas, prior to the device passivation step. Fig. 3.13 shows a small mesa pattern fabricated with $BCl_3/SiCl_4$ dry etching followed by a buffered (1:1:10) H_3PO_4 etchant cleaning.

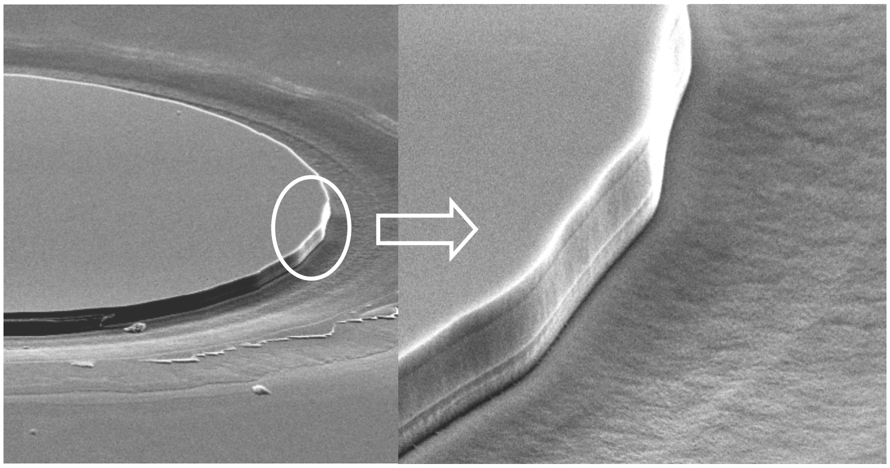

Fig. 3.13 (a) SEM picture of the mesa morphology after SBW etching

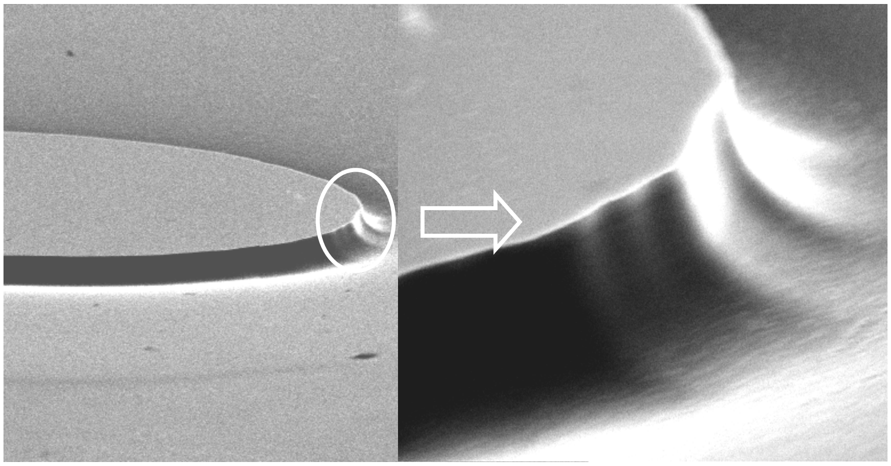

Fig. 3.13 (b) SEM picture of the mesa morphology after Br_2-CH_3OH etching

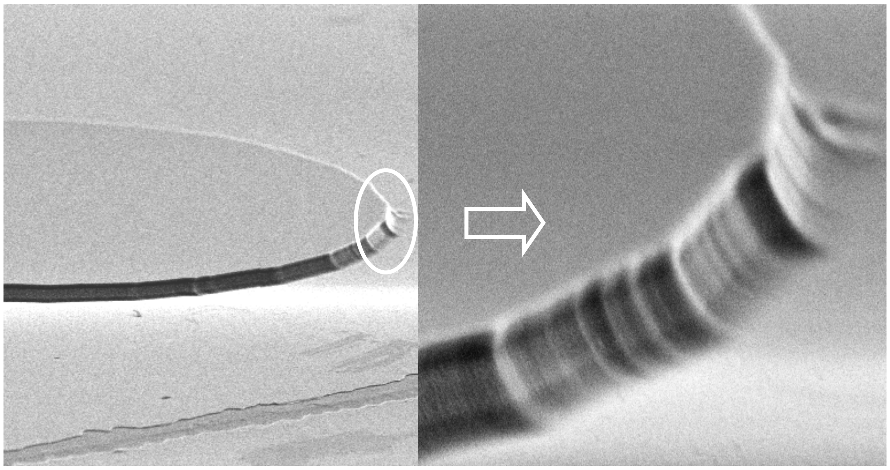

Fig. 3.13 (c) SEM picture of the mesa morphology after H_3PO_4 etching

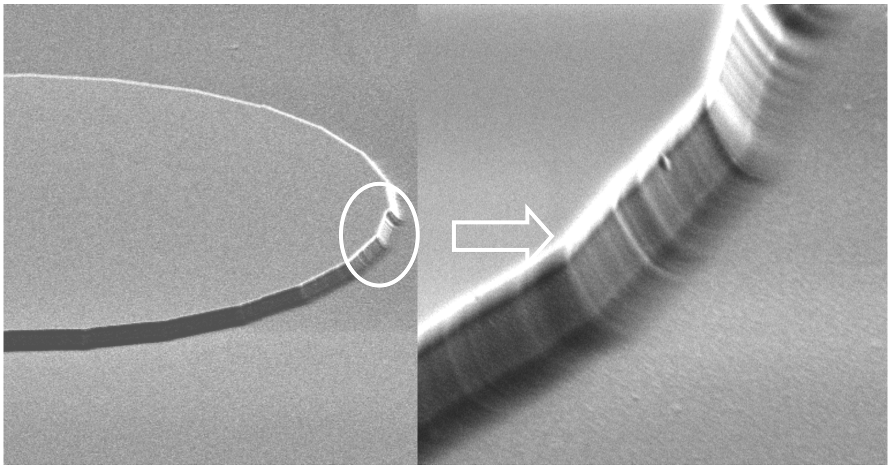

Fig. 3.13 (d) SEM picture of the mesa morphology after H_2SO_4 etching

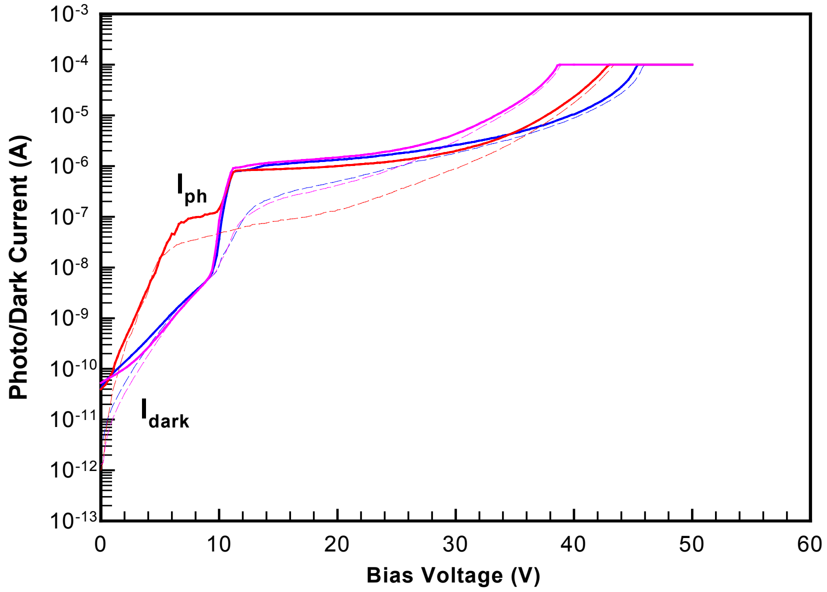

Fig. 3.13 (e) Typical APD I-Vs after SBW etching

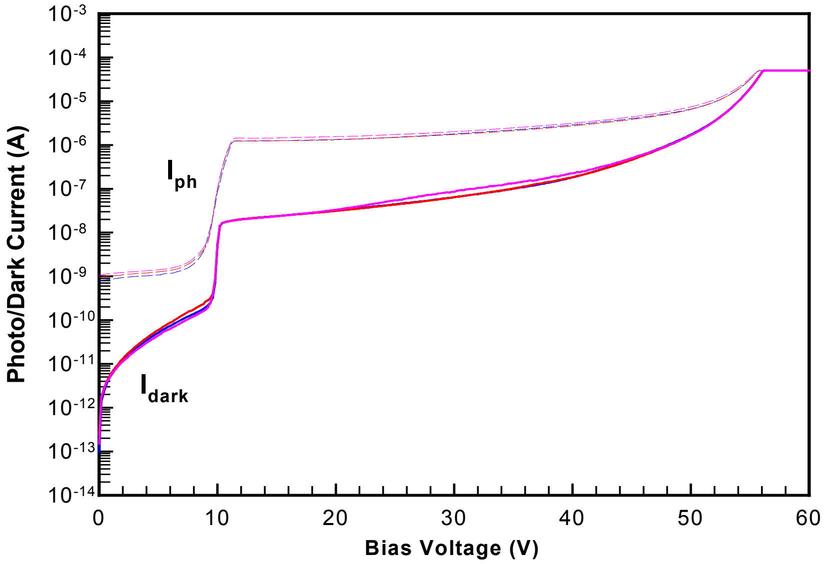

Fig. 3.13 (f) Typical APD I-Vs after Br_2-CH_3OH etching

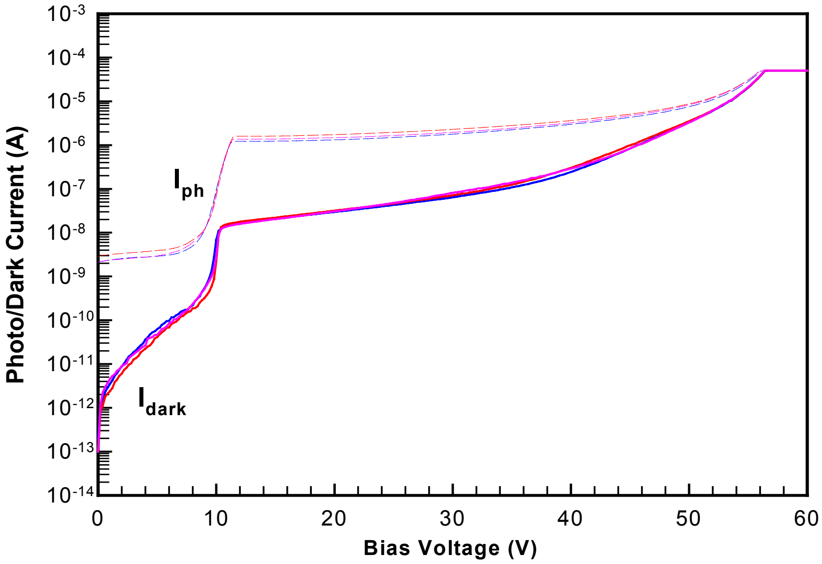

Fig. 3.13 (g) Typical APD I-Vs after H_3PO_4:H_2O:H_2O_2 etching

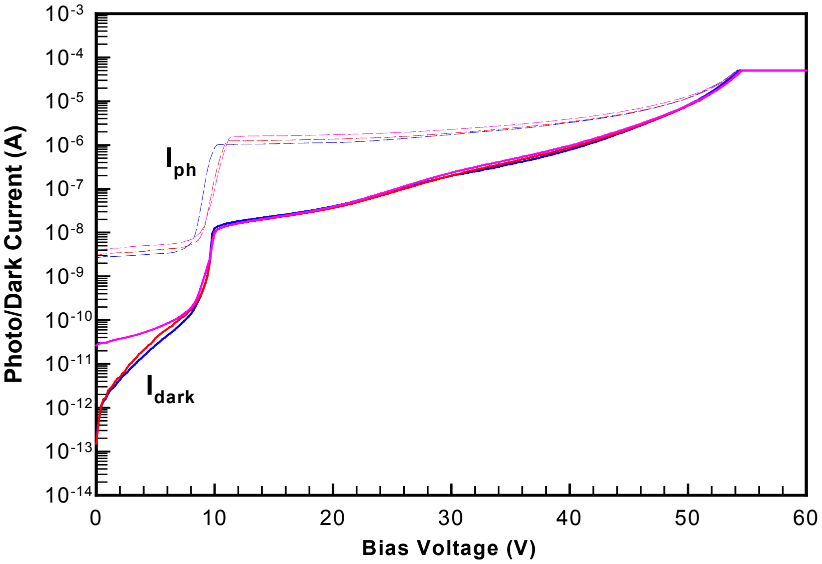

Fig. 3.13 (h) Typical APD I-Vs after H_2SO_4:H_2O:H_2O_2 etching

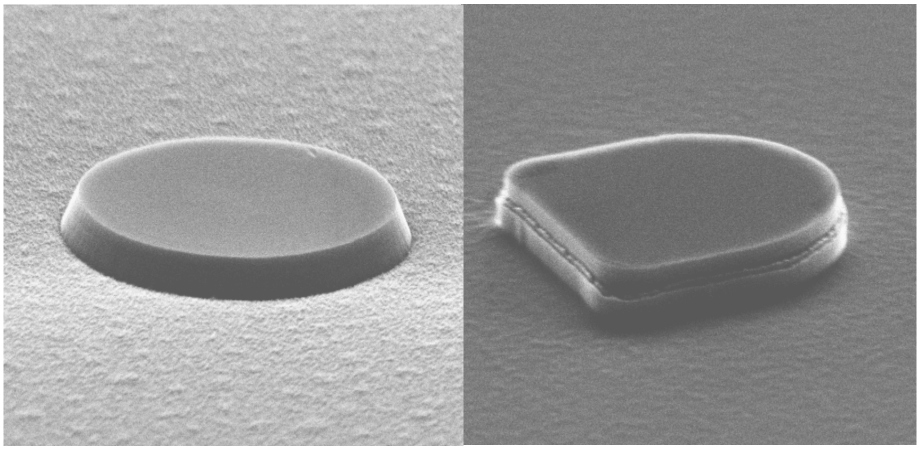

(a) (b)

Fig. 3.14 Mesa morphology after (a) single and (b) multiple *Cl*-based RIE etch

sec.) wet etch of mesa patterns is normally necessary, following a RIE process, in order to form an acceptable bevel shape and polish the sidewall surface of device mesas, prior to the device passivation step. Fig. 3.13 shows a small mesa pattern fabricated with $BCl_3/SiCl_4$ dry etching followed by a buffered (1:1:10) H_3PO_4 etchant cleaning.

Furthermore, to obtain a high quality dry etching result the etching rate should be calibrated carefully and all the etching should be finished in a single run, otherwise the mesa sidewall profile will exhibit irregular shape due to multiple etches, as shown in Fig. 3.14 (b). This profile degradation cannot be recovered by further wet etching polish. The resulting rough sidewall profile will degrade both the breakdown and the dark current properties of an APD, due to similar reasons that have been discussed previously.

3.3.2.3 Mesa Passivation

Mesa passivation is a very critical yet very challenging process step in the APD fabrication. Poor passivation quality will also bring about a poor breakdown as well as high leakage current in an APD. The standard passivation is performed in a plasma-enhanced chemical vapor deposition (PECVD) chamber by depositing a thin layer of silicon dioxide to protect the mesa sidewall from contamination. The basic function of a silicon dioxide film is to terminate dangling bonds at the etched mesa sidewall surface; therefore, the samples should be loaded into the PECVD chamber as soon as mesa etching and cleaning are finished. Passivation is also essential for materials containing aluminum, such as AlGaAs or InAlAs, to prevent degradation over time due to oxidation. A 2000Å-thick silicon dioxide film, which appears dark gray in color, is usually quite enough to meet most mesa passivation requirements.

3.3.2.4 Second Mesa Etch

As has been discussed in section 3.3.2, a high-speed APD structure is usually grown on a semi-insulating substrate to avoid large parasitic capacitance between contact pads. Consequently, an epitaxial *n*-type contact layer, which is normally heavily doped to minimize the *n*-contact resistance, must be removed from beneath the contact pad area. For this purpose, a second mesa etch is performed down to the semi-insulating substrate to remove all the excessive *n*-contact layer area. Also, in the APD structure design, an unintentionally-doped thin sacrificial InAlAs layer (100-nm) is placed just between the *n*-contact layer and the SI-InP substrate to segregate the possible silicon diffusion into the SI-InP substrate during the MBE growth, which will further generate parasitic capacitance between contact pads.

After finishing *n*-mesa pattern definition using standard photolithography, the silicon dioxide covering the *n*-mesa area should be removed prior to *n*-mesa etching. As the *n*-mesa is relatively large, a short chemical wet etch is quite adequate to remove the *n*-contact layer, which is normally less than a micron thick.

3.3.2.5 N-type Metallization

The next step after *n*-mesa definition is to deposit a silicon dioxide layer as the dielectric isolation between contact pads and SI-InP substrate. It was found from experiments that there exists leakage current between contact pads if they are directly deposited on a semi-insulating substrate. A silicon dioxide layer with a moderate thickness will provide good isolation between these contact pads, and, for this purpose, a 2500Å-thick SiO_2 layer is deposited to fulfill pad isolation.

N-type contact patterns are then defined by standard photolithography and contact windows are opened on the SiO_2 layer. A Ni(20nm)/AuGe(30nm)/Au (120nm) metal film is then deposited and alloyed with the n^+-type InAlAs contact layer by annealing samples at 400^oC for 30sec to form reliable *n*-type ohmic contacts. The typical specific contact resistance, which is obtained by on-wafer TLM pattern measurements, is usually far below $1\times10^{-6}\ \Omega\cdot cm^2$ and is much better than that of *p*-type contacts.

3.3.2.6 Planarization (optional)

At this stage, fully functional APDs have been fabricated on the SI-InP substrate, with both *p*-type and *n*-type contacts available for I-V characterization. For most APDs fabricated on SI-InP substrates, the planarization step is negligible and the next step is contact pad formation, as per 3.3.2.7. For an APD structure grown on a conducting substrate, however, a BCB planarization step is required to provide better device isolation with low parasitic capacitance between pads. BCB is an organic polymer that is photosensitive (negative) and can be used for planarization. BCB is usually spin-coated on the sample and the film thickness is controlled by the rotation speed. Openings in the BCB film may be prepared by direct photolithography (as it is a negative resist). The samples then need to be cured in several steps to harden the BCB film; these curing process steps will reduce the BCB film thickness by roughly 30-50%. An oxygen plasma treatment is then required to have the opening area cleaned to guarantee reliable connects between ohmic contact metals and pads.

3.3.2.7 Contact Pads

The final step of the full-scale high-speed APD processing is to connect the deposited contact pads and ohmic metals using an air-bridge interconnect technique. A thick PR (AZ5330) is first applied and patterned with the air-bridge mask set, using either AZ725 developer, or using buffered AZ400K (1:4) in DI water. Openings on the *p*-mesa, which must be prepared before any further processing steps, are made either using BOE dip or dry etching (CF_4+O_2), after hard-baking the PR patterns. A decent bevel profile is formed at the PR sidewalls, using a hard-bake at 90^oC for 30min. A thin Ti(10nm)/Au(50nm) film, which is then deposited as the base of the air-bridge metal, completely covers the PR bevels without any cracks. Another photolithography step, using a 3-4μm PR (AZ5330, or a double-coated AZ5214), is applied on samples to define the final pad patterns for electroplating. The samples are then electroplated in a MICROFAB AU-100 gold-plating solution, which is provided by Enthone-OMI Inc., at 75°C for about 20min, for a sample having roughly a $1cm^2$ dimension. The resulting metal thickness is around 2μm after electro-plating. The final air-bridge interconnects, after lift-off in an ultrasonic bath, are then formed. A finished high-speed APD device, with the above full-scale processing, is shown in Fig. 3.15.

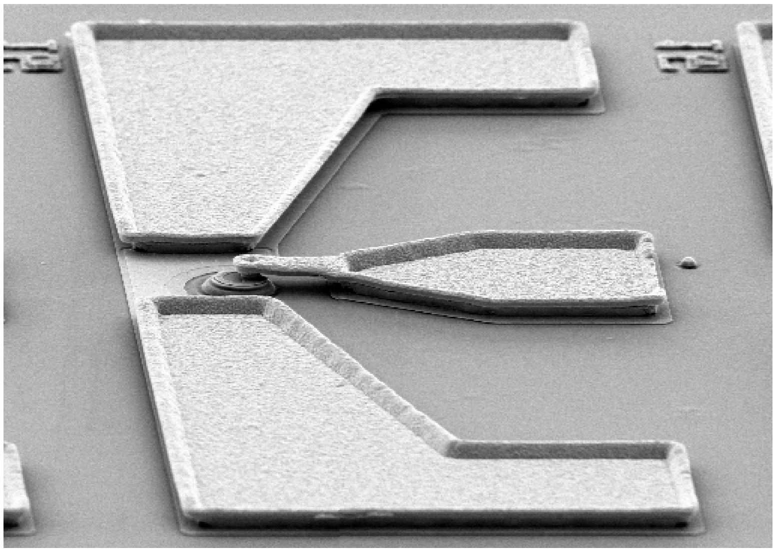

Fig. 3.15 SEM picture of a finished APD with air-bridge interconnects

3.4 Avalanche Photodiode Characterization

3.4.1 Current-Voltage and Capacitance-Voltage Measurements

DC current-voltage measurements were conducted using a probe station and an HP4145B or a HP4162C Semiconductor Parameter Analyzer. Photocurrents and dark currents are measured at different bias voltages, and multiplication gains can be calculated from the photocurrent and dark current measurement results, using the following equation

$$M = M_0 \frac{I_{ph} - I_{dark}}{I_{ph,0} - I_{dark,0}} \tag{3.16}$$

where $I_{ph,0}$ and $I_{dark,0}$ are primary photocurrent and dark current measured at a fixed voltage above punch through where the APD gain is M_0, and are used as a reference for further gain calculation; I_{ph} and I_{dark} are photocurrents and dark currents measured above the reference bias voltage. For a simple *p-i-n* structure APD, since punch through occurs, at low bias voltages, the unity gain (M_0=1) reference is not difficult to determine. Usually a reverse bias of –2.0V is quite satisfactory as the unity reference for a simple *p-i-n* structure APD. For a SACM structure, however, the unity gain can be difficult to determine because the multiplication region provides gain prior to punch through if the punch-through is high. So the gain at a reference point (a bias voltage above the punch-through) was usually determined by comparing the measured external quantum efficiency with the theoretical value. The gains at various bias voltages above the punch-through, could therefore be estimated.

APD capacitance is measured using the same probe station but with an

HP4275A LCR meter; a diagram of this setup is shown in Fig. 3.16.

The C-V measurement is basically used to examine the parasitic capacitance of a photodiode at a given reverse bias voltage. Sometimes the C-V measurement is also used to quantify the intrinsic region thickness, as in the case of the high-Al $Al_xGa_{1-x}As$ APD noise study in which unity-gain capacitance is obtained from the C-V measurements of a series of APDs with different mesa areas, based on which the intrinsic layer thickness can be extrapolated. The punch-through voltage of a SACM APD, when its value is ambiguous as determined from the I-V measurements, can be determined by the C-V measurement. The APD capacitance is very sensitive to the reverse bias due to strong dependence on the depletion layer thickness. For a SACM device whose punch-through is difficult to determine by I-V measurements, C-V measurement is definitely an effective option.

Fig. 3.16 I-V and C-V measurement setup

3.4.2 Excess Noise Measurement

Excess noise measurement is performed using a HP8970 noise meter. Through a microwave probe arm, the noise signal is amplified with a low noise amplifier and is then fed into a HP8970 noise figure meter. The center frequency value (normally 30MHz) of the HP8970 is chosen so that ambient noise is minimized. An Argon and a He-Ne laser are used to provide optical power in the UV and IR regions, respectively. For the homojuction APD noise measurements, shorter UV wavelength (at 361/365nm) is required to insure that most of the absorption occurs in the *p*-type contact region so that the single carrier injection assumption is maintained. For the long-wavelength SACM APDs, however, a He-Ne (λ=1.55μm) laser is used to provide the incident signal. Only the InGaAs absorber will absorb the incoming light and single carrier injection is perfectly satisfied under this condition. The photo-response generated using a He-Ne laser is usually much higher than that from the UV laser because most of the photogenerated carriers can be collected. The set-up diagram is illustrated in Fig. 3.17.

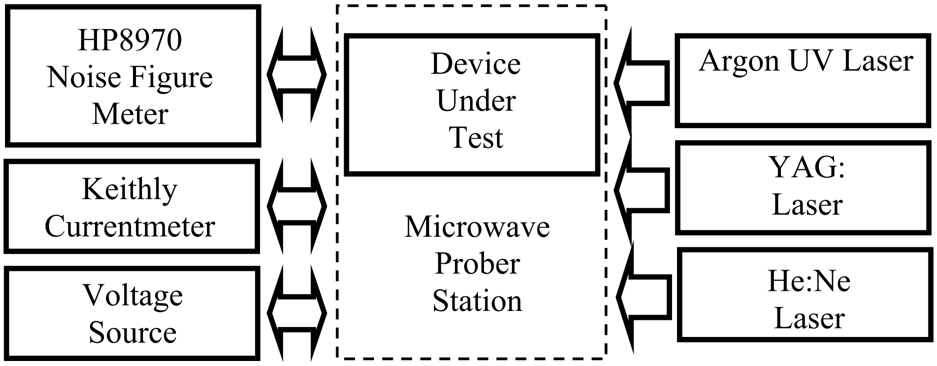

Fig. 3.17 (a) Diagram of the excess noise measurement setup

A high resolution Keithely current meter is utilized to measure both photo and dark currents, while a high-resolution digital voltage source is used to provide accurate device bias supply.

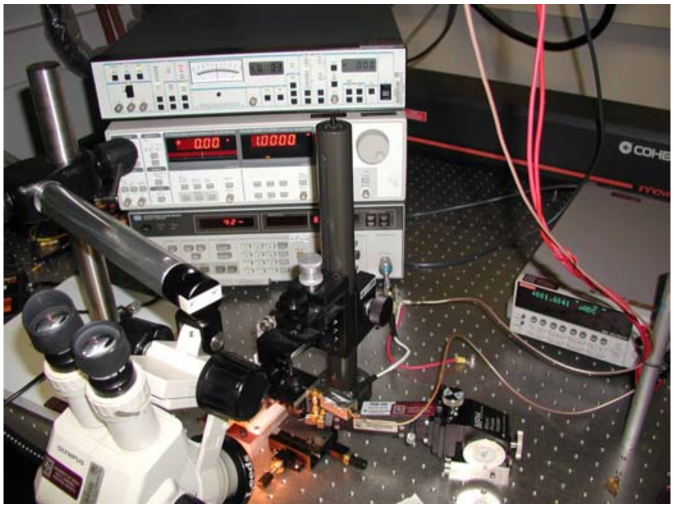

Fig. 3.17 (b) Photograph of the excess noise measurement setup

3.4.3 Quantum Efficiency Measurement

The quantum efficiency is measured using a tungsten-halogen light source, a spectrometer, and a lock-in amplifier, as shown in Fig. 3.18.

Measurement of normal incidence devices is straightforward. Since the optical output power of the tungsten-halogen source is low and the resulting photoresponse in the photodiode is weak, this light source is chopped at a frequency of - 200Hz and the photocurrent is detected using a Stanford Research SR850 lock-in amplifier. The position of the avalanche photodiode under test should be carefully adjusted to obtain maximum photoresponse. Then, at a specific reverse bias voltage above punched through, the photocurrents are measured in the wavelength range of interest. Without changing the optical path for the measurement, a calibrated germanium photodetector is loaded through which the photocurrent is maximized by adjusting the device's position. The photocurrents are measured within the same wavelength range used for APD. The photocurrents of the APD and the Ge detector are compared and external quantum efficiencies of the APD can be derived from the calibrated external quantum efficiencies of the Ge photodetector, as shown below

$$\eta_{ext,APD} = \frac{I_{ph,APD}}{I_{ph,Ge}} \eta_{ext,Ge}, \qquad (3.17)$$

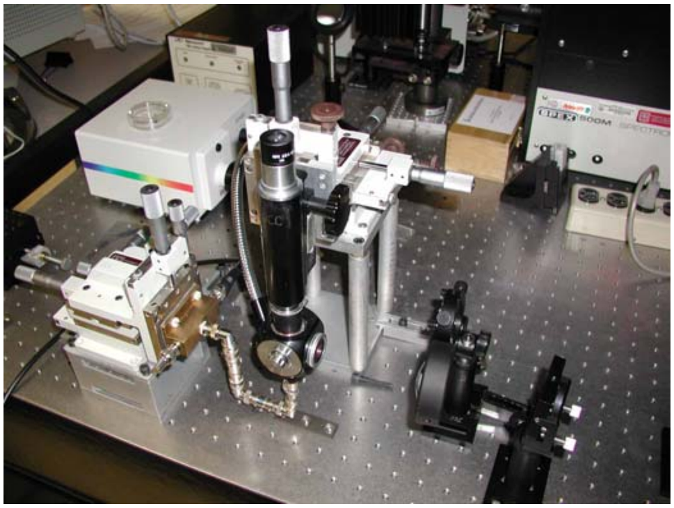

Fig. 3.18 Diagram of the I-V and C-V measurement setup

3.4.4 Speed Characterization

The photocurrent frequency response for 10Gb/s APDs and focal-plane arrays is usually measured using a HP 20 GHz lightwave component analyzer, as shown in Fig. 3.19, at a small signal condition. Free space coupling is fulfilled using a lensed fiber, through which a long wavelength beam spot is focused, either on top of a mesa or from the backside, with a beam waist less than 10μm. The light intensity is controlled using a variable optical attenuator. Gain is monitored and calculated using a Keithly 2400 source/meter, at a fixed light intensity. Frequency responses can be obtained at different gains and different input light power levels, either by changing the APD bias or changing attenuation. The gain-bandwidth product at different light intensities can thus be obtained.

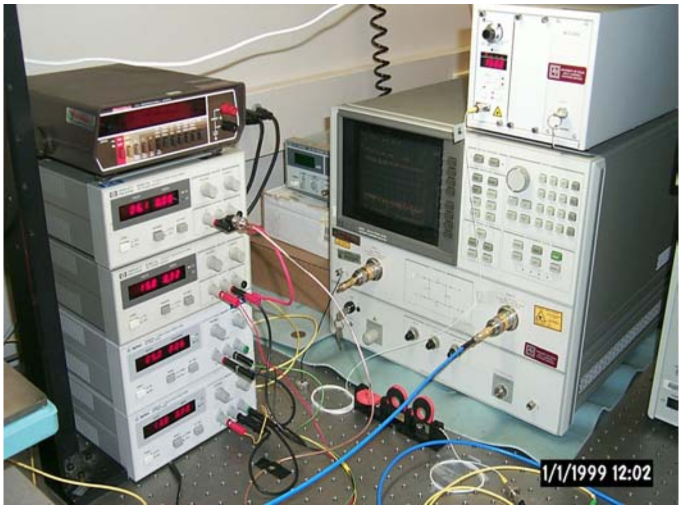

Fig. 3.19 Diagram of the speed measurement setup

A probe station has been modified to perform speed measurements both with front-side and backside illumination, with standard 50Ω GSG microwave probe tips. With this probe station, on-wafer bandwidth testing can be performed at a bandwidth up to 20GHz.

For higher speed measurements, the bandwidths and gain-bandwidth products of APDs are measured using a heterodyne system, as shown in Fig. 3.20. Free space coupling is necessary for waveguide devices in order to deliver the maximum optical incident power to achieve an adequate signal level for the measurement**.** Gain is monitored and calculated using the DC current level obtained from a Keithly 2400 source/meter.

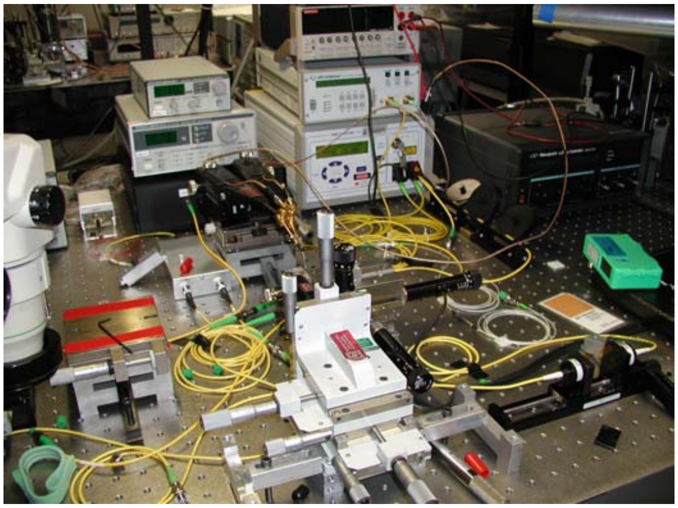

Fig. 3.20 Diagram of the speed measurement setup

3.4.5 Sensitivity Characterization

Sensitivity measurements are a critical part of characterizing an APD's performance; the sensitivity eventually reflects the true APD performance in an integrated receiver. As shown in Fig. 3.21, the sensitivity setup is comprised of an electrical path and an optical path. In the electrical path, a frequency synthesizer is used to provide a time base for an Advantest 10Gb/s pattern generator, which provides coded electrical pulse trains for the BER testing. The output of the pattern generator is used to modulate the optical input signal for the integrated receiver through the amplification of a 10GHz modulator driver. The electrical output of the integrated receiver (DUT) was connected to an Advantest OC-192 error detector and to an Agilent 86000 digital oscilloscope for further eye-diagram observation.

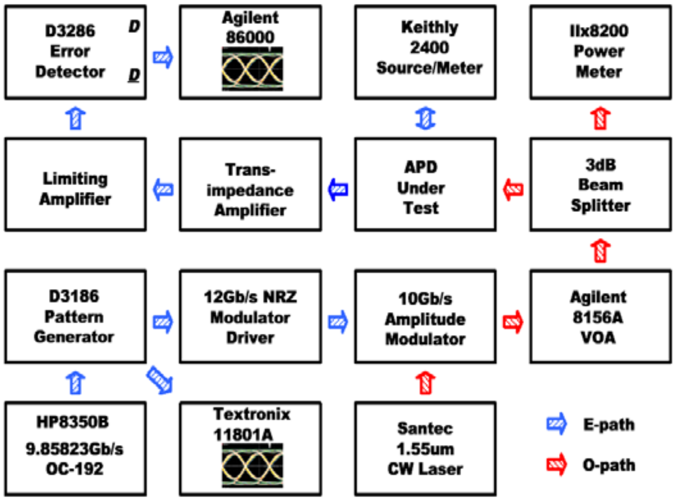

Fig. 3.21 Diagram of the 10Gb/s sensitivity measurement setup

The optical source is a Santec tunable long-wavelength laser, as shown in Fig. 3.21, from which a CW mode, 1.55μm long wavelength signal is provided. After a polarization compensator, this CW light is modulated by an OC-192 pattern generator through a 12GHz Mach-Zender modulator, and is fed into a variable optical attenuator for power attenuation. One portion of the attenuator output is coupled to an optical power meter using a 3-dB directional coupler, the other 3-dB optical power is transmitted into the integrated receiver as input optical signal. The input optical power can be controlled by the variable attenuator and monitored by the optical power meter. Bit-error-rate at a specified data-rate, which is controlled by the frequency synthesizer, can thus be measured using the Advantest error detector.

3.5 Summary

In this Chapter, various types of photodetector structures and design methods were analyzed and compared. The SACM device structure was chosen for my high-speed telecommunications APD and focal-plane APD array design. A normalized optical coupling scheme was adopted for both 10Gb/s telecommunications APDs and focal-plane APD arrays. Advantages of waveguide optical coupling scheme were also analyzed. The waveguide APD structure has been chosen for the 40Gb/s telecommunications APDs to obtain both an adequate responsivity and an ample operating bandwidth at a 40Gb/s data rate. An air-bridge based high-speed APD fabrication technology has also been designed and developed for high-speed photodiode fabrication (both for 10Gb/s and 40Gb/s).

Chapter 4

Noise Study of $Al_xGa_{1-x}As$ APDs

Photodiode sensitivity is one of the key issues in a long-haul fiber optic communication system, as has been discussed in previous chapters. An APD is frequently the photodetector of choice for “long-haul” applications because it usually provides 5 to 10 dB sensitivity improvement in an optical receiver, compared to a *p-i-n* photodiode, due to its internal gain, which originates from carrier impact ionization. The multiplication region of an APD plays the central role in determining its overall gain, multiplication noise, and achievable bandwidth at high gain values in terms of the gain-bandwidth product. According to the local-field avalanche theory [4-1]-[4-7], both the multiplication noise and the gain-bandwidth product of an APD are determined by the ratio of electron and hole impact ionization coefficients. For most of the III-V compound materials, however, this ratio normally approaches unity at high electric field intensities. It has been shown that this condition results in poor device performance [4-4], [4-6].

The impact ionization properties of GaAs/$Al_xGa_{1-x}As$ bulk materials and multiple quantum wells with low *Al* ratio have been thoroughly studied [4-8]-[4-12]. Recently, GaAs and $Al_xGa_{1-x}As$ ($x \leq 0.4$) APDs with thin multiplication regions have been studied and it was found that the multiplication noise decreases with decreasing thickness of the multiplication region [4-13]-[4-20], and gain-bandwidth product increases due to the same reason [4-21], [4-22]. However, the impact ionization properties of $Al_xGa_{1-x}As$ materials with high *Al* content (>60%) have not yet been reported. It is thus very instructive to investigate the impact ionization and noise properties of $Al_xGa_{1-x}As$ APDs that have higher *Al* contents.

4.1 APD Structure for Noise Study

The device structure utilized for APD noise study is the simple *p-i-n* type, as shown in Fig. 4.1.

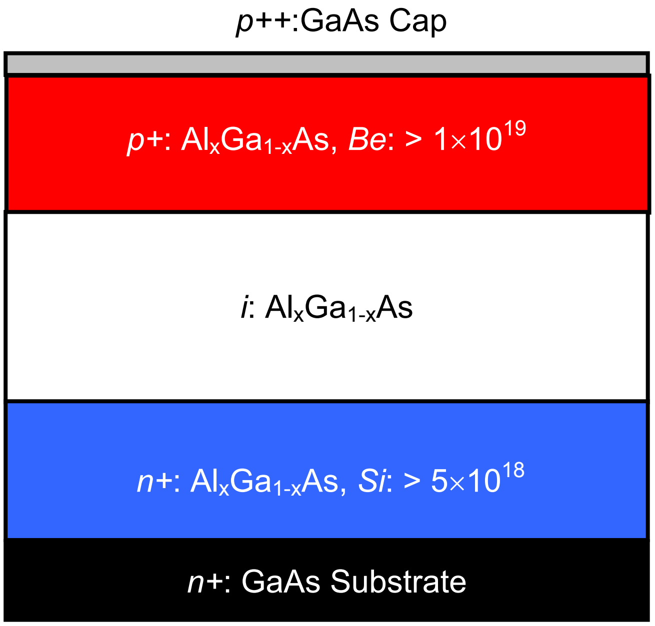

Fig. 4.1 Illustration of the typical device structure for APD noise study

There are basically three considerations for this device structure design: 1) the unity gain reference of a simple *p-i-n* structure APD is easier to determine than for the case of a SACM APD structure, 2) a homo-junction structure is preferable for the noise study because there exists no hetero-structure induced spatial modulation of carrier impact ionization events within the active region, which can change the overall excess noise of the APDs, and 3) simplicity in device processing is another important reason for using *p-i-n* device structures. Neither the bandwidth nor the quantum efficiency of this type of APD is a very critical issue both for gain and for noise study as long as an APD has a 3-dB bandwidth ≥ 300MHz, which is the maximum noise measurement frequency. APD gains are normally measured at DC bias condition. The APD excess noise is measured within a bandwidth of <290MHz, where a primary photocurrent of 10nA is quite ample to satisfy the sensitivity requirement of the whole noise measurement setup. All requirements for noise study can be easily satisfied using this simple type of APD structure.

In GaAs and $Al_xGa_{1-x}As$ materials, the impact ionization coefficients of electrons (α) is greater than that of holes (β). Accordingly, pure electron initiated carrier multiplication is preferable to obtain the lowest multiplication noise in APDs. In order to ensure pure electron injection, the thickness of the absorptive *p*-layer needs to be much larger than the photon absorption length so that most of the incoming photons will be absorbed before they reach the gain (multiplication) region. On the other hand, it beneficial to collect a high fraction of the photon-generated electrons to ensure acceptable quantum efficiency for the noise measurement accuracy. This requires that the thickness of the *p*-region be comparable to the diffusion length of the electrons. It is always desirable to obtain both high quantum efficiency and a low mixed-injection ratio concurrently. This requires that the optical absorption length be much shorter than the diffusion length of the minority carrier. This can be done with an optical source that has a short wavelength (i.e. $h\nu > E_g$) to reduce the photon absorption length.

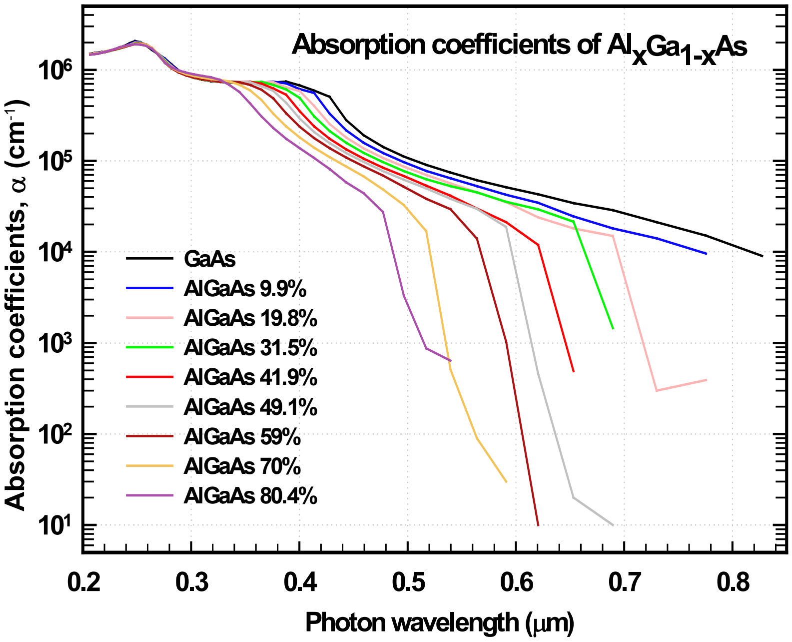

Fig. 4.2 Optical absorption coefficients in Al$_x$Ga$_{1-x}$As (*x* from 0 to 0.9) materials

In my APD noise study, a CW UV-laser with dual wavelengths of 351 and 363 nm was used. Fig. 4.2 shows the optical absorption coefficients of Al$_x$Ga$_{1-x}$As materials (*x* ratio from 0 to 0.8) in the wavelength range of 200-nm to 850-nm [4-23]. For the Al$_{0.9}$Ga$_{0.1}$As, this number is between 10 and 20 μm^{-1} [4-24]. For GaAs and Al$_{0.2}$Ga$_{0.8}$As, a 1.5-*μ*m-thick absorber was used because of relatively long electron diffusion length in these materials. For Al$_x$Ga$_{1-x}$As APDs with *x* from 0.4 to 0.9, however, a 0.75-*μ*m absorber was used due to shorter minority carrier diffusion length. The calculated photon absorption lengths and the photon leakage values of a given absorber thickness at wavelengths of 351 and 363 nm are listed in Table 4.1 for various Al$_x$Ga$_{1-x}$As APD structures (*x* from 0 to 0.9).

material	absorption coefficient (μm^{-1})	absorption length (μm)	typical thickness (μm)	photon leakage $e^{-a_0 d}$
GaAs	71.5	0.0140	1.5	2.6x10^{-47}
$Al_{0.2}Ga_{0.8}As$	72.9	0.0137	1.5	3.2x10^{-48}
$Al_{0.4}Ga_{0.6}As$	70.4	0.0142	0.75	1.2x10^{-23}
$Al_{0.6}Ga_{0.4}As$	60.4	0.0166	0.75	2.1x10^{-20}
$Al_{0.8}Ga_{0.2}As$	30.7	0.0326	0.75	1.0x10^{-10}
$Al_{0.9}Ga_{0.1}As$	10-20	0.1-0.05	0.75	5.5x10^{-4} - 3.1x10^{-7}

Table 4.1 Photon absorption coefficients and the calculated absorption lengths in $Al_xGa_{1-x}As$ (x from 0 to 0.9) materials

4.2 Experiment

4.2.1 Material Growth

All the APDs for this study were grown on n^+ (100) GaAs substrates in a Varian GEN-II MBE reactor. The nominal thickness of the intrinsic multiplication regions was 200-nm and 800-nm and the range of *Al* concentration was from 0 to 0.9. The "*i*" region was unintentionally doped with an estimated *n*-type background doping concentration of ~2 x 10^{15} cm^{-3}. The "*i*" region was sandwiched between a Be-doped p^+ layer on the top and a 200-nm-thick *Si*-doped n^+-contact layer below. The *p*-contact layer thickness for all $Al_xGa_{1-x}As$ APDs (x from 0 to 0.9) is listed in Table 1. All contact layers were highly doped (up to >5 x 10^{18} cm^{-3}) in order to confine most of the electric field in the intrinsic region. The high doping in these cladding layers, however, resulted in *Be* diffusion from the top and *Si* diffusion from below the "*i*" layers, which reduced the "*i*" layer thickness to less than the nominal value. To compensate for this, the intrinsic region thickness was checked either by SIMS or by C-V measurements. Initial SIMS results indicated beryllium diffusion from the *p*-contact layer into the intrinsic region during MBE growth. Further results revealed that beryllium diffusion was more serious for high *Al* content material, which can be attributed to the larger diffusion length of *Be*-dopant in the larger lattice constant high *Al* content $Al_xGa_{1-x}As$ alloys. Typical SIMS results for the high-*Al*-content APD structures are shown in Figure 4.3. In addition, Auger electron spectroscopy (AES) measurements were employed to verify the Al concentration for the high Al content APD devices. The AES results showed that the concentrations were within 2% of the target values.

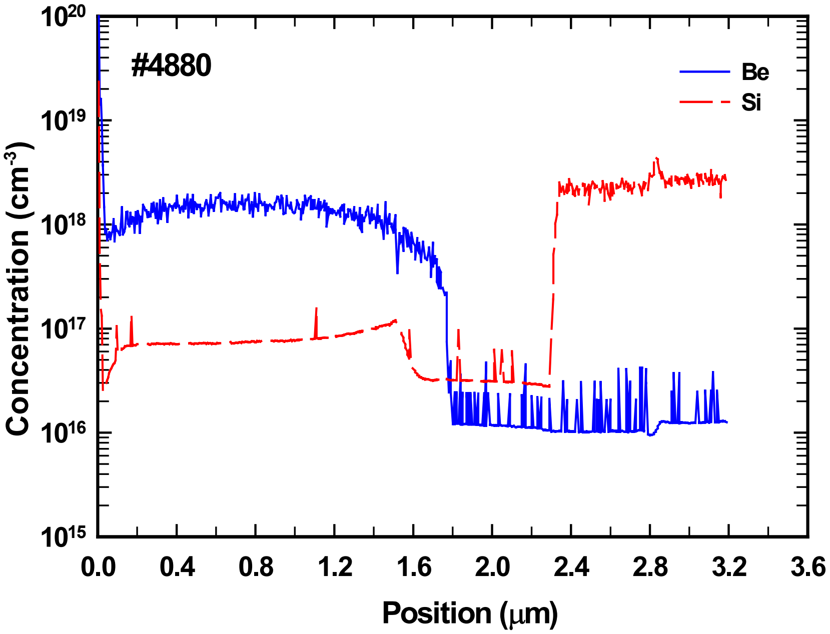

Fig. 4.3 Beryllium diffusion in the 90% $Al_xGa_{1-x}As$ APD structure

4.2.2 Device Processing

Good *p*-type ohmic contact was insured with a top layer of 30-nm-thick, heavily Be-doped (> 10^{19} cm^{-3}) p^+ GaAs. Device mesas with a diameter of 100 μm were formed using standard phosphorous wet-chemical etching. The ohmic contacts were patterned with a standard photolithography and lift-off process. Au-Cr served as the *p*-contact and Ni-AuGe-Au was used as the *n*-contact. In order to facilitate microwave probing and minimize the contact resistance, the *n*-contact covered the whole surface of the wafer except the mesa areas. Fig. 4.4 shows a top-view of a typical APD after simple-mesa processing.

Fig. 4.4 Simple-mesa APD for noise study, after the final processing step

4.2.3 Measurements

As has been discussed in section 4.2, pure electron injection was achieved with a stable continuous-wave (CW) Argon UV laser that has two lines at 351 nm and 363 nm. The light beam was carefully focused onto the top of the mesa via a 10× UV microscope objective and an iris was placed in front of the lens to shield all but the central light beam. According to the published absorption coefficient data for $Al_xGa_{1-x}As$ [4-23], [4-24], we estimate, as detailed in Ref. 19, that the ratio of hole injection to the total is less than 0.1%.

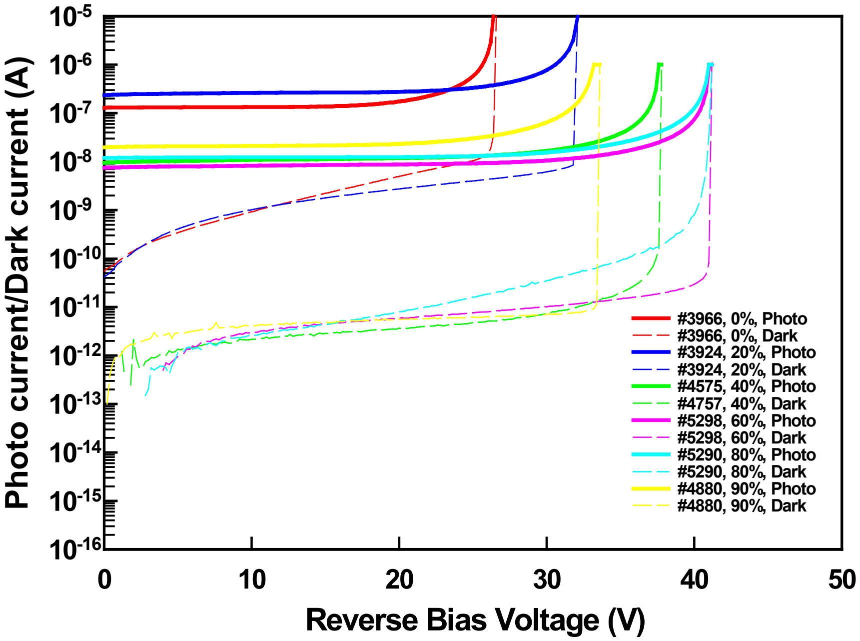

Fig. 4.5 Typical APD I-Vs of the 800-nm-thick $Al_xGa_{1-x}As$ APDs (*x* from 0 to 0.9)

The photocurrent and dark current of all the $Al_xGa_{1-x}As$ APDs with various multiplication regions were measured with a HP4145B semiconductor parameter analyzer, as shown in Fig. 4.5. Very low dark current density ($<2\times10^{-6}$ A/cm^2) at 90% of the device breakdown was consistently found for the APDs with higher Al ratio (>0.4). For very wide Eg even generation-recombination current is small because most of the effective traps are located near mid gap.

As a result of the bias-dependent collection efficiency, the I-V characteristic of the $Al_{0.9}Ga_{0.1}As$ device at low bias was not flat. This can lead to overestimation of the gain and thus an underestimate of the measured excess noise and the estimated *k* value. The gain has been "corrected" downward by a simple linear approximation between applied bias and primary photocurrent [4-25]. By fitting the measured photocurrent at low bias region we can extract the fitting parameters and calculate the corrected multiplication gain values at each bias voltage for the $Al_{0.9}Ga_{0.1}As$ APDs. For all the other devices the correction was negligible.

The noise power spectral density of the APDs was measured with an HP 8970B noise figure meter that can be programmed to operate at different center frequencies and bandwidths. The environmental noise was reduced by probing the devices with a shielded microwave probe. The noise of the circuit after the photodiode was normalized using a standard calibrated noise source to maintain the accuracy and consistency of the measurement. Plots of the extracted excess noise factors versus the gain for $Al_xGa_{1-x}As$ APDs with different Al mole fractions (0.1 to 0.9) are shown in Fig. 4.6 (a) and Fig. 4.6 (b) for thick and thin multiplication regions, respectively. For reference, the dashed lines show the calculated excess noise for different *k* values using the local field model.

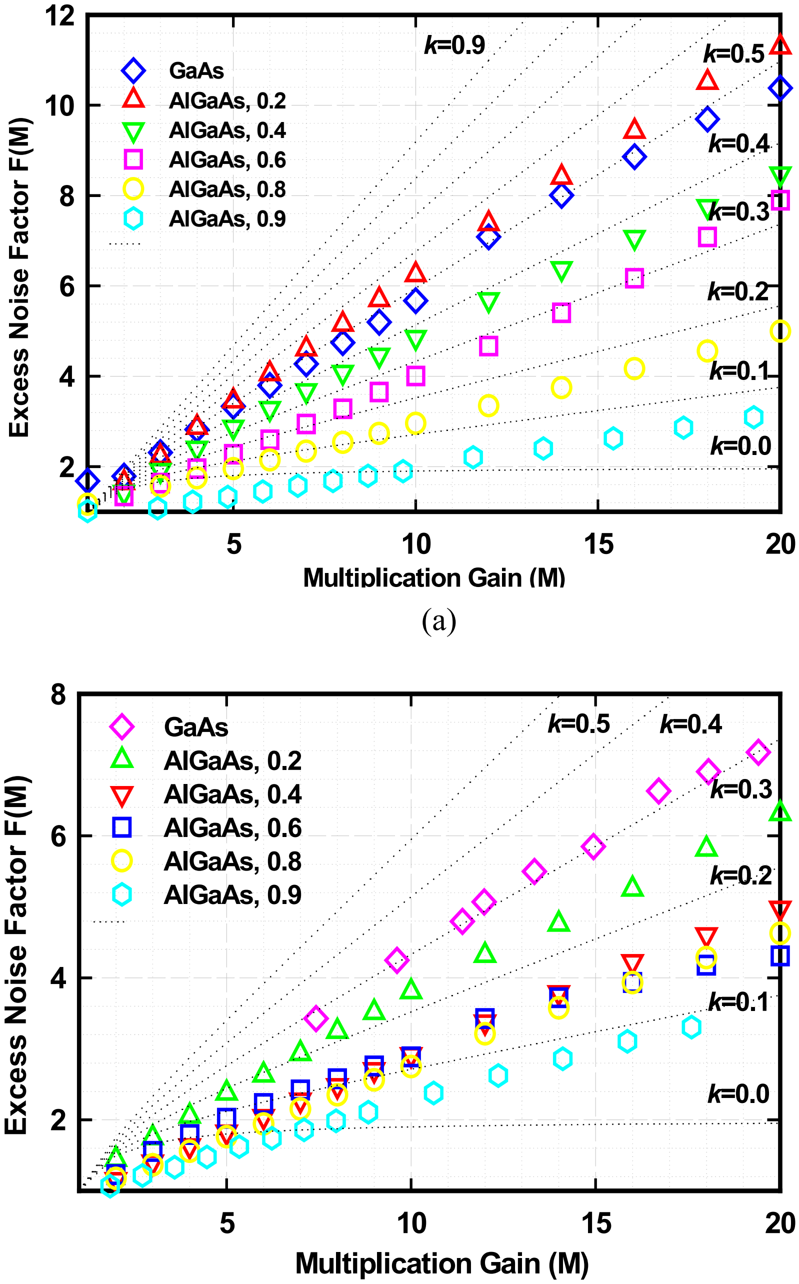

(a)

(b)

Fig. 4.6 APD noise of the (a) 800-nm-thick and (b) 200-nm-thick $Al_xGa_{1-x}As$ APDs (*x* from 0 to 0.9)

4.3 Results and Discussion

Table 4.2 shows the fitted *k* values from the extracted excess noise factors for all the $Al_xGa_{1-x}As$ APDs using the local-field model. The nominal *k* values were obtained with a least squares fit to the local field expression for F(M) [4-3]. The measured thickness (SIMS and/or C-V) of the "*i*" regions are shown below the *k* values. Here we do not suggest that the *k* values represent the actual ratios of the ionization coefficients, particularly for the thin samples. The *k* values do, however, provide a widely recognized figure of merit for evaluating the excess noise. For the thick GaAs APDs, a good fit to the data is obtained with a *k* value of 0.48, which agrees with the results reported by Ando and Kanbe (*k*=0.4-0.6) [4-26] and by Bulman et al. (0.6) for bulk GaAs [4-27]. For $Al_xGa_{1-x}As$ with different Al concentrations (from 0.2 to 0.9), the fitted *k* values decrease with increasing Al concentration. The decrease in multiplication noise is particularly significant for $x \geq 0.8$. These results are somewhat at variance with those of V. M. Robbins et al., who reported that *k* is relatively constant for $Al_xGa_{1-x}As$ ($0.1 \leq x \leq 0.4$) [4-8]. Their conclusion was based on the observation that at the high electric field intensities that are required for impact ionization, the electrons have sufficient energy to scatter freely into *X* and *L* valleys, which results in relatively uniform distribution throughout the Brillouin zone. They concluded that changes in the relative positions of the energy band minima (caused by Al mole fraction change) do not significantly alter the scattering environment and thus no obvious changes in the ratio of the electron and hole impact ionization coefficients would be expected. However, as listed in Table 4.2, we observe a decrease in *k* of approximately 40% as *x* increases from 0 to 0.6 and k drops to $k<0.1$ for $Al_{0.9}Ga_{0.1}As$. These results indicate that the energy band structure may influence impact ionization and the multiplication noise in $Al_xGa_{1-x}As$ APDs. The diffusion from the p^+ and n^+ layers during growth was greater for $Al_{0.8}Ga_{0.2}As$ and $Al_{0.9}Ga_{0.1}As$ APDs which made their "*i*" regions thinner than the lower Al-content devices. Nevertheless, it can be seen in Table 4.2 that for the thick high-Al-content APDs, the excess noise (k value) is much lower than that of APDs with equivalent thickness of GaAs.

Al conc.	0%	20%	40%	60%	80%	90%
i: thick	k=0.48 0.79μm[b] k=0.39[c] 0.50μm k-0.3-0.4[d] 0.50μm	k=0.54 0.74μm[b]	k=0.36 0.75μm[a]	k=0.30 0.77μm[a]	k=0.15 0.65μm[a]	k<0.1 0.52μm[a]
i: thin	k=0.31[e] 0.17μm[a] 0.16μm[b] k≥0.30[f] 0.20μm	k=0.24[e] 0.19μm[b]	k=0.15 0.17μm[a]	k=0.14 0.17μm[a]	k=0.13 0.15μm[a]	k<0.1 0.14μm[b]

[a] Intrinsic region thickness measured by SIMS.
[b] Intrinsic region thickness measured by C-V technique.
[c] See Ref. 19. [d] See Ref. 15. [e] See Ref. 25. [f] See Ref. 14.

Table 4.2 Excess noise in the $Al_xGa_{1-x}As$ (x from 0 to 0.9) APDs

The measured excess noise factors versus gain for $Al_xGa_{1-x}As$ APDs with thin multiplication regions are shown in Fig. 4.6(b). As expected, the excess noise factors also decreased with increasing Al concentration, as was observed for the thick samples. Consistent with previous reports [4-14]-[4-17], [4-19], the non-local characteristics of impact ionization yields lower noise in all of the thin APDs compared to the corresponding thick devices. For the $Al_{0.9}Ga_{0.1}As$ APDs, even after correction for bias-dependent injection efficiency, the excess noise is below the k=0.1 reference curve. Further, it appears that the excess noise of $Al_{0.9}Ga_{0.1}As$ APDs does not change significantly with the *i*-region thickness, in contrast to what has been observed for lower Al concentration (x<0.9). The fitted k value of $Al_{0.9}Ga_{0.1}As$ APDs is the lowest (<<0.1) among all the $Al_xGa_{1-x}As$ samples, as shown in Figure 4.6. Low excess noise phenomenon observed from high *Al* content $Al_xGa_{1-x}As$ APDs was further corroborated by the results reported from the other group [4-28], [4-29].

4.4 Summary

In short summary, I have shown that the multiplication noise of an $Al_xGa_{1-x}As$ homojunction APD (with x from 0.0 to 0.8), at a given multiplication gain value, decreases as the multiplication layer thickness decreases due to more pronounced non-local impact ionization effect. I have also shown that at a given multiplication gain the excess noise of an $Al_xGa_{1-x}As$ homojunction APD decreases with the increasing Al content due to larger differences of the impact ionization coefficients of electrons and holes. The devices with high Al content (x≥0.8) exhibit particularly low noise. $Al_{0.9}Ga_{0.1}As$ APDs with thin multiplication regions (140nm) exhibit even lower noise that is comparable to Si APDs.

Chapter 5

Temperature Dependence of Impact Ionization in $Al_xGa_{1-x}As$ APDs

The GaAs-based material systems have been the focus of greatest interest for semiconductor device research, both for optoelectronics and microelectronics applications. In the optoelectronics area, GaAs-based materials have been served as the platform for the 980-nm related optoelectronic components, such as lasers (especially the VECSEL type). Excellent device performance, aided by the freedom of choices of both bandgap energy and band structure from GaAs-based material systems, which are indispensable for the optoelectronic devices, can be obtained. For example, $Al_xGa_{1-x}As$ APDs with high-*Al* ratios exhibited extremely low multiplication noise that is comparable to that of silicon APDs, as has been discussed in the previous chapter. In the microelectronics area, high power performance of GaAs heterojunction bipolar transistors (HBTs) is exclusively advantageous over that achievable from other types of materials. However, HBT high power performance is strongly affected by carrier impact ionization in the base-collector junction region, where the electric field strength is usually very strong and the junction temperature is high. Wide applications of $Al_xGa_{1-x}As$ materials in microwave and millimeter-wave power devices require a thorough understanding of their avalanche properties. Since the carrier impact ionization process depends strongly on temperature, it is very instructive to investigate the impact ionization properties of the GaAs-based material [5-1]-[5-5] over a larger temperature range to understand the physics of impact ionization in $Al_xGa_{1-x}As$ materials and devices.

5.1 Experiment

Owing to good lattice match to GaAs substrates, $Al_xGa_{1-x}As$ is almost an ideal material system for the device physics study. The aluminum ratio, x, can be adjusted continuously from 0 to 1.0 without sacrificing any crystal quality induced by the lattice-mismatch. Both the bandgap energy and the band structure of $Al_xGa_{1-x}As$ material can be tailored, by merely changing the aluminum ratio x, to the required value. In this study, a series of homojunction $Al_xGa_{1-x}As$ APDs with different aluminum ratios (0-0.9) and with a nominal multiplication region thickness of 0.8 μm, which have been thoroughly studied for their multiplication noise at room temperature, were further investigated for temperature dependence of their impact ionization coefficients.

Prior to the temperature dependence study, all the finished $Al_xGa_{1-x}As$ APDs were carefully measured using a HP4145B semiconductor parameter analyzer. Devices with good I-V characteristics were then selected for further temperature dependence characterization. In order to control the device temperature, all these devices were mounted on a thermoelectric heater and the temperature was monitored using a thermal-couple close to the devices under test. Two stable continuous-wave (CW) lasers, a YAG laser (5mW, λ=532 nm) and an Argon UV laser (500mW, λ=351 nm and 363 nm), were employed in the I-V measurements in order to control the optical absorption length. For $Al_xGa_{1-x}As$ APDs with x ratio up to 0.4, a YAG laser provided good single carrier injection, which has been corroborated by room temperature noise measurements, as discussed in Chapter 4. For APDs with higher aluminum ratios, a UV laser was used to achieve pure single carrier injection in the *p*-type absorber. In order to avoid mixed carrier injections at the mesa sidewall, the light beam was carefully focused onto the top of the device mesa via a microscope objective, in front of which an iris was placed to shield all but the central beam. A small focal spot and a large working distance were obtained for the 532-nm beam with a 40x Zeiss objective. A 10x UV objective was essential to alleviate the insertion loss in the UV region.

All these APDs were then measured at low temperatures, from room temperature down to below 20K. A Janis ST-100 liquid-helium cryostat was used for the device measurements below 80K and a Janis 6DNT liquid-nitrogen cryostat was used for the measurements between 80K and room temperature. The dark currents were measured using a HP4145B, which was connected with the standard BNC cable to the cryostat. For the photocurrent measurement, a white light source was used to avoid the difficulty of coupling the UV light into the cryostat. All these devices measured achieved maximum multiplication gains ≥20 at different temperatures.

5.2 Parameter Extraction

Through the I-V measurements, pure electron injection initiated device breakdown voltages and multiplication gains over a wide temperature range were obtained, using the standard measurement techniques described in Chapter 3. The noise power spectral density was measured at 50 MHz with a bandwidth of 4 MHz using a HP 8970B noise figure meter, at room temperature and above. In order to eliminate the environmental noise and any signal resonance in the transmission line, the devices were contacted with a shielded microwave probe. The noise of all the components following the photodiode was carefully calibrated and normalized with a standard noise source. This calibration step is essential because the impedance and the contact resistance may vary from device to device, especially over a wide temperature range. The avalanche noise power density was measured as a function of gain both under illumination and in the dark. The ionization coefficient ratios (*k* values) can thus be obtained by fitting the excess noise curves with the multiplication gains.

The impact ionization coefficients of $Al_xGa_{1-x}As$ APDs ($x \leq 0.4$, which is the normal range of most HBT applications) [5-6] were extracted using a unique method, as was initiated by G.E. Stillman et al [5-1], in which APD multiplication gains under pure electron injection and hole injection were compared and the impact ionization coefficients were thus derived. There were basically two reasons for developing this new method for ionization coefficients measurements. Since the two gain curves (for electrons and holes) are quite close to each other at high electric field intensities and the extraction of the coefficients depends on the difference between the two, the accuracy of the final result is subject to the influence of many factors in the experiment. In order to avoid deviations caused by variations in crystal growth, it is preferable if the two gain curves can be measured on the same device. This requirement can be satisfied with heterojunction structures, however, this often results in a higher-than-zero punch-through voltage, which, in turn, makes it difficult to determine the unity-gain reference. It is in this context that noise measurements under pure electron injection were used to determine the ionization coefficients of electrons and holes for the case where the local-field avalanche theory is effective.

According to local-field theory [5-7]-[5-13], in a homojunction APD, the position-dependent gain can be expressed as

$$M(x) = \frac{\exp\left[-\int_x^w dx' \cdot \left(\alpha(E) - \beta(E)\right)\right]}{1 - \int_0^w dx' \cdot \alpha(E) \cdot \left[-\int_{x'}^w dx'' \cdot \left(\alpha(E) - \beta(E)\right)\right]} \tag{5.1}$$

Although this theory fails to accurately model the noise when the multiplication region is thin (<0.5 μm) [5-14]-[5-22], it is still useful for analyzing the characteristics of relatively thick device structures. Since the ionization coefficient (α(E)) of electrons is greater than that of holes (β(E)) in $Al_xGa_{1-x}As$, these device structures have been designed to ensure that essentially all of the incident photons are absorbed in the top *p* layer, which provides pure electron injection into the multiplication region. For a narrow range of electric field intensity, the ratio of α and β can be treated as a constant $k=\beta/\alpha$. Under these conditions, the gain can be expressed in terms of k and α as

$$M_e = \frac{1}{1 - \frac{1}{1-k}\left[1 - \exp\left(-w \cdot \alpha \cdot (1-k)\right)\right]} \tag{5.2}$$

Since the electric field range in which an avalanche diode has appreciable gain is relatively narrow, the constant-ionization-coefficient-ratio approximation is quite reasonable. Combined with the gain curve obtained from the *I-V* measurement, the ionization coefficients can be calculated with

$$\alpha = \frac{-\ln\left[1 - \frac{(M_e - 1)\cdot(1-k)}{M_e}\right]}{(1-k)\cdot w} \tag{5.3}$$

$$\beta = k \cdot \alpha \tag{5.4}$$

The ionization coefficients were expressed as follows

$$\alpha(E) = A_e \cdot \exp(-\frac{E_{c,e}}{E}) \tag{5.5}$$

$$\beta(E) = A_h \cdot \exp(-\frac{E_{c,h}}{E}) \tag{5.6}$$

where E is the electric field and A_e, A_h, $E_{c,e}$ and $E_{c,h}$ are empirical constants.

5.3 Discussions

5.3.1 High Temperature Situation

In essence, an APD's gain originates from the electron-hole pair generation resulting from impact ionization in the high electric field region. However, various scattering mechanisms in the semiconductors impede carriers gaining energy from the applied electric field through energy transfer to the lattice vibration. Eventually a balance between energy gain (from electric field) and loss (to the lattice) will be established. Even though several scattering mechanisms contribute to this process, phonon scattering will ultimately dominate due to strong interaction between carriers and the lattice vibration. The average carrier's free path length (l) and the relaxation time (τ) of carriers can be expressed as

$$\bar{l} = \frac{\pi \cdot \hbar^4 \cdot c_l}{m^2 \cdot \in_d \cdot k_B \cdot T} \tag{5.7}$$

$$\bar{\tau} = \frac{\pi \cdot \hbar^4 \cdot c_l}{m^2 \cdot \in_d \cdot k_B \cdot T} \cdot v^{-1} = \frac{\bar{l}}{v} \tag{5.8}$$

where m is the carrier mass, c_l is sheer transverse modulus, $\in_d$ is the dielectric constant, k_B is Boltzman constant, and T is temperature in Kelvin. As temperature increases, the free mean path length of carriers will decrease as a function of T^{1}, which means that carriers are scattered more frequently at elevated temperatures.

Through I-V measurements at various temperatures, the dark currents were consistently found to increase with the increasing temperatures for all $Al_xGa_{1-x}As$ APDs with x from 0 to 0.9. Fig. 5.1 shows a typical set of measured photocurrent and dark current curves at different temperatures of a GaAs APD.

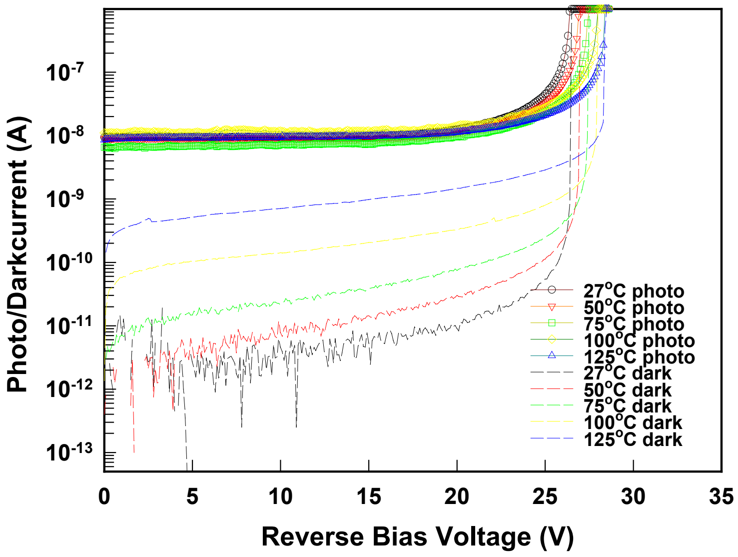

Fig. 5.1 Photocurrents/dark currents of an 800-nm-thick GaAs APD at elevated temperatures (27°C to 125°C)

The excessive dark current at elevated temperatures is due to enhanced thermal carrier generation rate in the depleted "*i*-region", which is strongly dependent on the ambient temperature.

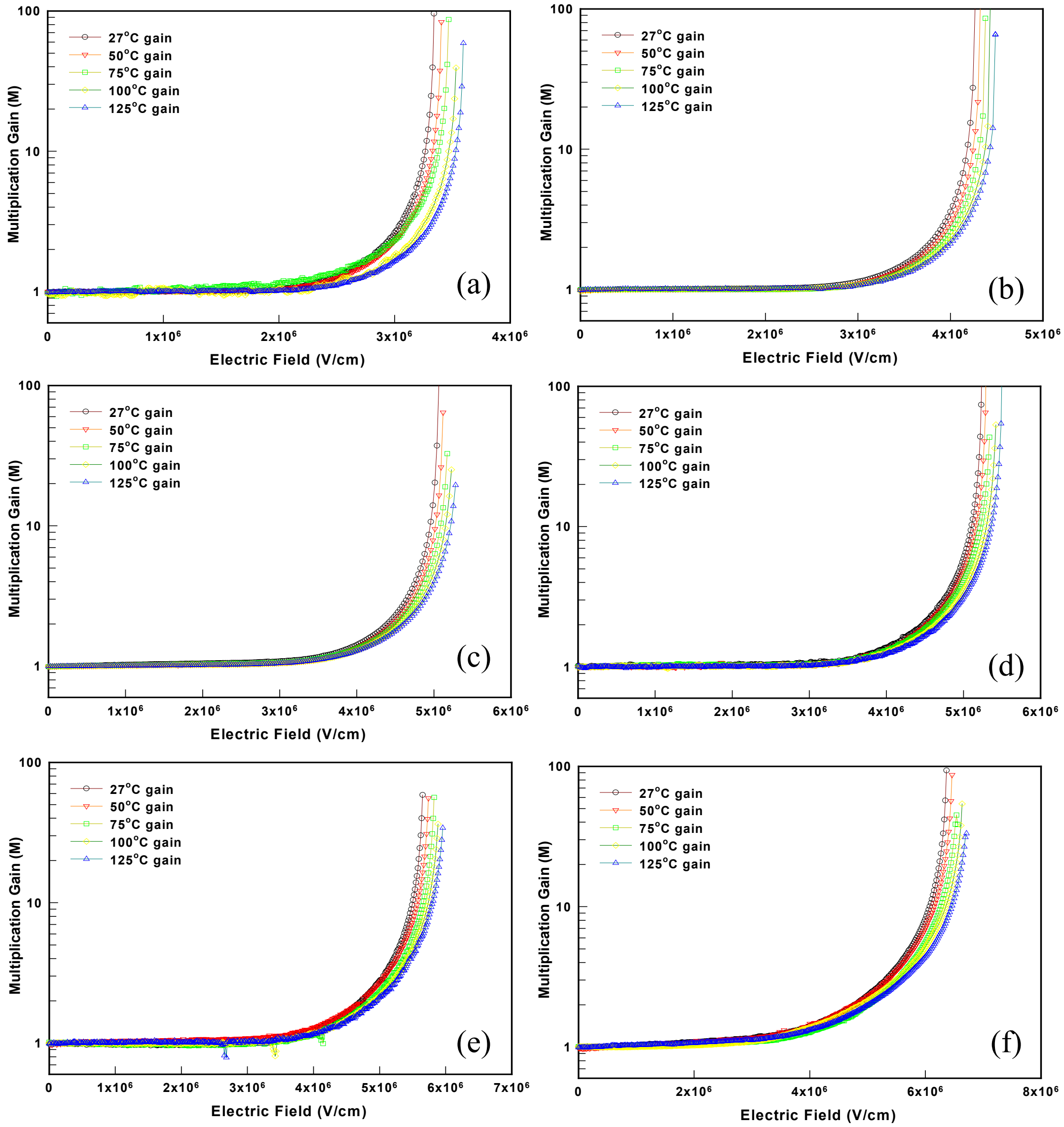

Fig. 5.2 (a)-(f) Gain and breakdown temperature dependence of $Al_xGa_{1-x}As$ APDs

As a result of increased phonon scattering rate at high temperatures, both an APD's gain and breakdown voltage exhibit a dependence on temperature, as shown in Fig. 5.2 (a) through (f) for six different types of APDs. Owing to the intrinsic region thickness shrinkage caused by beryllium diffusion, as has been discussed in Chapter 4, the normalized breakdown electric field was used in the plots rather than the breakdown voltage. All $Al_xGa_{1-x}As$ APD breakdowns were measured at elevated temperatures, from 298°K to 398°K, and were fitted with the first order approximation using the following linear equation:

$$V_{BR}(T) = V_{BRO} + \beta(T - T_O), \text{ where } T_O = 300^o K \tag{5.9}$$

The fitted temperature coefficients for $Al_xGa_{1-x}As$ APDs with various Al-contents were extracted and found to be in the range 19 m$V/^oK$ to 15 m$V/^oK$, with a slight decrease for the high-Al APDs, as shown in Fig 5.3.

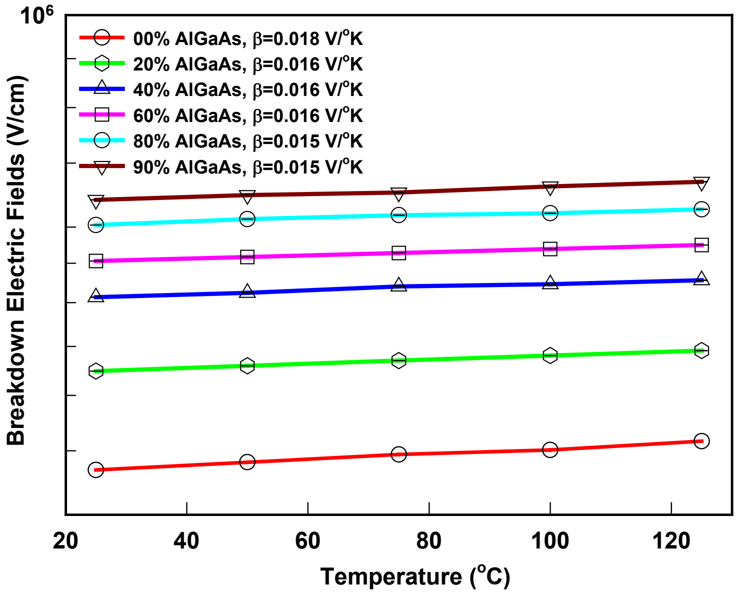

Fig. 5.3 Temperature coefficients of breakdown electric fields of $Al_xGa_{1-x}As$ APDs

This decrease of temperature coefficients as a function of increasing Al-content might be attributed to the increasing bandgap energy and the transition from direct to indirect band structure.

APD multiplication noise was also measured from room temperature up to 125°C, and the relevant *k* values were fitted using the method introduced in Chapter 4, as shown in Fig. 5.4. Even though the breakdown voltages were found to increase with increasing Al-content, the multiplication noise was relatively constant. Variations were within the error bars of the measurement. This can be explained as follows: even though the ionization coefficients of both electrons and holes increase with the increasing temperature, the relative value of these coefficients does not change very much, thus the fitted *k* value, does not change.

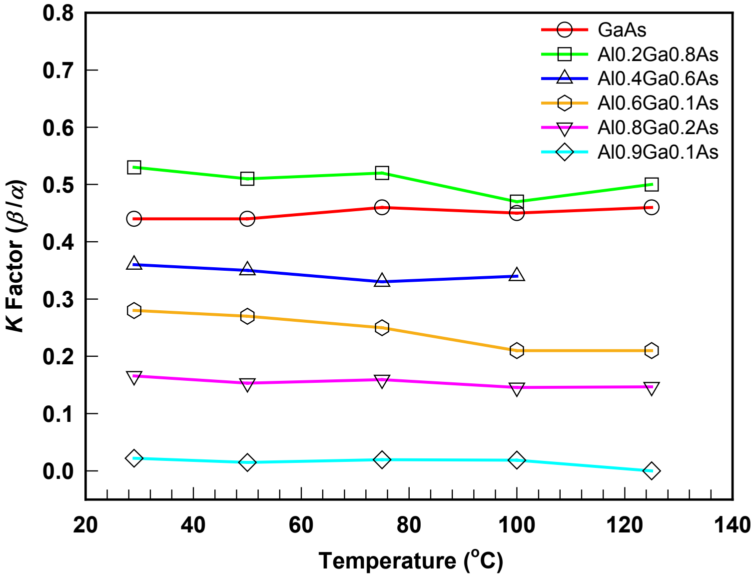

Fig. 5.4 Temperature dependence of $Al_xGa_{1-x}As$ APD multiplication noise

Due to increased phonon scattering, the acceleration of carriers becomes less effective at higher temperatures. As a result, the mean free path between ionization events and thus the gain at a fixed reverse bias voltage decreases with the increasing temperature. On the other hand, as indicated by the experimental results, the ionization coefficient ratios of GaAs and $Al_xGa_{1-x}As$ do not change significantly as temperature increases. Therefore, as shown in Fig. 5.5 (a)-(c), the ionization coefficients of $Al_xGa_{1-x}As$ (x from 0.0 to 0.4) generally undergo a slight decrease while the temperature increases from 29^oC to 125^oC.

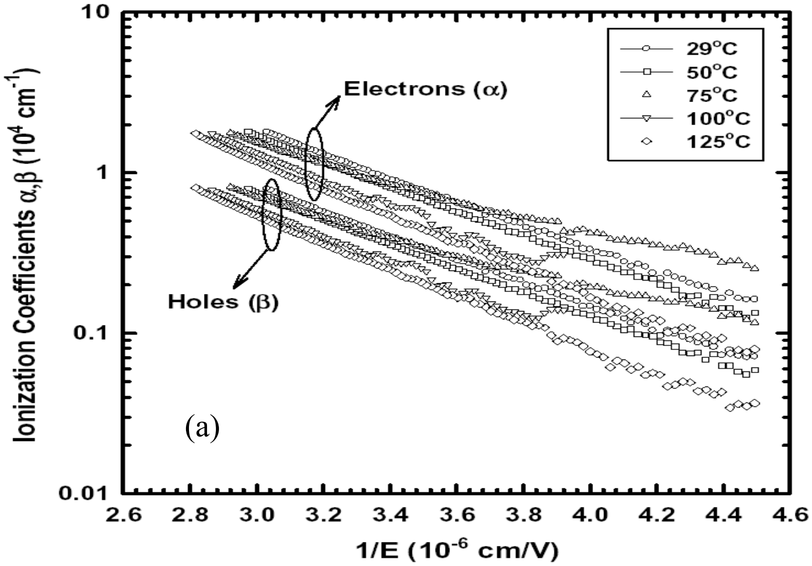

Fig. 5.5 (a) Temperature dependence of impact ionization coefficients (electrons: solid, holes: dotted) of GaAs APDs

The temperature dependence of the ionization coefficients of GaAs has been reported and widely cited by F. Capasso et al. in 1977 [2] and by V. M. Robbins et al. in 1988 [4-6].

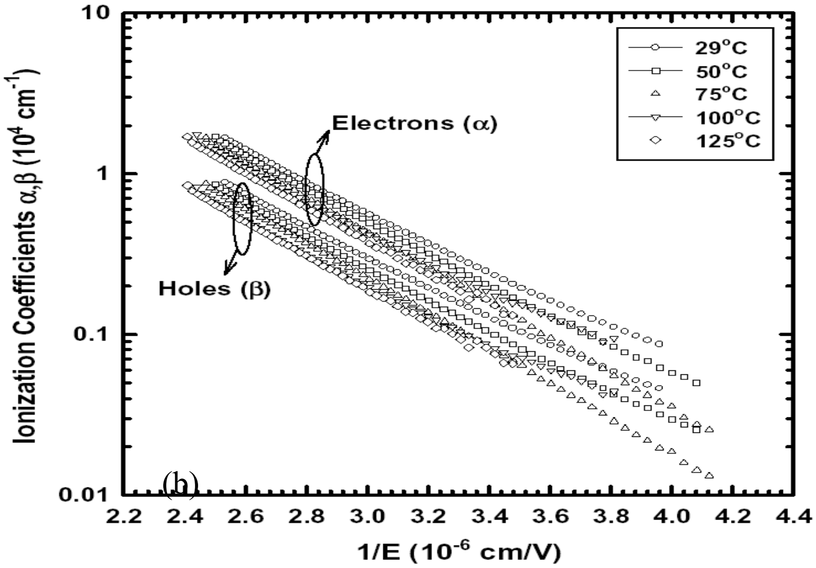

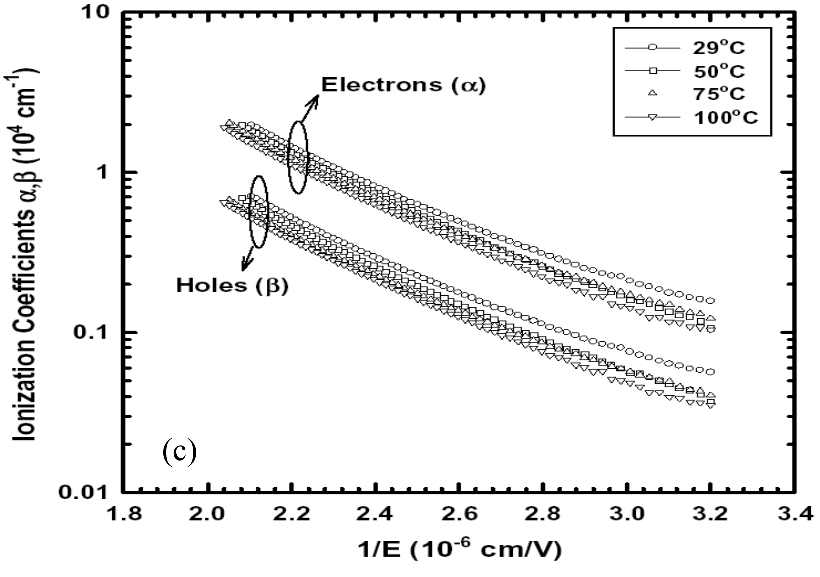

Fig. 5.5 Temperature dependence of impact ionization coefficients (electrons: solid, holes: dotted) of $Ga_{0.2}Al_{0.8}As$ APD (b) and $Ga_{0.4}Al_{0.6}As$ APD (c)

Table 1 the ionization coefficient parameters extracted using equation (5.6) and (5.7). Table 2 compares parameters of GaAs material extracted from the present work (c) with those obtained by Capasso etal. (a) and Robbins etal. (b). It should be noted that there are significant differences in the material growth methods, device fabrication techniques, device structures, and measurement techniques employed in this work and those of Capasso et al and Robbins et al.

Materials	Temperature (^{o}C)	A_e (10^6/cm)	$E_{c,e}$ (10^6V/cm)	A_h (10^6/cm)	$E_{c,h}$ (10^6V/cm)
GaAs	29	1.94	1.58	0.85	1.58
	50	1.73	1.58	0.76	1.58
	75	0.291	1.03	0.134	1.03
	100	3.16	1.83	1.42	1.83
	125	3.44	1.90	1.58	1.90
$Al_{0.2}Ga_{0.8}As$	29	3.17	2.10	1.68	2.10
	50	4.34	2.25	2.21	2.25
	75	8.17	2.52	4.25	2.52
	100	2.99	2.17	1.41	2.17
	125	4.83	2.38	2.41	2.38
$Al_{0.4}Ga_{0.6}As$	29	2.49	2.37	0.897	2.37
	50	3.83	2.59	1.34	2.59
	75	2.70	2.46	0.892	2.46
	100	3.21	2.58	1.09	2.58

Table 1 Parameters of the ionization coefficients in $Al_xGa_{1-x}As$ (x = 0.0, 0.2, 0.4) within temperature range from 29^{o}C to 125^{o}C.

Capasso etal. reported the measurements of ionization coefficients of GaAs from 29^{o}C to 250^{o}C. They investigated the ionization coefficients of GaAs by means of abrupt P^+N homojunction diodes ($p \approx 2\times10^{18}$ cm^{-3} and $n \approx 2\times10^{18}$ cm^{-3}, respectively) at a wavelength of 633 nm and impact ionization region greater than 1 μm thick. They observed that the ionization coefficients of holes and electrons decrease with increasing temperature as a result of increased phonon scattering. They reported that the ionization coefficient of electrons and holes were approximately equal with β slightly greater than α, and that the k factor was relatively insensitive to the temperature change.

	29 °C	100 °C	150 °C	200 °C	250 °C
α ($10^4$1/cm)	3.0	2.1	1.55	1.5	1.3
β ($10^4$1/cm)	3.2	2.4	2.0	1.4	1.0

Table 2 (a) GaAs parameters extracted by F. Capasso et al.

	27 °C	77 °C	117 °C	157 °C	192 °C
α ($10^4$1/cm)	4.0	3.2	2.8	2.9	3.0
β ($10^4$1/cm)	3.4	2.8	2.2	2.0	1.9

Table 2 (b) GaAs parameters extracted by V. M. Robbins et al

	29 °C	50 °C	75 °C	100 °C	125 °C
α ($10^4$1/cm)	6.5	6	4.5	4.0	4.0
β ($10^4$1/cm)	2.9	2.5	2.1	2.0	1.9

Table 2 (c) GaAs impact ionization coefficient parameters extracted in this work

The results presented here are in better agreement with those of Robbins et al, both the temperature dependence of the ionization coefficients of GaAs within the temperature range from 29°C to 125°C and the ionization coefficients of $Al_xGa_{1-x}As$ (with x from 0.0 to 0.4) at room temperature. Also, the temperature dependence of hole ionization coefficients agrees fairly well with those of Robbins et al. The decrease of ionization coefficients with increasing Al concentration reflects the increase in the band gap and hence an increase in the threshold energy for impact ionization. The ionization coefficients of $Al_xGa_{1-x}As$ exhibited the same temperature trends as those of GaAs. From the present results we conclude that while the ionization coefficients of GaAs and $Al_xGa_{1-x}As$ ($0 \leq x \leq 0.4$) decrease with increasing temperature, the temperature dependence in the range 29°C to 125°C is not strong and the k values are relatively constant.

5.3.2 Low Temperature Situation

From the low temperature measurements, the critical breakdown field of all $Al_xGa_{1-x}As$ APDs was found to decrease monotonously with the decreasing temperature, due to longer carrier mean free time at lower temperatures. The normalized breakdown electric field of each type of devices is plotted in Fig. 5.6.

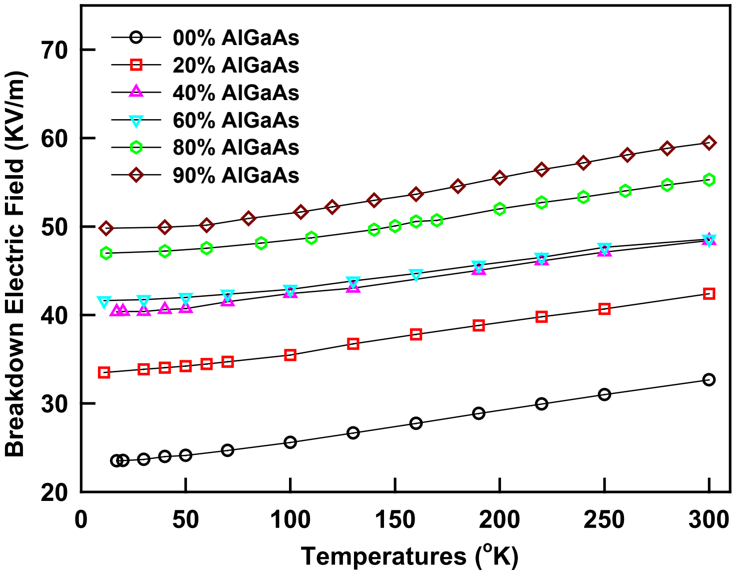

Fig. 5.6 Temperature dependence of breakdown electric field of $Al_xGa_{1-x}As$ APDs

The breakdown voltages were found, however, to saturate at fairly low temperatures below 20K, as shown in equation (5.10). This result was consistent with what has been reported by David et al [5-23]. This phenomenon can be partly explained by strong temperature dependence of the phonon scattering mechanism. The average phonon concentration at any given temperature *T* is

$$\langle n_q \rangle = \frac{1}{\exp(\hbar \varpi_q / kT) - 1} \tag{5.10}$$

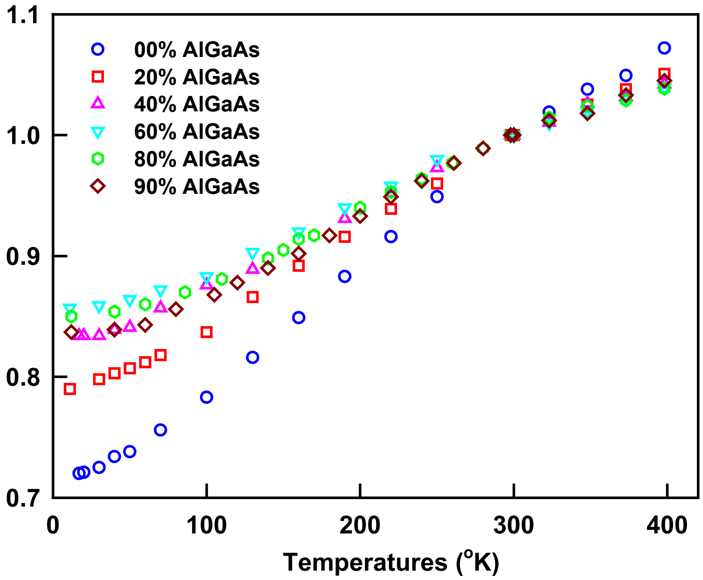

Fig. 5.7 Normalized breakdowns of $Al_xGa_{1-x}As$ APDs

The phonon emission rate is proportional to $<n_q>+1$ whereas the phonon absorption rate is proportional to $<n_q>$. Both the phonon emission rate and the phonon absorption rate, which are proportional to $<n_q>$, decreased to zero as the temperature, *T*, approached close to absolute zero. At extremely low temperatures the remaining scattering was only dominated by the spontaneous emission, which is not temperature dependent. As a consequence, the phonon scattering rate saturates at low temperatures and so does the critical breakdown electric fields.

5.4 Summary

Breakdown voltages, multiplication noise, and impact ionization coefficients of $Al_xGa_{1-x}As$ APDs with Al ratios from 0.0 to 0.9 were observed in the temperature range from <20K to 398K. The avalanche breakdown voltage increased with increasing temperature but the excess noise factors were relatively insensitive to the temperature (from 298K to 398K), for various electric field intensities in the range of 2.5×10^5 V/cm to 5.0×10^5 V/cm. The ionization coefficients of electrons and holes were also extracted from the noise and gain measurements for $Al_xGa_{1-x}As$ APDs with Al ratios from 0.0 to 0.4. As expected, impact ionization coefficients of both electrons and holes decrease with increasing temperature. Low temperature (room temperature down to <20K) investigation showed that the critical breakdown electric field of various AlGaAs APDs at fairly low temperatures is only dominated by the phonon scattering that is related to the spontaneous phonon emission, which is temperature independent.

Chapter 6

Long-Wavelength APDs Implemented by Direct Wafer Bonding

As discussed in previous chapters, avalanche photodiodes have been the favored candidate for optical communication applications, due to their internal avalanche gain. The primary figures of merit for APDs in fiber-optic systems are excess noise factor and gain-bandwidth product. Low noise and high gain-bandwidth product APDs can be achieved by using a gain region that has one of the following properties: (1) either the electron (α_i) or the hole (β_i) ionization coefficient is much greater than the other, (2) the multiplication layer is reasonably thin, (3) an impact-ionization-engineered hetero-structure is incorporated into the multiplication region [6-1]-[6-12].

From the material system point of view, high-speed APDs for optical fiber transmission systems have been exclusively fabricated on InP-based materials, because $In_{0.53}Ga_{0.47}As$, which is lattice-matched to InP substrates provides strong optical absorption in the wavelength range of $0.9\mu m \leq \lambda \leq 1.7\mu m$. Based on this, various types of compound materials, such as InAlAs, InAlGaAs quaternaries and InAlAs/InAlGaAs super-lattice structures, have been thoroughly studied in order to obtain low excess noise and high gain-bandwidth. The best gain-bandwidth product result of 320 GHz was achieved using an InGaAs/InAlAs waveguide APD structure and a 150nm thin ternary InAlAs multiplication region. The excess noise factor was only ~0.15 due to the non-local effect of carrier impact ionization [6-13]. Thinner

InAlAs multiplication regions, however, will lead to unacceptable high leakage (tunneling) current levels in APDs, even though it has been theoretically proven that a thinner gain region will yield a higher G-B product and lower multiplied (excess) noise.

As discussed in Chapter 4 GaAs based materials the multiplication noise of $Al_xGa_{1-x}As$ homojunction APDs decreases with increasing *Al* mole fraction. Thin $Al_xGa_{1-x}As$ APDs with high Al content (≥90%) exhibited very low multiplication noise comparable to that of Si APDs [6-14]. By means of impact-ionization-engineering, the multiplication noise of $GaAs/Al_xGa_{1-x}As$ APDs can be further decreased to below that of Si APDs [6-15]-[6-17]. It is thus very attractive to integrate these low noise APD structures with the long-wavelength absorbing $In_{0.53}Ga_{0.47}As$ to obtain APDs that have higher gain-bandwidth products and operate in the wavelength range of λ=1.3~1.55µm. Lattice mismatch has prevented direct integration of $In_{0.53}Ga_{0.47}As$ into GaAs-based APD structures, due to the large number of threading dislocations introduced during epitaxial growth, which will cause extremely high APD leakage current level. Wafer-bonding technology, on the other hand, might provide an alternative to circumvent the difficulty of direct epitaxial growth [6-18].

Direct wafer bonding between III-V compounds, which was initiated in 1989, has already been successfully utilized in many optoelectronic device applications [6-19]-[6-23]. A long-wavelength APD has been demonstrated based on InGaAs/Si bonding interface by Hawkins et. al. [6-24], but the possibility of using complete III-V compound wafer bonding for APDs had never been examined. The need for long wavelength APDs based-on GaAs low noise materials and structures motivated my research on direct wafer bonding, in which an InGaAs absorber is integrated with an AlGaAs avalanche gain region to demonstrate long-wavelength absorption on GaAs substrates.

6.1 Direct Wafer Bonding

For each specific material system, nature has dictated a set of physical properties, such as optical absorption coefficient, carrier mobility, etc.. The optimal properties, which are necessary for a specific application, might reside in a variety of disparate materials, as in my APD studies, in which long wavelength absorbing materials usually do not have good impact ionization properties, and vice versa. The lattice constant of each material is different from the others, and dislocations will form if one is grown on the other, either by MBE or by MOCVD, due to stress generated by lattice mismatch. This type of stress will be relaxed if the epi-layer thickness is within its critical limit, and no threading dislocation will be formed. However, a large density of threading dislocations will form if the epitaxtial layer thickness exceeds its critical limit. The epi-layer will even crack if the stress generated by the lattice mismatch is too high. Alternatively, dislocations resulting from wafer bonding are usually formed and localized in the vicinity of the bonded interface (within a few angstroms) and do not propagate into the bulk region if samples are annealed properly. No threading dislocation will form as a result, as sketched in Fig. 6.1. This characteristic of wafer bonding is very important to the APD application because elimination of threading dislocations is critical for obtaining APDs with low leakage current.

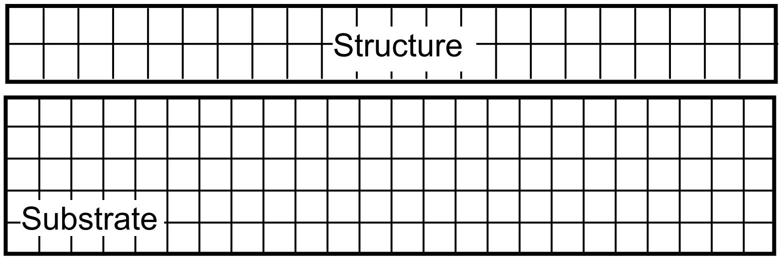

(a) Before growth

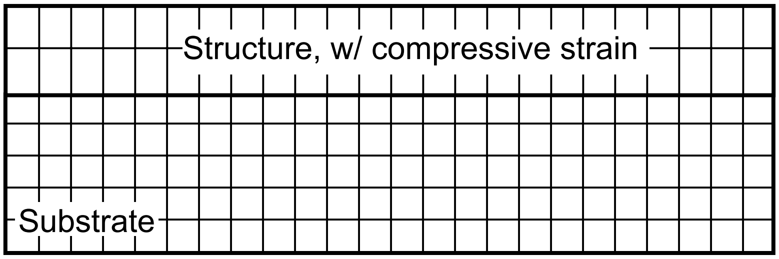

(b) After growth, within critical thickness

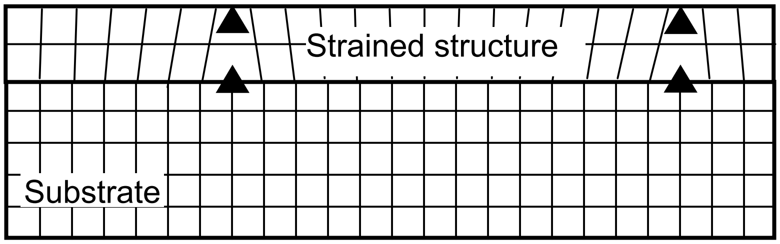

(c) After growth, beyond critical thickness

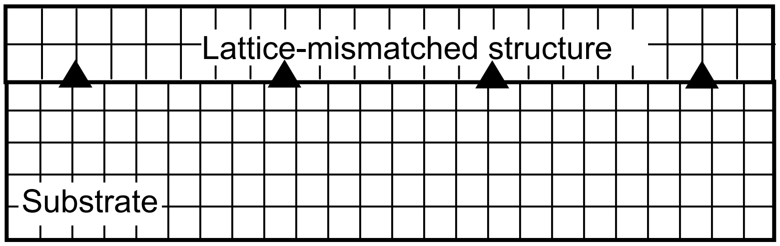

(d) After wafer bonding

Fig. 6.1 Illustration of defect formation in a lattice-mismatched wafer structure by epitaxial growth (a) ~ (c) and by wafer bonding (d)

The material systems used for my study are based on InP (lattice constant a_0 = 5.8687 Å) and GaAs (a_0 = 5.65325 Å) substrates. Due to large lattice mismatch (>3.6%) at room temperature, a very high density of volume dislocation and stacking faults will be formed in the epi-layer when directly grown by epitaxy. These can be observed by cross-sectional transmission electron microscopy (TEM) [6-20]-[6-21]. For example, a dislocation density of 2×10^{10} cm^{-2} was observed close to the interface when a GaAs epi-layer was grown on an InP substrate [6-20]. Using direct wafer bonding, however, the lattice mismatch can be accommodated by the edge dislocations that are localized at the bonding interface, especially when post annealing is executed after initial wafer bonding. Only small damage in the epi-layer can be observed [6-20]. This has been demonstrated by previous studies [6-19]-[6-23], and no indication of dislocation propagation into the bulk epi-region has been observed, as illustrated in Fig. 6.2.

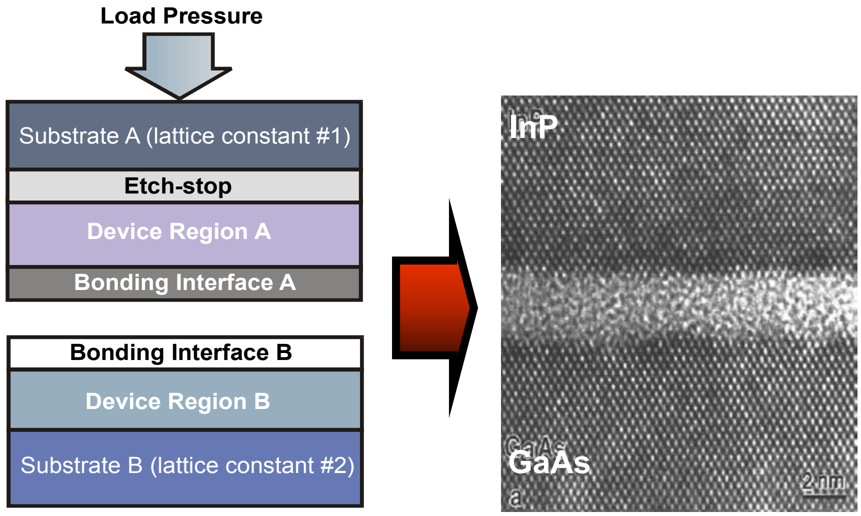

Fig. 6.2 Bonding interface morphology after bonding and annealing, after *Sagalowicz, et al, J. App. Phys., May 2000*

6.2 APD Structure Design and Material Growth

The first device structure was designed as a separate absorption, charge, and multiplication APD to achieve low noise and high gain bandwidth products. The advantages of this type of device structure were discussed in Chapter 2. The bonded interface was initially designed to be between *p*-type InP and *p*-type GaAs, since it has been shown that bonding these materials (*p*-InP/*p*-GaAs) yields both excellent optical and electrical properties [6-20].

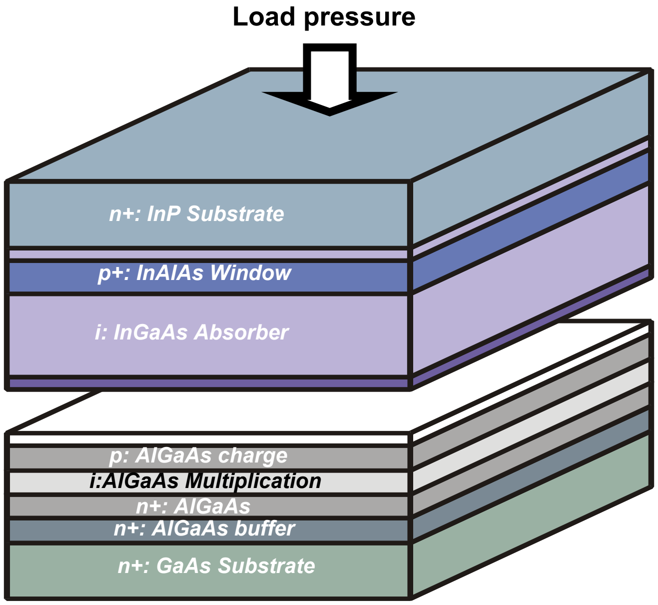

Fig. 6.3 Device structure for DWB long-wavelength APD

Fig. 6.3 shows the detailed device structure that was used for direct wafer bonding. The upper region was designed for absorption. It was grown on an InP substrate and consisted of a 50 nm-thick, heavily-doped p^+ (Be:1×10^{19} cm^{-3}) $In_{0.53}Ga_{0.47}As$ layer for *p*-type ohmic contact, a 200 nm-thick p^+ (Be:5×10^{18} cm^{-3}) InP window layer to block the diffusion of the photo-generated electrons from the InGaAs absorber, an 800 nm-thick unintentionally-doped $In_{0.53}Ga_{0.47}As$ absorption layer, and a 30 nm-thick *p*-type (Be:1×10^{18} cm^{-3}) InP layer used both as the bonding interface to GaAs and as part of the charge region.

The lower region, or the multiplication region, was grown on a GaAs substrate. The epitaxial layer structure consisted of a 200 nm-thick *n*-type (Si: 5×10^{18} cm^{-3}) $Al_{0.2}Ga_{0.8}As$ *n*-contact layer, a 200 nm-thick unintentionally-doped $Al_{0.2}Ga_{0.8}As$ multiplication layer, a 100 nm-thick *p*-type (Be:2×10^{17} cm^{-3}) $Al_{0.2}Ga_{0.8}As$ charge layer, and a 30 nm-thick *p*-type (Be:1×10^{18} cm^{-3}) GaAs layer used both as the bonding interface to InP and as part of the charge region. Since the bonding interface was located between the multiplication region and the absorption region, the direct wafer bonding was really a great challenge, because in the SACM structure both of these regions are fully depleted and the electric field is high, compared to direct wafer bonding in other types of devices, such as lasers.

The epi-structures both on InP and GaAs substrates were grown in a Varian GEN-II MBE chamber, and a buffer layer was employed in each wafer to reduce defects. The wafer surfaces were coated with photoresist immediately after they were removed from the MBE chamber to prevent particle contamination. Since surface roughness of the two wafers was a critical factor for the success of direct wafer bonding, extreme care was taken during growth calibration for the wafers. Surface morphology of the wafers was examined by atomic force microscopy (AFM) after MBE growth. AFM results consistently showed that the average roughness of the GaAs wafer was less than 1 nm, and a typical value for the InP wafers was usually 1-2 nm, as shown in Fig. 6.4 (a) and (b).

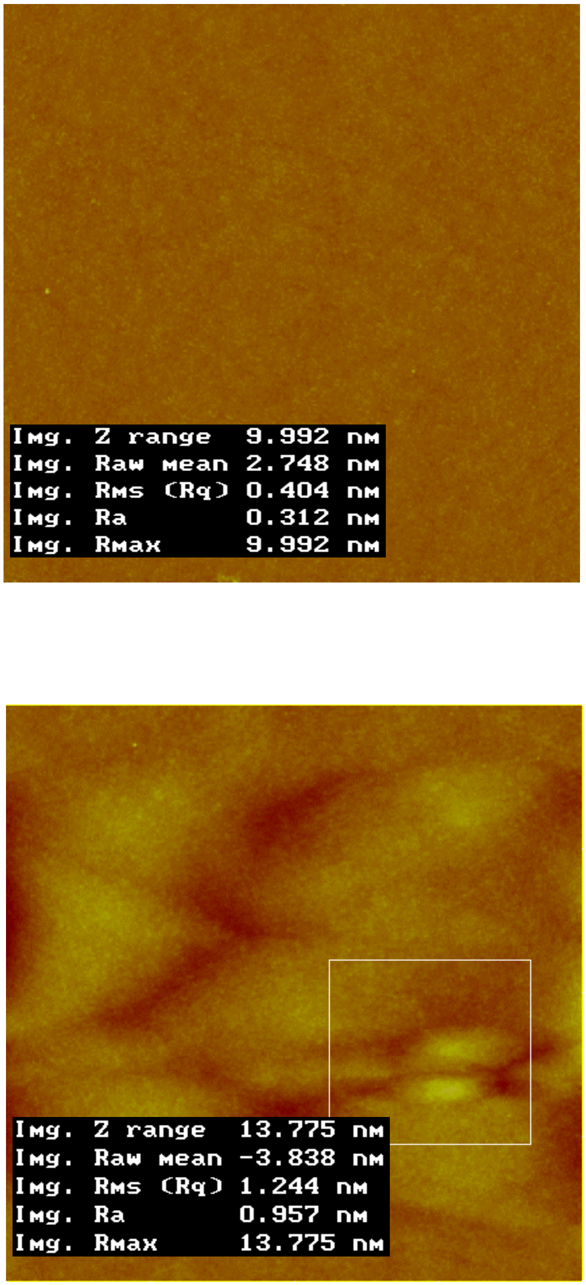

Fig. 6.4 Wafer surface roughness of (a) GaAs and (b)InP wafers after MBE growth

6.3 Wafer Bonding and Subsequent Device Processing

An array of 5-μm-wide by 0.5-μm-deep channels with a pitch distance of 500 μm was etched in the GaAs wafer surface with H_3PO_4:H_2O_2:H_2O (1:1:8). These channels have been found to improve the quality of the fused interface by enhancing the transport of desorbed gases from the bonding interface and reducing the defect density of voids and bubbles [6-20][6-21]. The wafer surface cleaning procedure started with an oxygen plasma treatment to remove hydrocarbons and to create a defined oxide film. This was followed by sequential immersion in buffered HF and NH_4OH in order to remove the oxides. Both samples were then brought into close contact and aligned in a methanol solution. The aligned wafers were mounted in a graphite fixture, as shown in Fig. 6.5, which was designed to provide uniform pressure to the wafer surfaces.

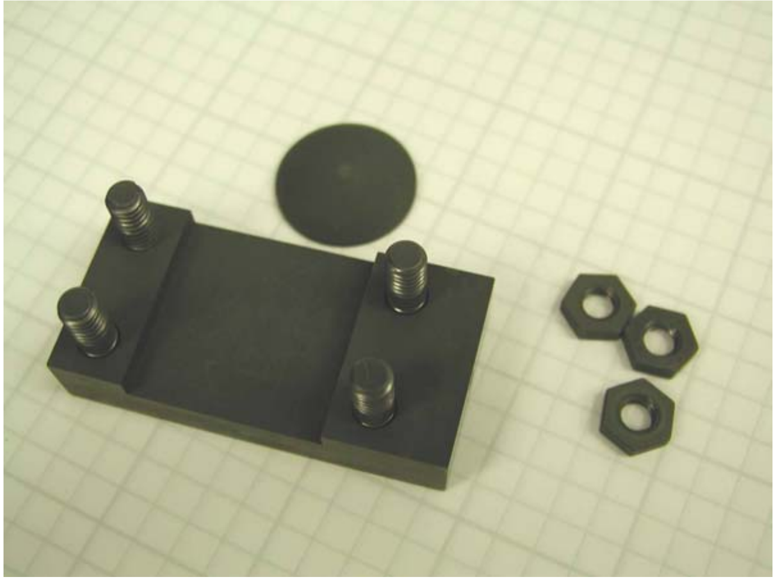

Fig. 6.5 Wafer holder specially designed for wafer annealing

The applied load was estimated to be 1-2×10^6 Pa at room temperature. The loaded samples were then annealed at a temperature of 650^{o}C for 30 min in an N_2 atmosphere, using a Lindburg annealing furnace, as shown in Fig. 6.6. After annealing, the sacrificial InP substrate and the buffer layer were selectively removed from the epitaxial layer in an HCL:H_2O (3:1) solution.

Fig. 6.6 Furnace used for high temperature annealing

The first step in processing was *p*-type ohmic contact formation. A Cr(250Å)/Au(800Å) film was deposited on the heavily-doped $In_{0.53}Ga_{0.47}As$ layer. The contacts were patterned with a standard photolithography and lift-off process. A SiO_2 etch mask was then deposited by PECVD and defined by photolithography. Mesas with a diameter of 150 μm were etched in bromine/methanol solution down to the n^+ GaAs buffer layer. A thin film of SiO_2 (1500Å) was then deposited for device passivation. Ni(200Å)/AuGe(300Å)/Au(800Å) was used as the *n*-type ohmic contact, which covered the whole surface of the wafer except the mesa areas in order to minimize the contact resistance. The cross section of the directly bonded SACM APD device structure is illustrated in Fig. 6.5, using an SEM picture.

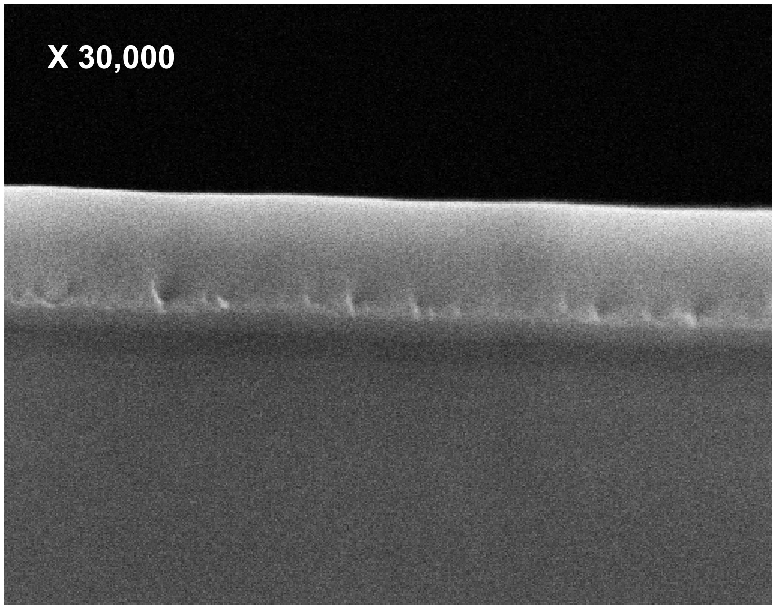

Fig. 6.5 Typical SEM picture of a bonded GaAs-InP interface

6.4 Results and Discussion

Direct bonding between bulk GaAs and InP substrates was performed prior to real photodiode bonding, to examine bonding qualities. Perfect ohmic contact between bonded *n*-type GaAs bulk materials is a good indication of the good contact at the bonded interface, as shown in Fig. 6.6. Further bonding between bulk *n*-GaAs to *p*-GaAs, *p*-GaAs to *n*-InP, and *p*-GaAs to *p*-InP, as shown in Fig. 6.7 to 6.9, all resulted in rectifying characteristics, which were solid indications of the formation of either a homo-junction or a hetero-junction at the bonded interfaces.

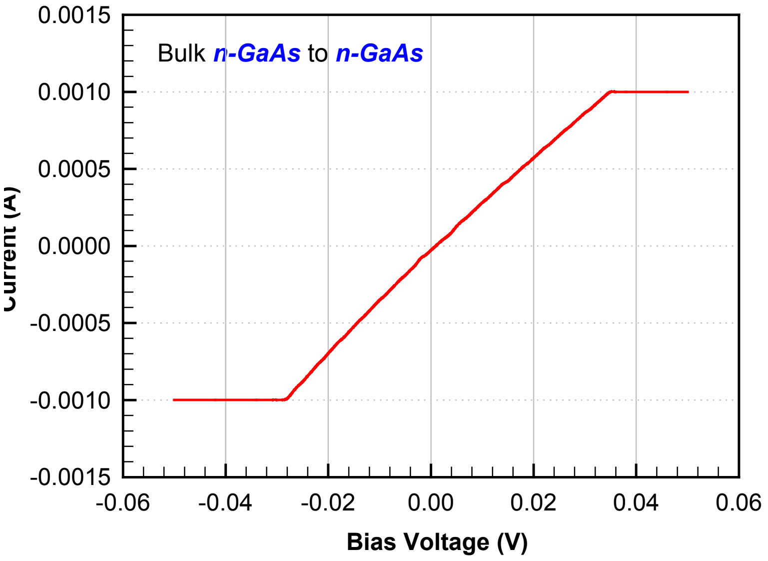

Fig. 6.6 Bonding result between bulk GaAs materials

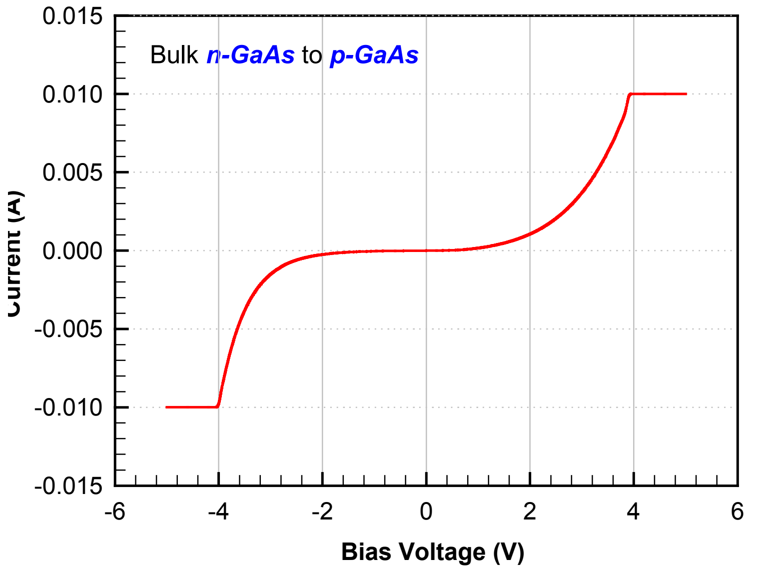

Fig. 6.7 Bonding result between bulk *n*-GaAs and *p*-GaAs materials

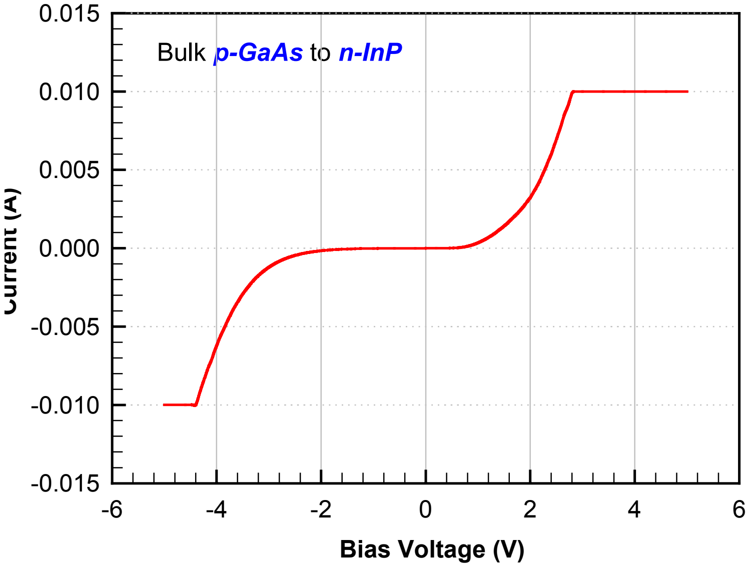

Fig. 6.8 Bonding result between bulk *p*-GaAs and *n*-InP materials

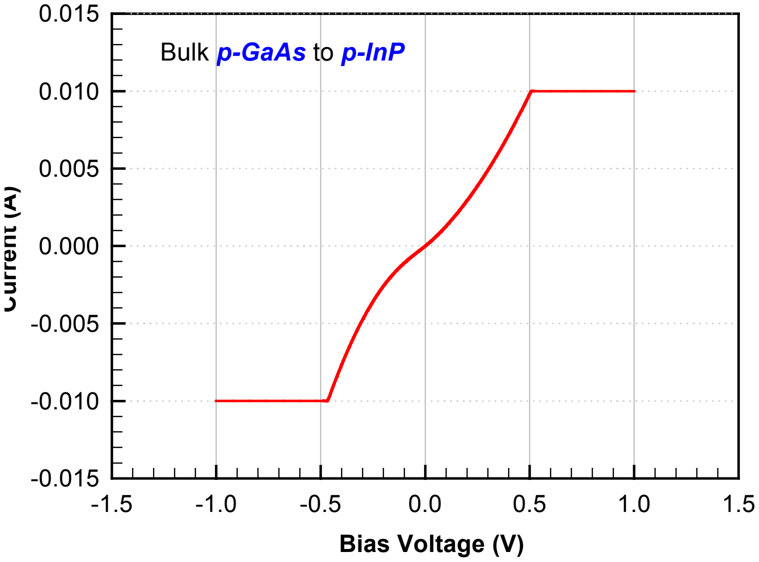

Fig. 6.9 Bonding result between bulk *p*-GaAs and *p*-InP materials

The photocurrent and dark current characteristics of the initially bonded InGaAs/InP-GaAs/AlGaAs SACM APDs were measured at room temperature with a HP 4145B semiconductor parameter analyzer, as shown in Fig. 6.10. The breakdown voltage was approximately 32.5V, and the punch-through voltage was close to 13.5V. This corresponded very well with a reference InGaAs/InAlAs SACM APD with a similar structure and doping profile. However, the photocurrent curve exhibited a small double-step punch-through, which was different from the reference InGaAs/InAlAs SACM APD. These steps probably occurred as the depletion region reached the bonded *p*-InP/*p*-GaAs interface first and then the edge of InGaAs absorption region. After the second step, the photocurrent curve saturated and then increased smoothly until avalanche breakdown occurred.

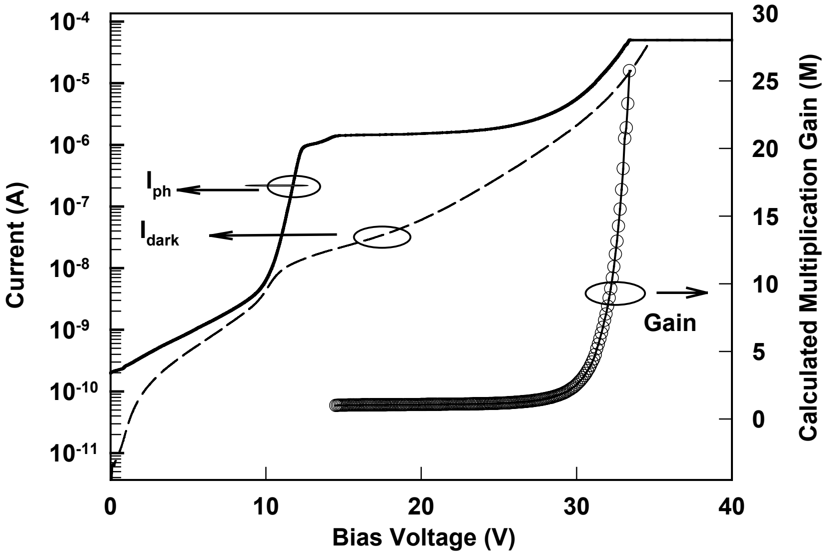

Fig. 6.10 Typical I-V curves of bonded GaAs-InP APD

The dark current of this bonded APD was higher than that of the reference InGaAs/InAlAs APD. Up to punch-through the dark current was ≤ 20nA, but above that point it increased rapidly. Thermally generated carriers from the fully depleted *p*-InP/*p*-GaAs interface are probably the source of the high leakage current. Secondary ion mass spectroscopy (SIMS) analysis has shown that high temperature annealing (over 600^{o}C) will cause *Be* diffusion in the bonded devices. This resulted in a decrease in the charge layer doping level from its nominal value, which leads to early punch-through in the charge region. The net result is a higher electric field in the InGaAs absorption material after punch-through, where tunneling and impact ionization may cause high leakage current. This phenomenon was also observed in the InGaAs/InAlAs SACM APDs if the charge layer doping was too low. Further optimization of the bonding conditions and modification of charge layer doping are expected to reduce the device dark current level. Avalanche multiplication gain was calculated based on the measured I-V characteristic by assuming unity-gain at the second punch-through (-13.5V). Gain values as high as 25 were observed before breakdown, which is sufficient for most device applications.

The external quantum efficiency of the bonded photodiode was measured from 1.0 μm to 1.65 μm at 13.5 V reverse bias, as shown in Fig. 6.11. The external quantum efficiency was 47% at 1.3 μm and 33% at 1.55 μm. For an 800 nm-thick InGaAs absorption layer with an absorption coefficient (α) of 1.16 μm^{-1} at 1.3 μm and 0.705 μm^{-1} at 1.55 μm [6-13], external quantum efficiencies of 51% at 1.3 μm and 34% at 1.55 μm would be expected, assuming an optical transmission of 85% at 1.3 μm and 80% at 1.55 μm through the air-SiO_2-semiconductor interface. There is 8% disparity at 1.3μm and 4% at 1.55μm between the measured and expected external quantum efficiencies. These differences may be due to the loss (trapping/recombination) of photo-generated carriers at the bonded *p*-InP/*p*-GaAs interface.

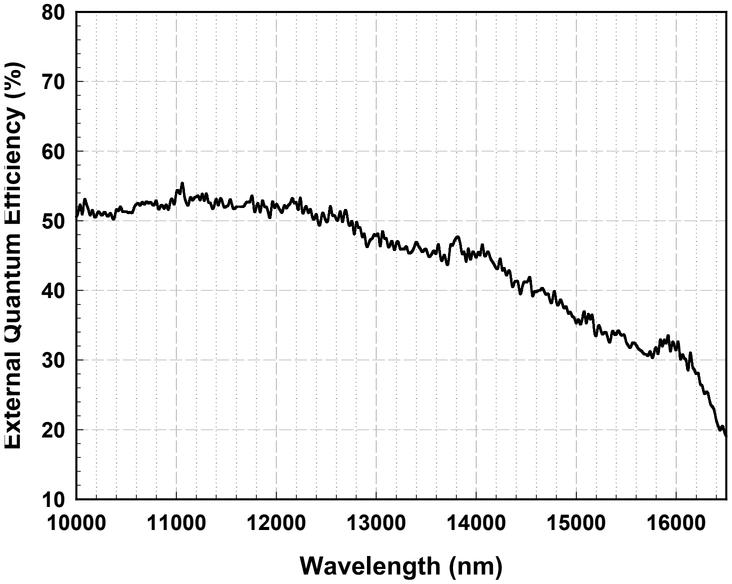

Fig. 6.11 Typical external quantum efficiencies of a bonded GaAs-InP APD

6.5 Direct Wafer Bonded APDs with an InAlAs-GaAs Interface

The direct wafer bonding between InAlAs and GaAs was also investigated, partly due to a problem with the MBE growth chamber; the phosphorus cracker was unable to provide sufficient phosphorous beam flow, and InP epi-layer growth was no longer available. Direct wafer bonding using an InAlAs-GaAs interface was the first available alternative solution. The device structure for DWB was then modified for the new bonding interface. The InP and GaAs wafers were grown in a Varian

GEN-II MBE chamber using standard group-III sources and an arsenic cracker.

The bonding procedure started with etching an array of 5-µm-wide by 1-µm-deep channels with a pitch distance of 500 µm on the GaAs wafer surface using H_3PO_4:H_2O_2:H_2O (1:1:10), to improve the quality of the fused interface and to reduce the defect density of voids and bubbles, as discussed previously. Both the InP and GaAs wafers were cleaned to remove contaminants. Details of the cleaning procedure were outlined in section 6.3. For the bonding, the samples were place in a graphite fixture and pressure was applied before placing them in the bonding furnace. The applied pressure was estimated to be ~1-2×10^6 Pa at room temperature. After annealing, the InP substrate was removed to the InGaAs etch stop using a HCl:H_20 (3:1) solution.

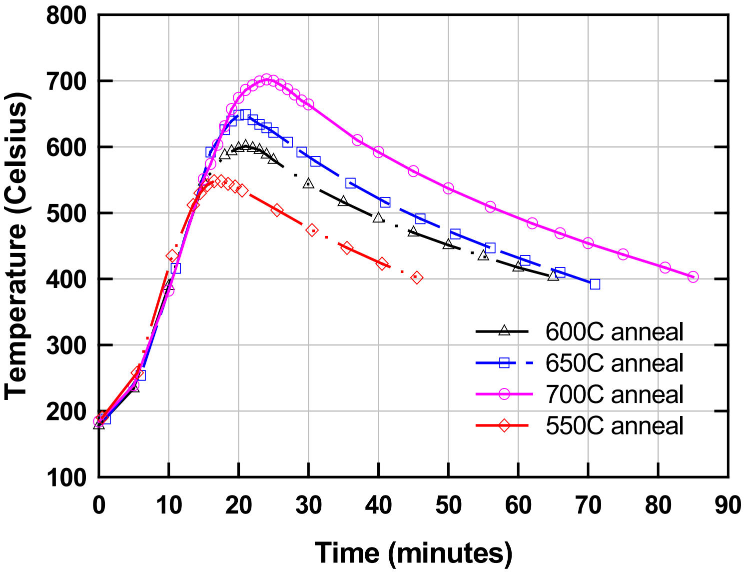

Fig. 6.12 Temperature profiles in the bonding furnace

Preliminary bonding of $In_{0.52}Al_{0.48}As$ to GaAs was investigated at 600C, 650C, and 700C under both N_2 and H_2 atmospheres, using simple *p-i-n* structures. In order to observe the effect of the annealing conditions on the device dark current level, various homojunction *p-i-n* diodes were bonded using a variety of annealing temperature profiles, as shown in Fig. 6.12. Fig. 6.13 shows dark current curves resulting from bonded *p-i-n* diodes that have similar device sizes. An optimum temperature, close to 650^{o}C, was obtained in terms of dark current density. Using an H_2 atmosphere instead of N_2 also decreaseed the device dark current level, possibly by reducing the number of dangling bonds at the bonded InAlAs-GaAs interface.

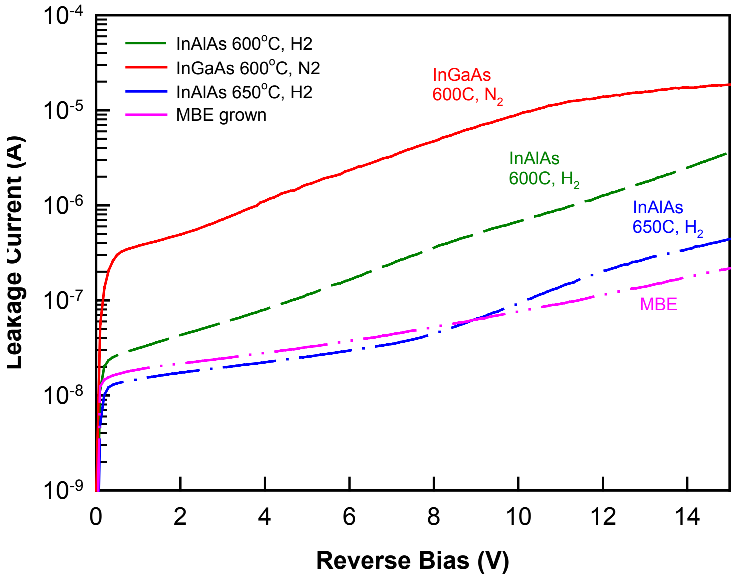

Fig. 6.13 Dark current level comparison between the bonded *p-i-n* photodiodes with the MBE grown

It should also be noted that despite having an $Al_{0.52}Ga_{0.48}As$/GaAs interface in the high electric field region, the dark current density from devices under the best bonding conditions is not higher than the MBE grown reference sample, at least up to a reverse bias of 10V. Based on this experiment, 650^{o}C and H_2 atmosphere were chosen as the conditions for bonding a SACM APD structure, which has a device structure similar to that shown in Fig. 6.3, except using an InAlAs-GaAs bonding interface. The current-voltage characteristics of both the bonded APD devices and a reference SACM APD device, which has a 200-nm InAlAs multiplication region and a 1500-nm InGaAs absorbing region, were measured and compared. The measurement results, as shown in figure 6.14, showed that the dark current at 90% of breakdown of both bonded and MBE-grown reference samples are approximately the same. At a 90% breakdown voltage of 37V the dark current is approximately 100nA for a 150μm diameter bonded device. Using this direct wafer bonding technique, an avalanche photodiode was successfully demonstrated, in which an InGaAs absorber chosen for long wavelength applications was bonded to an AlGaAs multiplication region.

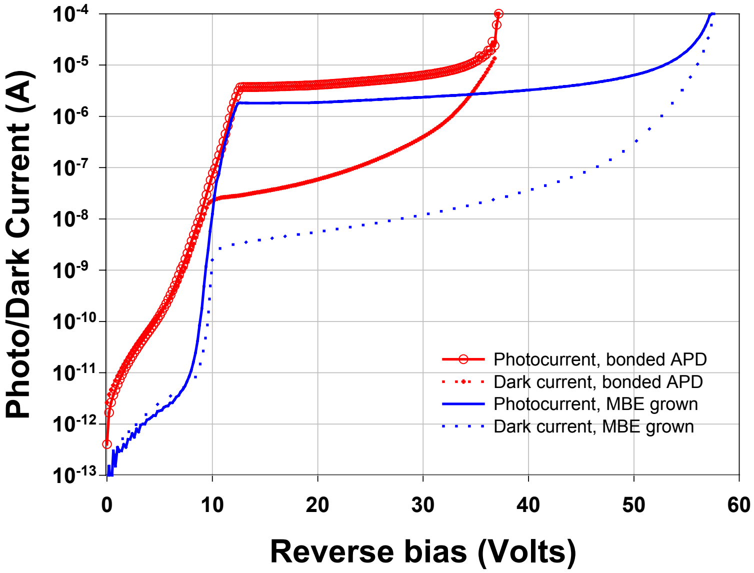

Fig. 6.14 Comparison of a bonded APD with an MBE grown device

6.6 Summary

Using direct wafer bonding, a long-wavelength SACM APD was demonstrated by combining an InGaAs absorber with an $Al_{0.2}Ga_{0.8}As$ *p-i-n* structure through a *p*-InP/*p*-GaAs interface. The bonded APD exhibited avalanche multiplication gain >25, before avalanche breakdown. The external quantum efficiency was ~47% at 1.3 μm and ~33% at 1.55 μm. Subsequent investigation of the direct wafer bonding between InAlAs and GaAs further indicated the possibility of obtaining APDs from this type of bonding interface. Optimized gas and ambient temperature conditions for the successful wafer bonding between InAlAs-GaAs have also been obtained, through numerous bonding experiments.

Chapter 7

Long-Wavelength $In_{0.53}Ga_{0.47}As$/ $In_{0.52}Al_{0.48}As$ APD Focal-plane Arrays

Avalanche photodiode focal plane arrays have been widely used to detect weak optical signals for applications such as high resolution Positron Emission Tomography (PET) [7-1], Detection of Internally Reflected Cherenkov light (DIRC) [7-2], and Scintillating Fiber Readouts [7-3]. For these applications, APD arrays were used as compact alternatives to photo-multiplier tubes (PMTs). To date, all of these arrays have utilized Si APDs, thus the operation was restricted to wavelengths of $\lambda \leq 1.0\mu m$ [7-1]-[7-4]. Even though the MCT focal-plane array provides excellent detection through the infrared wavelength range, the cooling condition required for standard operation eventually limited their usefulness in such applications. The rapidly emerging technology of three-dimensional imaging requires high-sensitivity detector arrays that provide a short wavelength infrared (SWIR) detection range (wavelength: $0.8\mu m \leq \lambda \leq 2.2\mu m$), a gigahertz bandwidth [7-5], and room temperature operation. In order to meet the above requirements, a 12 × 12 array with an $In_{0.53}Ga_{0.47}As$ absorption region and a thin $In_{0.52}Al_{0.48}As$ multiplication region were developed. The APDs in this array exhibit good uniformity of breakdown voltage, photo response, dark current, and avalanche multiplication gain. The unity-gain external quantum efficiency was greater than 40% in the wavelength range from 1.0 μm to 1.6 μm, ~57% at 1.3 μm and ~45% at 1.55 μm. The speed performance, in terms of gain-bandwidth product, was <30GHz, which was lower than the expected value for a 200-nm-thick InAlAs multiplication region. Subsequently, an 18 × 18 array was developed by improving the device structure to enhance APD speed performance. As a result, a low gain bandwidth of ~8GHz and a gain bandwidth product of >120GHz have been achieved at room temperatures. Recent studies of a 40×40 APD array have shown the potential of the MOCVD-grown InGaAs/InAlAs material for larger pixel number focal plane arrays.

7.1 Focal-plane Array Design

A 3-D imaging system requires fast, high-sensitivity photodetector arrays to detect the pulsed *IR* optical signals reflected from distant targets, even if those targets are hidden in camouflage, as shown in Fig. 7.1.

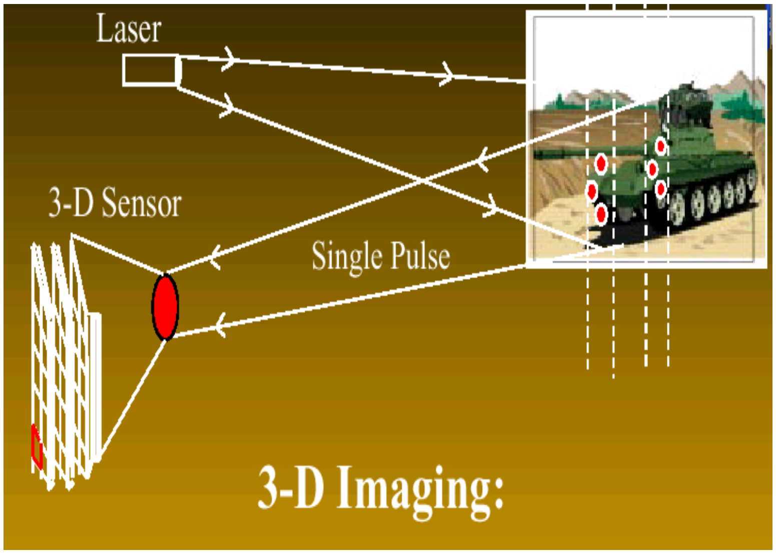

Fig. 7.1 Illustration of the basic working principle of a 3-D imaging system

The sensitivity and operation bandwidth of each individual detector in the focal-plane array determines the spatial detection range and spatial resolution of the 3-D imaging system. Assuming ideal reflection from the target surface, an optical attenuation coefficient in the transmission wavelength window in air α_o ($0.8\mu m \le \lambda \le 2.2\mu m$), an average output power from the pulsed laser P_O, and a minimum detectable average power of the focal-plane array P_M, the maximum detection range is

$$Range = \frac{1}{2\alpha_o} \ln(\frac{P_O}{P_M}) \tag{7.1}$$

The minimum time resolution of the photodetectors, τ_M, determines the minimum spatial resolution of the imaging system. Assuming uniform optical transmission in free space and a refractive index of air in the wavelength window of transmission n, the minimum spatial resolution d can be obtained as

$$d = \frac{c}{4 \cdot \pi \cdot n \cdot f_{3dB}}, \qquad f_{3dB} = \frac{1}{2 \cdot \pi \cdot \tau_M} \tag{7.2}$$

where f_{3dB} is the 3-dB bandwidth of the photodiodes in the array. To meet all the above requirements, a separate absorption, charge, and multiplication (SACM) device structure was utilized for the focal-plane APD array, as shown in Fig. 7.2, to obtain both high sensitivity and high speed. Design details for this device structure have been discussed in the previous chapters. With proper optimization of the device structure, this APD concurrently exhibits low dark current, low multiplication noise, and high speed [7-6]~[7-10]. A 1.5μm $In_{0.53}Ga_{0.47}As$ absorber was used to provide acceptable responsivity (>0.8A/W) at unity-gain. A low-gain bandwidth of >5GHz and a gain-bandwidth of >120GHz were expected as a result of using a 200-nm-thick InAlAs multiplication layer. A high gain-bandwidth product gives APDs an advantage over *p-i-n* photodiodes for imaging applications, in terms of sensitivity.

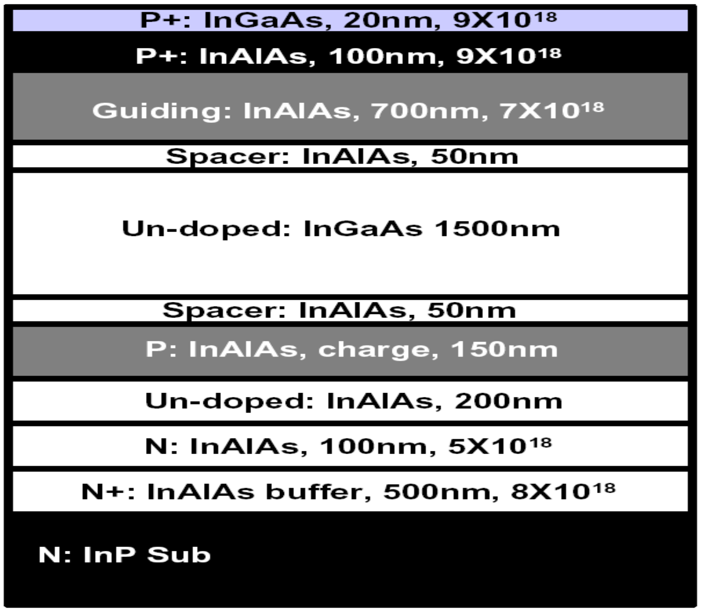

Fig. 7.2 Basic device structure for the 3-D focal-plane APD array

7.2 Material Growth and Calibration

Extreme care was taken for the MBE calibration and growth for the APD array due to stringent requirements for device yield and uniformity. After any period of maintenance on the growth chamber, a set of x-ray calibration samples was grown to determine the group-III fluxes necessary to grow InGaAs and InAlAs lattice-matched to InP. The procedure is to use a fixed indium flux while growing two or three layers on the same sample with different Ga (or Al) fluxes, which is accomplished by incrementing the relevant Ga (or Al) cell temperature by a degree or two between each layer. After x-ray diffraction is measured from the family of all (400) planes in the sample, response peaks can be observed, which correspond to the substrate and each of the three relaxed epitaxial layers. The location of each InGaAs (or InAlAs) peak relative to the substrate peak indicates the appropriate cell temperature required to achieve good lattice match of the epitaxial layers to the InP substrate. Once the source temperatures have been determined, the resulting beam flux is recorded for future use.

The accuracy of this calibration method varies from time to time, according to an investigation done at UCSB. The precision afforded by the beam flux measurement is sufficient to keep the X-ray diffraction within 100 arc seconds. Normally, these compositions are clustered within 100 arc seconds or less of the substrate peak. Calibration by beam flux tends not to provide the same level of accuracy for determining the final wafer composition. Nonetheless, epi-layer thickness, as calibrated by beam flux, is typically within an accuracy of 2 ~ 4%. An improved accuracy of less than 1% can also be achieved, by growing the calibration sample on the same day prior to the real growth.

Starting with a substrate temperature of 500 °C with an arsenic beam flux of 1.2×10^{-5} torr, the substrate temperature was ramped to 570 °C in a span of 15 seconds to remove the surface oxide. The substrate was then immediately cooled to the growth temperature (500°C). The first layer grown was a 500 nm-thick layer of *n*-type $In_{0.52}Al_{0.48}As$ doped to 8×10^{18} cm^{-3} with silicon. Next, a 100nm-thick layer of *n*-type (5×10^{18} cm^{-3}) $In_{0.52}Al_{0.48}As$, a 200 nm-thick intrinsic $In_{0.52}Al_{0.48}As$ layer was grown as the multiplication region. Subsequently, a charge layer consisting of 150 nm *Be*-doped, *p*-type (4×10^{17} cm^{-3}) $In_{0.52}Al_{0.48}As$ was deposited. Finally, 1500 nm of intrinsic $In_{0.53}Ga_{0.47}As$ sandwiched between two 50 nm-thick unintentionally-doped $In_{0.52}Al_{0.48}As$ spacer layers was grown as the absorption layer. This was followed by a 700 nm-thick *p*-type (*Be*: 7×10^{18} cm^{-3}) $In_{0.52}Al_{0.48}As$ layer. The *p*-type contact layers consisted of 100 nm of $In_{0.52}Al_{0.48}As$ (*Be*: 9×10^{18} cm^{-3}) capped with 20 nm of $In_{0.53}Ga_{0.47}As$, doped at the same level.

7.3 APD Focal-plane Array Fabrication

The device processing also focused on improving device yield in order to demonstrate a functional focal-plane APD array, with a reasonable pixel number. The focal-plane array processing began the *p*-type ohmic contact formation. A Cr (25 nm)/Au (85 nm) film was deposited using E-beam evaporation onto the heavily-doped $In_{0.53}Ga_{0.47}As$ cap layer. These *p*-type contacts were patterned with standard photolithography and lift-off processing. A SiO_2 etch mask was then deposited by PECVD and mesa etch patterns were defined. The SiO_2 etch mask was used to ensure mesa pattern uniformity and smooth mesa edges, which has been proven as a critical step for device yield. Mesas with a diameter of 50 μm were etched in phosphoric etchant (H_3PO_4:H_2O_2:H_2O = 1:1:8) to the n^+ InP buffer layer. After mesa etching, both the photoresist and the SiO_2 mask were removed. The wafer was quickly transferred to the PECVD chamber where a thin film of SiO_2 (~150 nm) was deposited for sidewall passivation. A Ni (20 nm)/AuGe (30 nm)/Au (80 nm) film was deposited by E-beam evaporation as a common *n*-type ohmic contact to all the APDs in the array. The p-contacts were then opened using standard photolithography and BOE etching. A microscope picture of a 12×12 focal-plane APD array, after processing, is shown in Fig. 7.3.

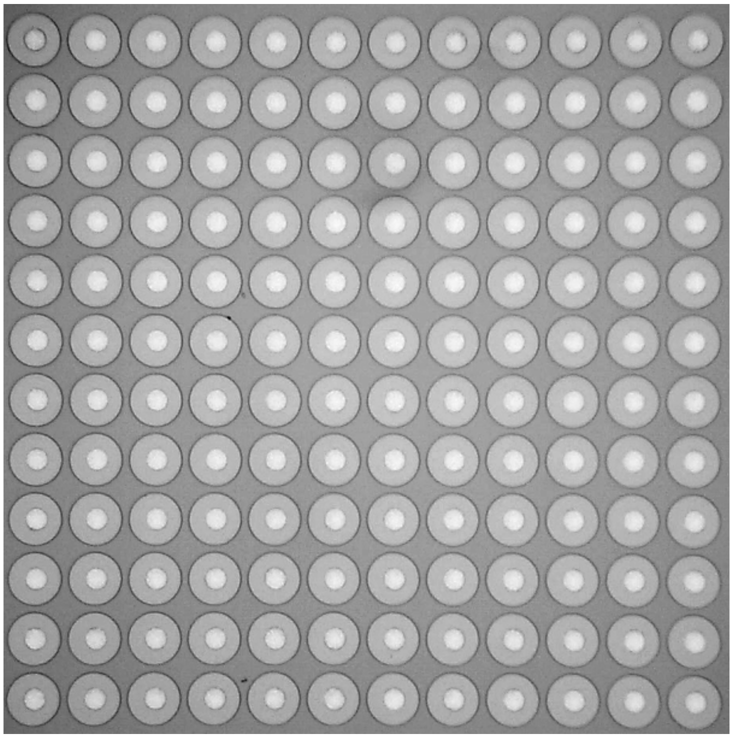

Fig. 7.3 InGaAs/InAlAs 3-D focal-plane APD array after processing

7.4 First 12 × 12 Focal-plane APD Array

The photocurrent and dark current of the InGaAs/InAlAs SACM APDs were characterized at room temperature using a HP 4145B semiconductor parameter analyzer. Uniform top illumination was used to characterize the photo response. Figure 3 shows the measured photocurrent and the dark current curves of all 144 APDs in the array. The mean breakdown voltage was 57.9V and the standard deviation was less than 0.1V. Since the breakdown voltage is very sensitive to small variations in thickness and impurity concentration in the epitaxial layers, it can be inferred that the MBE growth was very uniform. The punch-through voltages were close to 12.5V; however, the distribution was not as tight as that of the breakdown voltages. This most likely results from small variations in the beryllium concentration in the charge region and beryllium diffusion at the growth temperature (≥500°C).

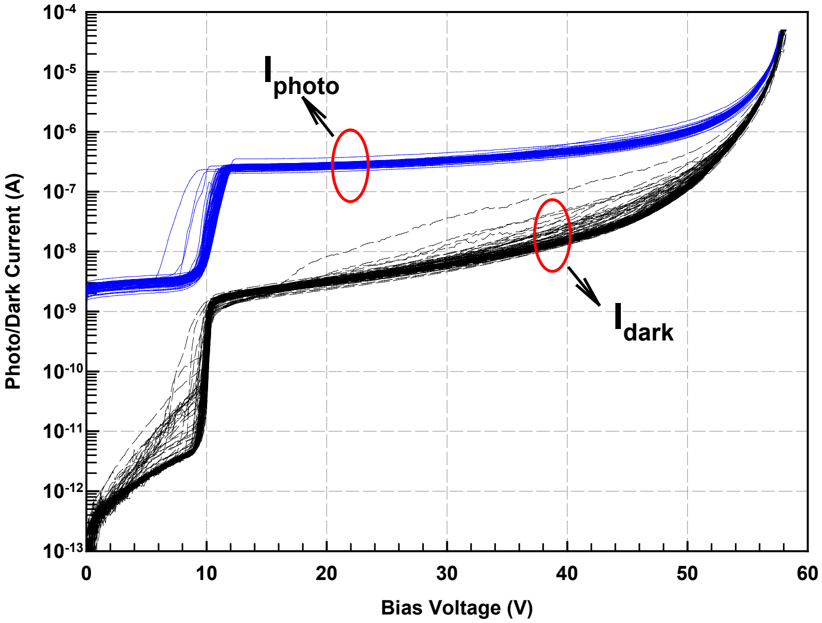

Fig. 7.4 Typical I-V characteristics of APD devices on the InGaAs/InAlAs 3-D focal-plane APD array

Plentiful latitude in the selection of the unity-gain reference was afforded by the fact that all the APDs showed flat responses after punch-through, as shown in Fig. 7.4. In order to ensure that each APD was measured above punch through, a reverse bias voltage of 13.5V (one volt above the punch-through) was selected as the unity-gain reference bias. The mean dark current and standard deviation at the selected unity-gain reference bias were ~2nA and ~0.19nA, respectively. The mean dark current and standard deviation increased up to ~300nA and ~60nA at 90% of the breakdown voltage, as shown in Fig. 7.5 (a) and (b). Larger standard deviation of the dark current at higher reverse biases indicates a more pronounced gain variation at higher reverse biases, which will result in a larger spread in the distribution, due to multiplied dark current in the total dark current term.

The external quantum efficiencies were measured using a tungsten-halogen light source, a spectrometer, and a lock-in amplifier, at 13.5V, to verify the validity of the selection of unity gain reference. The measured unity-gain external quantum efficiency was greater than 40% throughout the wavelength range from 1.0 μm to 1.6 μm, as shown in Fig. 7.6. External quantum efficiencies as high as ~57% at 1.3 μm and ~45% at 1.55 μm were observed. The total external quantum efficiency of the APDs under test should be governed by the following expression

$$\eta_{ext} = (1-R)\cdot(1-e^{-\alpha\cdot d}) \tag{7.3}$$

where R is the reflection coefficient of the air-semiconductor interface; α is the absorption coefficient of $In_{0.53}Ga_{0.47}As$ at the relevant incident wavelength; and d is the absorption layer thickness. For a SACM APD with a 1.5 μm-thick $In_{0.53}Ga_{0.47}As$ absorption region that has absorption coefficients (α) of 1.16 μm^{-1} at 1.3 μm and 0.705 μm^{-1} at 1.55 μm [7-10], the ideal external quantum efficiencies are ~58% and ~46%, respectively, assuming an optical transmission of 70% (R=0.3) at the air-semiconductor interface. These values are consistent with the measured external quantum efficiencies at these two wavelengths, which further corroborated the unity gain reference selection.

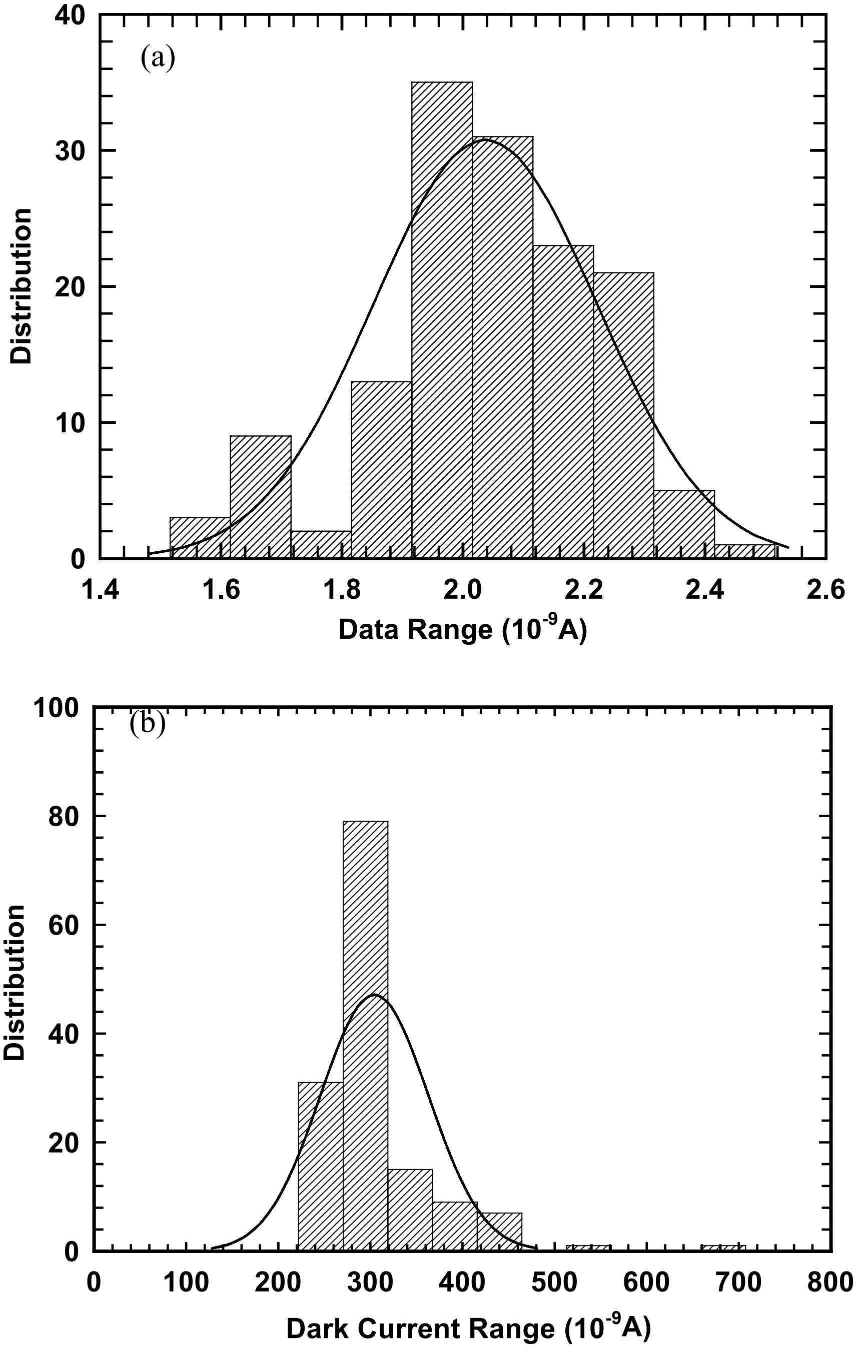

Fig. 7.5 Dark current distributions of APD devices on the InGaAs/InAlAs 3-D focal-plane APD array, (a) at unity-gain and (b) at 90% breakdown

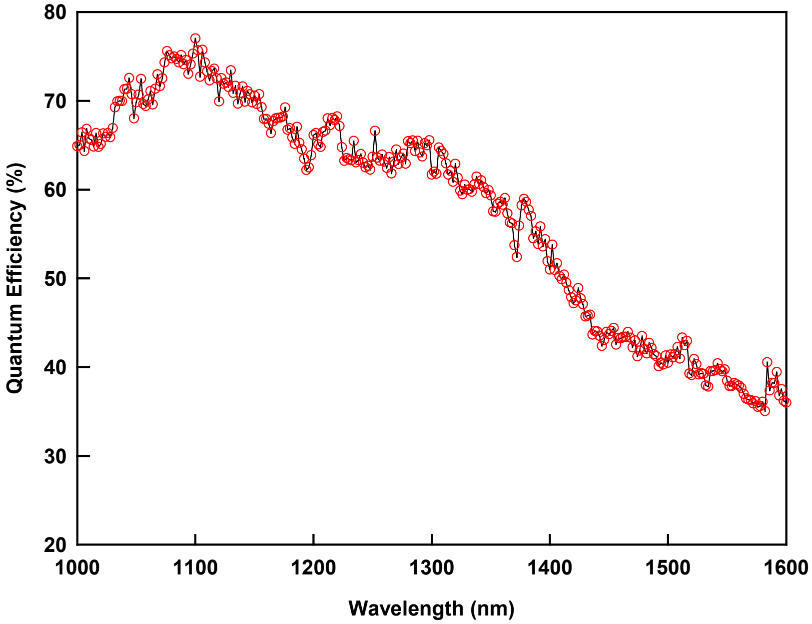

Fig. 7.6 External quantum efficiency of APD devices on the InGaAs/InAlAs 3-D focal-plane APD array

The APD gain was thus determined using the following expression

$$M = \frac{I_p - I_d}{I_{pu} - I_{du}} \tag{7.4}$$

where I_p and I_d are the photocurrent and dark current for bias values above punch through; I_{pu} and I_{du} are the primary photocurrent and dark current at unity-gain (V_{bias}=13.5V). In Fig. 7.7, gain curves of all the APDs in the focal-plane array are plotted as a function of the reverse bias voltage. The mean value of the gain was 10.2, 15.1, 20.2, and 42.4 at reverse bias voltages of 55.8V, 56.6V, 57V, and 57.6V, respectively. The standard deviations of the multiplication gain distribution at each of the above reverse bias voltages were 0.28, 0.56, 1.09, and 5.64, respectively. The multiplication gain distributions at each of the above reverse bias voltages are plotted in Fig. 7.7 (a) to (d).

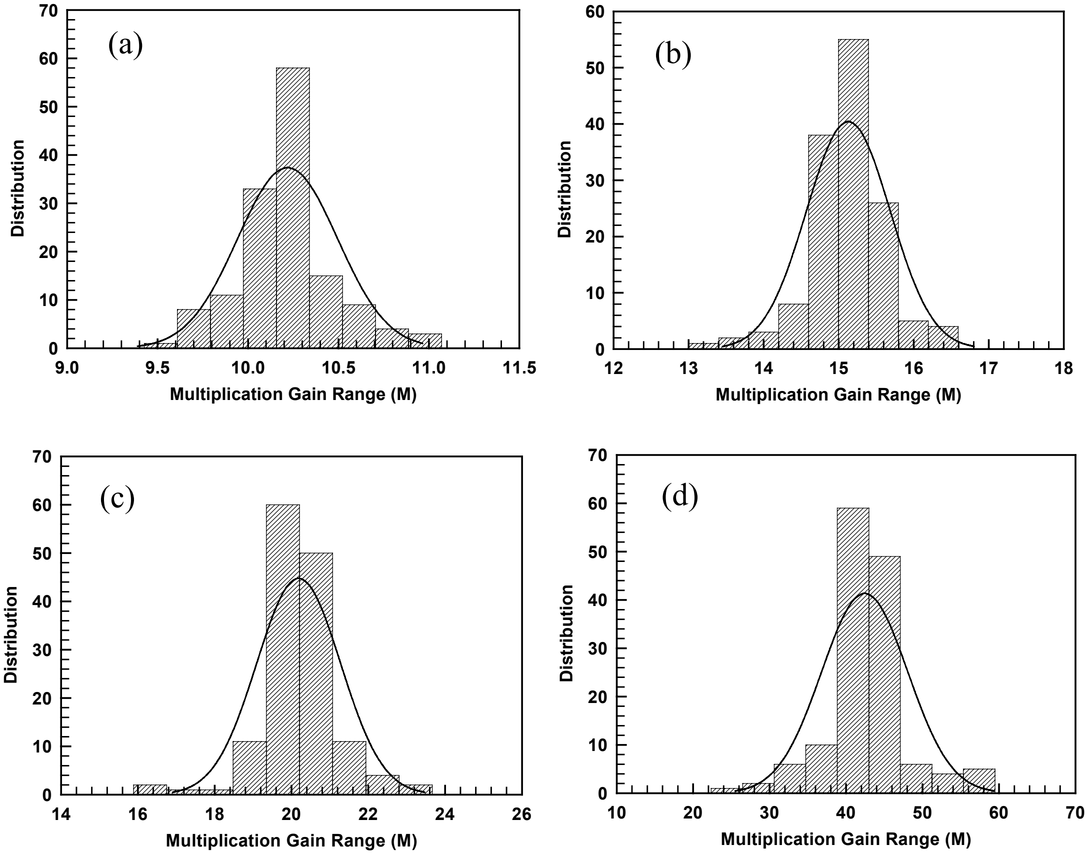

Fig. 7.7 Gain distributions of APDs on the InGaAs/InAlAs 3-D focal-plane APD array at biases of (a) 55.8V and (b) 56.6V (c) 57.0V (d) 57.6V

The bandwidth was measured with a HP8703A lightwave component analyzer at the wavelength of 1.3μm. The unity-gain bandwidth of 50μm APD devices was 13GHz. At higher gains a gain-bandwidth product of 23GHz was observed, as shown in Fig. 7.8.

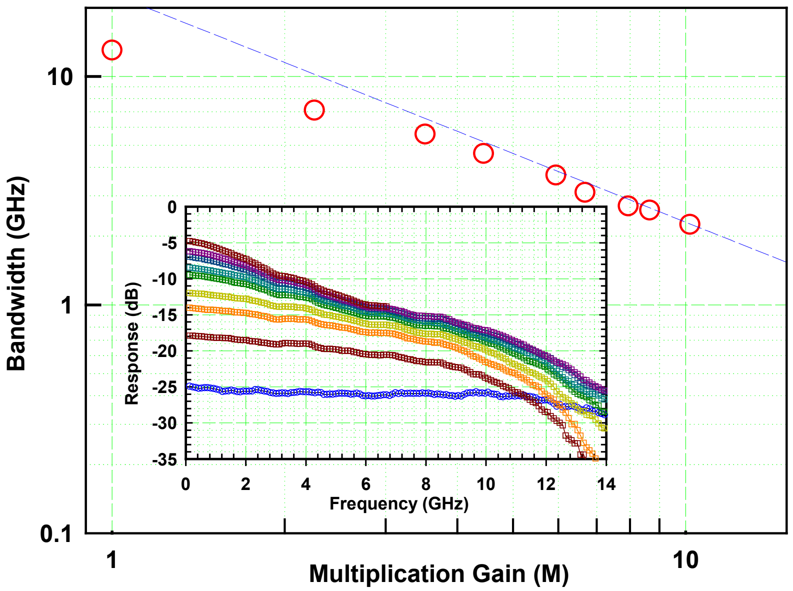

Fig. 7.8 Deficient APD gain-bandwidth product obtained from the 12X12 array

This relatively low gain-bandwidth product resulted from a low level of avalanche gain in the $In_{0.53}Ga_{0.47}As$ absorption region, in which the electric field at high gains (e. g. ~228kV/cm at gain of 10) was close to the critical breakdown field in bulk $In_{0.53}Ga_{0.47}As$ (~250kV/cm) [7-11]. This low level of gain in the absorption region results in carrier feedback from the absorption region to the multiplication region. The long feedback path (~1.9μm) associated with this type of gain significantly degrades the excess noise and the gain-bandwidth product of the APDs [7-12]. Avalanche gain in the $In_{0.53}Ga_{0.47}As$ absorption layer can be eliminated through increasing the doping or thickness of the charge layer.

7.5 An 18X18 Array with Improved Speed Performance

Based on the previous 12 × 12 APD array results, the charge layer doping level was adjusted to decrease the electric filed intensity in the $In_{0.53}Ga_{0.47}As$ absorber at high gains. Using the method discussed in Chapter 3, the charge layer doping level was increased 1.42 times to decrease the E-field to less than 100KV/cm in the $In_{0.53}Ga_{0.47}As$ absorber. For this reason, the charge layer (beryllium) doping level was re-calibrated and several wafers were re-grown at UCSB. The thickness, composition, and doping concentration of each layer were examined with SIMS to guarantee the consistency between the design specifications and wafer structures after MBE growth, as shown in Fig.7.9.

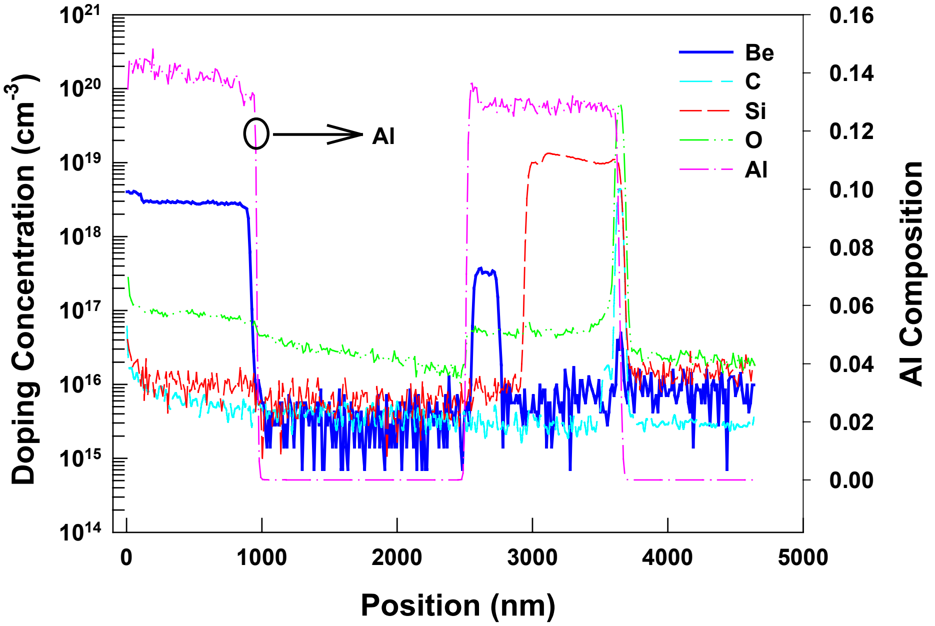

Fig. 7.9 SIMS results of the new APD array wafer, by EVANS TEXAS

New focal-plane APD arrays were fabricated with an improved array mask, on which design concern focused on improving device yield associated with device processing. A new focal-plane array of 40 × 40 50μm-mesa-diameter APDs was fabricated, as shown in Fig. 7.10.

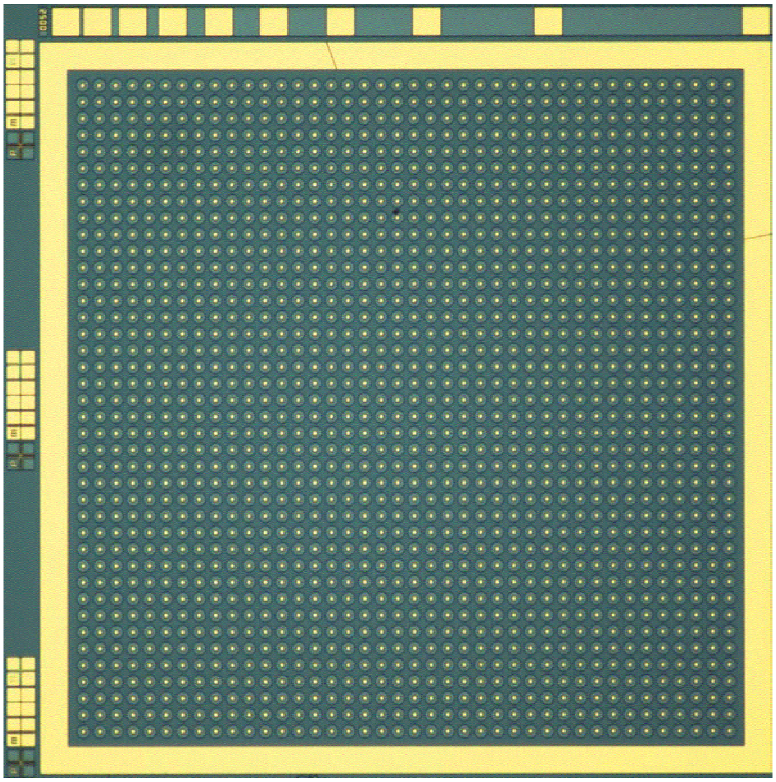

Fig. 7.10 A single die on the new 40X40 APD array wafer, after processing

Photocurrent, dark current, and gain of APDs were characterized in one quarter of this array. An 18X18 sub-array on this 40X40 array was functional, with only three failed devices, which was caused by improper probing. Statistical analysis of the dark current for the other 321 devices exhibited a mean value of ~4.4nA and a standard deviation of 1.5nA at bias voltage of 16.0V (gain ~1.8), as

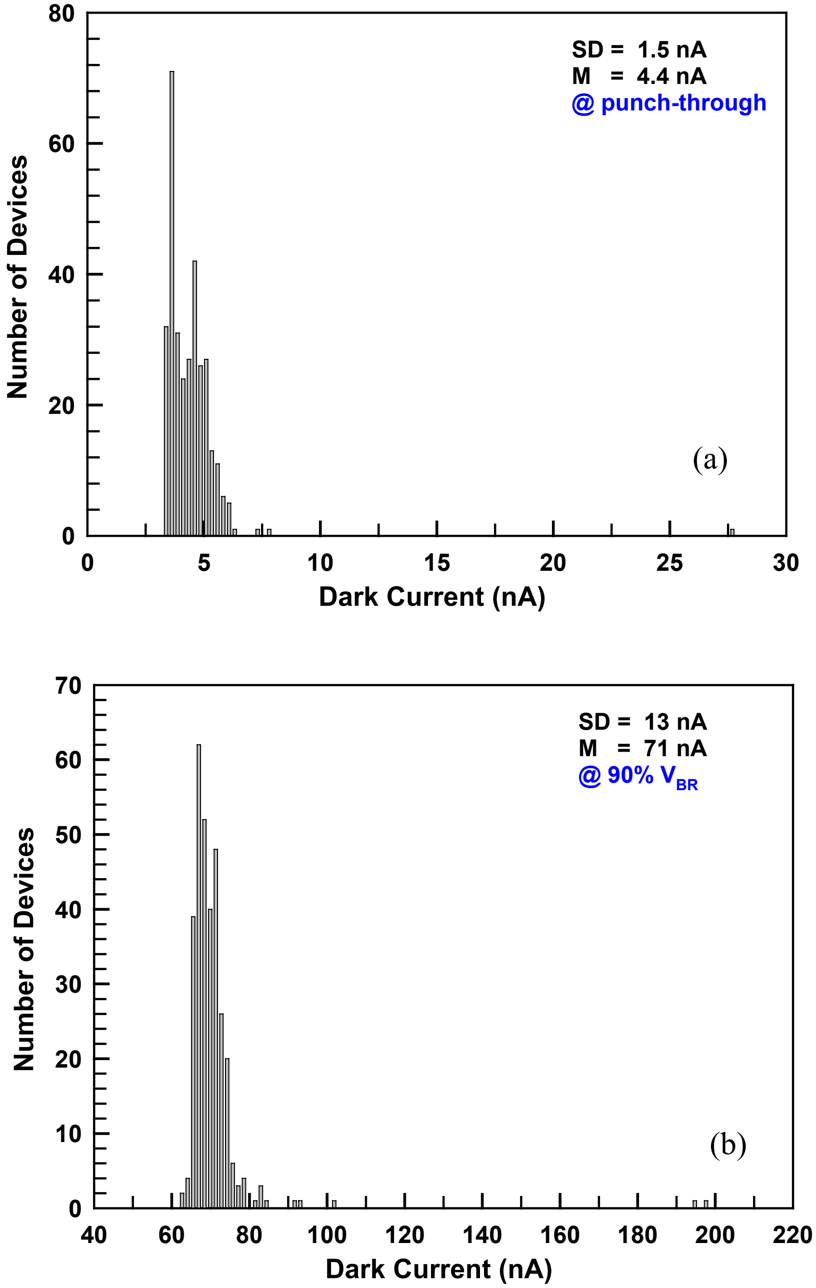

Fig. 7.11 Dark current distributions of APDs on an 18X18 InGaAs/InAlAs 3-D focal-plane APD array, (a) at unity-gain and (b) at 90% breakdown

shown in Fig. 7.11 (a). The dark current distribution at 90% of breakdown demonstrated a mean value of ~71nA and a standard deviation of 13nA, as shown in Fig. 7.11(b). Several devices with relatively poor sidewall passivation on this APD array contributed to the increased spread in the dark current distribution at higher bias voltages.

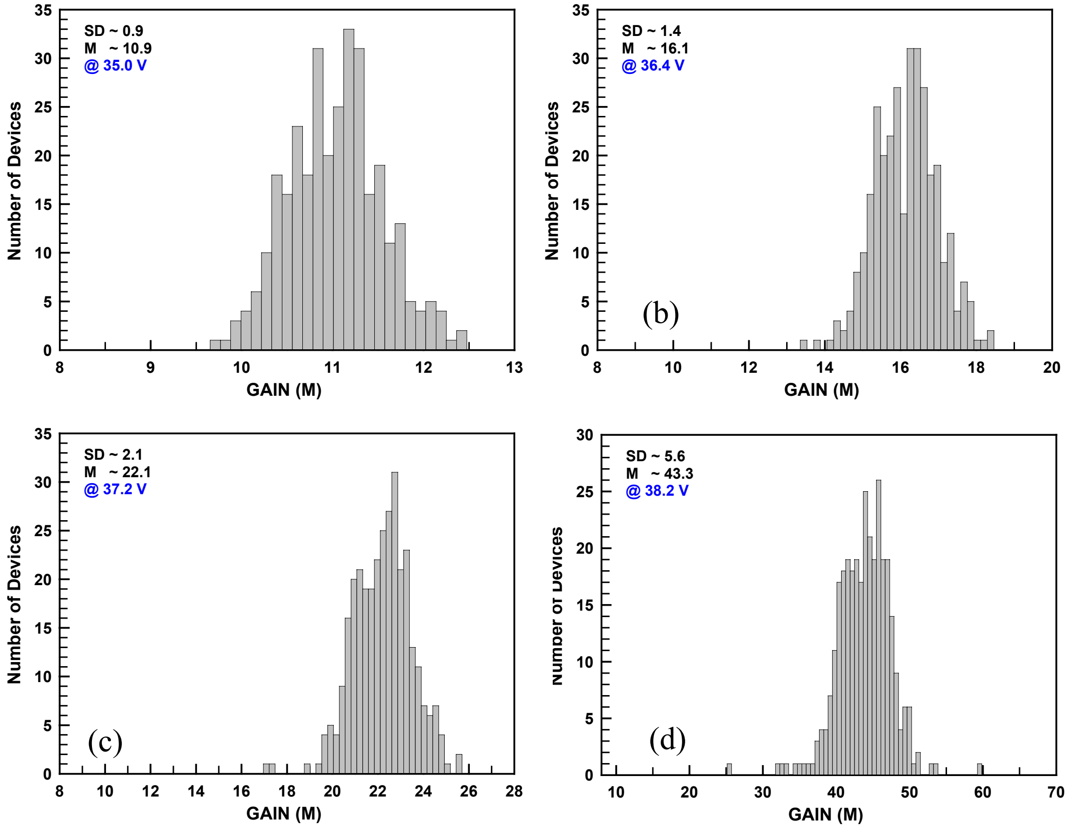

Fig. 7.12 Gain distributions of APDs on the InGaAs/InAlAs 3-D focal-plane APD array at biases of (a) 35.0V and (b) 36.4V (c) 37.2V (d) 38.2V

Uniform photocurrent was consistently observed across this 18 × 18 array and the gain distributions were calculated, as shown in Fig. 7.12 (a) to (d). The mean gain was 10.9, 16.1, 22.1, and 43.4 at reverse bias voltages of 35.0V, 36.4V, 37.2V, and 38.2V, respectively. The standard deviation of the multiplication gain distribution at each of the above reverse bias conditions was 0.9, 1.4, 2.1, and 5.6, respectively. These results agree quite well with our previous 12 × 12 APD array results, as discussed in the previous section, especially the distribution in the high gain regime.

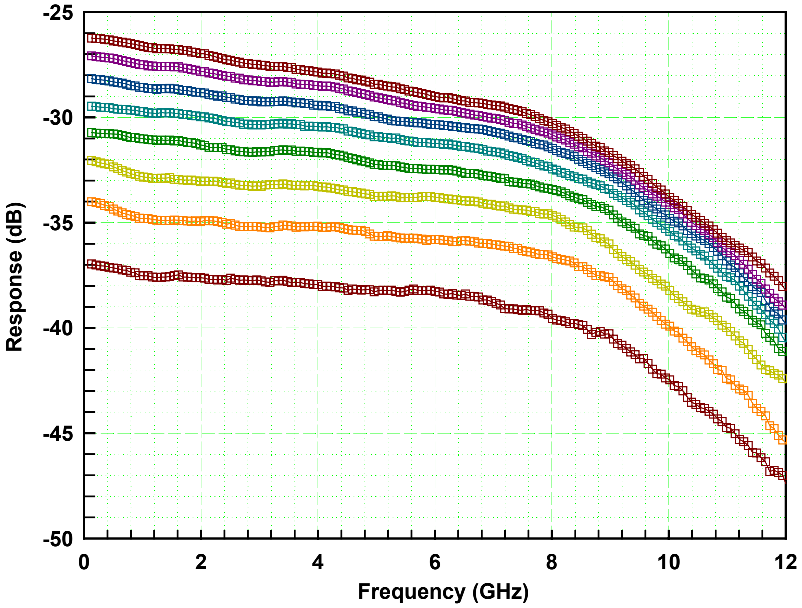

Fig. 7.13 Photoresponse curves of a 50μm APD measured at 1.3μm wavelength

The bandwidth of the APD array devices was measured with a HP8703A light-wave component analyzer at a wavelength of 1.3μm. The unity-gain bandwidth of a 50μm-diameter APD device was ~8GHz, as shown in Fig. 7.13. The bandwidth in the low gain region was determined by the long carrier transport path (~3.9μm) associated with the depleted absorption, charge, and multiplication regions, thus the bandwidth was primarily transit-time limited. To verify this, the capacitance-voltage dependence was characterized using the C-V measurement of a 500μm-diameter APD, as shown in the inset of Fig. 7.14. A capacitance of ~13pF (~6.6×10^{-2} fF/μm^2) at a bias voltage of 16.0V was obtained at low frequency (1MHz) and agrees reasonably well with the calculated unity capacitance value (6.3×10^{-2} fF/μm^2). The capacitance curve exhibited a sharp decrease before punch-through, but only a slight change was observed after punch-through, due to total depletion of the charge region. For a 50-μm APD, the measured capacitance by C-V is ~120fF at a bias voltage of 16.0V, as plotted in Figure 7.14.

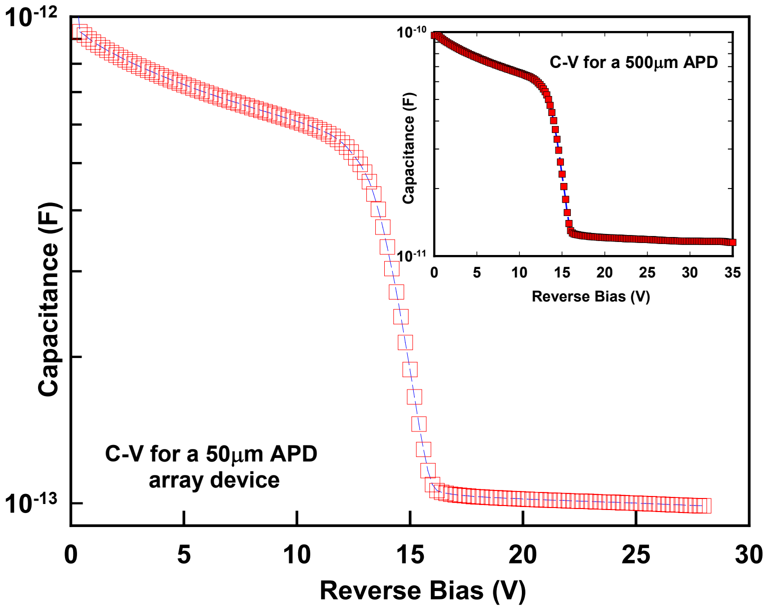

Fig. 7.14 C-V measurement results from a 50μm and a 500μm (inset) APD

The parasitic capacitance and resistance of the photodiodes was also measured using a HP8703A spectrum analyzer, with an RF calibration frequency up to 10GHz. From the measured S-parameters, a capacitance of ~100fF and a total load resistance of ~60Ω (~10Ω contact resistance + 50Ω terminal resistance) were extracted, based on a simplified *R-C* equivalent circuit model. The 3-dB *RC* bandwidth was therefore estimated at >20GHz, which is far above the carrier transit time limitation. The slight discrepancy between the high frequency RF measurement and the low frequency C-V measurement was partly attributed to the frequency dependence of the dielectric constant of the relevant semiconductors.

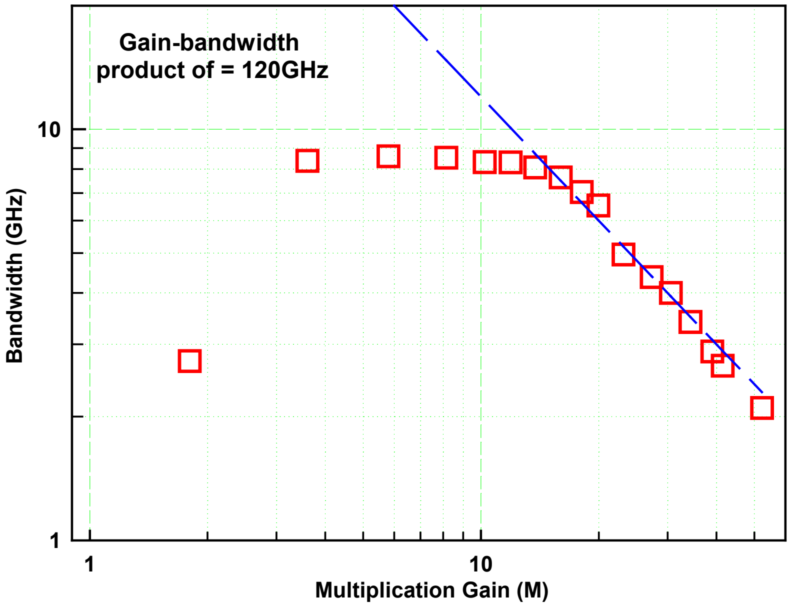

Fig. 7.15 Gain-bandwidth product of a 50μm APD in an 18×18 array

At higher gains, a gain-bandwidth product of 120GHz was observed. In comparison with our previous 12×12 array results, the gain-bandwidth increased >5 times due to optimization of electric field in the 1500nm-thick $In_{0.53}Ga_{0.47}As$ absorption region. By increasing the charge layer doping, the electric field strength in the $In_{0.53}Ga_{0.47}As$ absorber decreased from >250KV/cm to <150KV/cm at bias voltages close to the breakdown. The measured bandwidth as a function of multiplication gain was plotted in Figure 7.15.

7.6 A 40×40 APD Array Based on MOCVD Materials

As a follow-up step, a 40×40 InAlAs/InGaAs APD array was designed and fabricated, using MOCVD material provided by SpectroLab. To our knowledge this is the largest InAlAs-based APD array that have been characterized, using automatic probing station. Device testing has been a challenge for the manual APD array characterization and is extremely time consuming. The 40μm diameter detectors are suitable for 3-D imaging applications that require response bandwidths in excess of 1GHz, in the short wavelength infrared range from 1.0 to 1.6 μm.

The device layers were grown by metal-organic vapor phase epitaxy on 2” sulphur-doped (100) InP n+ substrates. Trimethylindium, trimethylgallium, trimethylaluminum, 100% arsine, and 100% phosphine were used as source materials. Figure 7.16 is a cross section of the device.

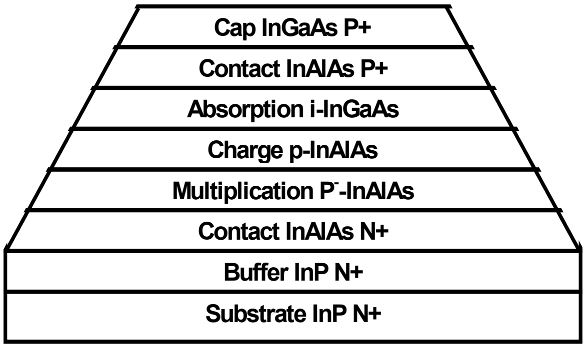

Fig. 7.16 The InAlAs APD cross section

Avalanche photodiodes were fabricated by wet chemical mesa etching followed by passivation. Front-illuminated arrays of 40x40 elements were fabricated.

The array elements were 40 µm in diameter on a 60µm pitch. Figure 7.17 displays a scanning electron micrograph of a section of one array. Metal pads were placed on the center of each pixel to provide for anode contact, with the substrate providing a common cathode.

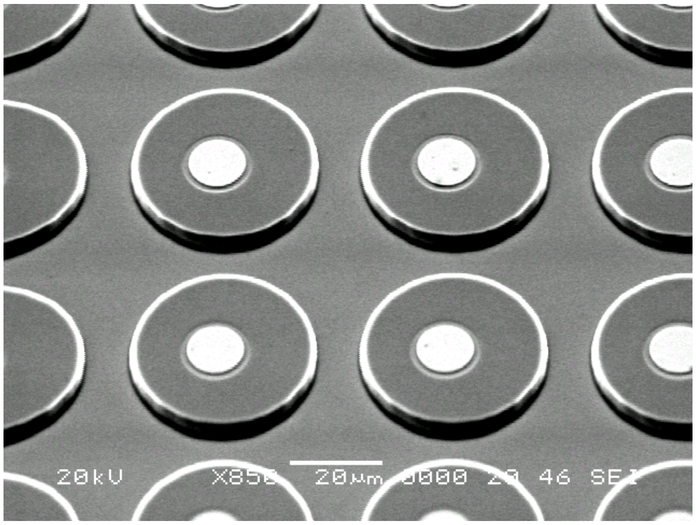

.

Fig. 7.17 An SEM micrograph of one section of the 40x40 element APD array

The 40×40 element APD arrays were subsequently characterized for dark current and photocurrent performance. The arrays were first characterized for dark current and screened with a requirement that each element display <20nA of dark current at a nominal operating bias determined from one element of the array. This operating bias was chosen to give a nominal M=10 operating point. Figure 7.18 shows the pass/fail results for one array which had >99% operability. The dark current histogram is shown in Figure 7.19 and demonstrates a uniform dark current distribution.

Optical response is a key performance figure-of-merit for any imaging array. Figure 7.20 displays the response uniformity across a 40×40-pixel APD array. The data was collected at an operating bias chosen to give an a-priori gain of 10 for each device of the array. The data revealed that there is some non-uniformity in optical response for a single bias point. However, in the focal plane array application each pixel will be individually biased, which will remove gain non-uniformities due to bias related issues.

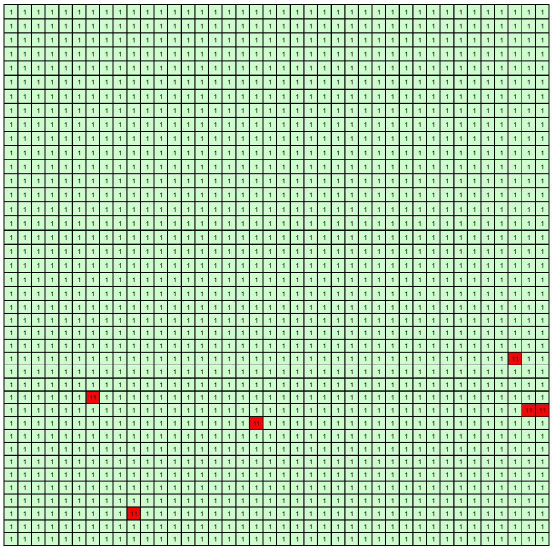

1	1	1	1	1	1	1	1	1	1	1	1	1	1	1	1	1	1	1	1	1	1	1	1	1	1	1	1	1	1	1	1	1	1	1	1	1	1	1	1
1	1	1	1	1	1	1	1	1	1	1	1	1	1	1	1	1	1	1	1	1	1	1	1	1	1	1	1	1	1	1	1	1	1	1	1	1	1	1	1
1	1	1	1	1	1	1	1	1	1	1	1	1	1	1	1	1	1	1	1	1	1	1	1	1	1	1	1	1	1	1	1	1	1	1	1	1	1	1	1
1	1	1	1	1	1	1	1	1	1	1	1	1	1	1	1	1	1	1	1	1	1	1	1	1	1	1	1	1	1	1	1	1	1	1	1	1	1	1	1
1	1	1	1	1	1	1	1	1	1	1	1	1	1	1	1	1	1	1	1	1	1	1	1	1	1	1	1	1	1	1	1	1	1	1	1	1	1	1	1
1	1	1	1	1	1	1	1	1	1	1	1	1	1	1	1	1	1	1	1	1	1	1	1	1	1	1	1	1	1	1	1	1	1	1	1	1	1	1	1
1	1	1	1	1	1	1	1	1	1	1	1	1	1	1	1	1	1	1	1	1	1	1	1	1	1	1	1	1	1	1	1	1	1	1	1	1	1	1	1
1	1	1	1	1	1	1	1	1	1	1	1	1	1	1	1	1	1	1	1	1	1	1	1	1	1	1	1	1	1	1	1	1	1	1	1	1	1	1	1
1	1	1	1	1	1	1	1	1	1	1	1	1	1	1	1	1	1	1	1	1	1	1	1	1	1	1	1	1	1	1	1	1	1	1	1	1	1	1	1
1	1	1	1	1	1	1	1	1	1	1	1	1	1	1	1	1	1	1	1	1	1	1	1	1	1	1	1	1	1	1	1	1	1	1	1	1	1	1	1
1	1	1	1	1	1	1	1	1	1	1	1	1	1	1	1	1	1	1	1	1	1	1	1	1	1	1	1	1	1	1	1	1	1	1	1	1	1	1	1
1	1	1	1	1	1	1	1	1	1	1	1	1	1	1	1	1	1	1	1	1	1	1	1	1	1	1	1	1	1	1	1	1	1	1	1	1	1	1	1
1	1	1	1	1	1	1	1	1	1	1	1	1	1	1	1	1	1	1	1	1	1	1	1	1	1	1	1	1	1	1	1	1	1	1	1	1	1	1	1
1	1	1	1	1	1	1	1	1	1	1	1	1	1	1	1	1	1	1	1	1	1	1	1	1	1	1	1	1	1	1	1	1	1	1	1	1	1	1	1
1	1	1	1	1	1	1	1	1	1	1	1	1	1	1	1	1	1	1	1	1	1	1	1	1	1	1	1	1	1	1	1	1	1	1	1	1	1	1	1
1	1	1	1	1	1	1	1	1	1	1	1	1	1	1	1	1	1	1	1	1	1	1	1	1	1	1	1	1	1	1	1	1	1	1	1	1	1	1	1
1	1	1	1	1	1	1	1	1	1	1	1	1	1	1	1	1	1	1	1	1	1	1	1	1	1	1	1	1	1	1	1	1	1	1	1	1	1	1	1
1	1	1	1	1	1	1	1	1	1	1	1	1	1	1	1	1	1	1	1	1	1	1	1	1	1	1	1	1	1	1	1	1	1	1	1	1	1	1	1
1	1	1	1	1	1	1	1	1	1	1	1	1	1	1	1	1	1	1	1	1	1	1	1	1	1	1	1	1	1	1	1	1	1	1	1	1	1	1	1
1	1	1	1	1	1	1	1	1	1	1	1	1	1	1	1	1	1	1	1	1	1	1	1	1	1	1	1	1	1	1	1	1	1	1	1	1	1	1	1
1	1	1	1	1	1	1	1	1	1	1	1	1	1	1	1	1	1	1	1	1	1	1	1	1	1	1	1	1	1	1	1	1	1	1	1	1	1	1	1
1	1	1	1	1	1	1	1	1	1	1	1	1	1	1	1	1	1	1	1	1	1	1	1	1	1	1	1	1	1	1	1	1	1	1	1	1	1	1	1
1	1	1	1	1	1	1	1	1	1	1	1	1	1	1	1	1	1	1	1	1	1	1	1	1	1	1	1	1	1	1	1	1	1	1	1	1	1	1	1
1	1	1	1	1	1	1	1	1	1	1	1	1	1	1	1	1	1	1	1	1	1	1	1	1	1	1	1	1	1	1	1	1	1	1	1	1	1	1	1
1	1	1	1	1	1	1	1	1	1	1	1	1	1	1	1	1	1	1	1	1	1	1	1	1	1	1	1	1	1	1	1	1	1	1	1	1	1	1	1
1	1	1	1	1	1	1	1	1	1	1	1	1	1	1	1	1	1	1	1	1	1	1	1	1	1	1	1	1	1	1	1	1	1	1	1	1	11	1	1
1	1	1	1	1	1	1	1	1	1	1	1	1	1	1	1	1	1	1	1	1	1	1	1	1	1	1	1	1	1	1	1	1	1	1	1	1	1	1	1
1	1	1	1	1	1	1	1	1	1	1	1	1	1	1	1	1	1	1	1	1	1	1	1	1	1	1	1	1	1	1	1	1	1	1	1	1	1	1	1
1	1	1	1	1	1	11	1	1	1	1	1	1	1	1	1	1	1	1	1	1	1	1	1	1	1	1	1	1	1	1	1	1	1	1	1	1	1	1	1
1	1	1	1	1	1	1	1	1	1	1	1	1	1	1	1	1	1	1	1	1	1	1	1	1	1	1	1	1	1	1	1	1	1	1	1	1	1	11	11
1	1	1	1	1	1	1	1	1	1	1	1	1	1	1	1	1	1	11	1	1	1	1	1	1	1	1	1	1	1	1	1	1	1	1	1	1	1	1	1
1	1	1	1	1	1	1	1	1	1	1	1	1	1	1	1	1	1	1	1	1	1	1	1	1	1	1	1	1	1	1	1	1	1	1	1	1	1	1	1
1	1	1	1	1	1	1	1	1	1	1	1	1	1	1	1	1	1	1	1	1	1	1	1	1	1	1	1	1	1	1	1	1	1	1	1	1	1	1	1
1	1	1	1	1	1	1	1	1	1	1	1	1	1	1	1	1	1	1	1	1	1	1	1	1	1	1	1	1	1	1	1	1	1	1	1	1	1	1	1
1	1	1	1	1	1	1	1	1	1	1	1	1	1	1	1	1	1	1	1	1	1	1	1	1	1	1	1	1	1	1	1	1	1	1	1	1	1	1	1
1	1	1	1	1	1	1	1	1	1	1	1	1	1	1	1	1	1	1	1	1	1	1	1	1	1	1	1	1	1	1	1	1	1	1	1	1	1	1	1
1	1	1	1	1	1	1	1	1	1	1	1	1	1	1	1	1	1	1	1	1	1	1	1	1	1	1	1	1	1	1	1	1	1	1	1	1	1	1	1
1	1	1	1	1	1	1	1	1	11	1	1	1	1	1	1	1	1	1	1	1	1	1	1	1	1	1	1	1	1	1	1	1	1	1	1	1	1	1	1
1	1	1	1	1	1	1	1	1	1	1	1	1	1	1	1	1	1	1	1	1	1	1	1	1	1	1	1	1	1	1	1	1	1	1	1	1	1	1	1
1	1	1	1	1	1	1	1	1	1	1	1	1	1	1	1	1	1	1	1	1	1	1	1	1	1	1	1	1	1	1	1	1	1	1	1	1	1	1	1

Fig. 7.18 A pass/fail map on one 40x40 APD array with >99% operability. The pass/fail criterion is the dark current level @ M=10 < 20 nA.

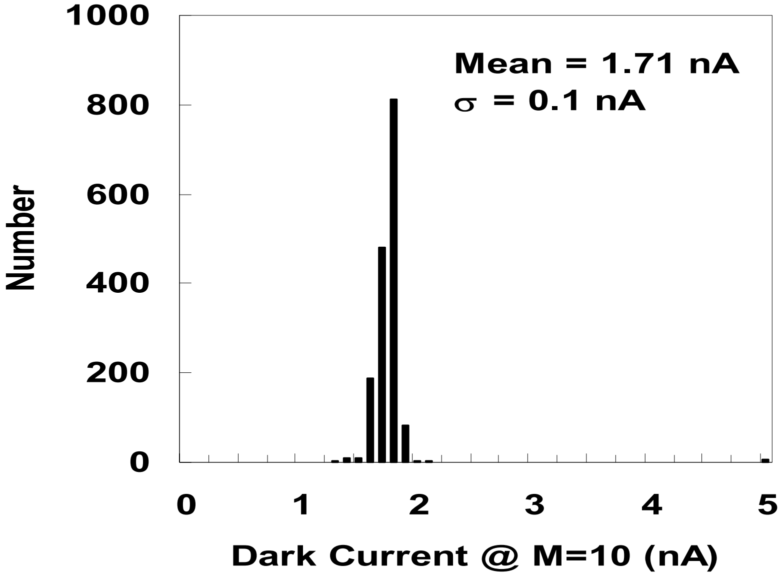

Fig. 7.19 Histogram of the dark current at a gain of 10 for the 1600 elements of the 40x40 APD array.

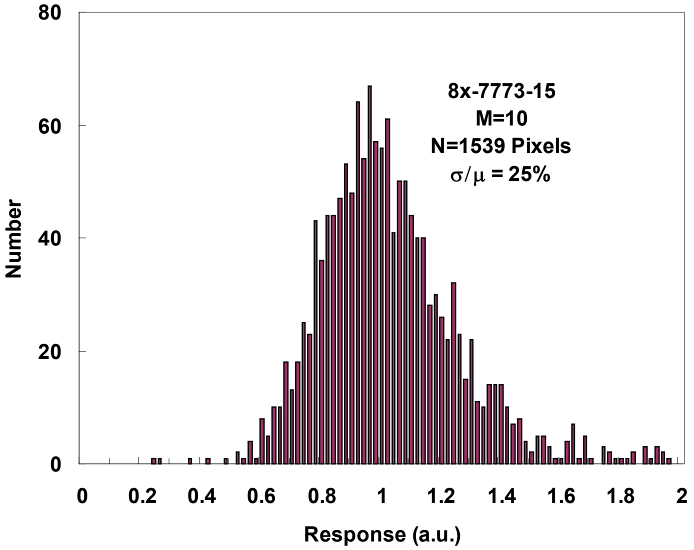

Fig. 7.20 The optical response uniformity for a 40x40 APD array.

7.7 Summary

A 12 × 12 $In_{0.53}Ga_{0.47}As/In_{0.52}Al_{0.48}As$ SACM avalanche photodiode array has been demonstrated. The APDs exhibited uniform distributions of breakdown voltage, photo response, dark current, and multiplication gain. The measured external quantum efficiency was above 40% within the wavelength range from 1.0 μm to 1.6 μm, ~57% at 1.3 μm and ~45% at 1.55 μm, respectively. However, the speed performance in terms of gain-bandwidth product, was <30GHz and lower than the expected values for a 200-nm-thick InAlAs multiplication region. To solve this problem, a new 18 × 18 focal-plane APD array was developed with improved speed performance, a bandwidth of ≥8GHz at low gains and a gain bandwidth product of ≥120GHz have been achieved. Furthermore, a 40×40 pixels APD array was demonstrated using MOCVD-grown wafers. This APD array exhibited higher device yield, lower dark current level, and improved dark current uniformity, due to improved material quality. More distributed APD gains (~25% at gain of 10), in comparison with MBE-grown APD arrays (~9% at gain of 22), may be attributed both to variation of InAlAs multiplication layer thickness and fluctuation of the total charge amount in the charge layer.

Chapter 8

Long-Wavelength $In_{0.53}Ga_{0.47}As$/ $In_{0.52}Al_{0.48}As$ Large-Area APDs

$In_{0.53}Ga_{0.47}As/In_{0.52}Al_{0.48}As$ avalanche photodiodes have been widely studied for optical communication applications. Most of the research efforts emphasized improving speed performance, in terms of gain-bandwidth product, by reducing device size in order to overcome the RC time limit and meet the strong demand of 10~40Gb/s system applications. However, optical measurement systems that operate in the eye-safety wavelength range (~1.5μm) require long-wavelength, high-sensitivity photodiodes with a large detection area. Furthermore, as was discussed in Chapter 7, three-dimensional infrared imaging systems require APD arrays that operate in the short wavelength infrared (SWIR) range ($0.8\mu m \leq \lambda \leq 2.2\mu m$) and have gigahertz bandwidths.

All these requirements create exciting challenges for epi-layer quality and device passivation on the InP-based material system. Large defect densities introduced during material growth (MBE or MOCVD) generate high bulk leakage current [8-1], severe micro-plasma-induced speed degradation [8-2], and poor device reliability for large-area APDs and arrays [8-3]. Sidewall passivation quality is critical to the APD dark current since sidewall leakage current constitutes a significant part of the total dark current, without proper passivation [8-4]. A 100μm-mesa-diameter InAlGaAs-InAlAs super-lattice APD integrated with a 200μm diameter microlens has been reported for eye-safety optical measurement purposes [8-5]. To the best of our knowledge, long-wavelength APDs with larger mesa area have not yet been reported.

Here I present large-mesa-area $In_{0.53}Ga_{0.47}As/In_{0.52}Al_{0.48}As$ long-wavelength APDs that exhibited high multiplication gains, high-gain bandwidth products, and low dark current densities. APDs with mesa diameters up to 500μm have demonstrated multiplied dark current densities $\leq 2.5\times10^{-2}$ nA/μm^2 at 90% of the breakdown. This large-area APD array also exhibited a gain-bandwidth product >120 GHz. Origins of the dark current were analyzed based on the measured results, and primary dark current was dominated by the thermal-generation current induced by deep-level traps in the bulk $In_{0.53}Ga_{0.47}As$ absorber.

8.1 Device Structure Design and Material Growth

A separate absorption, charge, and multiplication (SACM) APD structure was utilized for the large-area device studies, since this type of device structure exhibits low dark current, low multiplication noise, and high speed if the device parameters are properly optimized. Fig. 8.1 shows the detailed device structure used for the large-area APD study. This type of device structure has been successfully used in the previous focal-plane APD array studies, as presented in Chapter 7.

The APD wafer was grown by molecular beam epitaxy on an *n*-type InP (100) substrate. The control over layer composition, thickness, and dopant density afforded by epitaxial growth allows several refinements in the APD design that are not possible to implement in homojunction APDs formed by standard dopant diffusion techniques. The low bandgap material necessary to receive the long-wavelength (1000–1700 nm) light is susceptible to leakage via inter-band tunneling when placed under strong bias. This source of dark current can be suppressed by isolating the low bandgap material in a dedicated absorption layer, in which the electric field is moderated by an adjacent charge layer. A second advantage of epitaxial growth is the ability to accurately control the epi-layer thickness in order to grow a thin multiplication layer, so as to produce spatial modulation of impact ionization events, thereby suppressing multiplication noise [8-1], [8-6]. However, these advanced designs typically involve multiplication layers on the order of 150 - 200 nm thick, supporting electric field strength above 700 kV/cm.

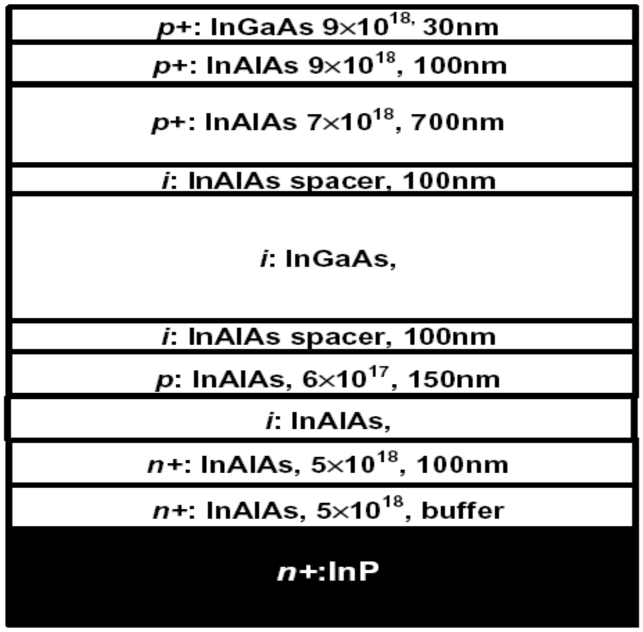

Fig. 8.1 Device structure for the large-area APD study

Consequently, small variations in epi-layer thickness caused by rough growth can have a large impact on device performance. In particular, premature breakdown can occur at thin spots in the multiplication layer, allowing excessive dark current to pass through the conductive micro-plasmas. Growth of smooth layers of uniform thickness is therefore essential.

8.2 Device Processing

Device processing began with *p*-type ohmic contact formation. A Cr (25 nm)/Au (85 nm) film was deposited by E-beam evaporation onto the heavily-doped $In_{0.53}Ga_{0.47}As$ cap layer. The contacts were patterned with standard photolithography and lift-off processing. A SiO_2 etch mask was then deposited by PECVD and mesa etch patterns were defined. The SiO_2 etch mask was used to ensure mesa pattern uniformity and smooth mesa edges. Mesas of different diameters (from 20μm to 500μm) were etched in phosphoric etchant (H_3PO_4:H_2O_2:H_2O = 1:1:8) to the n^+ InP buffer layer. After mesa etching, both the photoresist and the SiO_2 mask were removed. The wafer was quickly transferred to the PECVD chamber where a thin film of SiO_2 (~150 nm) was deposited for sidewall passivation. A Ni (20 nm)/AuGe (30 nm)/Au (80 nm) film was deposited by E-beam evaporation onto the InP buffer layer in order to form a common *n*-type ohmic contact.

8.3 Device Characterization and Discussions

8.3.1 Large-area InGaAs/InAlAs APDs

Most of the APDs exhibited relatively uniform I-V characteristics after processing. The punch-through voltage was ~15.0V, and the breakdown voltage was ~39.2V. The typical photoresponse and dark current curves of a 500μm-diameter APD are shown in Fig. 8.2.

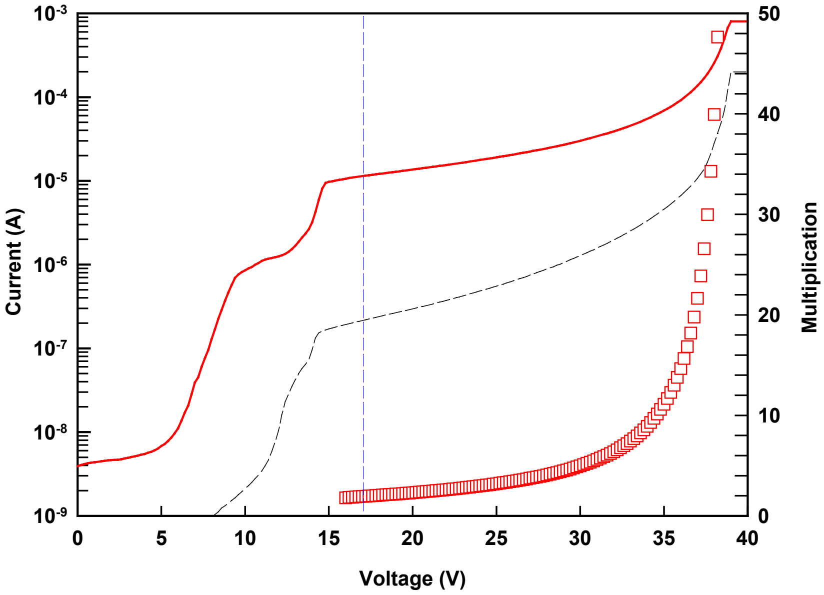

Fig. 8.2 Typical photo/dark current curve for a large-area (500μm diameter) APD

The photocurrent curve of the APD exhibited an obvious slope after punch-through, which might indicate multiplication gain at punch-through [8-1]. In order to characterize the multiplication gain, external quantum efficiencies were measured under different bias conditions above the punch-through voltage, using a tungsten-halogen light source, a spectrometer, and a lock-in amplifier. At a bias voltage of 16.0V, the APD was fully depleted and the measured external quantum efficiency was ~85% at a wavelength of 1.55μm, as shown in Fig. 8.3. The expected external quantum efficiency of an APD at unity-gain can be estimated by the following expression:

$$\eta_{ext} = (1 - R) \cdot (1 - e^{-\alpha \cdot d}) \tag{6.4}$$

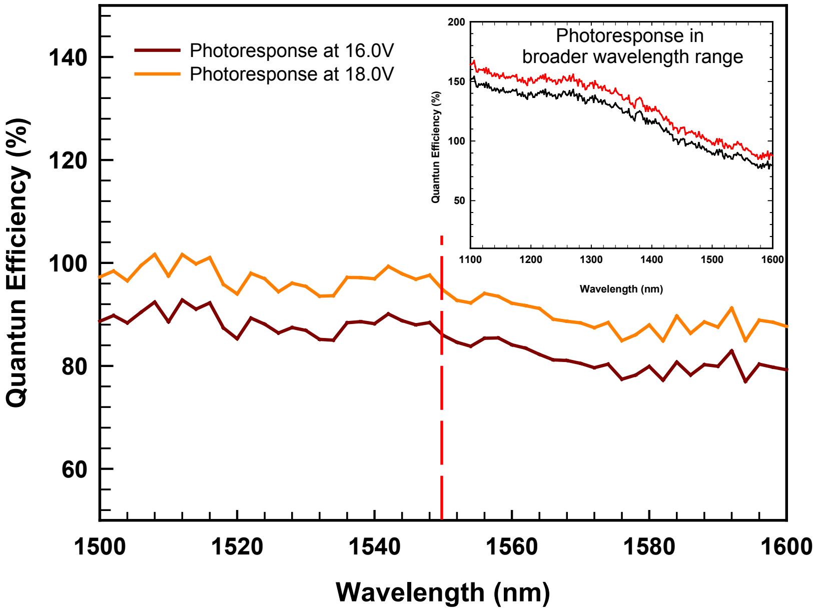

Fig. 8.3 Typical external quantum efficiency at a bias voltage of 16.0V and 18.0V

where R is the reflection coefficient of the air-semiconductor interface; α is the absorption coefficient of $In_{0.53}Ga_{0.47}As$ at the relevant incident wavelength; and d is the absorption layer thickness. For a SACM APD, with a 1.5 μm-thick $In_{0.53}Ga_{0.47}As$ absorber that has an absorption coefficient (α) of 0.705 μm^{-1} at 1.55 μm [8-7], [8-8], the expected external QE is ~46% at 1.55μm assuming an optical transmission of 70% (R=0.3) at the air-semiconductor interface. The measured value (~85%) is 1.8 times higher than the expected quantum efficiency value (~46%). We attribute this large quantum efficiency to the gain at punch-through, and the gain at a bias voltage of 16.0V is calculated as 1.8, without overestimation. The assertion of multiplication gain at punch-through can also be corroborated by electric field strength analysis. At a reverse bias voltage of 16.0V, the electric field in the $In_{0.52}Al_{0.48}As$ multiplication region can be estimated as ~580kV/cm using the simple depletion approximation, assuming a 200nm $In_{0.52}Al_{0.48}As$ un-doped multiplication region and a 150nm *p*-type (6×10^{17} cm^{-3}) $In_{0.52}Al_{0.48}As$ charge region. This calculated value of electric field strength agrees well with the published homo-junction APD result [8-9], from which the electric field strength in the 200nm-thick multiplication region of an $In_{0.52}Al_{0.48}As$ APD at a gain of 1.8 can be inferred as ~560KV/cm.

The gain of the APD was then calculated using the following expression:

$$M^* = \frac{I_p - I_d}{I_{pu} - I_{du}}, \quad M = M_0 \cdot M^* \tag{6.5}$$

where M_0 is the gain factor determined by a quantum efficiency measurement at the specific reference bias voltage after punch-through (e.g. 16.0V). I_p and I_d are the photocurrent and dark current for bias values above the reference voltage; I_{pu} and I_{du} are the primary photocurrent and dark current at the reference voltage. M^* is the gain from the I-V measurement and M is the final calculated gain of the APD. The calculated gain curve of a 500μm-diameter APD was plotted on Fig. 8.2, and all the APDs with mesa diameters ranging from 20μm to 500μm exhibited gain values greater than 40, at a reasonably low dark current level.

8.3.2 APD Surface Leakage Current

Even though thin multiplication region avalanche photodiodes provide low multiplication noise and high gain-bandwidth products due to non-local impact ionization effects, the APD dark current is a very critical performance parameter. This due to the fact that the gain is increased until the APD noise is comparable to that of the following circuitry. Consequently, the dark current is a determining factor in the signal to noise ratio.

Previously, dark current studies of SACM APDs primarily focused on sidewall passivation quality and various device passivation techniques, such as sidewall passivation using PECVD deposited SiN_x films [8-10] and SiO_2 films [8-3], polymide-based materials [8-11], and even BCB-based materials [8-3], to achieve low surface leakage current density. Even though recently published results have shown that the surface leakage current, if properly passivated, could be negligible in comparison to bulk material related dark current [8-3], the nature of this bulk-related dark current was not very clear.

To examine the dark current dependence on surface passivation, dark currents of APDs with different mesa sizes were characterized at room temperature with a HP 4145B semiconductor parameter analyzer, as shown in Fig. 8.4. The dark current of the 30μm-diameter APD was compared to previous results [8-3], [8-10], [8-11]. The value of the measured dark current at a bias voltage of 35.2V (90% of breakdown, gain >10) was ~26.7nA, which is much less than that of the SiN_x-passivated APDs (0.7μA/30μm by Kagawa et al, 0.41μA/30μm by Kim et al, and 0.4μA/80μm by Makita et al), the polyimide-passivated APDs (67nA/30μm by Kim et al), or the BCB-passivated APDs (38nA/30μm reported by Kim et al).

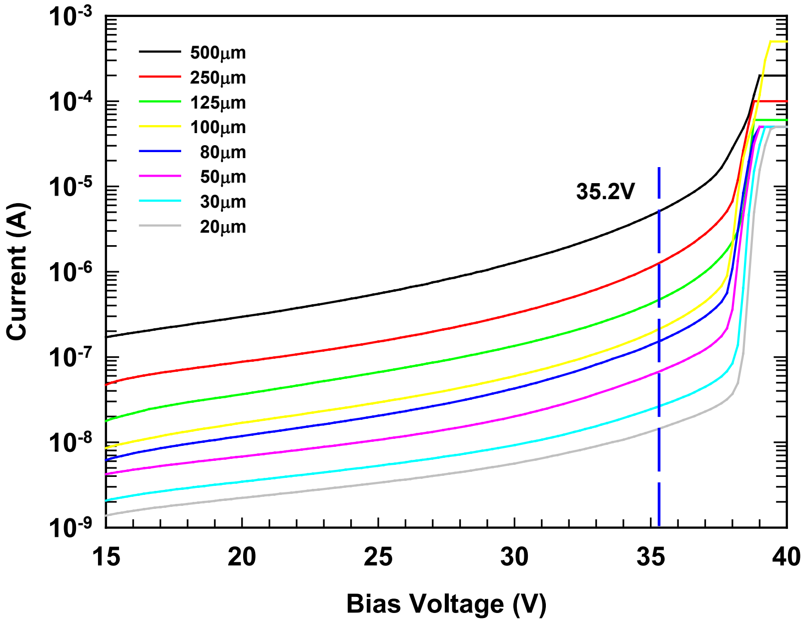

Fig. 8.4 Typical dark current curves from APDs of various diameters

The APD dark current can be divided into two categories by the leakage path: the bulk leakage current, which is proportional to the mesa area, and the sidewall leakage current, which is only proportional to the mesa perimeter, neglecting the mesa sidewall curvature caused by wet etching. The total dark current can be expressed as:

$$I_{total} = J_{sidewall} \cdot \pi \cdot d + \frac{J_{bulk} \cdot \pi \cdot d^2}{4} \tag{8.6}$$

where J_{sidewall} is the sidewall leakage current density (A/m), and J_{bulk} is the bulk leakage current density (A/m^2). The measured dark currents were fitted to the mesa diameter using a quadratic fit at a bias voltage of ~35.2V (90% of the breakdown), as shown in Fig. 8.5.

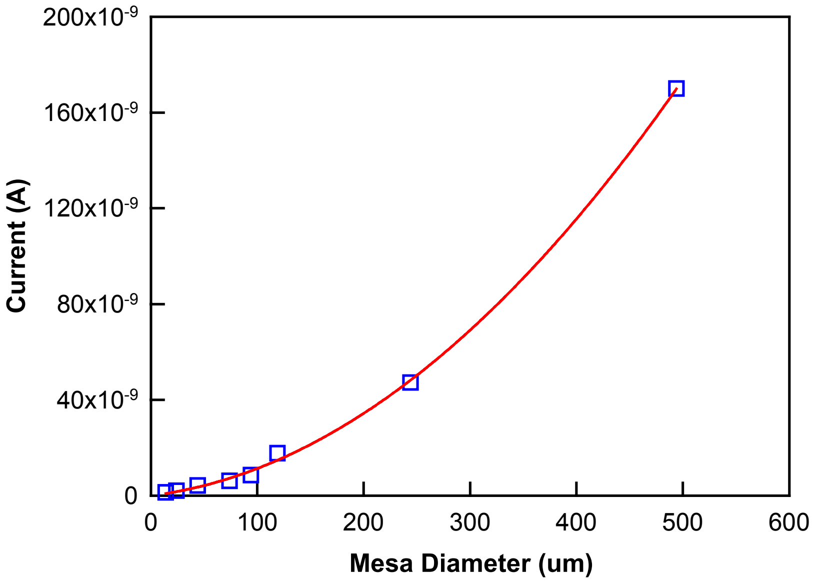

Fig. 8.5 Dark current as a function of the device diameter, at a bias of 16.0V

An almost perfect quadratic fit was achieved, thus the bulk leakage current was found to be dominant for large area devices. The fitted surface dark current density J_{sidewall} was 0.19nA/µm, and the bulk dark current density was 0.023 nA/µm^2 at 90% of the breakdown voltage. The dark current can be also divided into two components by the multiplication mechanism: the multiplied dark current that flows through the bulk and the un-multiplied dark current that normally flows through the mesa sidewall, as expressed in the following equation:

$$I_{total} = I_{un-multiplied} + I_{multiplied} \cdot M \tag{8.7}$$

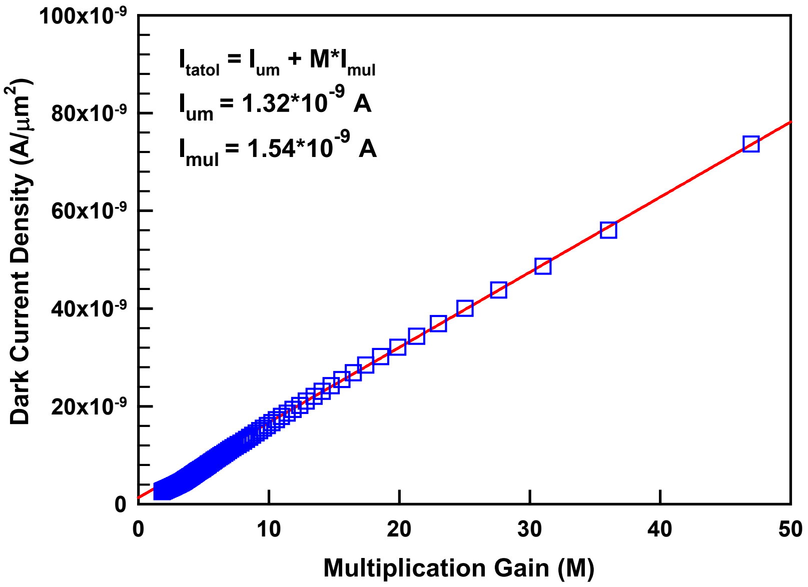

Fig. 8.6 APD dark current as a function of the multiplication gain

The dark current of a 100μm-diameter APD was fitted with the above equation, as shown in Fig. 8.6. The un-multiplied dark current (density) was ~1.32nA (4.2pA/μm) and the multiplied dark current was ~1.54nA. The dependence of dark current on gain remains linear even at gains of 50. The un-multiplied dark current (density) is rather small compared to the multiplied dark current component and is negligible for APDs biased at high gains.

The spatial photoresponse profile of the large-mesa-area APD was measured by the raster-scanning technique. A 1.5-μm-wavelength He-Ne laser beam with a beam-waist <5um was scanned across a 500μm-diameter APD at a bias voltage of 36.8V (gain≥20). A flat, uniform photoresponse profile was obtained across the entire device mesa area, as shown in Fig. 8.6. No obvious photoresponse peak was found around the mesa edge at high gains, which indicates that the electric field strength at the mesa edge is not approximately equal to that in the mesa bulk region, thus no strong evidence of edge-breakdown has been observed.

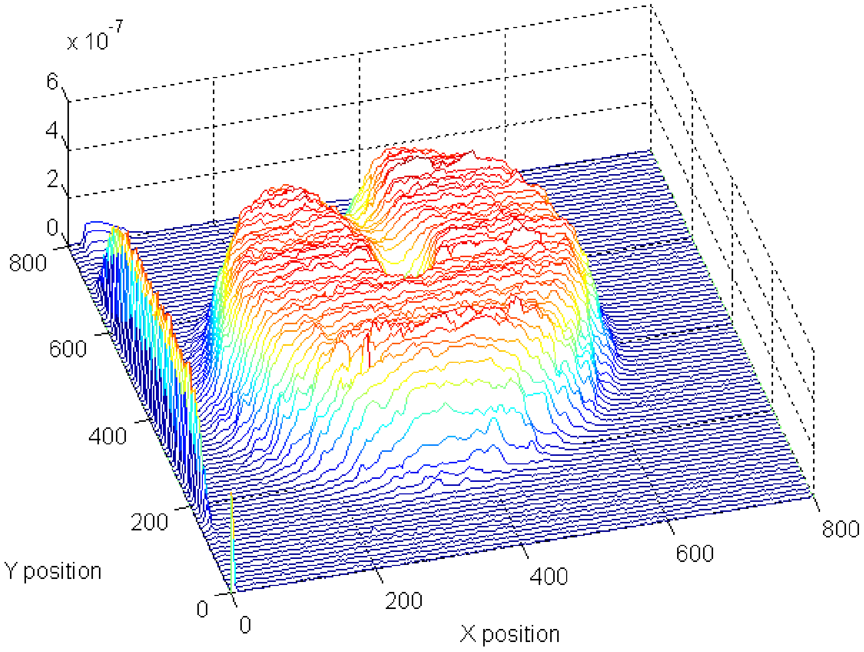

Fig. 8.6 Spatial distribution of the photoresponse, by 2-D raster scanning

8.3.3 Dark Current Dependence on Surface Morphology

Dark current dependence on surface morphology was also examined using SACM APD structures, in collaboration with A. Hungtinton, et al, at UCSB. The SACM APD wafer design was based on the considerations discussed in previous chapters. Several $In_{0.53}Ga_{0.47}As/In_{0.52}Al_{0.48}As$ SACM APD wafers, in which three variants of multiplication layer thickness were utilized, were grown and categorized by wafer surface morphology conditions. Five of the resulting wafers were selected for the morphology study. These five wafers, labeled #1 to #5, cover the full range of morphology conditions. Detailed information about each wafer is listed in Table 1.

Sample	M-layer Thickness (Å)	Defect Density (cm^{-2})	Roughness ΔZ/RMS (Å)	Dominant Morphological Feature
#1 (021029D)	2000	150	99.3/10.5	-
#2 (021029C)	2000	200	392.9/48.6	Moderate μ-roughness
#3 (021028A)	2000	200	461.5/70.6	Severe μ-roughness
#4 (021029E)	1500	4,000	255.9/44.0	loading dust
#5 (021028B)	1500	> 10,000	415.4/51.9	desorption defects

Table 1 Surface morphology of SACM APD wafers, after MBE growth

Defect density, as listed in the second column, was estimated by visual inspection of defect counts on the wafer surface, using a Nomarski microscope. Defect assignments were obtained through a combination of inference based on variations in growth conditions and direct inspection via AFM, as illustrated in Fig.8.7 (a) through (c).

From surface morphology observations, at a growth temperature of 500°C, optimal surface conditions were obtained from sample #1, which was grown under 8×10^{-6} Torr of arsenic pressure, as shown in Fig. 8.7 (a). However, a metal-rich polycrystalline surface, was obtained from using a lower arsenic pressure (4×10^{-6}

Torr) (Fig. 8.7(b)), and significant three-dimensional islanding was observed using a higher arsenic pressure (1.2×10^{-5} Torr) (Fig. 8.7(c)).

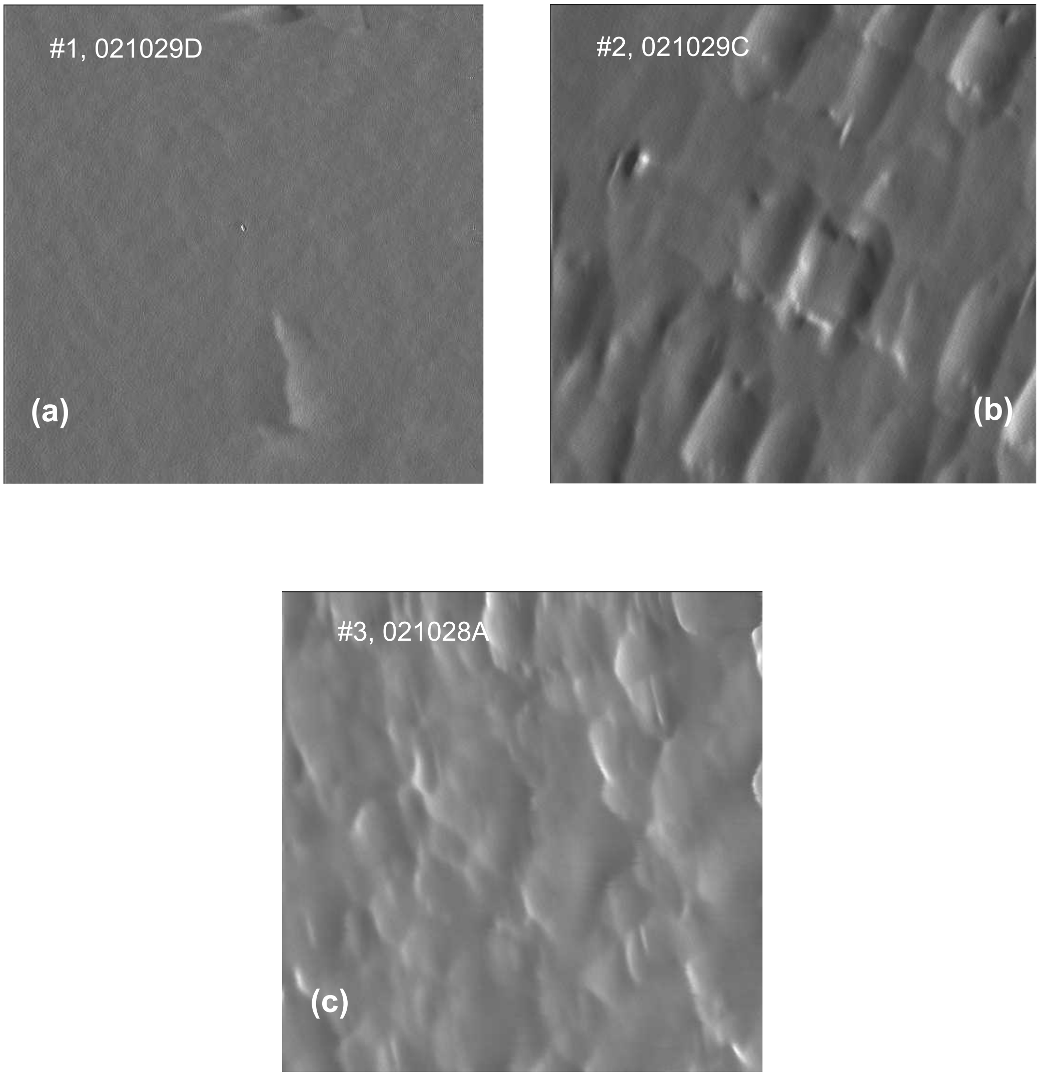

Fig. 8.7 Illustration of various morphology conditions of SACM APD wafers, (a) 021029D, (b) 021029C, (c) 021028A

Devices obtained from five wafer samples were carefully measured to quantify the relationship between surface roughness and leakage (dark) current, and devices from all these wafers were grouped into three different sets to characterize APD dark current properties.

Wafer #1, #2, and #3 were included in the first device set, in which the APD multiplication region thickness was similar (200nm) but the wafer surface morphology was different. Devices with a moderate mesa diameter (125µm) were used to represent typical APD behaviors, since the mesa size is large enough to include enough defects, if present. The qualitative relationship between surface roughness and leakage current can be found in Fig. 8.8. In ascending order, samples #1, #2, and #3 cover the entire roughness range in this study. It is quite clear from this observation that surface roughness is strongly correlated to dark current levels.

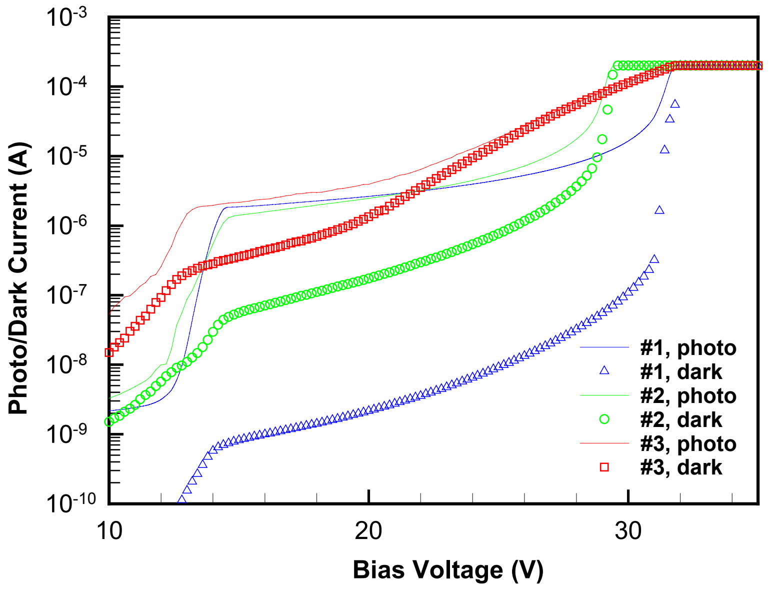

Fig. 8.8 Dark current dependence on surface roughness of SACM APD wafers

A more quantitative investigation of this behavior can be obtained by examining the dark current under similar device testing conditions, such as at unity gain. When I_{dark} is plotted versus peak-to-peak roughness, an approximately exponential dependence can be fitted, as shown in Fig. 8.9.

So far, only the impact of roughness on the dark current characteristics of devices from wafers with different surface morphologies has been compared. A complete study of surface roughness requires an understanding of how the wafer surface condition causes device performance variation across a single wafer. Thus, 15 devices each from wafers #4, #2, and #5 were measured in order to investigate performance uniformity. For this study, the 125µm diameter devices were selected to exclude gross defects, in order to isolate the effects of surface roughness.

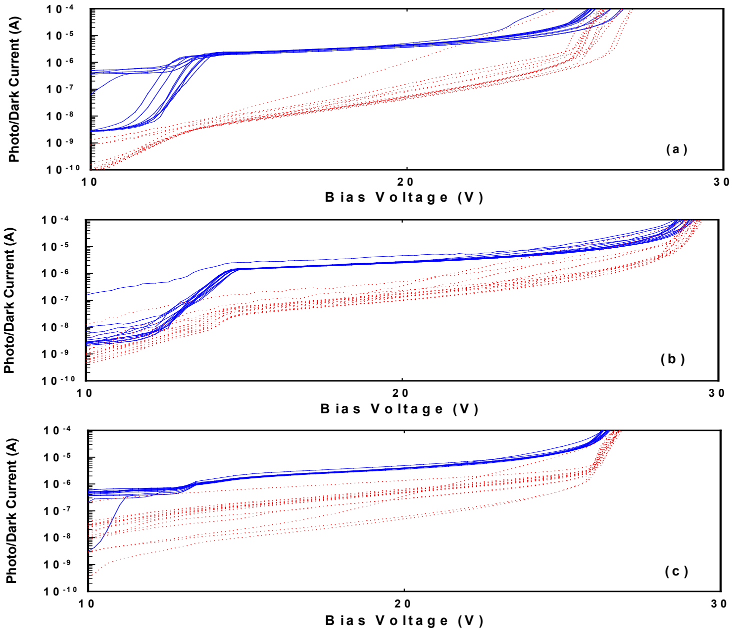

Fig. 8.10 I-V characteristics of 15 devices, from wafer (a) #4, (b) #2, and (c) #5.

It appears that, in addition to the degraded mean dark current value, large variations in surface roughness also increase the spread in the dark current distribution across an entire wafer, as shown in Fig. 8.10 The observation that I-V characteristics become more scattered for rougher wafers is further strengthened by the previous APD array study. Although those APD focal-plane array results did not directly address the issue of roughness, the APD array in question was fabricated from a relatively smoother wafer (similar to sample #1), and the standard deviation of the dark current at punch-through was ~10%, a fraction of the mean value, compared to 42% for sample #4, 61% for sample #2, and 90% for sample #5, as tabulated in table 2.

Sample	RMS Roughness (Å)	$\langle I_{dark} \rangle$ at M = 1	σIdark	$\frac{\sigma_{Idark}}{\langle I_{dark} \rangle}$
Array	~ 10.5	2.00 nA	0.19 nA	9.5%
#4	44.0	9.38 nA	3.96 nA	42.2%
#2	48.6	53.57 nA	32.47 nA	60.61%
#5	51.9	191.18 nA	172.88 nA	90.43%

Table 2 Surface morphology impacts on device variation in a SACM APD wafer

A third set of 250μm-diameter devices, 30 devices in each group from wafers #2, #4, and #5, were examined to observe the affects of defects, originating from either dust or a bad desorption procedure, on device performance. Devices with larger diameters were also investigated in order to potentially include more defects generated from either the initial substrate, further material growth, or the final device processing steps. The 250 μm devices from the data set had a large enough area and were measured in sufficient numbers to provide a range of how the two types of defects affect final device yield. All three wafers suffer to varying degrees from surface roughness, but beyond this, two distinct failure mechanisms are apparent in the I-V characteristics, as shown in Fig. 8.11.

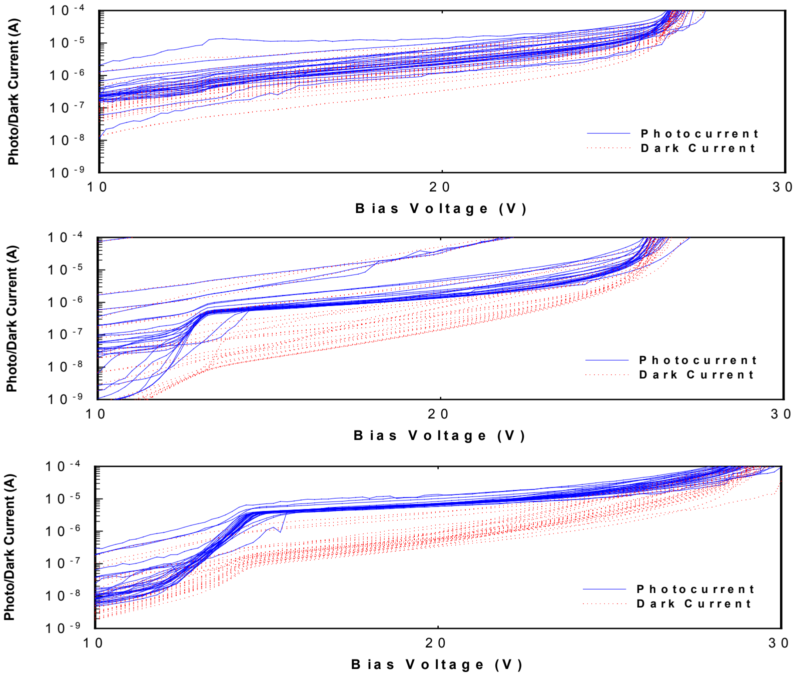

Fig. 8.11 DC characteristics of samples #2 (top), #4 (middle), and #5 (bottom).

Sample #4, which had the highest density of dust-related defects, produced a number of devices that failed to behave like photodiodes. These devices pass high current at low voltage and are insensitive to illumination, which are essentially caused by shorts. Sample #5 has at least one short in it, while the great majority of its devices have photodiode-like I-V characteristics, but with extremely high dark current. This behavior, characterized by preservation of the basic APD I-V curve shape but with excessive leakage, is similar to that associated with extreme roughness.

The failure mechanisms associated with the two different types of defects can be attributed to their structural differences. As revealed by AFM, cratering caused by dust tends to pierce the entire epitaxial structure, creating an alternative current leakage path that shorts the entire APD structure. That is why dust-related failures do not preserve the basic shape of an APD I-V characteristic. On the other hand, desorption defects look more like a patch of hyper-roughness under the AFM. It seems plausible that they would have an analogous effect upon device performance. Fortunately, the influence of these defects is limited only to their immediate area. Functional devices can be obtained from wafers with a relatively high defect density by fabricating small-diameter devices.

In summary, precise control of the growth conditions that create surface is extremely critical in the growth of good quality SACM APD wafers, especially for those with very thin multiplication layers (e.g. <200-nm). In APDs with thick multiplication layers, surface roughness will result in relatively minor variations in electric field strength over the area of the thick multiplication region. When the peak-to-peak roughness of epi-layers approaches similar dimensions to the multiplication layer, it might become the deciding factor in the final device characteristic, particularly for a high-speed focal-plane APD array with a thin multiplication region.

8.3.4 Modeling of InGaAs/InAlAs APD Dark Currents

APD dark current has been a big issue for both InGaAs-InAlAs APD design and fabrication. If too high, the dark current will degrade the achievable APD sensitivity by increasing minimum detectable signal level at high gains. Based on previous experimental results, a preliminary picture of APD dark current was developed, as shown in Fig. 8.12, in which APD dark current mechanisms are illustrated.

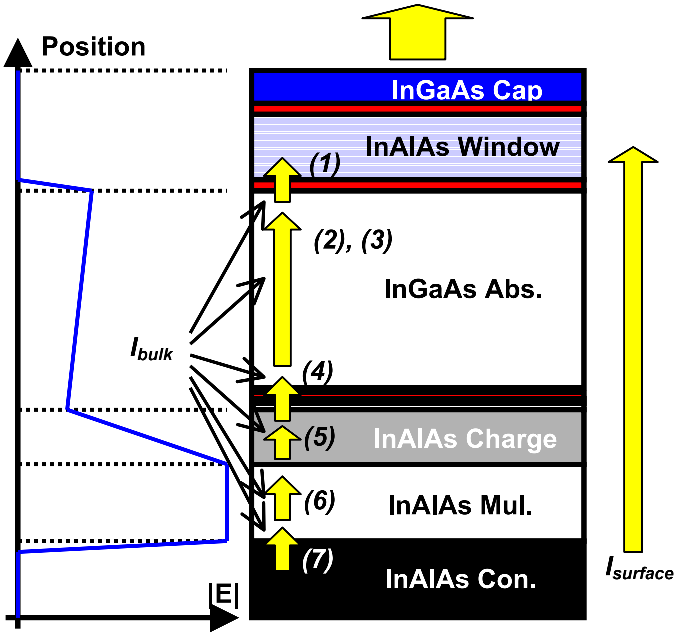

Fig. 8.12 Possible dark current sources of an InGaAs/InAlAs SACM APD

Theoretically, the main contribution to the APD dark current comes from thermal generation in the depleted intrinsic region. At room temperature, a dark current density of ~ 10^{-7}A/cm^2 would be expected from an InGaAs-InAlAs APD, if only band-to-band thermal generation is considered. Practically, however, a dark current density of ~10^{-5}A/cm^2 is usually observed. A bump close to the punch-through voltage on the dark current curve is always observed at room temperature, as shown in Fig. 8.13. This may be a clue to isolating the exact source(s) of the observed excess dark current density.

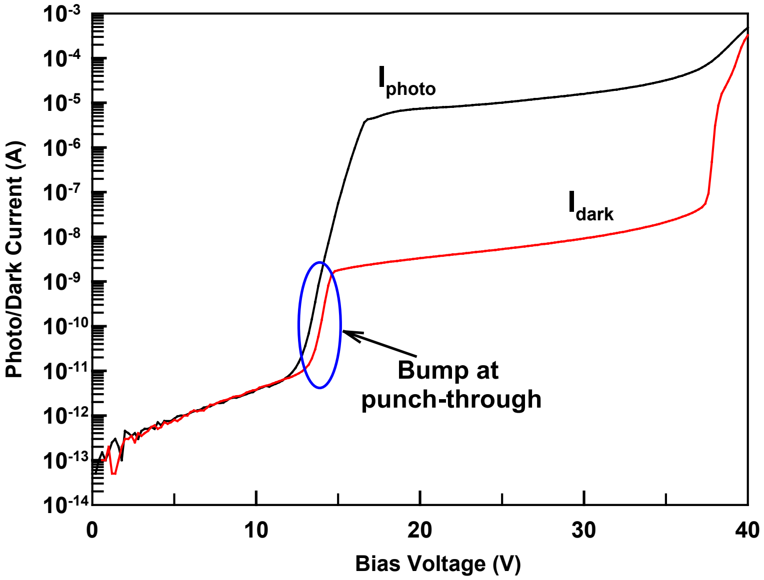

Fig. 8.13 Bump on the dark current curve of an InGaAs/InAlAs SACM APD

Dark current originates from various sources, as categorized in equation (8.8), which can be found in many semiconductor textbooks

$$\begin{aligned} I_{d,tot}(T) &= I_{diff}(T) + I_{thermal-gen}(T) + I_{bulk-trap}(T) + I_{interface-trap}(T) \\ &+ I_{surface}(T) + I_{tunneling}(T) + I_{defect}(T) + \ldots\ldots \end{aligned} \tag{8.8}$$

In this equation, all dark current components are functions of ambient temperature, and they all have distinguishing signatures as a function of temperature. Diffusion currents $I_{diff}(T)$, or more precisely, reverse generation currents, which exist in the heavily-doped, neutral *p*- and *n*-InAlAs contact regions (region 1 and 7 in Fig. 8.12), constitute a negligible component of the total APD dark current. Tunneling current $I_{tunneling}(T)$, either in the narrow bandgap InGaAs absorption region (regions 2 and 3) or in the thin InAlAs multiplication region (region 6), is a minor dark current source if the electric field profile in the APD is optimized. Also, since tunneling current has a specific exponential signature, it can be easily identified if it exists. The surface leakage, if the device is not passivated well, may comprise a large component of the total dark current. Proper device passivation, either using silicon dioxide or BCB polymers, could reduce the leakage current to an insignificant contribution, as corroborated previously in 8.4.2. Defects, either by dust or improper desorption, could also generate large dark current levels in an APD. With optimized growth conditions and proper device processing, obtaining a defect-free device is quite feasible.

Trap-assisted thermal generation might be responsible for the bump on the dark current curve. To verify this, APD dark current was measured at elevated temperatures (25^{o}C to 150^{o}C) to observe the dependence on ambient temperature. Here elevated temperature is preferred over low temperature because incomplete dopant ionization at low temperatures might occur, which would decrease the total charge amount in the charge layer. As a result, at a fixed bias above punch-through, the APD gain increases as does the multiplied dark current. Temperature induced gain variation at a fixed bias voltage complicates experimental data acquisition and further data analysis. At a moderate elevated temperature less than 200^{o}C, the APD gain at punch-through remains nearly constant. The measured APD dark current as a function of the temperature is plotted in Fig. 8.14.

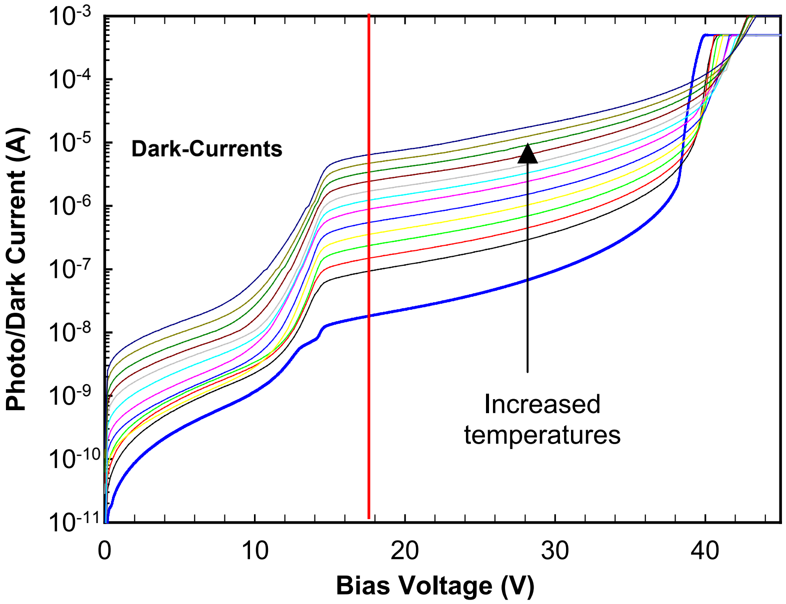

Fig. 8.14 Dark current temperature dependence of InGaAs/InAlAs SACM APDs

The temperature dependence of the APD dark current demonstrated that the logarithm of the dark current densities were proportional to the inverse temperature, as shown in Fig. 8.15. As temperature increases, higher thermal generation rates, which are exponentially dependent on the ambient temperature, cause higher dark current levels. Further fitting of the extracted data from the temperature measurements was done using a thermal emission current model, which indicated that the APD dark currents primarily originated from thermal generation originated. The extracted average activation energy of traps, which might be generated during MBE growth, was approximately ~0.45eV.

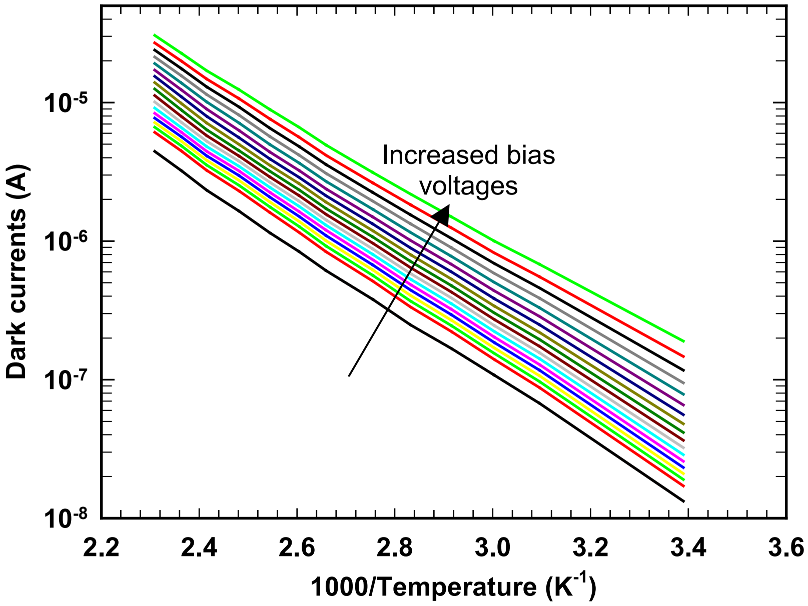

Fig. 8.15 InGaAs/InAlAs APD dark current as a function of 1000/T

To better understand the origin of the bulk leakage current, a new set of SACM APD structures were fabricated. These APD structures have the same multiplication layer thickness (200 nm) but different absorption layer thickness, 1.0μm (sample A), 1.3μm(sample B), and 1.5μm (sample C). In these wafers, digital alloy transition layers were also incorporated in InAlAs-InGaAs interfaces to smooth carrier transport across the hetero-junction. The electric field in the multiplication region in these devices was similar at punch-through. Two other samples, one with a 1.3μm-thick absorber (sample D) and another with a 1.5μm-thick absorber (sample E), were also grown as reference wafers for samples A through C, but without incorporating digital alloy transition layers. All these samples were grown in growth runs close to each other, in order to obtain the most consistent epi-layer quality among wafers. Simple mesa devices were processed using conditions discussed previously, and the dark currents were measured from those devices at room temperature. A nearly linear relation between the dark current density and the InGaAs absorber thickness, as shown in Fig. 8.16, was observed from three different wafers. Devices from the other two wafers exhibited excessive dark current densities, probably due to inferior wafer quality. This result indicated that trap-induced thermal generation currents, from which the main constituent of the total InGaAs/InAlAs APD dark current was comprised, are bulk-related in the $In_{0.53}Ga_{0.47}As$ absorption region.

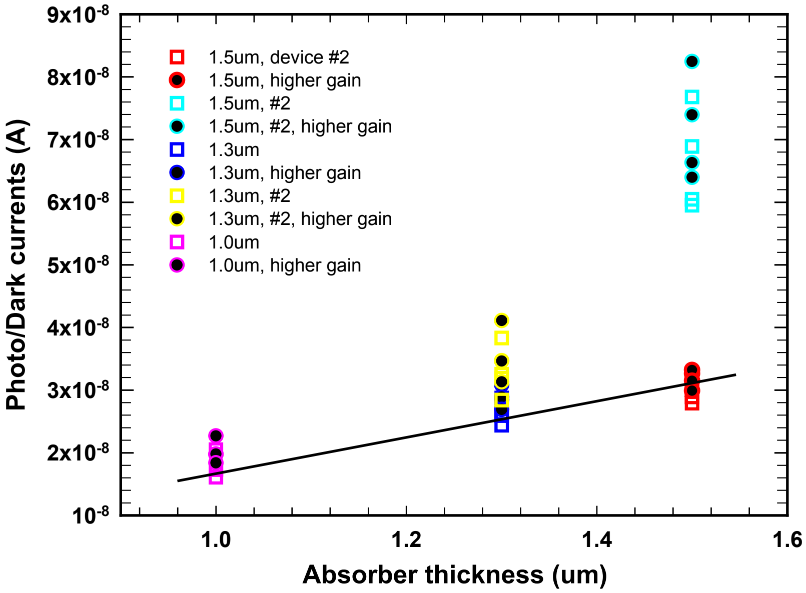

Fig. 8.15 InGaAs/InAlAs APD Dark current dependence on absorber thickness

8.4 Summary

Large-area $In_{0.53}Ga_{0.47}As/In_{0.52}Al_{0.48}As$ APDs for eye-safe optical signal detection applications, with a mesa diameter of 500μm, have been demonstrated at room temperature. These devices exhibited a very low dark current density of $\sim 2.5\times10^{-2}$nA/μm^2 at 90% of breakdown. Very low surface leakage current density (~4.2pA/μm) was achieved with wet chemical etching and SiO_2 passivation. Further investigation and analysis of the dark current has shown that, APD bulk leakage current, which is a dominant part of the total APD dark current, originates from the thermal generation assisted by deep-level traps in the $In_{0.53}Ga_{0.47}As$ absorber.

Chapter 9

InGaAs/InAlAs APDs for 10Gb/s Telecom Receivers

Even though Erbium-doped fiber optical amplifiers (EDFA) are gradually becoming a prevailing component for high-bit-rate (≥OC-192) long-haul optical links, important application sectors such as metropolitan optical transmission (10Gb/s) still require low-cost optical receivers to provide optical links at a moderate link-span (e.g. less than 100 kilometers) [9-1]. For this reason, there still exists a strong push from the telecommunication market to improve the compactness and cost-effectiveness of conventional optical receiver technology, in which photodetectors and the subsequent electrical amplifiers are integrated. Since an integrated APD optical receiver usually provides at least a 5dB sensitivity improvement over a *p-i-n* integrated receiver, research on high sensitivity 10Gb/s integrated APD receivers for OC-192 related applications continue. As a consequence, higher and higher APD receiver sensitivity results have been reported [9-2]~[9-5].

As discussed in previous chapters, low noise and high gain bandwidth product can be achieved by incorporating a thin mulitplication region in APDs [9-6]~[9-8]. Based on the previous focal-plane APD array studies, a 200-nm-thick InGaAs/InAlAs APD provided a gain-bandwidth product of more than 120GHz. It is very attractive to investigate the receiver sensitivity of the thin InGaAs/InAlAs APD combined with a low noise pre-amplifer and following amplitude-limiting amplifier. This use the focus of a collaboration between the University of Texas at Austin and Multiplex Incorporated, a telecommunication component company.

9.1 APD Device Structure Design

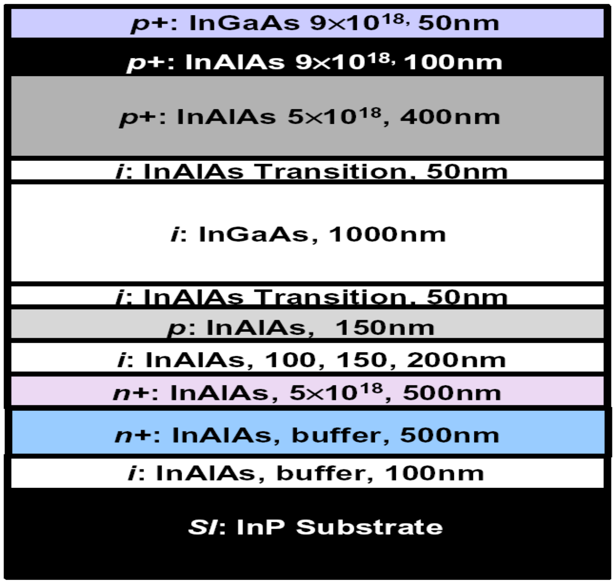

Fig. 9.1 Detailed device structure of the 10Gb/s InGaAs-InAlAs APDs

To investigate the 10Gb/s APD receiver sensitivity, a separate absorption, charge, and multiplication (SACM) APD structure was utilized, as shown in Fig. 9.1. APD bandwidth at low gains was estimated based on the saturation velocity model, as discussed in Chapter 2. As a result, a 1.0μm-thick absorbing layer was incorporated in the SACM APD structure to provide ≥ 8GHz bandwidth at low gains, which is primarily limited by the carrier transit time for small devices (e.g.

diameter ≤ 50μm). This ample bandwidth value relaxes the inter-symbol-interference (ISI) burden on the integrated APD receivers by providing open signal eye-patterns. To sustain an adequate bandwidth value at high gains, a thin InAlAs multiplication region was incorporated into these SACM APD structures. Thickness values of 100-nm, 150-nm, and 200-nm were utilized to provide a sufficiently high gain-bandwidth product (≥120GHz). As a consequence, acceptable bandwidths and moderately low excess noise levels at high gains, from these thin APDs, were expected to yield high APD receiver sensitivity.

The doping level of the 150-nm-thick charge layer in these SACM APD structures was optimized using the method discussed in Chapter 2 to obtain a reasonably low electric field strength (below 150KV/cm) in the InGaAs absorber, especially at high APD gains, in order to eliminate the possible carrier multiplication in the absorption region [9-9]. High electric field strength, e.g. > 180KV/cm in the absorption layer in combination with long path length results in level of impact ionization that greatly degrades both the excess noise level and gain-bandwidth product. On the other hand, to obtain a maximum bandwidth that is limited by the carrier transit time, a lower boundary of the electric field intensity value in the InGaAs absorber needs to be sustained (>45KV/cm, in my design) to guarantee that both electrons and holes are transported at their saturation velocities in the depleted InGaAs region.

Differing from previous APD gain-bandwidth investigations in our group, in which only the gain region characteristic (e.g. G-B product) was focused on while the APD absolute responsivity was not a critical concern, this receiver sensitivity study required APDs that exhibit high unity-gain responsivity as well as a high G-B product. Optical coupling thus becomes a very important issue in the APD device structure and the integrated receiver design, which greatly affects the ensemble sensitivity of the APD receiver. In my APD receiver design, a simple but effective optical coupling technique, the backside illumination scheme, was adopted to obtain high APD external quantum efficiency and to simplify the optical integration technology as well. Fig. 9.2 illustrates front-side (a) and backside (b) optical coupling scheme. For a 1.0μm-thick InGaAs absorber, using backside illumination will provide at least 1.49 times greater responsivity than front-side coupling at a 1.55μm wavelength, assuming a $0.707\mu m^{-1}$ absorption coefficient, perfect reflection at the reflecting metal surface, and the same anti-reflection coating at the semiconductor-air interface.

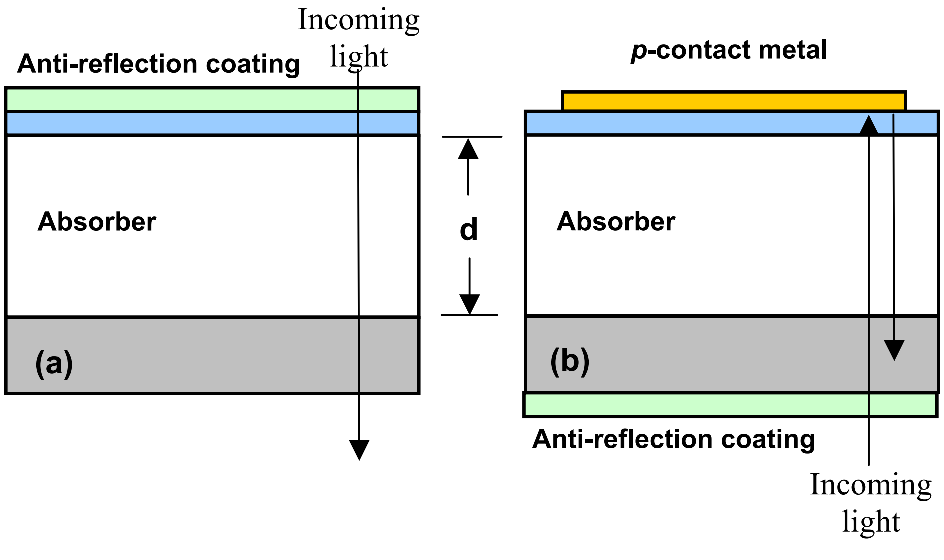

Fig. 9.2 Comparison of illumination from front-side (a) and backside (b)

9.2 Material Growth and Calibration

To obtain APD wafers that have an optimum charge layer doping level and the expected electric field profile, multiple wafer growth runs were performed at UCSB, using molecular beam epitaxy on semi-insulating InP (100) substrates. The composition of InP lattice-matched $In_{0.53}Ga_{0.47}As$ and $In_{0.52}Al_{0.48}As$ alloys was initially calibrated using x-ray diffractometry for each single wafer. The growth rate of the alloys was then calibrated by optical cavity measurements, and the wafer surface morphology was measured by AFM after each growth run. The substrate temperature was measured by optical pyrometry during the growth session. Starting from a substrate temperature of 500 °C and an arsenic beam flux of 1.2×10^{-5} torr, the substrate temperature was ramped to 570 °C in the span of 15 seconds to remove the surface oxide. The substrate was then immediately cooled to the growth temperature (500°C).

The first layer grown was a 100 nm-thick unintentionally doped $In_{0.52}Al_{0.48}As$ sacrificial layer whose function was to prevent silicon diffusion into the SI-InP substrate from the InAlAs *n*-contact layer, which could potentially cause extra parasitic capacitance between contact pads, changing the 50Ω characteristic impedance of the co-planar transmission lines. A 500 nm-thick heavily-doped n^+-type (silicon, $\geq 8 \times 10^{18}$ cm^{-3}) $In_{0.52}Al_{0.48}As$ layer was grown as a buffer layer and followed by another 500-nm n^+-type (silicon, $\geq 5 \times 10^{18}$ cm^{-3}) $In_{0.52}Al_{0.48}As$ layer, which was grown as an *n*-type contact layer. Following the *n*-type contact layer, an intrinsic $In_{0.52}Al_{0.48}As$ layer was grown with thickness of 100-nm, 150-nm, or 200-nm, in order to obtain APDs with different gain region thickness. Next, the charge layer, consisting of 150 nm, *p*-type (*Be*-doped) $In_{0.52}Al_{0.48}As$, was deposited. A 1000 nm-thick intrinsic $In_{0.53}Ga_{0.47}As$ layer, sandwiched between two 50 nm-thick unintentionally-doped $In_{0.52}Al_{0.48}As$ spacer layers, was grown as the absorbing layer. Extreme attention was paid to keeping the absorber background doping as low as possible during the MBE growth. This was followed by a 400 nm-thick *p*-type (*Be*-doped, 9×10^{18} cm^{-3}) $In_{0.52}Al_{0.48}As$ window layer. The *p*-type contact layers consisted of 100 nm of $In_{0.52}Al_{0.48}As$ (*Be*: $\geq 1 \times 10^{19}$ cm^{-3}) capped with 50 nm of $In_{0.53}Ga_{0.47}As$ doped at the same level.

As a result of multiple wafer growth runs on the UCSB side, which were necessary for the optimum charge doping adjustment, several APD wafers with different charge layer doping levels were obtained. The charge layer doping level in each wafer has been examined using a simple-mesa process. Any APD wafer, once verified functional by test devices, was processed with the full-scale procedure to obtain high-speed APD devices for further receiver sensitivity investigation.

9.3 Full-scale Device Processing

All the functional 10Gb/s APD wafers were fabricated using air-bridge based high-speed device processing, as was comprehensively described in Chapter 3. The basic processing parameters used are briefly listed here as the following. A 140-nm-thick Ti(10nm)/Pt(30nm)/Au (100nm) composite metal film was deposited as the *p*-type ohmic contact, in a CHA chamber using E-beam evaporation. Mesa patterns were then defined by standard photolithography and patterned using wet chemical etching, using 1:1:10 buffered phosphoric etchant, to decrease sidewall damage that will cause excessive APD leakage current. The undercut from wet chemical etching was compensated for during the photomask design step, by using a larger mesa diameter mask. Expected mesa diameter size can thus be obtained despite the wet etching undercut. After routine silicon dioxide passivation (~200nm), the *p*-metal layer, encapsulated with the SiO_2 film, was alloyed with the InGaAs cap layer at 420°C for 30sec in a RTA chamber, to obtain a good *p*-type ohmic contact.

The *n*-mesa patterns were also defined using wet chemical etching, through the InAlAs sacrificial layer down to the SI-InP substrate. On top of the initial silicon passivation layer, another thin silicon dioxide dielectric layer was deposited to provide good isolation both between contact pads and between contact pads and SI-InP substrate. *N*-contact windows were then opened on top of the *n*-contact mesas, by removing the pre-deposited silicon dioxide films. A composite Ni(10nm)/AuGe(30nm)/Au(100nm) film was then deposited in the CHA chamber and, after lift-off, was annealed in the RTA chamber to form good ohmic contact to the *n*-type $In_{0.52}Al_{0.48}As$ contact layer. The air-bridge-based interconnects were made, using the methods described in Chapter 3, to provide connection between the *p*-contacts and the contact pads. A typical finished 40μm diameter 10Gb/s APD device, which was processed for backside illumination, is shown in Fig. 9.3.

As shown in the picture, the device mesa area has been completely covered by the *p*-type contact metal so that any incident light from the backside will be completely reflected, resulting in a double absorption path length. The APD total external quantum efficiency at unity-gain was estimated as at least 1.47 times that expected from front side illumination.

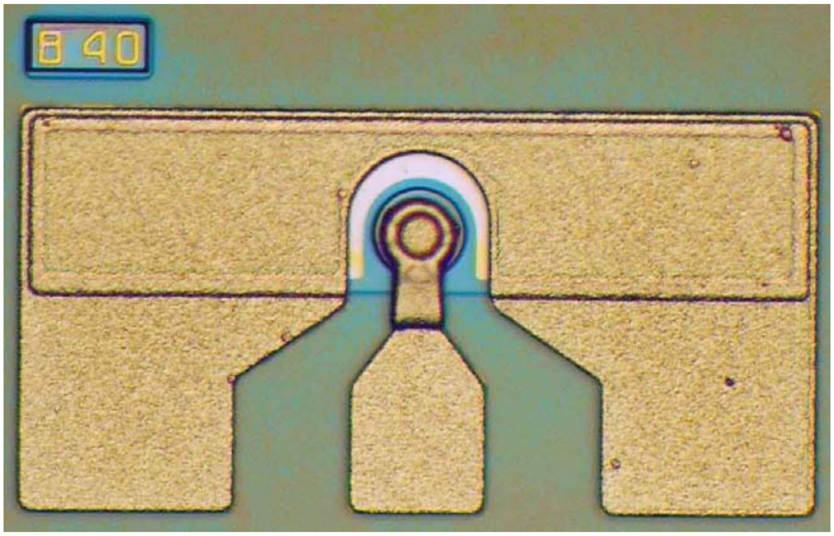

Fig. 9.3 Finished 10Gb/s InGaAs-InAlAs APD using full-scale processing

9.4 Device Characterization

The photocurrent and the dark current of the 10Gb/s InGaAs/InAlAs SACM APDs were characterized at room temperature, after full-scale processing, using a HP 4145B semiconductor parameter analyzer. A 1.55µm wavelength light source from a SANTAC DFB laser was used to characterize APD photoresponse. Figure 9.4 shows typical photocurrent and dark current curves from several SACM APDs with a mesa diameter of 40µm. APDs on each wafer exhibited uniform breakdown voltages across the entire wafer. Since breakdown voltage is sensitive to variations in thickness and impurity concentration in the epitaxial layers, it can thus be inferred that the MBE growth was very uniform. The APD dark current was found to scale with the device area, which means the bulk-related thermal generation current, as discussed in the previous chapter, was still the dominant component in the telecom APD total dark current. The highest dark current density was observed from APDs in wafer #6, which had an extremely thin multiplication region (100 nm) where high electric field induced tunneling in the InAlAs gain region might contribute a pronounced portion to the total dark current.

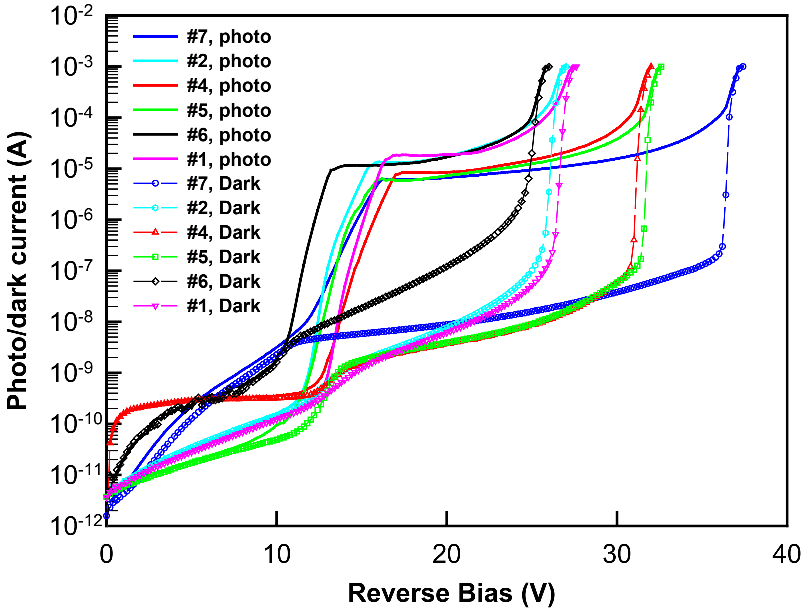

Fig. 9.4 Typical I-Vs from various 40μm 10Gb/s InGaAs-InAlAs APDs

All six types of APD wafers were further examined with C-V measurements to pinpoint their actual punch-through voltages, as plotted in Fig. 9.5. Consistent with each wafer structure, APDs exhibited capacitance values in a descending order corresponding to increasing multiplication region thickness values, at low bias voltages prior to device punch-through. This indicated that, before punchthrough, the APD total capacitance is dominated by the multiplication region capacitance. Once the device punched through, the capacitance of each device roughly converged to a similar value, corresponding to a wholly depleted layer thickness of 1.3~1.4μm. Sharp transition of the APD capacitance value is a true indicator of the device punch-through process, and V_{pt}, the APD punch-through voltage, can therefore be determined from the point where the transition has just finished, as shown in Fig. 9.5.

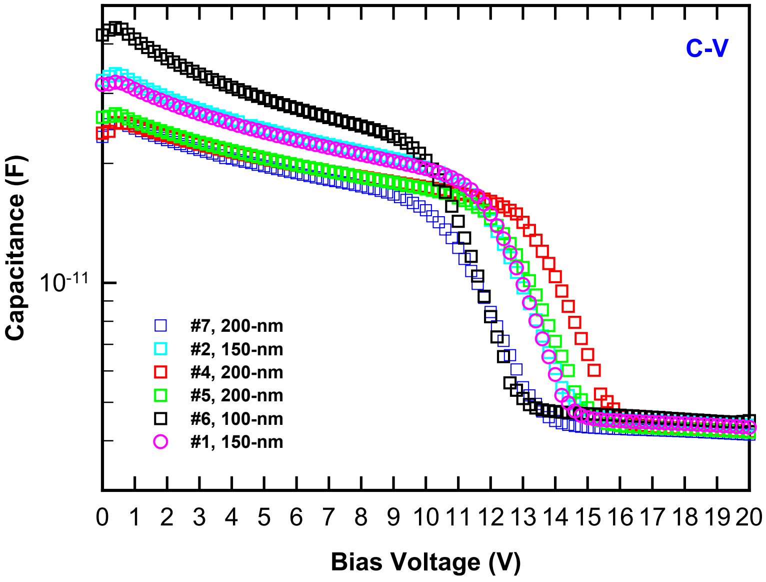

Fig. 9.5 Typical C-Vs from various 160μm InGaAs-InAlAs APDs

After the punch-through voltage for each wafer has been determined from the C-V measurements, the external quantum efficiency of each device was measured using a tungsten-halogen light source, a spectrometer, and a lock-in amplifier, as described in Chapter 2. All of the APDs, with a diameter of 250μm, exhibited higher external quantum efficiencies than expected for a 1.0μm-thick $In_{0.53}Ga_{0.47}As$

absorber, using top illumination. The measured external quantum efficiency surplus, compared to the calculated value, originated from APD gain at the relevant bias, which was provided by carrier multiplication in the high electric field corresponding to the onset of punch-through. The external quantum efficiency at APD unity-gain reference, $\eta_{ext,0}$, can be expressed as

$$\eta_{ext,0} = (1 - R) \cdot (1 - e^{-\alpha \cdot d}) \tag{9.1}$$

and device external quantum efficiency at the reverse bias for measurement is

$$\eta_{ext} = M^* \cdot \eta_{ext,0} \tag{9.2}$$

where R is the reflection coefficient at the air-semiconductor interface, α is the light absorption coefficient of $In_{0.53}Ga_{0.47}As$ at the relevant incident wavelength, d is the absorption layer thickness, η_{ext} is the external quantum efficiency obtained at the measurement reference bias, and M^* is the gain to be determined. External quantum efficiencies for each type of device were extracted from the measured photocurrent data in the wavelength range from 1.0 μm to 1.6 μm at a fixed reverse bias voltage above each device punch-through, as plotted in Fig. 9.6. Devices from wafer #6 exhibited the highest value, while wafer #7 had the lowest. This result corresponded very well with the electric field intensity value at each device's punch-through. APDs in wafer #6 had the highest electric field at punch-through, while wafer #7 had the lowest.

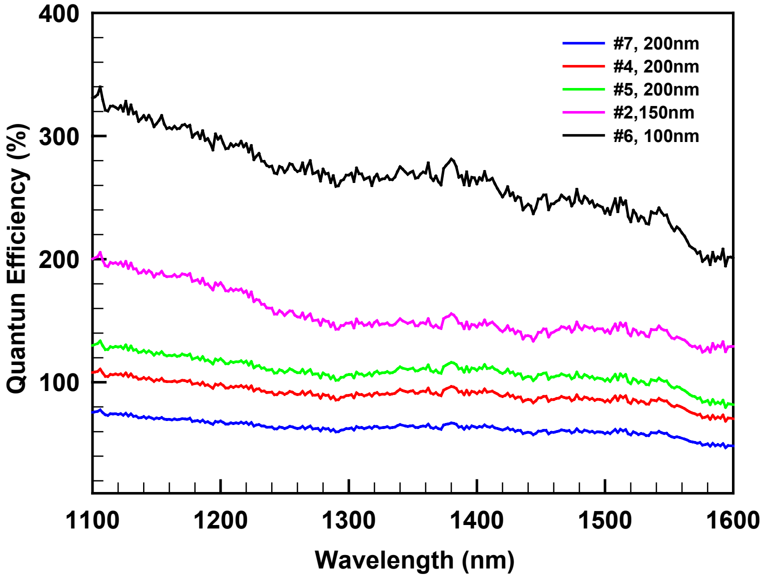

Fig. 9.6 External quantum efficiencies from various 250μm-diameter APDs

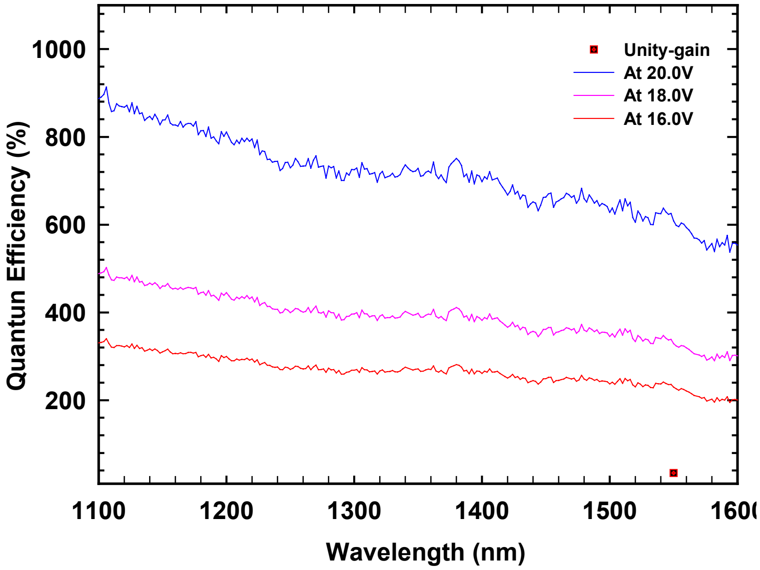

Fig. 9.7 External quantum efficiencies at different reverse bias voltages, from a 250μm InGaAs-InAlAs APD with 100-nm-thick multiplication region

For a SACM APD that has a 1.0 μm-thick $In_{0.53}Ga_{0.47}As$ absorption region with absorption coefficients (α) of 1.16 μm^{-1} at 1.3 μm and 0.705 μm^{-1} at 1.55 μm [9-8], the ideal external quantum efficiencies are ~58% and ~46%, respectively, assuming an ideal optical transmission of 70% (R=0.3) at the air-semiconductor interface. The gain, M^*, at the relevant reverse bias, was determined using (9.2), with the results listed in Table 9.1. The DC gain of each APD, at reverse bias above punch-through, can be thus determined using the following expression

$$M = \frac{I_p - I_d}{I_{pu} - I_{du}} \cdot M^* \tag{9.3}$$

where I_p and I_d are photo and dark current for bias values above the reference; I_{pu} and I_{du} are primary photo and dark current at the reference bias. High external quantum efficiencies at various biases above punch-through, as shown in Fig. 9.7, were consistently observed from APDs on wafer #6, which is a good evidence of high gain at and above punch-through.

Wafer number	M-region thickness	Breakdown (V)	Punch-through (V)	Gain at –16.0V
#4	200-nm	31.9	-15.2V	2.35
#5	200-nm	32.6	-15.9V	2.94
#7	200-nm	37.3	-14.1V	1.67
#2	150-nm	27.6	-15.0V	4.05
#6	100-nm	26.8	-13.4V	≥6.8

Table 9.1 Device properties of various 10Gb/s telecom APDs

The linearity of each APD photoresponse at various incident light intensities was also examined prior to packaging in the receiver. Good linearity was consistently observed, as shown in Fig. 9.8, from all the APDs selected for packaging. Perfect linearity measured in the input power range indicated that no gain saturation occurred when the input power ramped up from an extremely low level of –30dBm up to –5dBm.

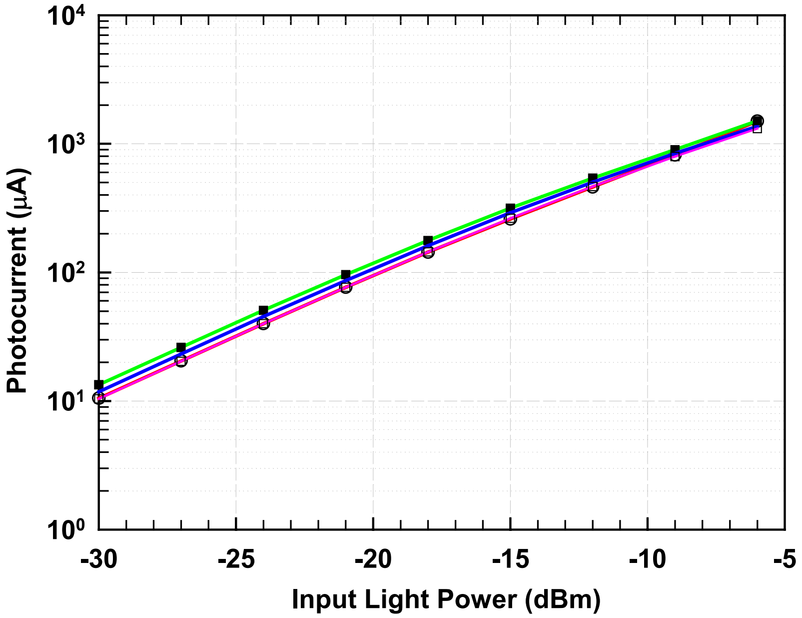

Fig. 9.8 Linearity of photoresoponse of 200nm InGaAs-InAlAs APDs

The bandwidth of every selected 10Gb/s APD device at low-gain was examined using a small signal input, with a HP8703A lightwave component analyzer at a wavelength of 1.3μm. Every 40μm-diameter 10Gb/s APD exhibited a low-gain bandwidth >8GHz, which corresponded very well to the estimated value based on the velocity saturation model. The relatively long carrier (for both electrons and holes) transport path length (~2.8μm) associated with the total depleted absorption, charge, and multiplication regions determines the bandwidth in the low-gain regime, which was primarily transit-time limited, as shown in Fig.9.9.

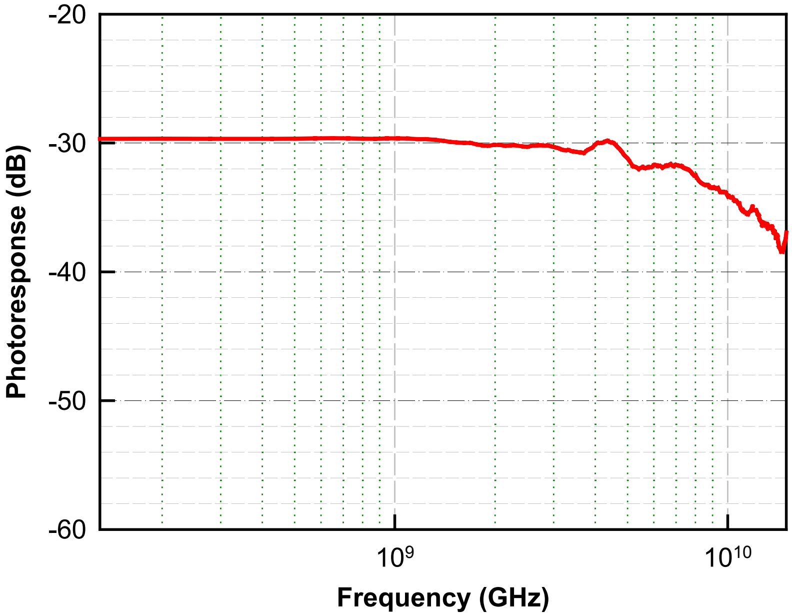

Fig. 9.9 A typical 10Gb/s telecom APD photoresponse at low gains

The gain-bandwidth product of APDs was also measured at high-gain values, before shipping to Multiplex for receiver integration. The AC gain was calculated by comparing the device responsivity at each testing point to the corresponding value at a specific reference bias. The method used here was similar to the previously discussed gain calculation method based on the external quantum efficiency measurements. Typical gain bandwidth products of several 200-nm-thick APDs are plotted in Fig. 9.3. The nominal gain-bandwidth product observed from these devices was >140GHz at high APD gain values.

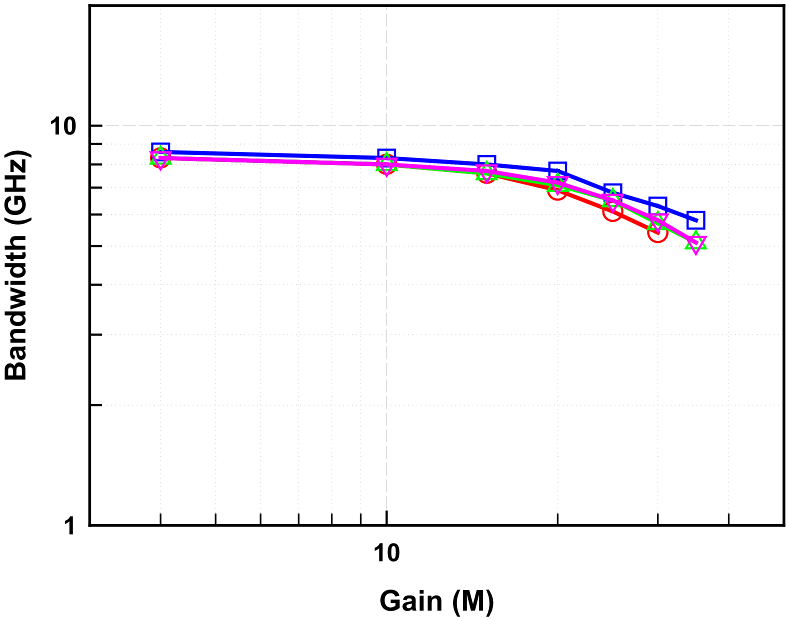

Fig. 9.10 Bandwidth versus gain for 200nm InGaAs-InAlAs APDs

9.5 APD Receiver Integration and Characterization

After complete device characterization at UT Austin, five types of APD samples with different multiplication region thickness (one 100 nm, two 150 nm, and two 200 nm) were sent to Multiplex Incorporated to be packaged into 10Gb/s receivers. Only three out of five types of APDs from wafer #2, #5 and #7, two with a 200-nm-thick gain region and one with a 150-nm-thick gain region, respectively, passed the device qualification at Multiplex Inc. This was due to high leakage current in the 100-nm-thick and the remaining 150-nm-thick APDs. However, the 100-nm-thick APDs, even with a high dark current level, were also packaged into

APD receivers to investigate the sensitivity, compared to that from the other thicker devices.

Backside illumination was utilized to enhance APD receiver sensitivity by achieving a double optical absorption path in the InGaAs absorber. All APD wafers were initially thinned from the InP substrate side, using lapping and polishing. An anti-reflection coating was then deposited on the polished substrate side to enhance light transmission from the optical-fiber to the APD active region.

In order to decrease the coupling loss by collecting more light from the optical fiber, APDs with larger mesa size were preferred for receiver fabrication. Another important reason for using larger devices was alleviating further difficulty with optical fiber alignment. However, larger area introduced higher parasitic capacitance, which reduced the APD bandwidth, and therefore shrank the receiver bandwidth by increasing the *RC* time constant. In the second-order trans-impedance amplifier (TIA) approximation, the bandwidth of an integrated receiver is

$$f_{-3db} = \frac{1}{2\pi} \cdot \frac{\sqrt{2} \cdot A_0}{R_F \cdot C_D}, \tag{9.4}$$

where A_0 is TIA open-loop gain, R_F is the current feedback resistance, and C_D is the equivalent parasitic capacitance from the photodiode. As a compromise, devices with a 40μm-diameter mesa size were utilized in the receivers, to simultaneously satisfy the requirements of acceptable light coupling efficiency and high *RC* bandwidth, which minimizes the inter-symbol interference.

A block diagram of the APD receiver is shown in Fig. 9.11. After all on-wafer characterizations, both DC and AC, all four APD wafers were cleaved into individual die. The best APDs were selected, as determined by the to DC and AC measurements, and subsequently packaged with low noise trans-impedance amplifiers (TTAs), using a hybrid integration technique. An amplitude-limiting amplifier (LA) was placed after the TIA to further enhance receiver sensitivity by boosting the small analog output of the TIA to a larger digital output, which has a pronounced threshold level and superior noise margins for both logic "high" and logic "low". The TIA utilized for integration was a low noise pre-amplifier, KGA4130D, provided by TMCC, which was based on an advanced GaAs fabrication technology.

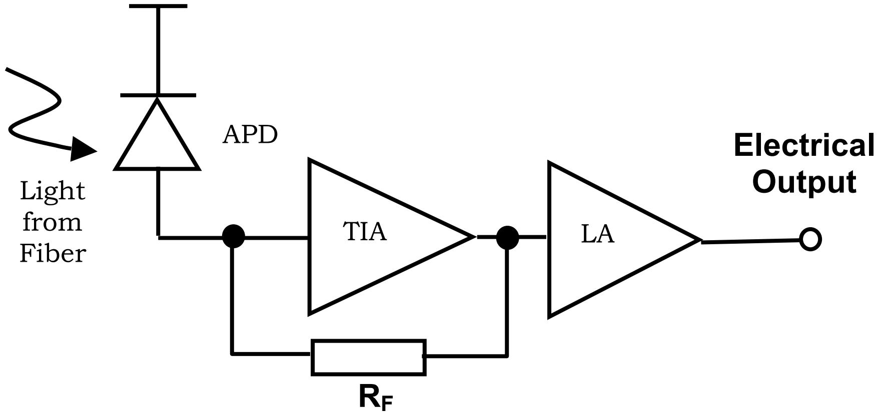

Fig. 9.11 Simplified structure of an optical receiver

This TIA has an equivalent trans-impedance of 1.2KΩ (~61.2dBΩ) and an equivalent input noise current of 10 *p*A/Hz$^{1/2}$. The closed-loop 3-dB bandwidth of this TIA was ≥10GHz. The cascaded amplitude-limiting amplifier (KGA4219) further increased the TIA analog output, from a relatively small amplitude (~20mV$_{p-p}$) to a typical digital output amplitude (~600mV), while driving a standard 50Ω load. This circuit configuration greatly increases the overall sensitivity of the integrated APD receiver, as has been confirmed by earlier work on *p-i-n* receivers. All of the APD receivers were packaged into a dual 12-pin butterfly-type package with a pig-tailed fiber input port. Proper optical alignment was confirmed by monitoring and maximizing the APD photoresponse during receiver packaging. Wire-bonding was used to connect the APD to the input pad of the mounted TIA and the TIA to the following LA circuit. The output of the LA was connected to a standard SMA output adaptor through a pre-fabricated micro-strip transmission line on the packaging substrate.

The sensitivity of all packaged integrated APD receivers were measured using a bit-error-rate tester at a data rate of ~9.9853 Gb/s, with a pseudo-random binary sequence (PRBS) length of 2^{31}-1, at Multiplex Inc.. An evaluation board, used to mount the packaged APD receiver, was utilized to provide a connection to the peripheral circuits and power supplies, and to de-couple parasitic signals. Dark currents and bandwidths measured at an approximate APD gain of ten, prior to receiver fabrication at Multiplex Inc., are listed in Table 9.2. Sensitivity results from all APD receivers, packaged with avalanche photodiodes from wafer #2, #5, #6, and #7, were also listed. After packaging, all of the APD receivers exhibited sensitivities better than –27dBm at a BER of 10^{-12} with a PRBS of 2^{31}-1. At a BER of 10^{-9} with a similar PRBS of 2^{31}-1, all of the APD receivers exhibited sensitivities better than –29dBm, except receiver #G2, which was fabricated using a 100-nm-thick APD that had the highest dark current level.

Device number	M-region thickness	Dark current @ reverse bias (V)	Bandwidth @ gain of ~10	Sensitivity @ BER=10^{-9} (dBm)
A1, #5	200-nm	150.0nA / 27.8V	~8.0 GHz	-29.2 dBm
A2, #5	200-nm	15.9nA / 27.7V	~8.3 GHz	<-29.6 dBm
C1, #7	200-nm	64.3nA / 33.8V	~8.0 GHz	-29.4 dBm
C2, #7	200-nm	65.0nA / 33.8V	~8.0 GHz	-29.0 dBm
E1, #2	150-nm	34.0nA / 23.2V	~8.1 GHz	-29.2 dBm
E2, #2	150-nm	38.0nA / 23.3V	~8.0 GHz	-29.3 dBm
G1, #6	100-nm	261.0nA / 20.3V	~8.3 GHz	-29.0 dBm
G2, #6	100-nm	440.0nA / 20.18V	~8.3 GHz	-28.6 dBm

Table 9.2 Several sensitivity measurement results from the 10Gb/s APDs

The receivers packaged with the 100-nm-thick APDs were expected to yield a better sensitivity result than those using the other APDs, due to lower excess noise. However, the high multiplied dark current value appears to be a critical limiting factor leading to lower sensitivity compared to the other devices.

The relatively lower dark current levels in the 150-nm and 200-nm APDs yielded better APD receiver sensitivities, as shown in the Table 9.2, despite variations in the amplification circuit parameters and differences in packaging, which could cause slight variations in APD receiver sensitivity.

The best sensitivity result obtained so far was from an APD receiver packaged with an avalanche photodiode from wafer #5, which had the lowest multiplied dark current, ~15.9nA. The optimum APD gain value corresponding to the best APD receiver sensitivity was ~15. The sensitivity measured was -29.6dBm at a BER of 10^{-9}, with a data rate of ~9.9853 Gb/s and a PRBS of 2^{31}-1., as shown in Fig. 9.12. This is one of the best 10Gb/s APD receiver sensitivity results reported to date [9-2]~[9-5].

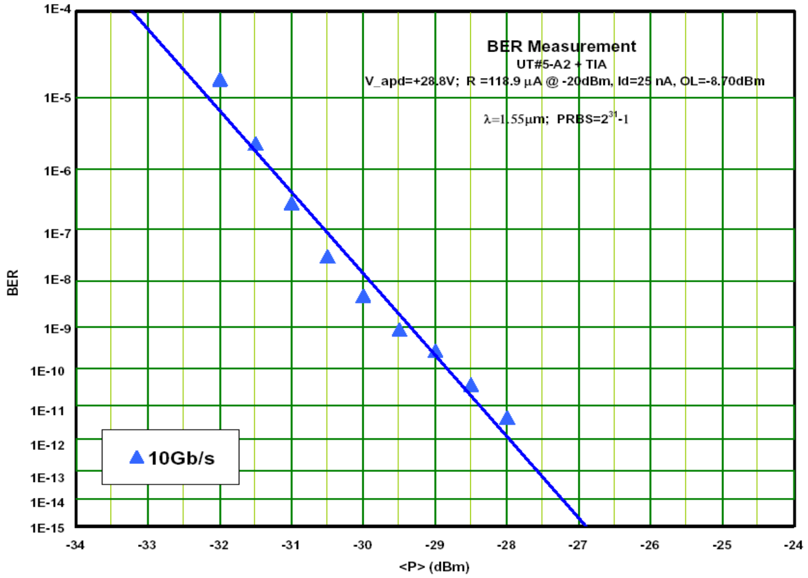

Fig. 9.12 Sensitivity measurement results from a 10Gb/s APD receiver

High multiplied dark currents in the thin (100nm and 150nm) MBE-grown InAlAs APDs still remain as one of the limiting factors for achieving better APD receiver sensitivity at 10Gb/s data rate, as indicated by the APD receiver results at Multiplex. Improving epi-structure quality in order to decrease the InAlAs APD dark current is therefore important to obtain better InAlAs APD receiver sensitivity.

Considerable improvement of the InAlAs APD receiver sensitivity can still be achieved by modifying the device structure, even before the dark current issue is completely solved. As shown in Fig. 9.10, the achievable APD bandwidth value at APD gains up to 15 is still above 8GHz, while a typical bandwidth of ≥7.5GHz is sufficient to satisfy the requirement of a 10Gb/s APD receiver. Slightly increasing the InGaAs absorbing layer thickness in the InAlAs APDs, or using a partially depleted absorbing region, may provide additional APD responsivity thus increasing APD receiver sensitivity, if properly designed, fabricated, and packaged.

Obtaining a higher APD gain-bandwidth product is the most effective way to obtain higher receiver sensitivity. Impact-ionization engineering can ultimately be utilized to increase the APD gain-bandwidth product without significantly increasing the APD excess noise, as long as the excessive (tunneling) leakage current is effectively suppressed. Further optimization of the TIA circuit, either through modifying the current circuit structure or completely changing the fabrication technology (e.g. using HEMT-based low-noise circuitry), may be another option to improve APD receiver sensitivity. All of these potential solutions require further investigation.

9.6 Summary

InAlAs APDs with a thin multiplication region (ranging from 100-nm to 200-nm) have been developed for 10Gb/s telecommunication applications. These APDs exhibited acceptable gains, sufficient bandwidths, and ample gain-bandwidth products for APD receiver fabrication. At BER of 10^{-9}, an APD receiver sensitivity of better than -29.6dBm at a data rate of ~9.9853 Gb/s and a PRBS of 2^{31}-1 has been achieved by utilizing a 200-nm InAlAs APD. This among the best sensitivity results reported to date. High multiplied APD dark current level in the thinner InAlAs APDs was identified as a limiting factor for obtaining higher APD receiver sensitivity. Improving the epi-layer quality and decreasing the APD dark current is one approach to enhance the sensitivity of these receivers. On the device end, ample low-gain bandwidth indicated that slightly increasing the InGaAs absorber thickness, or even by using a partially depleted absorber, could be other options to obtain better APD receiver sensitivity. In the future, an impact-engineered multiplication region could be incorporated into InAlAs APDs to obtain higher receiver sensitivity, by suppressing the excess noise and increasing the gain-bandwidth product. On the circuit end, APD receiver sensitivity could be further increased by optimizing the TIA circuitry.

Chapter 10

InGaAs/InAlAs Waveguide APDs for 40Gb/s Applications

Achieving high sensitivity in APDs for 40 Gb/s optical telecommunication applications has been a long time challenge. High unity-gain responsivity, a high bandwidth at low gains, and a high gain-bandwidth product are the critical figures of merits for these applications. Compared with the normal incidence srructures, the edge-coupled waveguide (WG) approach, combined with a separate absorption, charge and multiplication APD structure, is promising for 40 Gb/s signal detection, because this approach provides the possibility for de-coupling light absorption efficiency from carrier transit time and allows concurrent optimization of APD sensitivity and speed, as shown in Fig. 10.1.

To date, only a few edge-coupled waveguide APDs have been demonstrated. Cohen-Jonathan et. al. achieved a high external quantum efficiency of 72% by direct edge coupling into the 0.5μm absorbing layer, yet the bandwidth was only 20 GHz at low gains [10-1]. Even though a higher bandwidth of 35 GHz at low gains was achieved by employing a thinner multiplication layer, using a similar approach, the external quantum efficiency was only 58% and the gain-bandwidth product was ~140 GHz [10-2]. The highest reported gain-bandwidth product for WG-APDs was 320 GHz, which was demonstrated with a ~0.2μm thick absorbing layer. Unfortunately, the quantum efficiency was only approximately 5% for the small, high-speed devices [10-3]. By using an APD with a thinner (~0.12μm) absorbing thickness, an evanescently-coupled asymmetric twin-waveguide APD obtained a quantum efficiency of 48% [10-4], at the expense of developing a more complicated (thus more difficult to fabricate) device structure. The bandwidth at low gains was ~31.5 GHz and the gain-bandwidth product was 150 GHz. Previously, our group demonstrated a high efficiency (>80%) and broad bandwidth (>48 GHz) evanescently-coupled *p-i-n* photodiode that employed a planarized short multimode waveguide (PSMW) [10-5]. The idea of extending this PSMW approach to demonstrate a 40Gb/s APD by combining a waveguide structure and a SACM structure is tantalizing.

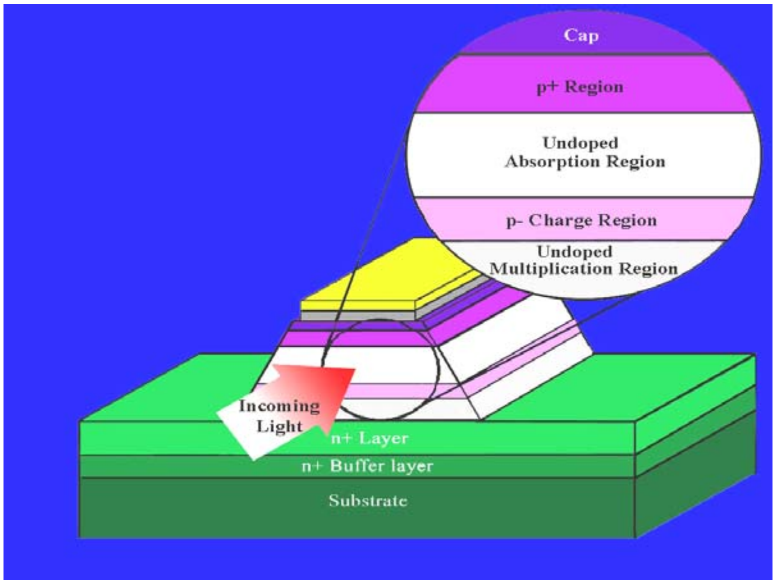

Fig. 10.1 Device structure of the early-stage waveguide APDs

10.1 Design of the 40Gb/s Waveguided APDs

In the early stages of WG-APD studies in our group, the APD structure itself was designed as a symmetric slab waveguide, as shown in Fig. 10.1 [10-3]. Even though the slab waveguide was designed to achieve good internal quantum efficiency, the optical coupling from fiber to the APD core region (absorber) was poor (<5%) due to excessive loss from coupling a round optical fiber (beam waist of ~3-5μm) to the slab waveguide with a very thin core region (<200 nm).

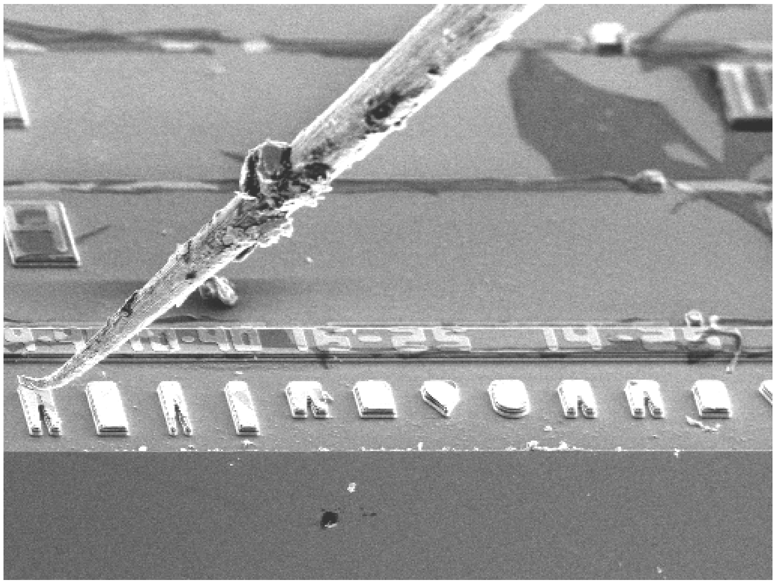

Fig. 10.2 Various facet patterns used to enhance optical coupling

Facet engineering was proposed, after an initial investigation of the quantum efficiency of the WG-APDs, and various facet patterns were designed and evaluated to improve the light coupling efficiency. In this initial study [10-6], facets with flat, lensed, wedged, deep-wedged or serrated-wedged surfaces were fabricated and compared, as shown in Fig. 10.2. The optical coupling efficiency of the lensed-facet proved similar to the flat-facet, even though theoretical simulation indicated a higher efficiency value. The reason might be attributed to the fabrication-induced facet geometry variation and distortion from the theoretical analyses. The lens-facet and flat-facet devices exhibited negligible differences between external quantum efficiencies. Better optical coupling efficiency was obtained from the wedged-facet WG-APDs. Based on the external quantum efficiency of the flat-facet long WG-APD, the wedged-facet APD achieved 43% higher coupling efficiency assuming a perfect anti-reflection coating [10-6]. But the external quantum efficiency (~22.9% for long WG-APDs) was still less than acceptable value for practical applications.

At the beginning of this project, the initial idea I proposed was to use an asymmetric tapered twin-waveguide coupling scheme, which was very similar to what has already been reported [10-4], as shown in Fig. 10.3. The initial design, for which much effort was devoted to simplify the WG-APD device structure, material growth, and device processing, proved too complicated to achieve with our current research capabilities, even though the simulated result indicated a promising optical coupling efficiency (>50%). Further breakthroughs in the PSMW *p-i-n* photodiode made by Stephane Demiguel et. al. [10-5] brought new hope for the high-responsivity 40Gb/s APD project. Collaborated with Stephane Demiguel, a more aggressive idea for incorporating a SACM structure on top of the PSMW in order to enhance the overall optical coupling efficiency was thus proposed.

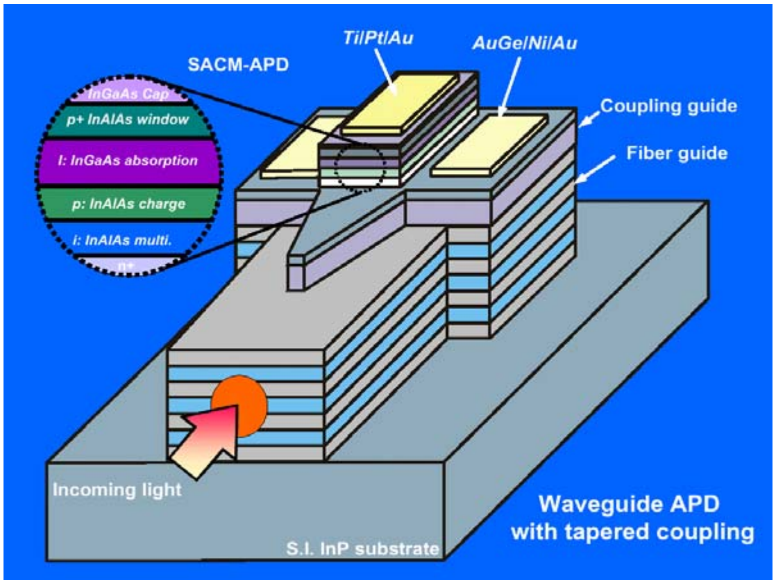

Fig. 10.3 Initially proposed waveguide APD structure, with a taper coupling scheme

10.1.1 Optical Design

As was discussed in Chapter 3, the most challenging work for the 40Gb/s APD sensitivity design was optimizing the lateral optical coupling efficiency for a given APD absorber thickness. The optical coupling efficiency, which can be expressed in terms of responsivity or external quantum efficiency, is determined by: *a)* optical coupling from the optical fiber to the photodiode, and *b)* light absorption in the thin APD absorber. The combined effects yield the final APD responsivity at unity-gain. Enlightened by several recent studies on high-responsivity waveguide *p-i-n* photodiodes, the idea of separating input light coupling and light absorption in a waveguide APD was formed.

For the early-stage WG-APD studies, excessive optical loss at stage *a)* yielded external quantum efficiencies too low, even for the later improved wedged-facet design. In the new WG-APD scheme, a multi-core-layer (diluted) waveguide, which has been widely adopted in waveguide coupling design, was used to enhance light coupling from the optical fiber into the WG-APD, as shown in Fig. 10.4.

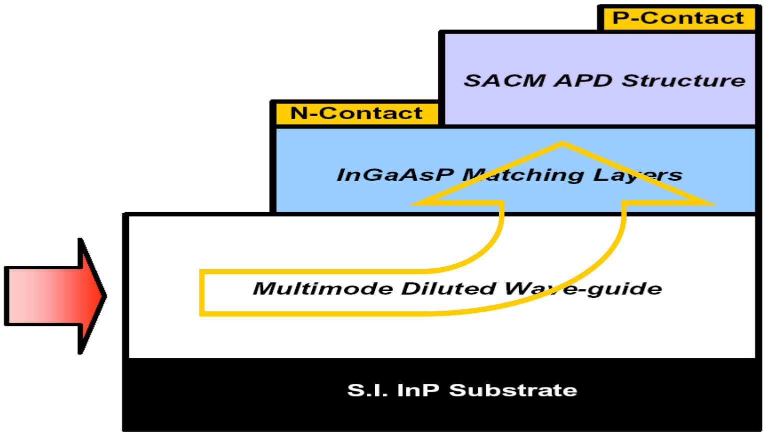

Fig. 10.4 The improved 40Gb/s telecom APD structure, using a multimode waveguide scheme

The optical coupling efficiency from a fiber to a slab waveguide, η_C, can be expressed as the overlap integral of the modal field from the fiber output (Ψ_{fiber}) and the field within the diluted input slab waveguide (Ψ_{guide})

$$\eta_C = \frac{\left|\int \Psi_{fiber}(x,y)\cdot\Psi^*_{guide}(x,y)dxdy\right|^2}{\int\left|\Psi_{fiber}(x,y)\right|^2 dxdy\cdot\int\left|\Psi_{guide}(x,y)\right|^2 dxdy} \qquad (10.1)$$

The coupling loss L_C from the input optical fiber to the waveguide is defined as

$$L_C = -10\log(\eta_C) \qquad (10.2)$$

The diluted input waveguide was optimized for both a lensed fiber and a cleaved fiber, with diameters of 6μm and 11μm, respectively. The coupling loss is 0.55dB for the lensed fiber and 2dB for the cleaved facet fiber. The TE/TM polarization dependence is 0.2dB for both optical fiber types. The associated alignment tolerances were ±1.3μm and ±2.1μm, respectively.

The light that was coupled into the diluted waveguide was then transferred to the upper photodiode absorber by the refractive index steps in the two optical matching layers. The bandgap of these layers were equivalent to absorption band edges of 1.1μm and 1.4μm. Figures 10.5(a) through 10.5(e) show cross sections of the field intensities and illustrate the process of light coupling, based on the simulated results.

10.1.2 Electrical Design

The separate absorption, charge, and multiplication APD structure was utilized for the 40Gb/s WG-APD. A thin absorption region was intended to guarantee a low-gain bandwidth >30GHz, dominated by the carrier transit time. This absorber thickness was optimized along with other APD parameters during the final simulation for O-E integration. The first APD parameter fixed was the InAlAs multiplication layer thickness. A thin (150nm) InAlAs multiplication region was incorporated into this SACM structure to provide low multiplication noise, as well as a high gain-bandwidth product. Previous studies on the InGaAs/InAlAs SACM APDs indicated that once the multiplication layer is too thin, i.e. less than 150nm, the inter-band tunneling effect will generate excessive dark (leakage) currents in

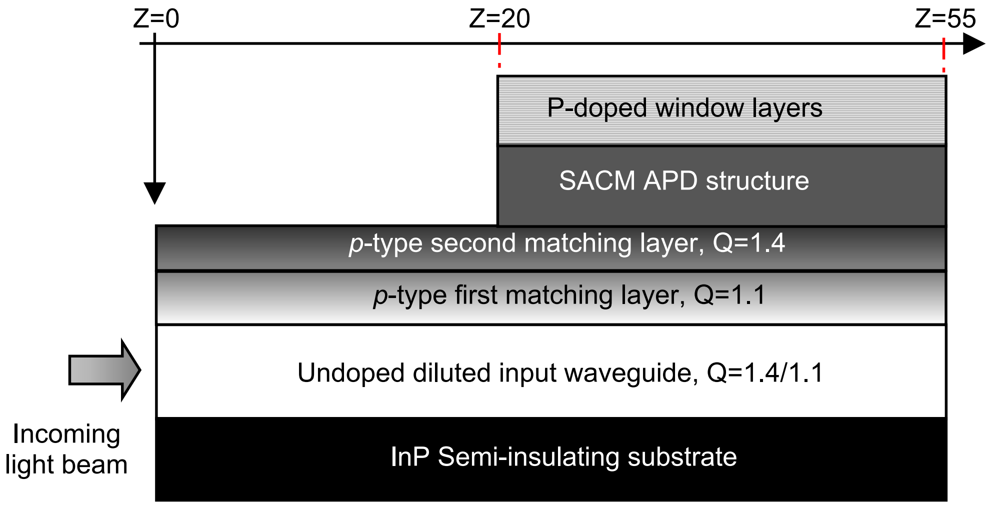

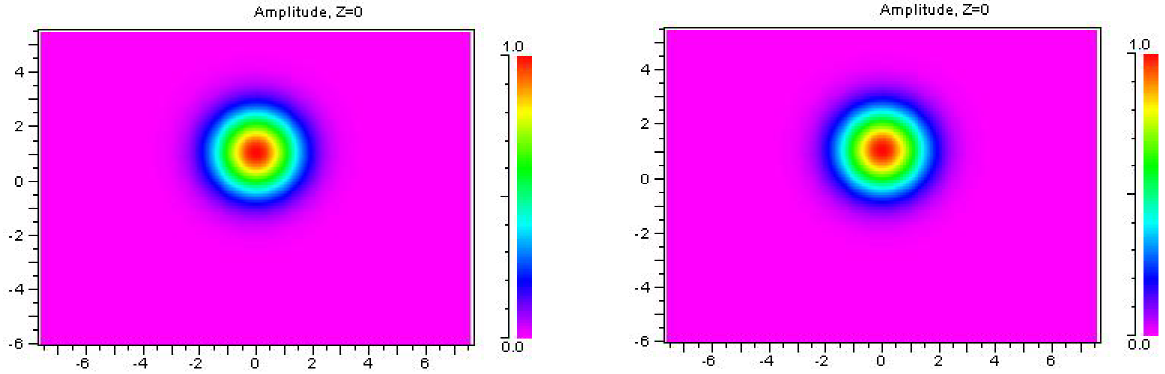

Fig. 10.5 (a) X-Y plane optical power distribution profile at Z=0.0 μm

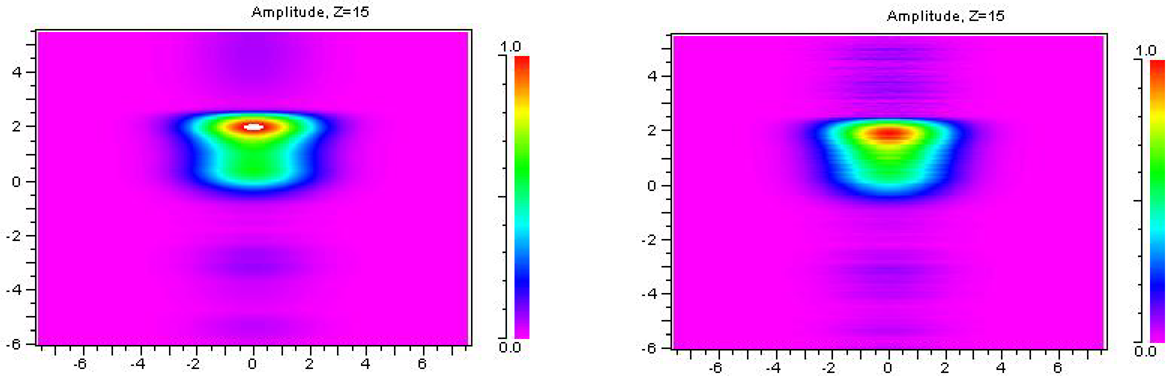

Fig. 10.5 (b) X-Y plane optical power distribution profile at Z=15.0 μm

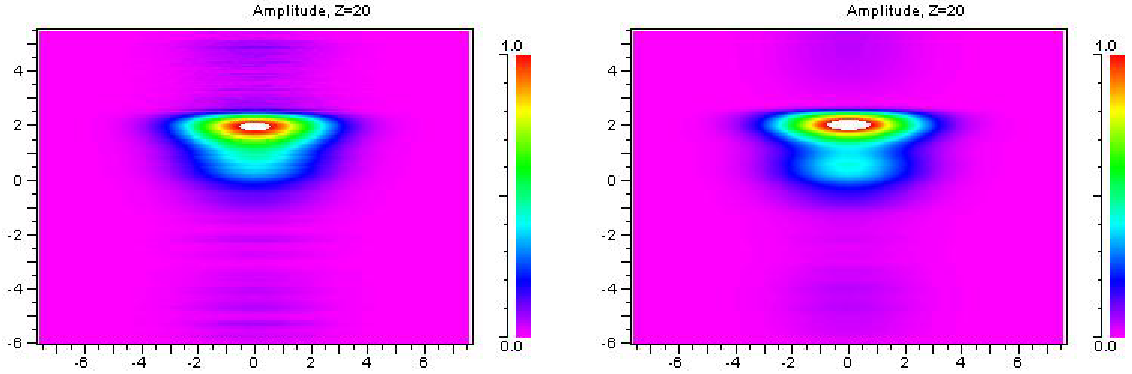

Fig. 10.5 (c) X-Y plane optical power distribution profile at Z=20.0 μm

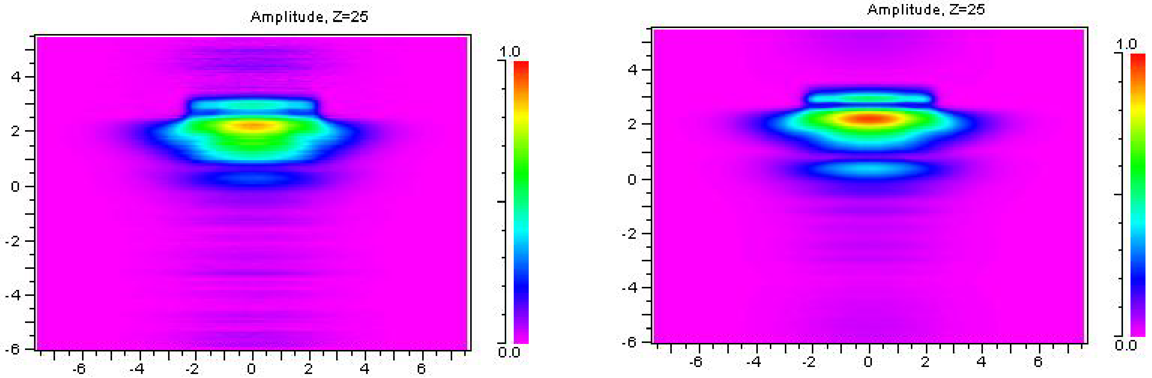

Fig. 10.5 (d) X-Y plane optical power distribution profile at Z=25.0 μm

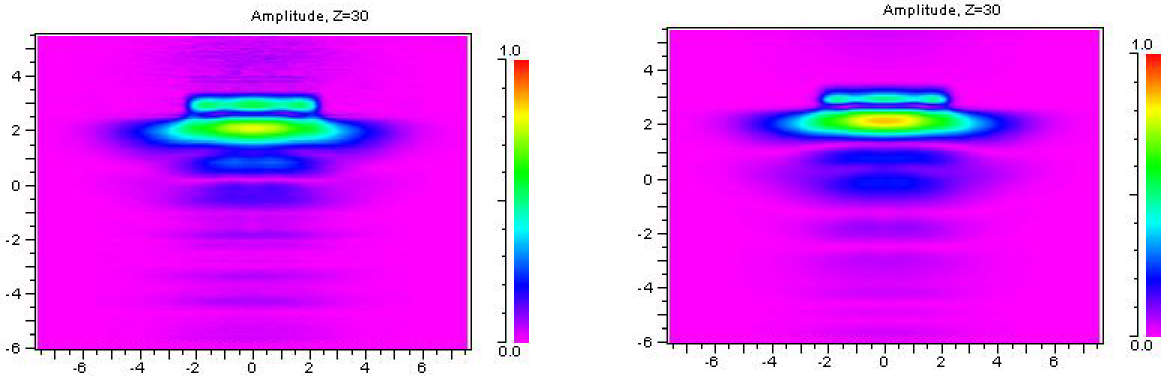

Fig. 10.5 (e) X-Y plane optical power distribution profile at Z=30.0 μm

the thin InAlAs multiplication layer at high electric field, which usually exceeds 750KV/cm for thin InAlAs layers. For the initial 40Gb/s APD design, simulations indicated that a 150nm-thick InAlAs multiplication layer would provide enough safety margin to obtain a functional APD.

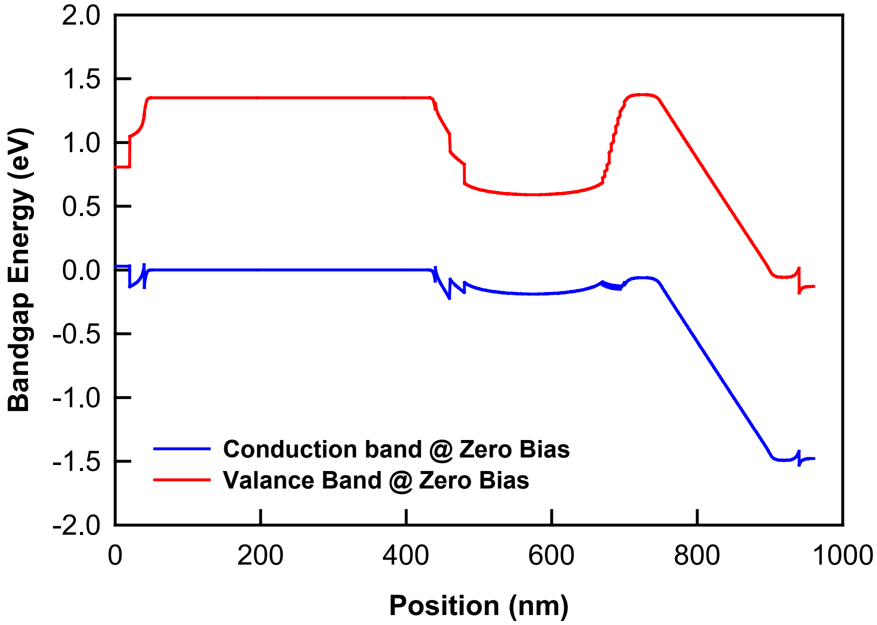

Fig. 10.5 Simulated band structure of the SACM APD, at zero bias

The total charge amount was optimized, using *BandProf* software, to limit the electric field strength in the InGaAs absorber below 150KV/cm and eliminate low field carrier multiplication in the InGaAs absorber, which can generate a long carrier multiplication path in the depleted region and degrade both the noise and gain-bandwidth product. The APD band diagram at zero bias is shown in Fig. 10.5, while Fig. 10.6 shows the APD band diagram above punch-through. Too low an electric field in the absorption layer was also avoided by adjusting the doping in the charge layer to guarantee that the electric field strength was high enough to enable both electrons and holes to reach their saturated velocities.

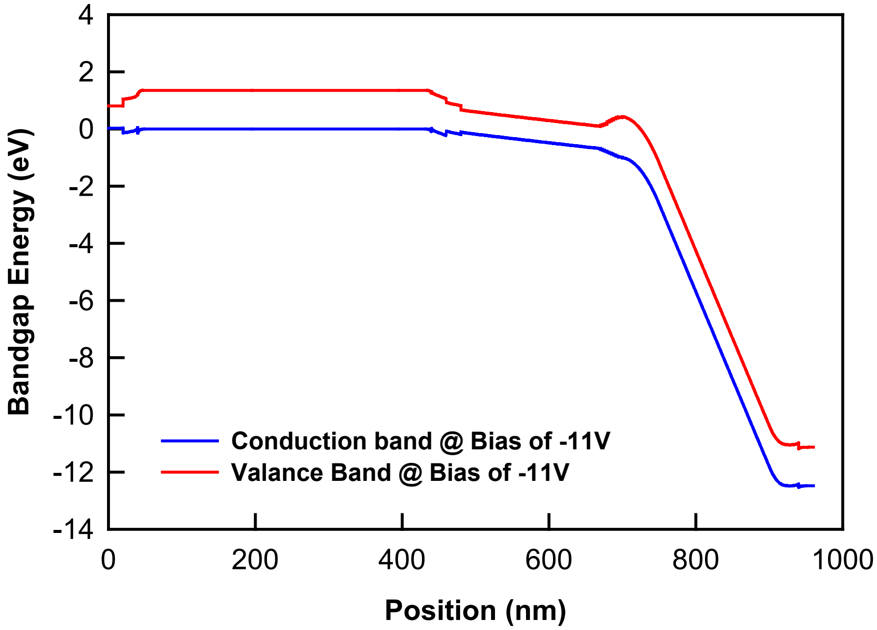

Fig. 10.6 Optimum charge layer doping, determined by punch-through

Graded digital alloy $(InGaAs)_y(InAlAs)_{1-y}$ transition layers were incorporated in each InGaAs-InAlAs hetero-junction interface to eliminate possible carrier trapping, due to offsets in both the conduction and valance bands. The 30nm transition layer thickness used in the device structure was limited by the MOCVD epi-layer growth rather than design-related constraints. The total thickness of the SACM structure and the thickness for each critical layer were optimized during the optical-electrical coupling simulations.

10.1.3 O-E Integration and Device Optimization

Based on the previous waveguide *p-i-n* structure, two matching layers comprised of quaternary InGaAsP alloys (Q1.1 and Q1.4, respectively) were utilized to enable light transfer from the lower diluted input waveguide to the upper SACM APD absorber, through a refractive index change, as shown in Fig. 10.8.

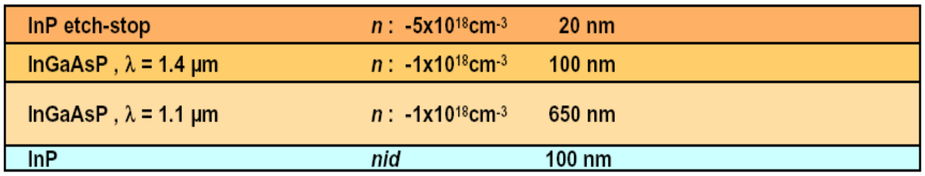

InP etch-stop	*n* : $-5\text{x}10^{18}\text{cm}^{-3}$	20 nm
InGaAsP , $\lambda = 1.4$ μm	*n* : $-1\text{x}10^{18}\text{cm}^{-3}$	100 nm
InGaAsP , $\lambda = 1.1$ μm	*n* : $-1\text{x}10^{18}\text{cm}^{-3}$	650 nm
InP	*nid*	100 nm

Fig. 10.7 Matching layer structure used in the waveguide APD

Even though the design of both the diluted input waveguide and the SACM APD structure was straightforward, efficient light coupling from the bottom input guide to the APD absorber remained a challenge. Optical design for a WG-APD is more difficult that for a *p-i-n* photodiode, because in a *p-i-n* photodiode structure the absorption region is directly adjacent to the input waveguide, thus the optical mode in the input-guide is more easily coupled into the absorption region. In a waveguide APD, however, both the charge and multiplication regions are located between the input-guide and the absorption region, which makes transfer of the optical mode from the diluted input-guide to the SACM absorber more difficult to achieve.

The absorber, charge layer, and multiplication layer thickness, as well as the thickness of the digital-alloy transition layers between the InGaAs and InAlAs layers, are all constraints on the WG-APD design. The thickness of the multiplication layer and digital-alloy transition layers was fixed by material and growth constraints, as discussed previously. Even though further simulations, using 3-D BPM software, showed that a 170-nm gain region thickness corresponded to the least TE-TM mode polarization of the total guided optical power loss, as shown in Fig. 10.8, a thinner 150-nm gain region was still adopted to reduce the APD excess noise and to obtain a higher G-B product. The thickness of both the charge layer and absorbing layer was then determined by further optical simulations, based on the best coupling (minimum guided power loss) from the input front of the diluted waveguide to the end of the APD InGaAs absorber, for both TE and TM modes.

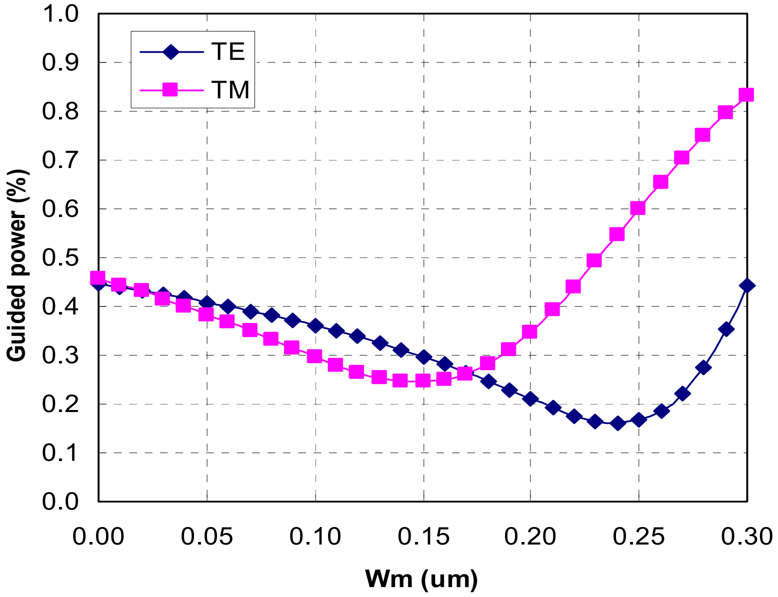

Fig. 10.8 Total guided optical power loss in the waveguide APD, as a function of the multiplication region thickness

Simulations of the overall WG-APD coupling efficiency were therefore performed to determine two remaining parameters: the absorber thickness and the charge layer thickness. The calculated guided power loss exhibited strong dependence on the absorber thickness, as shown in Fig. 10.9, assuming a fixed thin charge layer. The least quantum efficiency dependence on TE/TM mode was observed when the absorber layer (InGaAs) thickness was ~190nm. Further simulations indicated that the dependence of total guided optical power loss as a function of the charge (InAlAs) layer thickness was insignificant, as shown in Fig. 10.10, as long as the charge layer is thin (<50-nm). As a compromise, a 50-nm-thick charge layer thickness was utilized to avoid high charge layer doping concentration and excessive optical loss.

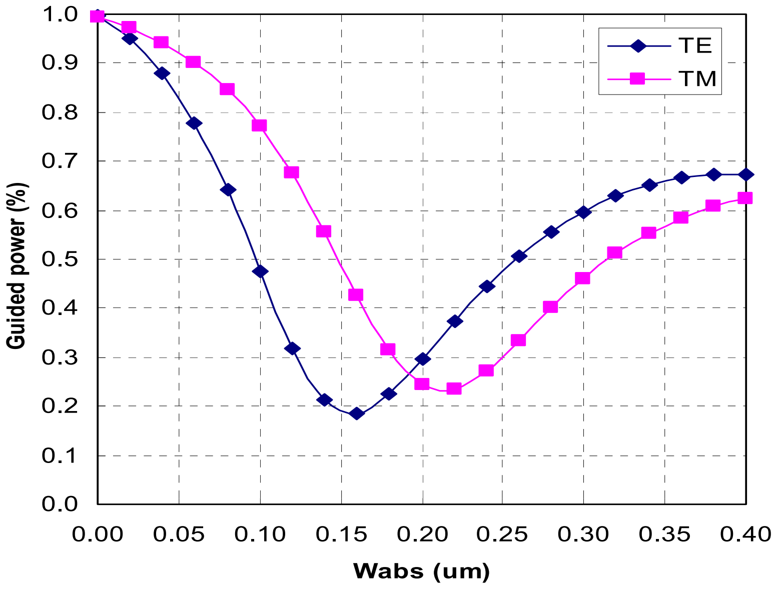

Fig. 10.9 Total guided optical loss in the waveguide APD, as a function of the absorber thickness

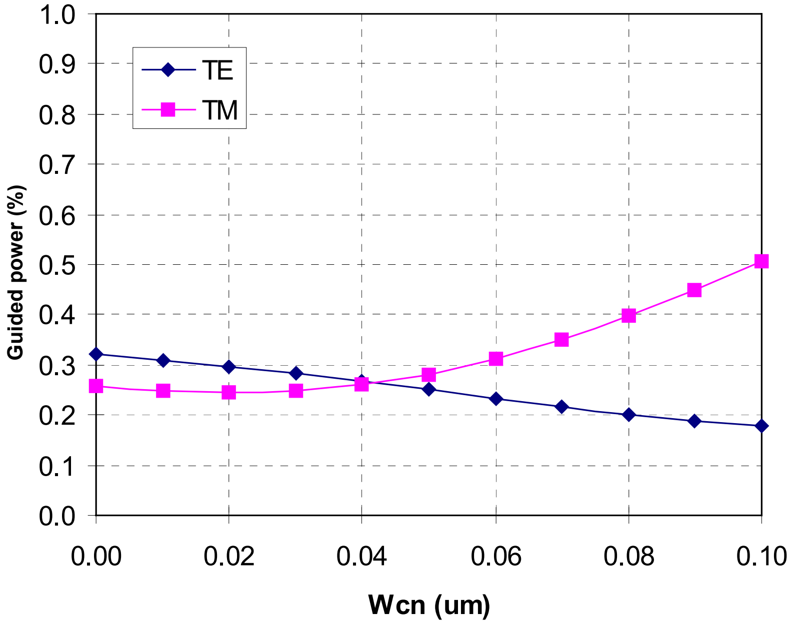

Fig. 10.10 Total guided power loss in the waveguide APD, as a function of charge layer thickness

The APD external quantum efficiency for TE and TM mode was examined using the determined device parameters. An optimum unity-gain external quantum efficiency of >50% was expected from this waveguide APD structure, as shown in Figs. 10.11 and 10.12.

The simulation results also indicated that the total APD external quantum efficiency is strongly dependent on the waveguide length. This issue can be addressed by using a V-groove technique, from which the accuracy of the length of the input waveguide can be controlled within ± 1.0μm, which is in turn determined by photolithography and V-groove etching.

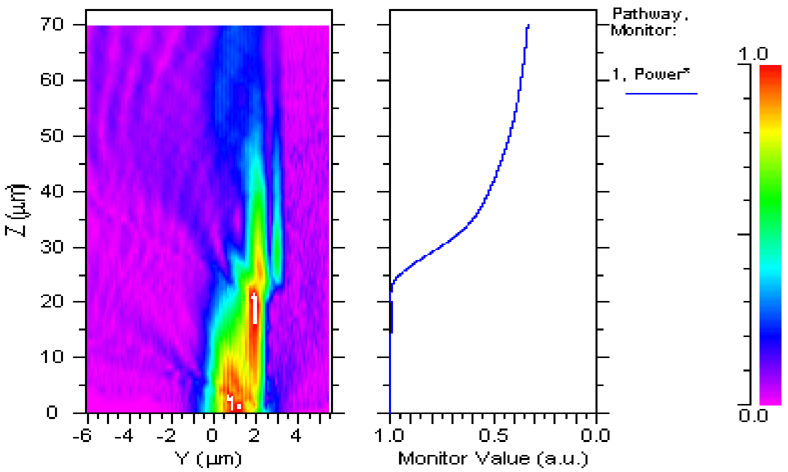

Fig. 10.11 TE mode responsivity as a function of optical path length

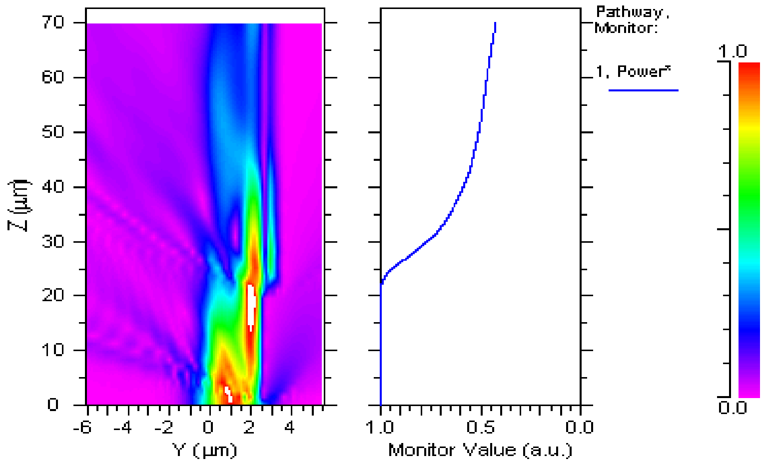

Fig. 10.12 TM mode responsivity as a function of optical path length

10.2 Wafer Growth and Calibration

The first WG-APD wafer was grown at Acatel. The epitaxial structure was grown using Low Pressure Metal Organic Vapor Phase Epitaxy (LP-MOVPE) at 670°C on a semi-insulating InP substrate. The precursors were trimethylgallium, trimethylaluminium, trimethylindium, arsine, phosphine, silane and diethylzinc. As stated above the PSMW consists of a diluted waveguide and two optical matching layers, and both the quaternary alloy ingredients and the refractive index of those layers were calibrated before the final growth of the WG-APD structure. Calibrated results are shown in Fig. 10.13 – 10.17, for the diluted waveguides and the matching layers.

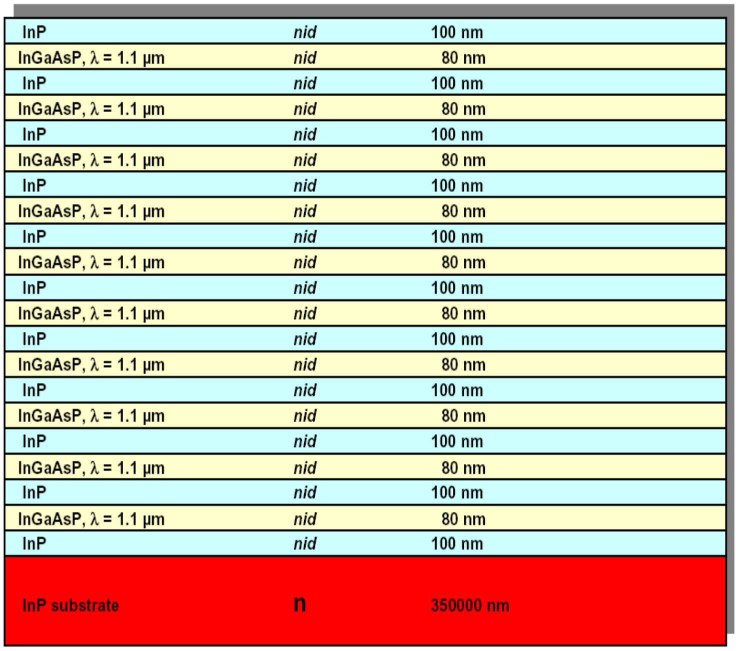

InP	*nid*	100 nm
InGaAsP, λ = 1.1 µm	*nid*	80 nm
InP	*nid*	100 nm
InGaAsP, λ = 1.1 µm	*nid*	80 nm
InP	*nid*	100 nm
InGaAsP, λ = 1.1 µm	*nid*	80 nm
InP	*nid*	100 nm
InGaAsP, λ = 1.1 µm	*nid*	80 nm
InP	*nid*	100 nm
InGaAsP, λ = 1.1 µm	*nid*	80 nm
InP	*nid*	100 nm
InGaAsP, λ = 1.1 µm	*nid*	80 nm
InP	*nid*	100 nm
InGaAsP, λ = 1.1 µm	*nid*	80 nm
InP	*nid*	100 nm
InGaAsP, λ = 1.1 µm	*nid*	80 nm
InP	*nid*	100 nm
InGaAsP, λ = 1.1 µm	*nid*	80 nm
InP	*nid*	100 nm
InGaAsP, λ = 1.1 µm	*nid*	80 nm
InP	*nid*	100 nm
InP substrate	n	350000 nm

Fig. 10.13 Structure of the diluted multimode input waveguide

For the SACM APD structure, a thin (20-nm-thick) *n*-type InP contact layer/etch-stop was initially grown above the InP-matching layer, followed by a 20-nm-thick *n*-type InAlAs contact layer. After that, an un-doped, 150-nm-thick InAlAs layer was grown as the multiplication region. Then a *p*-type InAlAs charge layer of 50-nm was grown with a nominal doping level of $8\times10^{17}\text{cm}^{-3}$, based on the estimated total charge. An un-doped graded layer of 30-nm was inserted between the InAlAs charge layer and the InGaAs absorbing layer in order to smooth the heterojunction. Two 20-nm InGaAsP layers (1.4-μm and 1.1-μm band gap) were used for the same purpose at the InGaAs/InP heterojunction. The absorbing layer thickness was 190-nm, yielding a 0.46μm-thick total active SACM structure, which resulted in a short transit time. SIMS analysis for each layer was performed after the test wafer growth to verify that all the design directives were satisfied.

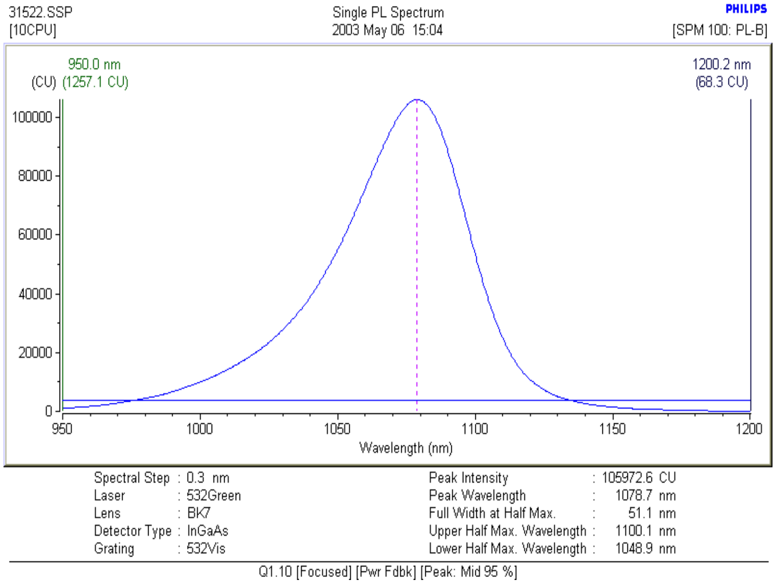

Spectral Step : 0.3 nm
Laser : 532Green
Lens : BK7
Detector Type : InGaAs
Grating : 532Vis

Peak Intensity : 105972.6 CU
Peak Wavelength : 1078.7 nm
Full Width at Half Max. : 51.1 nm
Upper Half Max. Wavelength : 1100.1 nm
Lower Half Max. Wavelength : 1048.9 nm

Q1.10 [Focused] [Pwr Fdbk] [Peak: Mid 95 %]

Fig. 10.14 Photo-luminescence (PL) spectrum of the diluted waveguide

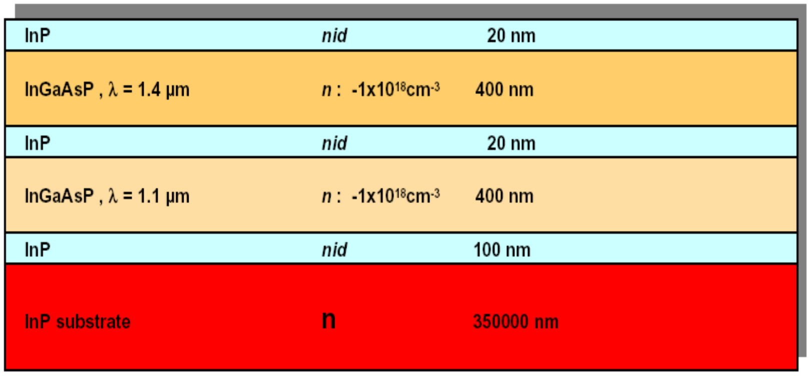

InP	***nid***	**20 nm**
InGaAsP , λ = 1.4 µm	***n* : -1×10^{18}cm^{-3}**	**400 nm**
InP	***nid***	**20 nm**
InGaAsP , λ = 1.1 µm	***n* : -1×10^{18}cm^{-3}**	**400 nm**
InP	***nid***	**100 nm**
InP substrate	**n**	**350000 nm**

Fig. 10.15 Test structure before the matching layer growth

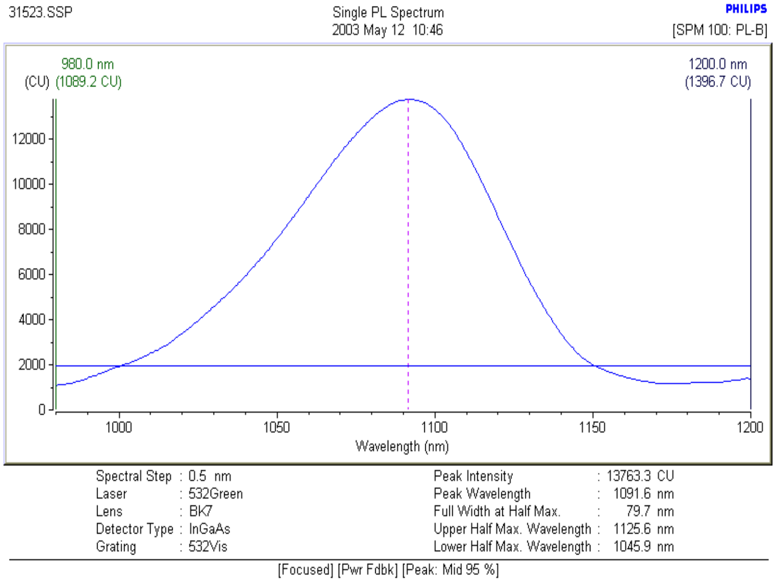

Spectral Step : 0.5 nm
Laser : 532Green
Lens : BK7
Detector Type : InGaAs
Grating : 532Vis

Peak Intensity : 13763.3 CU
Peak Wavelength : 1091.6 nm
Full Width at Half Max. : 79.7 nm
Upper Half Max. Wavelength : 1125.6 nm
Lower Half Max. Wavelength : 1045.9 nm

[Focused] [Pwr Fdbk] [Peak: Mid 95 %]

Fig. 10.16 Photo-luminescence (PL) spectrum of the InGaAsP quaternary, Q=1.1

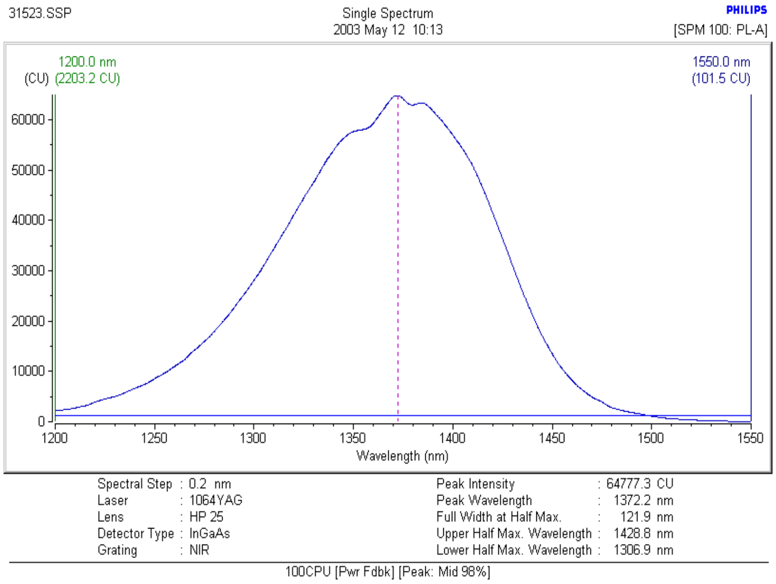

Fig. 10.17 Photo-luminescence (PL) spectrum of the InGaAsP quaternary, Q=1.4

After calibrating all of the sub-structures individually, as discussed, the entire waveguide APD device structure was grown on a 2-inch SI-InP substrate in a single run at Alcatel. The final wafer structure was examined with SIMS, as shown in Fig. 10.18, to guarantee that all the layers were consistent with the design, with regard to thickness and doping levels, prior to further device processing and characterization at the University of Texas at Austin.

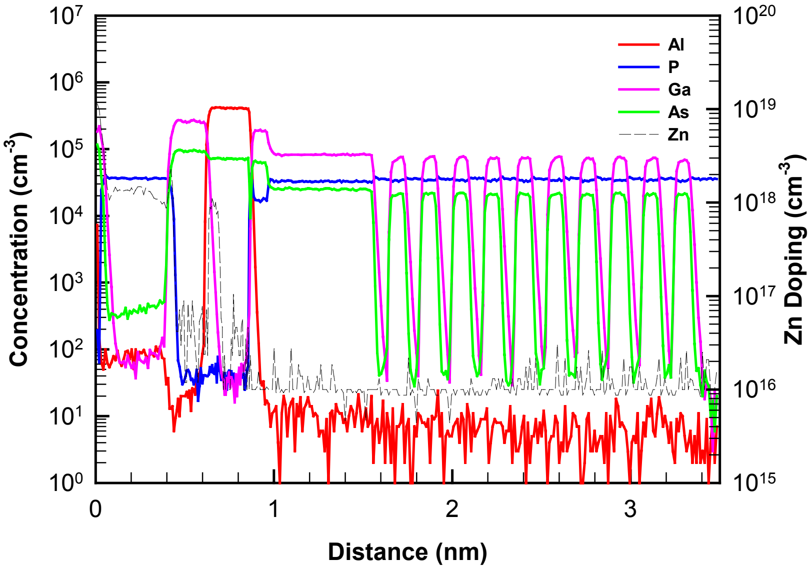

Fig. 10.18 SIMS verification after the whole wafer growth

10.3 Waveguide APD Fabrication

The process flow of the WG-APD was quite different from that of the 10Gb/s APDs, even though both processes were developed for fabricating high-speed devices using air-bridge interconnects. The process started with the p-contact formation. A thin (2000Å) SiO_2 film was pre-deposited prior to the metal deposition, and the p-contact patterns were defined on the silicon dioxide film using standard photolithography (PR AZ5209) to assist in the p-metal lift-off process. A Ti (100Å)/Pt(300Å)/Au(1000Å)/Ti(1000Å) metal film was deposited both as the p-contact metal and as the mesa etching mask. A rapid thermal anneal was then used to form p-type ohmic contacts. Another function of annealing before p-mesa formation is to eliminate possible side etching through the metal-semiconductor interface during the later wet chemical cleaning step, which would degrade the ohmic contact and result in larger contact resistance. The SiO2 mask was then removed before mesa-etching.

The photodiode mesas were patterned using reactive-ion-etching. The etch rate was calibrated carefully prior to device processing, to guarantee that the etch would stop before reaching the InP etch-stop. Here, the p-contact metal was used as the etching mask, and a thin InP layer on top of the second optical matching layer served as the etch stop for wet-chemical etching. A SiO2 film was then deposited for mesa sidewall passivition.

Deep (>4.0μm) trenches around the center signal pads were etched down to the InP substrate to isolate the contact pads between the p- and n-electrodes. The purpose of trench isolation was to realize planarized interconnects between the p-mesa electrode and the p-contact pads.

Contact windows were then opened for n-type ohmic contacts. AuGe(300Å)/Ni(200Å)/Au(1000Å) was used as the n-contact metal. RTA was employed after the n-metal lift-off process at 400°C for 40 seconds. After patterning the n-contact metal, an air-bridge process, very similar to the process described in Chapter 3, was performed to connect the photodiode and the signal pad.

Finally, the photodiode chips were precisely cleaved using the defined V-grooves on the wafer. This enable precise control of the length of each individual waveguide. An anti-reflection (AR) coating was deposited on the photodiode facet to enhance the optical coupling from the optical fiber core to the diluted input waveguide of the photodiodes. This simplified fabrication technology does not utilize etching steps for the waveguide or any other critical alignment steps, thus greatly decreasing the fabrication cost and time, which are the main concerns for the semiconductor industry. The finished waveguide APD is illustrated in Fig. 10.19.

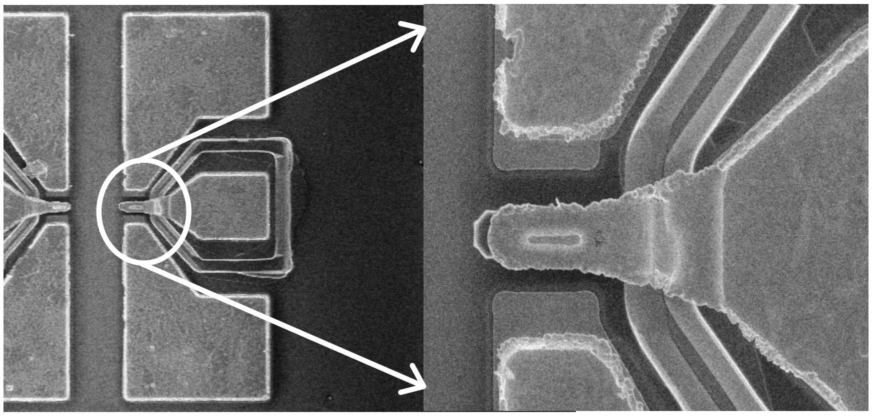

Fig. 10.19 SEM picture of the waveguide APD after full-processing

10.4 Results and Discussion

Fig. 10.20 shows a typical current-voltage characteristic for a 5×20-μm^2 PSMW APD, at different optical input power levels. The breakdown occurred close to 18.5V, and the dark current at 90% of breakdown was in the range of 100 to 500 nA, in various devices across a sample of ~1cm^2 dimension. Capacitance-voltage measurements were also performed in order to examine the punch-through. The C-V results from devices with different mesa diameters indicated a punch-through voltage of ~10 V, and the device capacitance scaled with to the device area, as shown in Fig. 10.21.

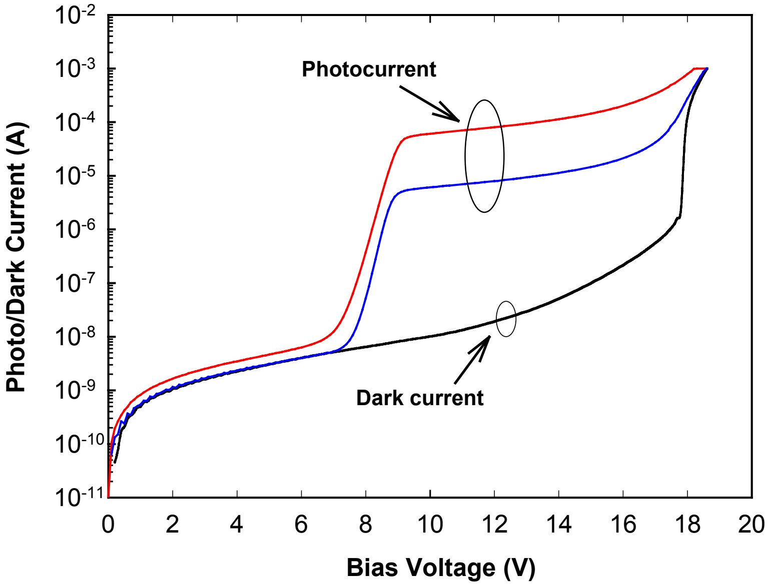

Fig. 10.20 Typical photocurrent and dark current curves of a 5×20-μm^2 APD

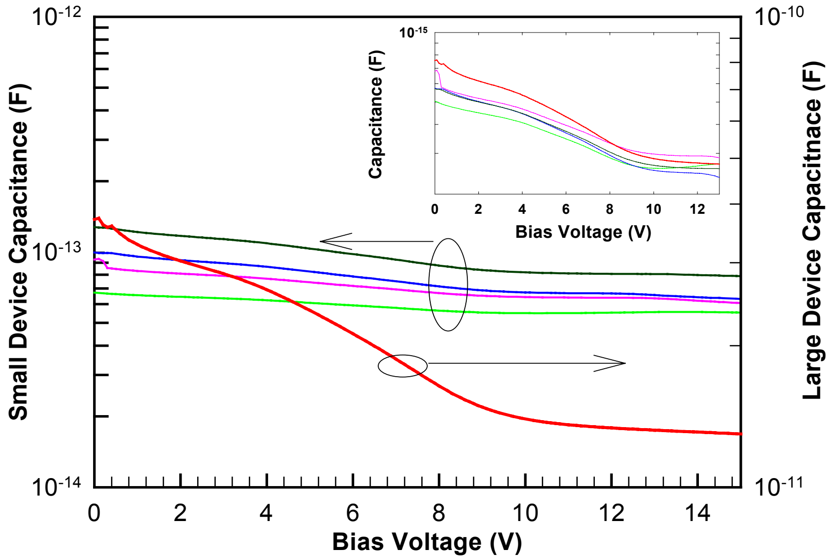

Fig. 10.21 Typical C-V curves from APDs with different mesa sizes

In order to determine the gain at punch-through, the quantum efficiency was measured at a reverse bias of ~10.0 V on a large area device, using top illumination. The measured external quantum efficiency was then compared to the maximum theoretical value based on a 190-nm-thick InGaAs absorber, which was verified by SIMS analysis. The minimum gain at punch-through was determined to be ~1.6, as shown in Figure 10.22.

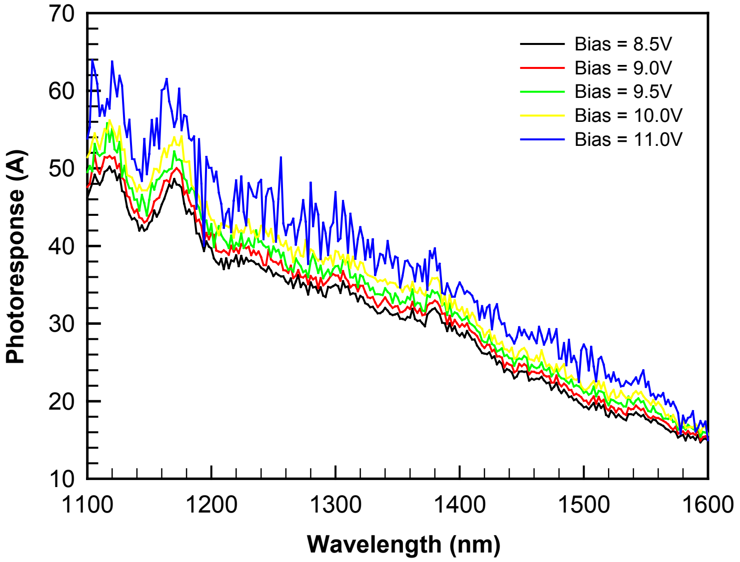

Fig. 10.22 External quantum efficiencies measured at different reverse biases

The –3 dB bandwidths were measured using a heterodyne setup, as shown in Fig. 10.23. A broadest bandwidth of 34.8 GHz was obtained for an avalanche photodiode at 11.0V reverse bias, which corresponded to a multiplication gain of 1.84. At the same gain, the 5×15-μm^2 and the 5×30-μm^2 photodiodes exhibited bandwidths of 35.5 GHz and 31.8 GHz, respectively, which suggests that the bandwidth was primarily dominated by transit-time limitations. Fig. 10.24 shows the measured –3 dB bandwidth versus the DC gain of three different photodiodes that have device areas of 5×20-µm^2, 5×25-µm^{2,} 5×30-µm^2. These devices exhibited a –3 dB bandwidth of 27 GHz at gains up to 4. The gain-bandwidth product was calculated to be ~160 GHz.

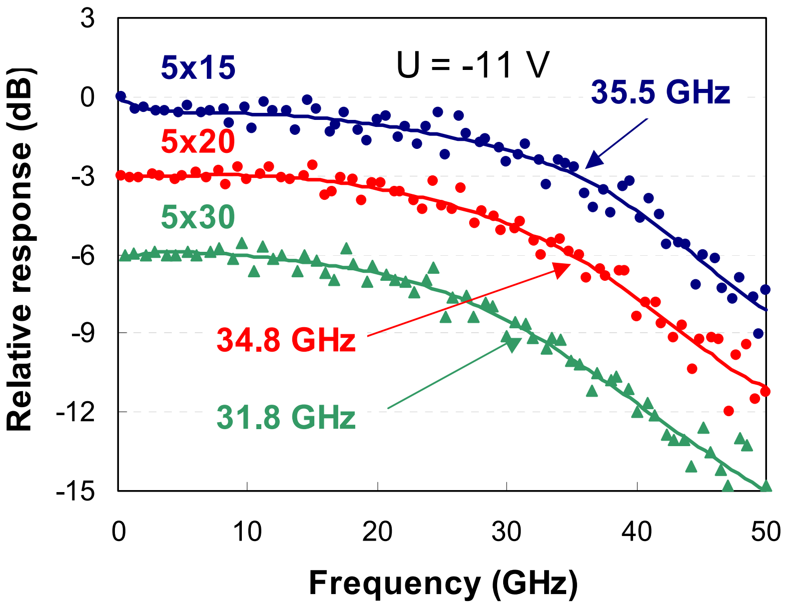

Fig. 10.23 -3dB bandwidths of APDs with various device areas

The unity-gain responsivity of a 5×20-µm^2 diode was measured and compared with the designed values, as shown in Fig. 10.25. The solid line in Fig. 10.25 represents the simulated responsivity of a 5×20-µm^2 diode as a function of waveguide length. The measured responsivity was >0.62, after an antireflection coating was deposited to the input waveguide facet. Owing to the lower refractive index of the multiplication and charge layers, the expected responsivity is lower than that of the evanescently-coupled *p-i-n* photodiodes [10-5].

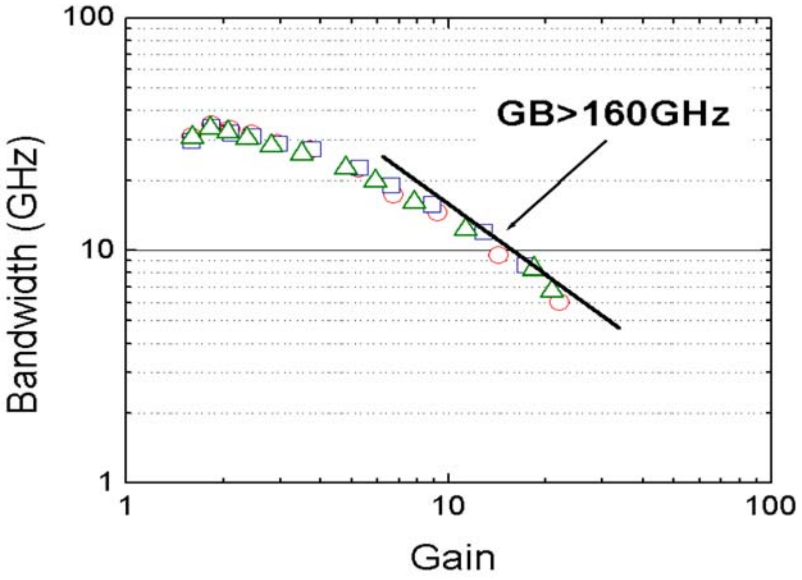

Fig. 10.24 Gain-bandwidth products of various waveguide APDs, with different device area

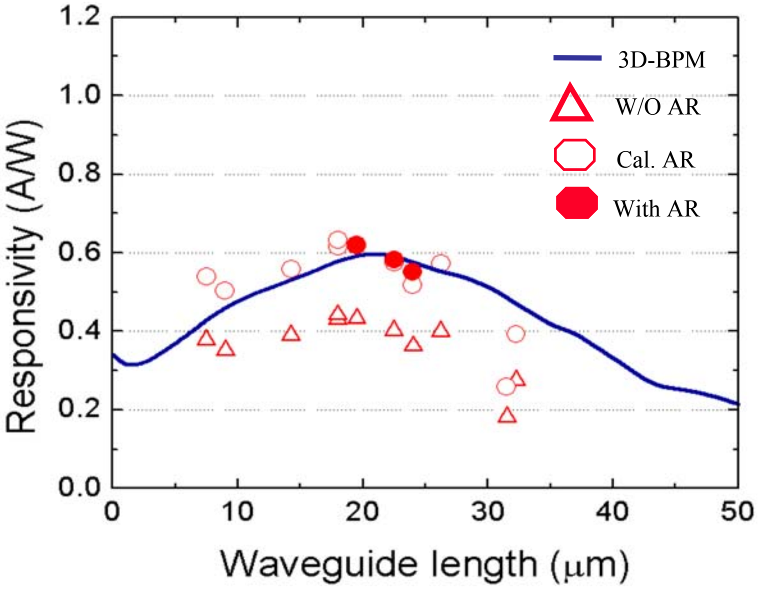

Fig. 10.25 Responsivity measured from APDs that have various waveguide lengths

10.5 Summary

Design of the first evanescently-coupled SACM APD with a planar short multimode waveguide has been completed. Fabrication technology associated with this type of high-speed avalanche photodiode design was also developed. The fabricated photodiodes exhibited high-responsivity (>0.62 A/W) at unity-gain. A broad bandwidth of ≥34.8 GHz was observed at low gains. A gain-bandwidth product of >160 GHz has also been achieved.

Chapter 11

Conclusions and Future Work

11.1 Conclusions

Noise reduction associated with the increasing Al-content and decreasing multiplication-layer thickness was observed from extensive $Al_xGa_{1-x}As$ APD noise measurements. Further investigations of $Al_xGa_{1-x}As$ APD noise at various temperatures indicated that APD multiplication noise, which determines APD sensitivity and speed, was not visibly degraded as ambient temperature increased up to 125^{o}C. By incorporating an $In_{0.53}Ga_{0.47}As$ absorbing layer with an $Al_{0.2}Ga_{0.8}As$ multiplication region using a direct wafer bonding technique, the possibility of obtaining long-wavelength APDs on GaAs substrates through heterogeneous integration was demonstrated. Reasonable multiplication gains, low dark current, and acceptable quantum efficiencies in the long-wavelength range were observed on the wafer-bonded APDs.

A 12 × 12 $In_{0.53}Ga_{0.47}As/In_{0.52}Al_{0.48}As$ SACM avalanche photodiode array was the first demonstrated on MBE-grown material. APDs in this array exhibited uniform distributions of breakdown voltage, photoresponse, dark current, and multiplication gain. An 18 × 18 focal-plane APD array was further developed with improved speed performance (gain-bandwidth >120GHz). Recently, a 40 × 40 InAlAs SACM APD array was also demonstrated on MOCVD-grown material, with low and uniform APD dark currents. High-sensitivity, long-wavelength APDs for sensing applications was another interesting topic of my research. Large-mesa-area $In_{0.53}Ga_{0.47}As/In_{0.52}Al_{0.48}As$ APDs, with a mesa diameter as large as 500µm. Further investigations and analyses of the APD dark current indicated that the bulk leakage current, the dominant component of the total dark current, originates from deep-level-trap related thermal generation in the entire bulk $In_{0.53}Ga_{0.47}As$ absorber.

Studies of SACM APDs with thin InAlAs multiplication regions indicated that a sensitivity better than -29.6dBm at a bit-error-rate of 10^{-9} and data-rate of 10Gb/s is attainable. This study also indicated that 10Gb/s APD receiver sensitivity could be further improved as long as the APD dark current level, gain-bandwidth product, and noise can be optimized through device structure and MBE growth improvements. By improving the optical coupling efficiency using the combination of a diluted multimode waveguide with an optimized thin-multiplication-region InGaAs-InAlAs SACM APD structure, a novel 40Gb/s evanescently coupled waveguide APD has been demonstrated, with a unity-gain responsivity >0.62A/W, low-gain bandwidth >34GHz, and a gain-bandwidth product >160GHz at high gains. The V-groove cleaving method, together with the cost-effectiveness associated with the simplified APD device fabrication process, made this novel technique a promising APD solution for future 40Gb/s telecommunication applications.

11.2 Future Perspectives

The APD multiplication region characteristics will determine the speed and noise performance at high gains. In Chapter 4, it was shown that a high-Al-ratio AlGaAs APD with a thin multiplication layer exhibited very low multiplication noise that is comparable to silicon APDs. Furthermore, impact-ionization-engineered

APDs exhibited multiplication noise even lower than silicon APDs. The possibility of heterogeneous integration between III-V compounds, by means of direct wafer bonding, has been proved through InGaAs-InP-GaAs-AlGaAs APD and InGaAs-InAlAs-GaAs-AlGaAs APD studies, as discussed in Chapter 6. Extremely low-noise, ultra-high-speed APDs are therefore expected by integrating long-wavelength absorbing materials, such as InGaAs, with either a high-Al content gain region or with an IIE structure.

Further improvements of both epitaxial layer quality and device processing quality are critical for obtaining larger-scale long wavelength focal-plane APD arrays with lower dark currents and better uniformities. Flip-chip bonding technology is also a critical technique for further integration of APD arrays with high-speed read-out circuits to build a fully functional module for 3-D imaging systems.

Even though one of the best sensitivity results has been achieved during my 10Gb/s APD receiver study, room still exists for further sensitivity improvement. Using a thinner multiplication region (<200nm) is one option, if APD dark current could be further minimized. Additionally, continuing the exploration of low noise IIE structures on InP-based material systems is also a feasible way to obtain high-sensitivity telecommunication APD receivers. So far, two types of IIE structures, one with a single-well gain region and another with a graded gain region, have been successfully incorporated into SACM APDs. Preliminary investigations on these APDs indicated that, even though those APDs exhibited acceptable gains, the high (tunneling) leakage current is still a big issue for their practical applications. Further exploration of long-wavelength IIE structures should be continued with emphasis on decreasing total APD dark current level. Recent progresses on high-Sb content AlAsSb alloy studies might be an immediate hope for the InP-based IIE research.

For both 10Gb/s and 40Gb/s applications, a semiconductor optical amplifier (SOA) combined with a high-power *p-i-n* structure is also promising for achieving “amplifler-less”, high-sensitivity optical receivers, by using optical amplification. Recently, my observation of high-power *p-i-n* photodiode sensitivity at 10Gb/s data-rate indicated that our current waveguide *p-i-n* photodiodes, which are mature for in-plane integration with SOAs, are capable of directly driving a 50-Ω load at high-speed. Subsequent advances in SOAs and further integration with waveguide *p-i-n* photodiodes are therefore expected to achieve high sensitivity SOA + PIN receivers for the telecommunication applications.

Appendix A: Publications

Scientific Journals

[1] X. G. Zheng, J. B. Hurst, X. Sun, S. Wang, A.L. Holmes, Jr., J. C. Campbell, “Long Wavelength InGaAs/InP–GaAs/AlGaAs Avalanche Photodiode Implemented by Direct Wafer Bonding”, Photonics Technology Letters, submitted.

[2] X. G. Zheng, J. Hsu, et al., “Long-wavelength InGaAs/InAlAs Large-area APDs and Arrays”, Photonic Technology Letters, IEEE, to be published.

[3] X. G. Zheng, J. Hsu, X. Sun, J. B. Hurst, X. Li, S. Wang, A.L. Holmes, Jr., J. C. Campbell, “A 12 x 12 $In_{0.53}Ga_{0.47}As/In_{0.52}Al_{0.48}As$ avalanche photodiode array,” IEEE J. Quant. Elec., vol. 38, no. 11, pp. 1536-40, Nov. 2002.

[4] X. G. Zheng, X. Sun, S. Wang, P. Yuan, G. S. Kinsey, A.L. Holmes, Jr., B. G. Streetman, J. C. Campbell, “Multiplication Noise of AlxGa1-xAs Avalanche Photodiodes with High Al Concentration and Thin Multiplication Region,” Appl. Phys. Lett. Vol. 79, no. 24, pp. 3833-3835, June 2001.

[5] X. G. Zheng, P. Yuan, X. Sun, G. S. Kinsey, A. L. Holmes, B. G. Streetman, J. C. Campbell, “Temperature Dependence of the Ionization Coefficients of AlxGa1-xAs”, IEEE Journal of Quantum Electronics, vol. 36, no. 10, Oct. 2000, pp.1168-1173.

[6] S. Demiguel, X. Zheng, N. Li, X. Li, J. Campbell, J. Decobert, N. Tscherptner and A. Anselm: High-responsivity and high-speed evanescently-coupled avalanche photodiodes integrating a short multimode. Electron. Lett. vol. 39, no. 5, pp. 1848-1849, October 2003.

[7] Joe C. Campbell, Shuling Wang, X. G. Zheng, G. S. Kinsey, A. L. Holmes, Jr., X. Sun, R. Sidhu, and P. Yuan, “Ultra-low-noise avalanche photodiodes,” Proc. SPIE, vol. 4283, pp.480-488, 2001

[8] Xiaowei Li, Xiaoguang Zheng, Shuling Wang, Feng Ma, J.C. Campbell, “Calculation of gain and noise with dead space for GaAs and AlxGa1-xAs avalanche photodiode”, IEEE Transactions on Electron Devices, Vol.49 No.7, pp. 1112 –1117, Jul. 2002

[9] G. Karve, X.G. Zheng, X. Zhang, X. Li, N. Li, S. Wang, F. Ma, A. Holmes, Jr., J. C. Campbell, G. S. Kinsey, J. C. Boisvert, T. D. Isshiki, R. Sudharsanan, D. S. Bethune, and W. P. Risk, “Geiger mode operation of and InGaAs-InAlAs avalanche

photodiode," IEEE J. Quant. Elec. , vol. 39, no. 10, pp.1281-6, Oct. 2003.

[10] P. Yuan, S. Wang, X. Sun, X. G. Zheng, A. L. Holmes, Jr, and J. C. Campbell, "Avalanche photodiodes with an impact-ionization-engineered multiplication region," IEEE Photonics Technology Letters, vol.12, no.10, Oct. 2000, pp.1370-2.

[11] X. Sun, S. Wang, X. G. Zheng, X. Li, J. C. Campbell, and A. L. Holmes, Jr., "1.31μm GaAsSb resonant-cavity-enhanced separate absorption, charge and multiplication avalanche photodiodes with low noise," J. Appl. Phys., vol. 93, no.1, pp. 774-6, Jan. 2003.

[12] S. Wang, F. Ma, X. Li, R. Sidhu, X. G. Zheng, X. Sun, A. L. Holmes, Jr., and J. C. Campbell, "Ultra-low noise avalanche photodiodes with a 'centered-well' multiplication region," IEEE J. Quan. Elec., vol. 39, no. 2, pp.375-378, Feb. 2003.

[13] X. Sun, S. Wang, J. Hsu, R. Sidhu, X.G. Zheng, X. Li, J. C. Campbell, and A. L. Holmes, Jr, "GaAsSb: a novel material for near infrared photodetectors on GaAs substrates," IEEE J. Select. Topics Quantum Electron., vol. 8, no. 4, pp. 817-822, July/August 2002.

[14] Xiaowei Li; Ning Li; Xiaoguang Zheng; Demiguel, S.; Campbell, J.C.; Tulchinsky, D.A.; Williams, K.J., "High-saturation-current InP-InGaAs photodiode with partially depleted absorber", IEEE, Photonics Technology Letters, Vol.15, No.9, pp.1276 - 1278, Sep. 2003

[15] N. Li, X. Li, S. Demiguel, X. Zheng, J. C. Campbell, D. A. Tulchinsky, K. J. Williams, T.D. Isshiki, G.S. Kinsey, R. Sudharsansan, "High-Saturation-Current Charge-Compensated InGaAs/InP Uni-Traveling-Carrier Photodiode," Photon. Tech. Lett., Vol. 16 No.3, pp864-866, 2004

[16] S. Wang, J. B. Hurst, F. Ma, R. Sidhu, X. Sun, X. G. Zheng, A. L. Holmes, Jr., J. C. Campbell, A. Huntington, and L. A. Coldren, "Low-noise impact-ionization-engineered avalanche photodiodes grown on InP substrate," IEEE Photonics Tech. Lett., vol. 14, no. 12, pp. 1722-24, 2002.

[17] S. Demiguel, N. Li, X. Li, X. Zheng, J. Kim, J. Campbell, H. Lu and A. Anselm: Very high-responsivity evanescently-coupled photodiodes integrating a short planar multimode waveguide for high-speed applications. IEEE Photon. Technol. Lett. ,vol. 15, no. 2, December 2003. S. Wang, R. Sidhu, G. Karve, F. Ma,
[18] X. Li, X. G. Zheng, J. B. Hurst, X. Sun, N. Li, A. L. Holmes, Jr., and J. C. Campbell, "A study of low-bias photocurrent gradient of avalanche photodiodes," IEEE Trans. Elect. Dev., vol. 49, no. 12, pp. 2107-2113, Dec. 2002.

[19] F. Ma, S. Wang, X. Li, K. A. Anselm, X. G. Zheng, A. L. Holmes, Jr., and J. C. Campbell, "Monte Carlo simulation of low-noise avalanche photodiodes with heterojunctions," J. Appl. Phys., vol. 92, no. 8, pp. 4791-5, Oct. 2002.

[20] S. Wang, R. Sidhu, X.G. Zheng, X. Sun, A.L. Holmes, Jr., and J. C. Campbell, “Low noise avalanche photodiodes with a graded Impact-Ionization-Engineered multiplication region,” IEEE Photonics Technology Letters, vol. 13, no. 12, pp.1346-8, 2001

[21] N. Li, R. Sidhu, X. Li, F. Ma, S. Demiguel, X. Zheng, A. L. Holmes Jr., D. Tulchinsky, K. J. Williams, "Charge-compensated high-saturation-current InGaAs/InAlAs uni-traveling-carrier photodiode," Electron. Lett., to be published

[22] N. Li, R. Sidhu, X. Li, F. Ma, X. Zheng, S. Wang, G. Karve, S. Demiguel, A. L. Holmes, Jr., and J. C. Campbell, "InGaAs/InAlAs Avalanche Photodiode with Undepleted Absorber," Appl. Phys. Lett., Vol. 82 No.13, pp2175-2177, Mar. 2003

[23] Xiaowei Li, Ning Li, Stephen Demiguel, Xiaoguang Zheng, Joe C. Campbell,H. Hoe Tan, Chennupati Jagadish, David L. Tulchinsky, Keith J. Williams, "A Partially Depleted Absorber Photodiode with Graded Doping Injection Regions", accepted by IEEE, Photonics Technology Letters

[24] Shuling Wang, Feng Ma, Xiaowei Li, Gauri Karve, Xiaoguang Zheng, and Joe C. Campbell, “Analysis of breakdown probabilities in avalanche photodiodes using a history-dependent analytical model,” Appl. Phys. Lett. , vol. 82, pp. 1971-1973, 2003.

International Conferences

[25] X. G. Zheng, J. Hsu, X. Sun, J. B. Hurst, X. Li, S. Wang, A.L. Holmes Jr., J. C. Campbell, “A 12 × 12 InGaAs/InAlAs Avalanche Photodetector Array”, OSA/IPR Conference, 2002

[26] S. Demiguel, X. Zheng, N. Li, X. Li, J. Campbell, J. Decobert, N. Tscherptner and A. Anselm : Evanescently-coupled avalanche photodiodes integrating a short multimode waveguide for high-responsivity and high-speed applications. 29th Optical Fiber Conference (OFC), Los Angeles, USA, Paper TuM3, March 2004.

[27] J. B. Hurst, X. G. Zheng, X. Sun, S. Wang, Joe C. Campbell, and Archie L. Holmes, Jr., “Long wavelength InGaAs/InAlAs/InP-GaAs/AlGaAs avalanche photodiode implemented by direct wafer bonding,” 2002 Electronic Materials Conference, Santa Barbara, California, June, 2002.

[28] S. Demiguel, X. Li, Ning Li, H. Chen, X. Zheng, J. C. Campbell, J. Wei and A. Anselm: Partially depleted absorber waveguide photodiodes. 17th IEEE Lasers & Electro-optics Society (LEOS), Puerto Rico, Submitted paper, November 2004.

[29] X. Li, N. Li, X. Zheng, S. Demiguel, J. Campbell, D. Tulchinsky and K. Williams: High-speed High-saturation-current partially depleted absorber photodetecters, 15th IEEE Lasers & Electro-optics Society (LEOS), Edimbourg, Scotland, Post Deadline Paper, November 2002.

[30] X. Li, N. Li, X. Zheng, S. Demiguel, J. Campbell, D. Tulchinsky and K. Williams : High-speed High-saturation-current InP/$InGa_{0.53}As_{0.47}$ Photodiode with partially depleted absorber 28th Optical Fiber Conference (OFC), Atlanta, USA, paper WF3, March 2003.

[31] X. Sun, S. Wang, X. G. Zheng, X. Li, J. C. Campbell, and A. L. Holmes, Jr., "Resonant-cavity-enhanced GaAsSb avalanche photodiodes with separate absorption, charge and multiplication regions operating at 1300nm," Optical Amplifiers and Their Applications and Integrated Photonics Research, Vancouver, Canada, July 14-19, 2002.

[32] S. Wang, R. Sidhu, X.G. Zheng, X. Sun, A.L. Holmes, Jr., and J. C. Campbell, "Low noise avalanche photodiodes with a graded Impact-Ionization-Engineered multiplication region", 59th Annual Device Research Conference, Latest news.

[33] S. Wang, X. Sun, X. G. Zheng, A. L. Holmes, J. C. Campbell, and P. Yuan, "Avalanche photodiodes with an impact-lonization-engineered multiplication region," Lasers and Electro-Optics Society 2000 Annual Meeting, 13th Annual Meeting, Vol.1, Page(s): 9 –10, 2000.

[34] N. Li, X. Li, S. Demiguel, X. Zheng, J. C. Campbell, D. A. Tulchinsky, K. J. Williams, T.D. Isshiki, G.S. Kinsey, R. Sudharsansan, "High-Saturation-Current Charge-Compensated InGaAs/InP Uni-Traveling-Carrier Photodiode," Lasers and Electro-Optics Society, 2003. LEOS 2003. The 16th Annual Meeting of the IEEE , Volume: 2 , 2003 Pages:790 – 791

[35] S. Wang, J. B. Hurst, F. Ma, R. Sidhu, X. G. Zheng, A. L. Holmes, Jr., J. C. Campbell, A. Huntington, and L. A. Coldren, "Low-noise InP-based avalanche photodiodes with an impact-ionization-engineered multiplication region," 2002 IEEE/LEOS Annual Meeting Conf. Proc., Glasgow, Scotland, pp. 488-489.

[36] X. Sun, S. Wang, R. Sidhu, X. G. Zheng, X. Li, J. C. Campbell, and A. L. Holmes, Jr., "MBE growth and device performance of GaAsSb resonant-cavity-enhanced avalanche photodiodes with separate absorption, charge and multiplication regions," 2002 Electronic Materials Conference, Santa Barbara, California, June, 2002.

Papers not directly related to current research topics

[37] X. G. Zheng, et al., “Development of Novel GaAs Logic Circuits and Applications on GaAs VLSIs”, Technical report, funded by Advanced GaAs Research Project, China, 1996

[38] X. G. Zheng, et al., “A 3000 Gates Very-High-Speed GaAs Gate Array”, Technical report, funded by Advanced GaAs Research Project, China, 1995

[39] X. G. Zheng, et al., “A 2-K GaAs Gate Array”, ASIC, 1993, 1st International Conference on, Beijing, China, 1993

[40] X. G. Zheng, et al., “A 2-bit GaAs High Speed A/D converter”, Semiconductor Information, No. 4, pp 48-53, 1992

[41] Xu, Yanyang; Zheng, Xiaoguang; Hao, Jingchen,“Direct Coupled FET Logic (DCFL) circuit for GaAs LSIC application”, Microwave and Millimeter Wave Technology Proceedings, 1998. ICMMT '98. 1998 International Conference on, 1998 Page(s): 913 –916

[42] Xu, Yanyang; Zheng, Xiaoguang; Hao, Jingchen; Song Macheng, “A GaAs 1:8 demultiplexer on 1 K-gates GaAs gate array”, ASIC, 1996., 2nd International Conference on , 1996 Page(s): 293 –296

Bibliography

Chapter 1

[1-1] Kazutoshi Kato, “Ultrawide-Band/High-Frequency Photodetectors,” IEEE Transactions on Microwave Theory and Techniques, Vol. 7, No. 7, July 199

[1-2] A. Chin, and T. Chang,” Multilayer Reflectors by Molecular Beam Epitaxy for Resonance Enhanced Absorption in Thin High-Speed Detectors,” *J. Vac. Sci. and Tech.*, vol. 8, no. 2, pp. 339-342, 1990.

[1-3] K. Kishino, M. Unlu, J-I. Chyi, J. Reed, L. Arsenault, and H. Morkoc, “Resonant Cavity Enhanced (RCE) Photodetectors,” *IEEE J. Quantum Electron.*, vol. 27, no. 8, pp. 2025-2034, 1991.

[1-4] S.W. Corzine, R.S. Geels, J.W. Scott, R-H, Yan, L.A. Coldren, “Design of Fabry-Perot surface-emitting lasers with a periodic gain structure,” *IEEE J. Quantum Electron.*, vol. 25, no. 6, pp. 1513-1524, 1989.

[1-5] A. G. Dentai, R. Kuchibhotla, J.C. Campbell, C. Tsai, and C. Lei, “High-quantum-efficiency, long-wavelength, InP/InGaAs microcavity photodiode,” *Electron. Lett.*, vol. 27, no. 23, pp. 2125-2127, 1991.

[1-6] K. Kato, A. Kozen, Y. Muramoto, Y. Itaya, T. Nagatsuma, and M. Yaita, “110-GHz, 50%-efficiency mushroom-mesa waveguide p-i-n photodiode for a 1.55 µm wavelength,” *IEEE Photon. Technol. Lett.*, vol. 6, no. 6, pp. 719-721, 1994.

[1-7] St. Kollakowski, A. Strittmatter, E. Dröge, E. H. Böttcher, D. Bimberg, O. Reimann, and K. Janiak, “65 GHz InGaAs/InAlGaAs/InP waveguide integrated photodetectors for 1.3-1.55 µm wavelength regime,” *Appl. Phys. Lett.*, vol. 74, no. 4, pp. 612-614, 1999.

[1-8] K. S. Giboney, R. L. Nagarajan, T. E. Reynolds, S. T. Allen, R. P. Mirin, M J. W. Rodwell, and J. E. Bowers, “Traveling-wave photodetectors with 172-GHz bandwidth and 76-GHz bandwidth-efficiency product,” *IEEE Photon. Technol. Lett.*, vol. 7, no. 4, pp. 412-414, 1995.

[1-9] G. S. Kinsey, J.C. Campbell and A.G. Dentai, “Waveguide Avalanche Photodiode Operating at 1.55 µm with a Gain-Bandwidth Product of 320 GHz,” IEEE Photonics tech. lett., 2001, 13, (8), pp. 842-844.

[1-10] Y. Shao, R.W. Silverman, R. Farrell, L. Cirignano, R. Grazioso, K. S. Shah, G. Visser, M. Clajus, T. O. Tummer, S. R. Cherry, "Design Studies of A High Resolution PET Detector Using APD Arrays", IEEE Trans. On Nuclear Science, Vol. 47, No. 3, 1051-1057, June 2000

[1-11] S. Vasile, R. J. Wilson, S. Shera, D. Shamo, M. R. Squillante, "High Gain Avalanche Photodiode Arrays for DIRC Applications", IEEE Trans. On Nuclear Science, Vol. 46, No. 3, 848-852, August 1999

[1-12] R. F. Grazioso, R. Farrell, L. Cirignano, K. Shah, "APD Arrays for Scintillating Fiber Readout", Nuclear Science Symposium, IEEE Vol. 2, 722 –724, 1999

[1-13] E. Gramsch, M. Szawlowski, S. Zhang, and M. Madden, "Fast, High Density Avalanche Photodiode Array", IEEE Trans. On Nuclear Science, Vol. 41, No. 4, 762-766, August 1994

Chapter 2

[2-1] S.E. Miller, I.P Kaminov, *Optical Fiber Telecommunications II*, Academic Press, 1997

[2-2] Kazutoshi Kato, "Ultrawide-Band/High-Frequency Photodetectors," IEEE Transactions on Microwave Theory and Techniques, Vol. 7, No. 7, July 199

[2-3] Stephen B. Alexander, "Optical Communication Receiver Design," SPIE Optical Engineering Press, 1997

[2-4] W. L. Hayden, M. A. Krainak, D. M. Cornwell, A. W. Yu, and X. Sun, "Overview of laser communication technology at NASA Goddard space flight certer," in *Proc. SPIE*, vol. 1866, pp. 45-55, 1993.

[2-5] P.W. Kruse, L.D. McGlauchlin, R.B. McQuistan, *Elements of Infrared Technology: generation, transmission, and detection*, Wiley, New York, 1962.

[2-6] J.E. Bowers, and Y.G. Wey, "High-speed Photodetectors," *Handbook of Optics*, vol.1, McGraw-Hill, New York, 1995.

[2-7] Y.G. Wey, K.S. Giboney, J.E. Bowers, M.J.W. Rodwell, P. Silvestre, P. Thiagarajan, and G.Y. Robinson, "108 GHz GaInAs/InP p-I-n Photodiodes with Integrated Bias Tees and Matched Resistors," *IEEE Photon. Tech. Lett.*, vol. 5, no. 11, pp.1310-1312, 1993.

[2-8] P. Bhattacharya, *Semiconductor Optoelectronic Devices*, Prentice-Hall, Englewood Cliffs, New Jersey, 1994.

[2-9] S.Y. Chou, M.Y. Liu, ”Nanoscale tera-hertz metal-semiconductor-metal photodetectors,” *IEEE J. Quantum Electron.*, vol. 28, no.10, pp.2358-2368, 1992.

[2-10] N. Emeis, H. Schumacher, and H. Beneking, “High-Speed GaInAs Schottky Photodetector,” *Electron. Lett*., vol. 21, no. 5, pp. 181, 1985.

[2-11] S. Forrest, “Sensitivity of Avalanche Photodetector Receivers for High-Bit-Rate Long-Wavelength Optical Communication Systems,” *Semiconductors and Semimetals, vol. 22, Lightwave Communications Technology*, Orlando, FL, Academic, 1985.

[2-12] A.Chin and T. Y. Chang, “Enhancement of Quantum Efficiency in Thin Photodiode through Absorptive Resonance,” vol. 9, no. 3, March, 1991 pp.321-328

[2-13] A. Chin, and T. Chang,” Multilayer Reflectors by Molecular Beam Epitaxy for Resonance Enhanced Absorption in Thin High-Speed Detectors,” *J. Vac. Sci. and Tech.*, vol. 8, no. 2, pp. 339-342, 1990.

[2-14] K. Kishino, M. Unlu, J-I. Chyi, J. Reed, L. Arsenault, and H. Morkoc, “Resonant Cavity Enhanced (RCE) Photodetectors,” *IEEE J. Quantum Electron.*, vol. 27, no. 8, pp. 2025-2034, 1991.

[2-15] J. E. Bowers and C. A. Burrus, “Ultra-wideband Long-wavelength pin Photodiodes,” J. Lightwave Technology, vol. 5, no. 10, 1987, pp.1339-1350

[2-16] G.A. Baraff, “Distribution functions and ionization rates for hot electrons in semiconductors,” Physics Review, vol. 128, pp. 2507-2517, 1962

[2-17] G. A. Baraff, “Current fluctuations in a semiconductor under the conditions of impact ionization and avalanche breakdown,” Fiz. Ttver. Tela, vol. 6, pp. 2418-2427, 1964

[2-18] R.J. McIntyre, “Multiplication noise in uniform avalanche diodes,” *IEEE Trans. on Electron Dev.*, vol. 13, no. 1, 1966

[2-19] R. B. Emmons, “Avalanche-Photodiode Frequency Response,” Journal of Applied Physics, vol. 38, no. 9, August 1967, pp.3705-3714

[2-20] C. Hu, K. A. Anselm, B. G. Streetman, and J. C. Campbell, “Noise characteristics of thin multiplication region GaAs avalanche photodiodes,” *Appl. Phys. Lett*., vol. 69, no. 24, pp. 3734-3736, 1996.

[2-21] P. Yuan, K. A. Anselm, C. Hu, H. Nie, C. Lenox, A. L. Holmes, B. G. Streetman, J. C. Campbell, and R.J. McIntyre, *IEEE Trans. on Electron Devices* 46, 8, 1632 (1999).

[2-22] S. A. Plimmer, et al., “Investigation of Impact Ionization in Thin GaAs Diodes”, IEEE Trans. On Electron Devices, Vol 43, No. 7, July 1996.

[2-23] P. Yuan, H. Chad, K. A. Anselm, C. Lenox, H. Nie, H. L. Holmes, B. G. Streetman, and J. C. Campbell, "Impact Ionization Characteristics of III-V Semiconductors in a Wide Range of Multiplication Region Thickness," *IEEE J. Quantum Electron.*, vol. 36, no. 2, pp.198-204, Feb, 2000.

[2-24] X. G. Zheng, X. Sun, S. Wang, P. Yuan, G. S. Kinsey, A.L. Holmes, Jr., B. G. Streetman, J. C. Campbell, "Multiplication Noise of AlxGa1-xAs Avalanche Photodiodes with High Al Concentration and Thin Multiplication Region," Appl. Phys. Lett. Vol. 79, no. 24, pp. 3833-3835, June 2001.

[2-25] P. Yuan, S. Wang, X. Sun, X. G. Zheng, A. L. Holmes, Jr., and J. C. Campbell, "Avalanche photodiodes with an impact-ionization-engineered multiplication region," *IEEE Photo. Tech. Lett.,* vol.12, pp. 1370-1372 (2000).

Chapter 3

[3-1] S. Forrest, M. DiDomenico, R. G. Smith, H. J. Stocker, "Evidence for tunneling in reverse-biased III-V photodetector diodes," *Appl. Phys. Lett*., vol. 36, no. 7, pp. 580-582, 1980.

[3-2] R. Chin, N. Holonyak Jr., G. E. Stillman, J. Y. Tan, and K. Hess, *Electron. Lett.* 16, 467 (1980)

[3-3] I. Watanabe, M. Tsuji, M. Hayashi, K. Makita, and K. Taguchi, *J. Lightwave Technol.* 15, 1012 (1997)

[3-4] C. Cohen-Jonathan, L. Giraudet, A. Bonzo, and J.P. Praseuth, "Waveguide AlInAs/GaAlInAs avalanche photodiode with a gain-bandwidth product over 160GHz," *Electronics Letters*, vol. 33, no. 17, pp.1492-1493, 1997

[3-5] C. Lenox, H. Nie, P. Yuan, G. Kinsey, A. L. Holmes, Jr., B. G. Streetman, and J. C. Campbell, "Resonant-Cavity InGaAs-InAlAs avalanche photodiodes with gain-bandwidth product of 290 GHz," *IEEE Photon. Technol. Lett*., vol. 11, no. 9, pp. 1162-1164, 1999

[3-6] P. Bhattacharya, *Semiconductor Optoelectronic Devices*, Prentice-Hall, pp. 349-351, 1994.

[3-7] L.E. Tarof, J. Yu, R. Bruce, D.G. Knight, T. Baird, and B. Oosterbrink, "High-Frequency Performance of Separate Absorption Grading, Charge, and Multiplication InP/InGaAs Avalanche Photodiodes," *IEEE Photon. Tech. Lett.*, vol. 5, no. 6, pp.672-674, 1993.

[3-8] J. S. Ng, C. H. Tan, J. P. R. David, G. Hill, and G. J. Rees, “Field Dependence of Impact Ionization Coefficients in $In_{0.53}Ga_{0.47}As$,” IEEE Trans. on Electron Devices, vol. 50, no. 4, April 2003, pp. 901-906

[3-9] M. Levinstein, S. Rumyantsev and M. Shur, “Handbook Series on Semiconductor Parameters,” vol. 2

[3-10] A.Chin and T. Y. Chang, “Enhancement of Quantum Efficiency in Thin Photodiode through Absorptive Resonance,” vol. 9, no. 3, March, 1991 pp.321-328

[3-11] Kazutoshi Kato, “Ultrawide-Band/High-Frequency Photodetectors,” IEEE Transactions on Microwave Theory and Techniques, Vol. 7, No. 7, July 199

[3-12] J. E. Bowers and C. A. Burrus, “Ultra-wideband Long-wavelength pin Photodiodes,” J. Lightwave Technology, vol. 5, no. 10, 1987, pp.1339-1350

Chapter 4

[4-1] N.R. Howard, *J. Electron. Contr.*, vol. 13, pp. 537, 1962.

[4-2] C.A. Lee, R.A. Logan, R.L.Batdorf, J.J. Kleimack, and W. Wiegmann, Phys. Rev., vol. 134, pp. A761, 1964.

[4-3] R.J. McIntyre, “Multiplication noise in uniform avalanche diodes,” *IEEE Trans. on Electron Dev.*, vol. 13, no. 1, 1966

[4-4] R.J. McIntyre, “The distribution of gains in uniformly multiplying avalanche photodiodes: Theory,” *IEEE Trans. on Electron Dev.*, vol. ED-19, pp. 703-713, 1972.

[4-5] R.J. McIntyre, “Factors affecting the ultimate capabilities of high speed avalanche photodiodes and a review of the state-of-the-art,” *Tech. Dig. International Electron Dev. Mtg.*, pp. 213-216, 1973.

[4-6] R.B. Emmons, “Avalanche-Photodiode Frequency Response,” *J. Appl. Phys.*, vol. 38, no. 9, pp. 3705-3714, 1967.

[4-7] R. B. Emmons, and G. Lucovsky, “The Frequency Response of Avalanching Photodiodes,” *IEEE Trans. on Electron Dev.*, vol. 13, no. 3, pp. 297-305, 1966.

[4-8] V. M. Robbins, S. C. Smith, and G. E. Stillman, “Impact Ionization in $Al_xGa_{1-x}As$ for x=0.1-0.4”, Appl. Phys. Lett. 52(4), 25 January, pp. 296-298, 1988.

[4-9] Toshiaki Kagawa, et al., “Dependence of the GaAs/AlGaAs superlattice ionization rate on Al content”, Appl. Phys. Lett. 54(1), 2 January, pp. 33-35, 1988.

[4-10] F-Y. Juang, et al., “Electron and hole impact ionization coefficients in GaAs-$Al_xGa_{1-x}As$ superlattices”, Appl. Phys. Lett. 47(9), 1 November, pp. 972-974, 1985.

[4-11] T. P. Pearsall, “Impact ionization in $Al_xGa_{1-x}As/GaAs$ superlattices”, Appl. Phys. Lett. 73(9), 31 August, pp. 1227-1229, 1998.

[4-12] J. P. R. David, et al, “Avalanche breakdown in $Al_xGa_{1-x}As$ alloys and $Al_{0.3}Ga_{0.7}As$ /GaAs multilayers”, Appl. Phys. Lett. 66(21), 22 May, pp. 2876-2878, 1995.

[4-13] S. A. Plimmer, et al., “Investigation of Impact Ionization in Thin GaAs Diodes”, IEEE Trans. On Electron Devices, Vol 43, No. 7, July 1996.

[4-14] K. F. Li, D. S. Ong, J. P. R. David, R. C. Tozer, G. J. Rees, P. N. Robson, and R. Grey, *Electronics Letters* 34, 18 (1998).

[4-15] D. S. Ong, K. K. Li, G. M. Rees, G. M. Dunn, J. P. R. David, and P. N. Robson, *IEEE Trans. Electron Dev*ices 45, 8 (1998).

[4-16] Kim F. Li, et al., “Avalanche Noise Characteristics of Thin GaAs Structures with Distributed Carrier Generation”, IEEE Trans. On Electron Devices, Vol 47, No. 5, May 2000.

[4-17] K. F. Li, D. S. Ong, J. P. R. David, G. J. Rees, R. C. Tozer, P. N. Robson, and R. Grey, “Avalanche multiplication noise characteristics in thin GaAs p^+-i-n^+ diodes,” *IEEE Trans. Electron Dev*., vol.45, no.10, pp.2102-7, 1998.

[4-18] C. K. Chia, et al., “Impact ionization in AlxGa1-xAs/GaAs single heterostructures”, Journal of Applied Physics, vol. 84, no. 8, pp. 4363-4369, 15 October, 1998.

[4-19] P. Yuan, K.A. Anselm, C. Hu, H. Nie, C. Lenox, A.L. Holmes, B.G. Streetman, J.C. Campbell, and R.J. McIntyre, “A New Look at Impact Ionization-Part II: Gain and Noise in Short Avalanche Photodiodes,” *IEEE Trans. on Electron Dev.*, vol. 46, no. 8, pp. 1632-1639, 1999.

[4-20] C. Hu, K. A. Anselm, B. G. Streetman, and J. C. Campbell, “Noise characteristics of thin multiplication region GaAs avalanche photodiodes,” *Appl. Phys. Lett.*, vol. 69, no. 24, pp. 3734-3736, 1996.

[4-21] K. A. Anselm, S.S. Murtaza, C. Hu, H. Nie, B.G. Streetman, and J.C. Campbell, “A Resonant-Cavity, Separate-Absorption-and-Multiplication, Avalanche Photodiode with Low Excess Noise Factor,” *IEEE Electron Dev. Lett.*, vol. 17, no. 3, pp.91-93, 1996.

[4-22] P. Yuan, O. Baklenov, H. Nie, A. L. Holmes , B.G. Streetman, J. C. Campbell, “High-Speed and Low-Noise Avalanche Photodiode Operating at 1.06 μm,” *IEEE Journal of Selected Topics in Quantum Electronics*, accepted.

[4-23] D. E. Aspnes, S. M. Kelso, R. A. Logan, and R. Bhat, "Optical properties of Al$_x$Ga$_{1-x}$As," J. Appl. Phys., vol. 60, no.2, pp. 754-767, July 1986.

[4-24] T.S. Moss, G.J. Burrell, and B. Ellis, *Semiconductor Opto-Electronics*, John Wiley & Sons, Inc. New York, 1973.

[4-25] Shuling Wang; Sidhu, R.; Karve, G.; Feng Ma; Xiaowei Li; Xiaoguang Zheng; Hurst, J.B.; Xiaoguang Sun; Ning Li; Holmes, A.L., Jr.; Campbell, J.C., “A study of low-bias photocurrent gradient of avalanche photodiodes,” Electron Devices, IEEE Transactions on ,Volume: 49 , Issue: 12 , Dec. 2002, Pages:2107 - 2113

[4-26] H. Ando and H. Kanbe, “Ionization coefficient measurement in GaAs by using multiplication noise measurements”, Solid-State Electron., vol. 24, pp. 629-634, 1981.

[4-27] G. E. Bulman, V. M. Robbins, et al., “Experimental Determination of Impact Ionization Coefficients in (100) GaAs”, IEEE Electron Device Letters, vol. EDL-4, No. 6, June 1983.

[4-28] B. K. Ng, J. P. R. David, S. A. Plimmer, M. Hopkinson, R. C. Tozer, and G. J. Rees, “Impact ionization coefficients of Al$_{0.8}$Ga$_{0.9}$As,” Appl. Phys. Lett. 77, 4374 (2000)

[4-29] J. P. R. David, J. Allam, A. R. Adams, J. S. Roberts, R. Grey, G. J. Rees, and P. N. Robson “Avalanche breakdown in Al$_x$Ga$_{1-x}$As alloys and Al$_{0.3}$Ga$_{0.7}$As/GaAs multilayers,” Appl. Phys. Lett. 66, 2876 (1995)

Chapter 5

[5-1] G.E. Stillman, and C.M. Wolfe, “Avalanche Photodiodes,” *Semiconductors and Semimetals, vol. 12, Infrared Detectors*, New York, Academic, 1977

[5-2] F. Capasso, R. E. Nahory, M. A. Pollack, and T. P. Pearsall, “Observation of electronic band-structure effects on impact ionization by temperature tuning,” *Phys. Rev. Lett.*,vol. 39, no.11, pp.723-726, 1977

[5-3] F. Capasso, R. E. Nahory, and M. A. Pollack, “Temperature dependence of impact ionisation rates in GaAs between 20 degrees and 200 degrees C,” *Electron. Lett.*,vol.15 no.4, pp. 117-118, 1979

[5-4] G. E. Bulman, V. M. Robbins, K. F. Brennan, K. Hess, and G. E. Stillman, “Experimental determination of impact ionization coefficients in (100) GaAs,” *IEEE Electron Dev. Lett.*, vol. 4, no. 6, pp. 181-185, 1983

[5-5] G. E. Bulman, V. M. Robbins, and G. E. Stillman, “The Determination of Impact Ionization Coefficients in (100) Gallium Arsenide Using Avalanche Noise and Photocurrent Multiplication Measurements,” *IEEE Trans. Electron Dev.*, vol. 32, no. 11, pp. 2454-2466, 1985

[5-6] V. M. Robbins, S. C. Smith, and G. E. Stillman, “Impact ionization in $Al_xGa_{1-x}As$ for x=0.1–0.4,” *Appl. Phys. Lett.*, vol. 52, no. 4, pp. 2996-2998, 1988.

[5-7] N.R. Howard, *J. Electron. Contr.*, vol. 13, pp. 537, 1962

[5-8] C.A. Lee, R.A. Logan, R.L.Batdorf, J.J. Kleimack, and W. Wiegmann, *Phys. Rev.*, vol. 134, pp. A761, 1964

[5-9] R.J. McIntyre, “Multiplication noise in uniform avalanche diodes,” *IEEE Trans. on Electron Dev.*, vol. 13, no. 1, 1966

[5-10] R.J. McIntyre, “The distribution of gains in uniformly multiplying avalanche photodiodes: Theory,” *IEEE Trans. on Electron Dev.*, vol. ED-19, pp. 703-713, 1972

[5-11] R.J. McIntyre, “Factors affecting the ultimate capabilities of high speed avalanche photodiodes and a review of the state-of-the-art,” *Tech. Dig. International Electron Dev. Mtg.*, pp. 213-216, 1973.

[5-12] R.B. Emmons, “Avalanche-Photodiode Frequency Response,” *J. Appl. Phys.*, vol. 38, no. 9, pp. 3705-3714, 1967

[5-13] R. B. Emmons, and G. Lucovsky, “The Frequency Response of Avalanching Photodiodes,” *IEEE Trans. on Electron Dev.*, vol. 13, no. 3, pp. 297-305, 1966

[5-14] J. C. Campbell, S. Chandrasekhar, W. T. Tsang, G. J. Qua, and B. C. Johnson, " Multiplication noise of wide-bandwidth InP/InGaAsP/InGaAs avalanche photodiodes," *J. Lightwave Technology*, vol. 7, no. 3, pp. 473-477, March, 1989

[5-15] C. Hu, K. A. Anselm, B. G. Streetman, and J. C. Campbell, "Noise characteristics of thin multiplication region GaAs avalanche photodiodes," *Appl. Phys. Lett*., vol. 69, no. 24, pp.3734-3736, Dec. 1996

[5-16] K. F. Li, D. S. Ong, J. P. R. David, G. J. Rees, R. C. Tozer, P. N. Robson, and R. Grey, “Avalanche multiplication noise characteristics in thin GaAs p^+-i-n^+ diodes,” *IEEE Trans. Electron Dev*., vol.45, no.10, pp.2102-7, 1998

[5-17] K.F. Li, D.S. Ong, J.P.R. David, R.C. Tozer, G.J. Rees, P.N. Robson, and R.Grey, “Low Excess Noise Characteristics in Thin Avalanche Region GaAs Diodes,” *Electron. Lett*., vol. 34, no. 1, pp. 125, 1997

[5-18] R.J. McIntyre, “A New Look at Impact Ionization-Part I: A Theory of Gain, Noise, Breakdown Probability, and Frequency Response,” *IEEE Trans. on Electron Dev.*, vol. 46, no. 8, pp. 1623-1631, 1999

[5-19] P. Yuan, K.A. Anselm, C. Hu, H. Nie, C. Lenox, A.L. Holmes, B.G. Streetman, J.C. Campbell, and R.J. McIntyre, “A New Look at Impact Ionization-Part II: Gain and Noise in Short Avalanche Photodiodes,” *IEEE Trans. on Electron Dev.*, vol. 46, no. 8, pp. 1632-1639, 1999

[5-20] M. M. Hayat, B. E. A. Saleh, and M. C. Teich, "Effects of dead space on gain and noise of double-carrier-multiplication avalanche photodiodes," *IEEE Trans. Electron Dev.,* vol. 39, pp. 546-552, 1992

[5-21] M. M. Hayat, W. L. Sargent, and B. E. A. Saleh, "Effect of dead space on gain and noise in Si and GaAs avalanche photodiodes," *IEEE J. Quantum Electron*.,vol. 28, pp. 1360-1365, 1992

[5-22] J. S. Marsland, R. C. Woods, and C. A. Brownhill, "Lucky drift estimation of excess noise factor for conventional avalanche photodiodes including the dead space effect," *IEEE Trans. Electron Dev*., vol. 39, pp. 1129-1134, 1992

[5-23] J.P.R David, R. Ghin, S. A. Plimmer, G. J. Rees, and R. Grey, Proceedings of the Third European Conference on High Temperature Electronics, (Abindon, UK, 1999), pp. 187

Chapter 6

[6-1] R.J. McIntyre, “Multiplication noise in uniform avalanche diodes,” *IEEE Trans. on Electron Dev.*, vol. 13, no. 1, 1966

[6-2] S. A. Plimmer, J. P. R. David, D. C. Herbert, T. -W. Lee, G. J. Rees, P. A. Houston, R. Greg, P. N. Robson, A. W. Higgs, and D. R. Wight “Investigation of Impact Ionization in Thin GaAs Diodes”, *IEEE Trans. Electron Dev.*, vol 43, No. 7, July 1996

[6-3] K. F. Li, D. S. Ong, J. P. R. David, R. C. Tozer, G. J. Rees, P. N. Robson, and R. Grey, “Low excess noise characteristics in thin avalanche region GaAs diodes,” *Electronics Letters*, vol. 34 No.18th January 1998

[6-4] C. K. Chia, J. P. R. David, G. J. Rees, S. A. Plimmer, R. Grey, and P. N. Robson,, “Impact ionization in $Al_xGa_{1-x}As/GaAs$ single heterostructures”, *Journal of Applied Physics*, vol. 84, no. 8, pp. 4363-4369, 15 October, 1998

[6-5] K. A. Anselm, H. Nie, C. Hu, C. Lenox, P. Yuan, G. Kinsey, J. C. Campbell, and B. G. Streetman, “Performance of Thin Separate Absorption, Charge, and Multiplication Avalanche Photodiodes,” *IEEE J. Quantum Electron*., vol. 34, no. 3, pp. 482-490, 1998

[6-6] K. A. Anselm, P. Yuan, C. Hu, C. Lenox, H. Nie, G. Kinsey, J. C. Campbell, and B. G. Streetman, “Characteristics of GaAs and AlGaAs homojunction avalanche photodiodes with thin multiplication regions,” *Appl. Phys. Lett.* 71 (26), 29 December 1997

[6-7] K. A. Anselm, S.S. Murtaza, C. Hu, H. Nie, B.G. Streetman, and J.C. Campbell, “A Resonant-Cavity, Separate-Absorption-and-Multiplication, Avalanche Photodiode with Low Excess Noise Factor,” *IEEE Electron Dev. Lett.*, vol. 17, no. 3, pp.91-93, 1996

[6-8] P. Yuan, H. Chad, K. A. Anselm, C. Lenox, H. Nie, H. L. Holmes, B. G. Streetman, and J. C. Campbell, "Impact Ionization Characteristics of III-V Semiconductors in a Wide Range of Multiplication Region Thickness," *IEEE J. Quantum Electron.*, vol. 36, no. 2, pp.198-204, Feb, 2000

[6-9] K. Makita, I. Watanabe, M. Tsuji, K. Taguchi, “150 GHz GB-Product and Low dark Current InAlGaAs Quaternary Well Superlattice Avalanche Photodiodes,” Proc. IOOC-95,1995

[6-10] Cohen-Jonathan, C., Giraudet, L., Bonzo, A., and Praseuth, J. P.: ‘Waveguide AlInAs/GaAlInAs avalanche photodiode with a gain-bandwidth product over 160GHz’, *Electron. Lett.*, 1997, vol. 33, no. 17, pp.1492-1493

[6-11] Nie, H., Anselm, K. A., Lenox, C., Yuan, P., Hu, C., Kinsey, G., Streetman, B. G., and Campbell, J. C. “Resonant-cavity separate absorption, charge, and multiplication avalanche photodiodes with high speed and high gain-bandwidth product,” *IEEE Photon. Technol. Lett*., 1998, vol. 10, no. 3, pp. 409-411

[6-12] Lenox, C., Nie, H., Yuan, P., Kinsey, G., Holmes Jr., A. L., Streetman, B. G., and Campbell, J. C. “Resonant-Cavity InGaAs-InAlAs avalanche photodiodes with gain-bandwidth product of 290 GHz,” *IEEE Photon. Technol. Lett*., 1999, vol. 11, no. 9, pp. 1162-1164

[6-13] G. S. Kinsey, J. C. Campbell, and A. G. Dentai, “Waveguide avalanche photodiode with a gain-bandwidth product of 320 GHz”, to be published

[6-14] X. G. Zheng, X. Sun, S. Wang, G. S. Kinsey, A. L. Holmes, B. G. Streetman, and J. C. Campbell, "Avalanche Multiplication Noise of $Al_xGa_{1-x}As$ APDs with High Al concentration and Thin Multiplication Region," *Appl. Phys. Lett.*, to be published

[6-15] P. Yuan, S. Wang, X. Sun, X. G. Zheng, A. L. Holmes, Jr., and J. C. Campbell, "Avalanche photodiodes with an impact-ionization-engineered multiplication region," *IEEE Photo. Tech. Lett.*, vol.12, pp. 1370-1372 (2000)

[6-16] S. Wang, R. Sidhu, X. G. Zheng, X. Sun, A.L. Holmes, Jr., and J. C. Campbell, "Low noise avalanche photodiodes with a graded Impact-Ionization-Engineered multiplication region", *Photonics Technology Letters,* submitted

[6-17] Wang, S.; Sun, X.; Zheng, X.G.; Holmes, A.L.; Campbell, J.C.; Yuan, P., "Avalanche photodiodes with an impact-lonization-engineered multiplication region," *Lasers and Electro-Optics Society 2000 Annual Meeting, 13th Annual Meeting*, Volume 1 , 2000, Page(s): 9 –10

[6-18] Z. L. Liau and D. E. Mull, "Wafer fusion: A novel technique for optoelectronic device fabrication and monolithic integration", *Appl. Phys. Lett.* 56 (8), 19 Feburary 1990, pp 737-739

[6-19] A. Black, A. R. Hawkins, N. M. Margalit, D. I. Babic, A. L. Holmes, Jr., Y.-L. Chang, P. Abraham, J. E. Bowers, and E. L. Hu, "Wafer Fusion: Material Issues and Device Results," *IEEE Journal of Selected Topics in Quantum Electronics*, vol. 3, no. 3, pp. 943-952, June 1997

[6-20] F. Salomonsson, K. Streubel, J. Bentell, M. Hammar, D. Keiper, and R. Westphalen, "Wafer fused *p*-InP/*P*-GaAs heterojunctions," *J. Appl. Phys.* 83 (2), pp. 768-774, 15 January 1998

[6-21] G. Patriarche, F. Jeannes, J.-L. Oudar, and F. Glas, "Structure of the GaAs/InP interface obtained by direct wafer bonding optimsed for surface emitting optical devices," *J. Appl. Phys.* 82 (10), pp.4892-4903, 15 November 1997

[6-22] Z.-H. Zhu, Felix E. Ejeckam, Y. Qian, Jizhi Zhang, Zhenjun Zhang, Gina L. Christenson, and Y. H. Lo, "Wafer Bonding Technology and Its Applications in Optoelectronic Devices and Materials," *IEEE Journal of Selected Topics in Quantum Electronics*, vol. 3, no. 3, pp. 927-936, June 1997

[6-23] Hiroshi Wada, Yoh Ogawa, and Takeshi Kamijoh, "Electricl characteristics of directly-bonded GaAs and InP," *Appl. Phys. Lett.*, 62 (7), pp. 738-740, 15 Feb. 1993

[6-24] Hawkins, A. R., Wu, W., Abraham, P., Streubel, K., and Bowers, J. E.: ‘High gain-bandwidth product silicon heterointerface photodetector’, *Appl. Phys. Lett.*, 1997, vol. 70, no. 3, pp. 303-305

Chapter 7

[7-1] Y. Shao, R.W. Silverman, R. Farrell, L. Cirignano, R. Grazioso, K. S. Shah, G. Visser, M. Clajus, T. O. Tummer, S. R. Cherry, “Design Studies of A High Resolution PET Detector Using APD Arrays”, IEEE Trans. On Nuclear Science, Vol. 47, No. 3, 1051-1057, June 2000

[7-2] S. Vasile, R. J. Wilson, S. Shera, D. Shamo, M. R. Squillante, “High Gain Avalanche Photodiode Arrays for DIRC Applications”, IEEE Trans. On Nuclear Science, Vol. 46, No. 3, 848-852, August 1999

[7-3] R. F. Grazioso, R. Farrell, L. Cirignano, K. Shah, “APD Arrays for Scintillating Fiber Readout”, Nuclear Science Symposium, IEEE Vol. 2, 722 –724, 1999

[7-4] E. Gramsch, M. Szawlowski, S. Zhang, and M. Madden, “Fast, High Density Avalanche Photodiode Array”, IEEE Trans. On Nuclear Science, Vol. 41, No. 4, 762-766, August 1994

[7-5] R. S. Balcerak, “3D imaging”, 3D imaging Receivers SPIE Conference, April, 2000

[7-6] K. Makita, I. Watanabe, M. Tsuji, K. Taguchi, “150 GHz GB-Product and Low dark Current InAlGaAs Quaternary Well Superlattice Avalanche Photodiodes,” Proc. IOOC-95,1995

[7-7] Cohen-Jonathan, C., Giraudet, L., Bonzo, A., and Praseuth, J. P.: ‘Waveguide AlInAs/GaAlInAs avalanche photodiode with a gain-bandwidth product over 160GHz’, *Electron. Lett.*, 1997, vol. 33, no. 17, pp.1492-1493

[7-8] Nie, H., Anselm, K. A., Lenox, C., Yuan, P., Hu, C., Kinsey, G., Streetman, B. G., and Campbell, J. C. “Resonant-cavity separate absorption, charge, and multiplication avalanche photodiodes with high speed and high gain-bandwidth product,” *IEEE Photon. Technol. Lett.*, 1998, vol. 10, no. 3, pp. 409-411

[7-9] Lenox, C., Nie, H., Yuan, P., Kinsey, G., Holmes Jr., A. L., Streetman, B. G., and Campbell, J. C. “Resonant-Cavity InGaAs-InAlAs avalanche photodiodes with gain-bandwidth product of 290 GHz,” *IEEE Photon. Technol. Lett.*, 1999, vol. 11, no. 9, pp. 1162-1164

[7-10] G. S. Kinsey, J. C. Campbell, and A. G. Dentai, "Waveguide avalanche photodiode with a gain-bandwidth product of 320 GHz", IEEE Photonics Technology Letters, Vol. 13, Issue 8, 842-844, August 2001

[7-11] K. Kato, "Ultrawide-Band/High-frequency Photodetectors," IEEE Trans. on Microwave Theory and Techniques, Vol. 47, no. 7, 1265-1281, July 1999

[7-12] J. N. Hollenhorst, "Frequency Response Theory for Multilayer Photodiodes," IEEE Journal of Lightwave Technology, Vol. 8, No. 4, pp. 531-537, April 1990

Chapter 8

[8-1] G. S. Kinsey, J. C. Campbell, and A. G. Dentai, "Waveguide avalanche photodiode with a gain-bandwidth product of 320 GHz", IEEE Photonics Technology Letters, Vol. 13, Issue 8, 842-844, August 2001

[8-2] Geoff S. Kinsey, "Waveguide Avalanche Photodetectors," Ph.D. Dessertation, The University of Texas at Austin, Chapter 8, p. 36.

[8-3] H.S. Kim, J.H. Choi, H.M. Bang, Y. Jee, S.W. Yun, J. Burm, M.D. Kim, and A.G. Choo, "Dark current reduction in APD with BCB passivation", Electronics Letters, pp 455-457, *29*,Vol. 37, no. 7, March 2001

[8-4] D. Schmidt and D. Trommer, "Conservation of low dark current of InGaAs photodiodes after NH_3F/HF etch a BCB passivation layer", Indium Phosphide and Related Materials, 2000 Conference Proceedings, Page 302 -305

[8-5] M. Hayashi, I. Wantababe, T. Nakata, M. Tsuji, K. Makita, S. Yamakata, and K. Taguchi, "Microlens-Integrated Large-Area InAlGaAs-InAlAs Superlattice APD's for Eye-Safety 1.5-μm Wavelength Optical Measurement Use", IEEE Photonics Technology Letters, pp 576-578 Vol. 10, no. 4, April 1998

[8-6] Lenox, C., Nie, H., Yuan, P., Kinsey, G., Holmes Jr., A. L., Streetman, B. G., and Campbell, J. C. "Resonant-Cavity InGaAs-InAlAs avalanche photodiodes with gain-bandwidth product of 290 GHz," *IEEE Photon. Technol. Lett.*, 1999, vol. 11, no. 9, pp. 1162-1164

[8-7] Humphreys, D. A., King, R. J.: 'Measurement of absorption coefficients of $Ga_{0.47}In_{0.53}As$ over the wavelength range 1.0-1.7μm', *Electron. Lett.*, 1985, vol. 21, no. 25/26, pp. 1187-1189

[8-8] Bacher, F. R., Blakemore, J. S., Ebner, J. T., Arthur, J. R.: 'Optical-absorption coefficient of $In_{1-x}Ga_xAs$/InP', *Phys. Rev. B*, 1988, vol. 37, no. 5, pp.2551-25

[8-9] Lenox, C., Yuan, P., Nie, H., Baklenov, O., Hansing, C., Campbell, J. C., Holmes Jr., A. L., Streetman, B. G.: ‘Thin multiplication region InAlAs homojunction avalanche photodiodes’, *Appl. Phys. Lett*., 1998, vol. 73, no. 6, pp. 783-784

[8-10] Kagawa, T., Kawamura, Y., and Iwamura, H., ‘A wide-bandwidth low-noise InGaAsP-InAlAs superlattice avalanche photodiode with a flip-chip structure for wavelength of 1.3μm and 1.55μm’, IEEE J. Quantum Electron., 1993, **29**, pp 1387-1392

[8-11] Makita, K., Watanabe, I., Tsuji, M., and Taguchi, K., “Dark current and breakdown analysis in In(Al)GaAs/InAlAs superlattice avalanche photodiodes”, Jpn. J. Appl. Phys., 1996, 35, pp. 3440-3444

Chapter 9

[9-1] A. H. Gnauck, “Recent progress in high capacity long-haul WDM system,” in OFC’96, Tech. Dig., paper TU15

[9-2] L. D. Tzeng, O. Mizuhzra, et. al., “A High-Sensitivity APD Receiver for 10-Gb/s System Applications,” IEEE Photonics Technology Letters, vol. 8, no. 9, September, 1996, pp. 1229-1231

[9-3] T. Y. Yun, M. S. Park, et. al., “10-Gigabit-per-second high-sensitivity and wide-dynamic-range APD-HEMT optical receiver,” IEEE Photonics Technology Letters, 1996, 8, pp. 1232-1234

[9-4] T. Nakata, T. Takeuchi, I. Watanabe, K. Makita, and T. Torikai, “10Gbit/s high sensitivity, low-voltage-operation avalanche photodiodes with thin InAlAs multiplication layer and waveguide structure,” Electronics Letters, pp. 2033-2034, vol. 36, no. 24, 23rd, November 2000

[9-5] H. Matsuda, A. Miura, et. al., “High-sensitivity and wide-dynamic-range 10 Gbit/s APD/preamplifier optical receiver module,” Electronics letters, 20th June, vol.38, no. 13, pp.650-651

[9-6] Nie, H., Anselm, K. A., Lenox, C., Yuan, P., Hu, C., Kinsey, G., Streetman, B. G., and Campbell, J. C. “Resonant-cavity separate absorption, charge, and multiplication avalanche photodiodes with high speed and high gain-bandwidth product,” *IEEE Photon. Technol. Lett*., 1998, vol. 10, no. 3, pp. 409-411

[9-7] Lenox, C., Nie, H., Yuan, P., Kinsey, G., Holmes Jr., A. L., Streetman, B. G., and Campbell, J. C. “Resonant-Cavity InGaAs-InAlAs avalanche photodiodes with gain-bandwidth product of 290 GHz,” *IEEE Photon. Technol. Lett.*, 1999, vol. 11, no. 9, pp. 1162-1164

[9-8] G. S. Kinsey, J. C. Campbell, and A. G. Dentai, “Waveguide avalanche photodiode with a gain-bandwidth product of 320 GHz”, IEEE Photonics Technology Letters, Vol. 13, Issue 8, 842-844, August 2001

[9-9] J. S. Ng, J. P. R. David, and G. J. Rees, “Avalanche breakdown voltage of $In_{0.53}Ga_{0.47}As$,” Journal of Applied Physics, vol. 91, no. 8, 15 Apr. 2002, pp. 5200-5202

Chapter 10

[10-1] C. Cohen-Jonathan, L. Giraudet, A. Bonzo and J.P. Praseuth, “Waveguide AlInAs/GaAlInAs avalanche photodiode with a gain-bandwidth product over 160 GHz”, Electron. Lett., 1997, 33, (17), pp. 1492-1493

[10-2] T. Nakata, T. Takeuchi, K. Makita, T. Torikai, “High-speed and high-sensitivity waveguide InAlAs avalanche photodiode for 10-40 Gb/s recievers”, Proc. LEOS’01, San Diego, USA, November 2001, paper ThN3, pp. 770-771

[10-3] G. S. Kinsey, J.C. Campbell and A.G. Dentai, “Waveguide Avalanche Photodiode Operating at 1.55 μm with a Gain-Bandwidth Product of 320 GHz,” IEEE Photonics tech. lett., 2001, 13, (8), pp. 842-844

[10-4] J. Wei, F. Xia, S.R. Forrest, “A High-Responsivity High-Bandwidth Asymmetric Twin-Waveguide Coupled InGaAs-InP-InAlAs Avalanche Photodiode,” IEEE Photonics tech. lett., 2002, 14, (11), pp. 1590-1592

[10-5] S. Demiguel, N. Li, X. Li, X. Zheng, J. Kim, J. C. campbell, H. Lu, and K. A. Anselm, “Very high-responsivity evanescently-coupled photodiodes integrating a short planar multimode waveguide for high-speed applications,” IEEE Photonics Tech. Lett., 2003, 15, (12)

[10-6] G. S. Kinsey, “Waveguide avalanche photodiode,” Ph. D. Dissertation, chapter 9, pp. 42-57

Vita

Xiaoguang Zheng (郑晓光) was born in Hebei, China, on July 24th, 1963, the son of Xue-ping Zheng (郑学平) and Shu-yuan He (何淑媛). Upon graduating from Affiliated Middle School of the Hebei General University, Hebei, China, in 1981, he entered Beijing Institute of Technology (BIT), where he received his B.S. degree in Electrical Engineering in 1985. He entered Hebei Semiconductor Research Institute (HSRI) in 1988 for his graduate study on high-speed III-V compound microelectronics, where he received his M.S.E.E. degree in Electrical Engineering in 1991. In August 1999, he joined the Microelectronics Research Center of the University of Texas at Austin for his Ph.D. degree.

Permanent Address

20975 Valley Green Drive, #301

Cupertino, CA 95014

U.S.A

This dissertation was typed by the author.